UNIVERSITY OF SOUTHAMPTON

FACULTY OF NATURAL AND ENVIRONMENTAL SCIENCES

Department of Chemistry

Volume 1 of 1

The Electrochemical Reduction of Oxygen in Room Temperature Ionic Liquids for use in a Lithium-Air Battery

by

Andrew William Lodge

Thesis for the Degree of Doctor of Philosophy

December 2014

UNIVERSITY OF SOUTHAMPTON

ABSTRACT

FACULTY OF NATURAL AND ENVIRONMENTAL SICENCES

Chemistry

Thesis for the Degree of Doctor of Philosophy

THE ELECTROCHEMICAL REDUCTION OF OXYGEN IN ROOM TEMPERATURE IONIC LIQUIDS FOR USE IN A LITHIUM-AIR BATTERY

Andrew William Lodge

Experiments were undertaken to investigate the electrochemical reduction of oxygen (O_2) in various room temperature ionic liquids (RTILs) with the aim of using a RTIL as an electrolyte in a lithium-air battery cell. Cyclic voltammetry (CV) in oxygenated RTILs was undertaken at Au and Pt microdisc electrodes. It was confirmed that the reduction of O_2 in pyrrolidinium based RTILs occurs in two one-electron reduction steps, from O_2 to superoxide ($O_2^{\bullet -}$) and from $O_2^{\bullet -}$ to peroxide (O_2^{2-}). It was found that the reduction of O_2 was fully reversible in pyrrolidinium based ionic liquids. It was found that the O_2 reduction reaction was unstable in imidazolium based RTILs, due to the reaction of $O_2^{\bullet -}$ with the imidazolium cations.

The diffusion coefficient (D_O) and solubilities (c_O) of O_2 in the RTILs were found at various temperatures at Au and Pt microelectrodes using potential step chronoamperometry (PSCA). It was found that D_O increases with temperature, due to the decreasing viscosity of the RTIL, while c_O in RTILs decreases with temperature. It was found that attaching fluorine groups to the anion of the RTIL increased c_O but also increased the viscosity and decreased D_O. The most suitable RTIL for use in the lithium-air battery was found to be 1-butyl-1-methyl pyrrolidinium Nonafluorobutylsulfonyl(trifluoromethylsulfonyl)imide.

Attempts were made to measure D_O and c_O in the RTILs containing significant concentrations of Li^+. The presence of Li^+ caused the formation of a passivating layer of lithium peroxide (Li_2O_2) on the working electrode, complicating the interpretation of the PSCA results. It was found that the addition of the Lewis acid tris(pentafluorophenyl)borane (TPFPB) increased the solubility of Li_2O_2 to a slight degree; however the increase was not sufficient to prevent electrode passivation. TPFPB also increased the viscosity of the RTIL and therefore decrease the value of D_O.

Experiments were undertaken to determine accurate values of D_O and c_O by measuring the pressure drop in a sealed vessel containing the RTIL and O_2. This method was also used to investigate the effect of a redox shuttle compound, reduced ethyl viologen ditriflate $[EtV]^+$, on the values of D_O and c_O. It was also found that the free volume of the RTIL influences D_O. The greater amount of free volume present in the RTIL, the faster O_2 is able to diffuse through the RTIL. It was also found that the presence of small quantities of $[EtV]^+$ increased the effective value of D_O, but large quantities decreased D_O due to the increasing viscosity. A novel optical method of measuring D_O was examined using the absorbance of $[EtV]^+$ as an oxygen indicator.

Table of Contents

List of Figures

List of Tables

DECLARATION OF AUTHORSHIP

I, Andrew William Lodge declare that this thesis and the work presented in it are my own and has been generated by me as the result of my own original research.

The Electrochemical Reduction of Oxygen in Room Temperature Ionic Liquids for use in a Lithium-Air Battery.

I confirm that:

1. This work was done wholly or mainly while in candidature for a research degree at this University;

2. Where any part of this thesis has previously been submitted for a degree or any other qualification at this University or any other institution, this has been clearly stated;

3. Where I have consulted the published work of others, this is always clearly attributed;

4. Where I have quoted from the work of others, the source is always given. With the exception of such quotations, this thesis is entirely my own work;

5. I have acknowledged all main sources of help;

6. Where the thesis is based on work done by myself jointly with others, I have made clear exactly what was done by others and what I have contributed myself;

7. Parts of this work have been published as: A. W. Lodge, M. J. Lacey, M. Fitt, N. Garcia-Araez, J. R. Owen, Critical appraisal on the role of catalysts for the oxygen reduction reaction in lithium-oxygen batteries, *Electrochimica Acta*, **2014**, *140*, 168-173, DOI: 10.1016/j.electacta.2014.05.026

Signed:.....

Date: .....

Acknowledgements

This thesis and the work contained within would not have been possible without the support and assistance of many people.

Firstly I would like to thank my supervisor, Professor John Owen, for his years of help, teaching and guidance during my Ph.D. His expertise, experience, insights and knowledge have been invaluable and have inspired me during this project.

I would also like to thank Doctor Nuria Garcia-Araez for her help, assistance and insight during my Ph.D. as well as for imparting her knowledge to me.

I would like to thank all past and present members of the Owen group for their help, assistance, friendship and kindness during my Ph.D., as well as all members of the Southampton Electrochemistry Section for their help and encouragement over the past four years.

I am indebted to the European Commission for funding this Ph.D. under the FP7 Framework, FP-7-2010-GC-Electrochemcial Storage Contract no. 265971.

I would like to thank all our partner members in the LABOHR project, especially those from the Passerini Group at Westfälische Wilhelms-Universität, Münster, Germany for providing the room temperature ionic liquids used in this experiment, and the Mastragostino Group at Università di Bologna, Bologna, Italy for allowing me to undertake training in electrochemical techniques.

I would like to thank my undergraduate project students Matt Fitt and Michael Leyland for their experimental help and assistance in the laboratory during their undergraduate research projects.

I would like to thank my parents and brothers for their love, encouragement and support during my Ph.D. Project.

Finally I would like to thank Marta for all her love, patience, guidance and encouragement during my project.

List of Abbreviations

Acronym	Meaning
AC	Alternating Current
b.p.	Boiling Point
BETI	Bis(perfluoroethylsulfonyl)imide
C_2MIM	1-ethyl-3-methyl imidazolium
C_4MIM	1-butyl-3-methyl imidazolium
CA	Chronoamperogram
CV	Cyclic Voltammogram
DC	Direct Current
EIS	Electrochemical Impedance Spectroscopy
EtV $(OTf)_2$	Ethyl Viologen Ditriflate
Fc	Ferrocene
FSI	Fluorosulfonylimide
GC	Glassy Carbon
IL	Ionic Liquid
IM_{14}	Nonafluorobutylsulfonyl(trifluoromethylsulfonyl)imide
LABOHR	Lithium-Air Battery with Split Oxygen Harvesting and Redox processes
LiTFSI	Lithium bis(trifluoromethylsulfonyl)imide
m.p.	Melting Point
PSCA	Potential Step Chronoamperometry
PYR_{12O1}	1- methoxyethyl-1-methyl pyrrolidinium
PYR_{14}	1-butyl-1-methyl pyrrolidinium
RTIL	Room Temperature Ionic Liquid

SEI	Solid-Electrolyte Interface
SPEIS	Staircase Potentio-Electrochemical Impedance Spectroscopy
TFSI	Bis(trifluoromethylsulfonyl)imide
TPFPB	Tris(pentafluorophenyl)borane
WWU	Westfälische Wilhelms Universität

List of Symbols

Symbol	Explanation	Units
a	Hydrodynamic Radius	cm
A	Surface Area of Electrode	cm^2
A	Surface Area of Ionic Liquid	cm^2
c	Bulk Concentration of Electroactive Species	mol cm^{-3}
C	Capacitance	F
C_{DL}	Double Layer Capacitance	F
c_O	Concentration of O_2	mol cm^{-3}
c_{Ox}	Bulk Concentration of Oxidised Species	mol cm^{-3}
c_{Red}	Bulk Concentration of Reduced Species	mol cm^{-3}
C_x	x-axis Intercept	$s^{-1/2}$
$c_{x=t=0}$	Concentration of Gas at Interface at the Start of the Experiment	mol cm^{-3}
Cy	Y-axis Intercept of Cottrell Plot	A
D	Diffusion Coefficient of a Species	cm^2 s^{-1}
d	Density	g cm^{-3}
D_{0K}	Diffusion Coefficient of O_2 at a temperature of zero K	cm^2 s^{-1}
D_O	Diffusion Coefficient of O_2	cm^2 s^{-1}
D_{Ox}	Diffusion Coefficient of Oxidised Species	cm^2 s^{-1}
D_{Red}	Diffusion Coefficient of Reduced Species	cm^2 s^{-1}
E	Potential	V
E^0	Standard Potential of Redox Couple	V
F	Faraday Constant	96485.3 C mol^{-1}
f	Frequency	Hz

$\boldsymbol{FW}$	Formula Weight	g mol^{-1}
$\boldsymbol{G}$	Gibbs Free Energy	J mol^{-1}
$\boldsymbol{I}$	Current	A
$\boldsymbol{I_P}$	Peak Current	A
$\boldsymbol{I_{SS}}$	Steady State Current at a Microdisc Electrode	A
$\boldsymbol{J}$	Flux	mol cm^{-2} s^{-1}
$\boldsymbol{k_B}$	Boltzmann Constant	1.38×10^{-23} J K^{-1}
$\boldsymbol{k_H}$	Henry's Law Constant	Pa, Bar, Pa mol^{-1}
$\boldsymbol{Ks}$	Solubility Product Constant	-
$\boldsymbol{L}$	Length of Diffusion Field	cm
$\boldsymbol{M}$	Total Amount of Gas Diffused into a Solution at Time = t	mol
$\boldsymbol{m}$	Slope of Plot of Δp vs. $t^{1/2}$	Pa $s^{-1/2}$
$\boldsymbol{Mr}$	Relative Mass of a Substance	g mol^{-1}
$\boldsymbol{M_t}$	Total Amount of Gas Diffused into Ionic Liquid at time = t	mol cm^{-2}
$\boldsymbol{n}$	Number of Electrons Transferred	-
$\boldsymbol{p}$	Pressure	Pa or Bar
$\boldsymbol{r}$	Radius of Electrode	cm
$\boldsymbol{R}$	Ideal Gas Constant	8.314 J K mol^{-1} or 8.314×10^{-3} cm^3 kPa K^{-1} mol^{-1}
$\boldsymbol{R}$	Resistance	Ω
$\boldsymbol{R_{CT}}$	Charge Transfer Resistance	Ω
$\boldsymbol{R_S}$	Solution Resistance	Ω
$\boldsymbol{S}$	Slope of Cottrell Plot	A $s^{1/2}$
$\boldsymbol{T}$	Temperature	K
$\boldsymbol{t}$	Time	s

V	Volume	cm^3
W_D	Warburg Diffusion	-
x	Length of Diffusion Field	cm
Z'	Real Impedance	Ω
Z''	Imaginary Impedance	Ω
Zw	Warburg Impedance	Ω
η	Viscosity	cP
θ	Bode Plot Impedance Phase Shift	Degrees
κ	Conductivity	$S\ cm^{-1}$
v	Scan Rate	$mV\ s^{-1}$
σ	Conductivity	$mS\ cm^{-1}$
σ	Slope of Warburg Impedance on Nyquist Plot	$\Omega\ s^{-1/2}$

1. Introduction and Background

Over the last decade many portable handheld devices such as MP3 players, smartphones and tablet computers have become commonplace in modern society. The lithium-ion (Li-ion) battery has been crucial in allowing this revolution in portable devices. The lithium-ion battery uses lithium to generate energy, giving a high specific capacity, specific energy[1,2] and rechargeability that allows these batteries to power almost all laptop computers, mobile phones, portable music players and other handheld electronic devices currently in use today. Lithium-ion batteries have also been used in electric vehicles such as the Tesla Roadster fully electric car or the Chevrolet Volt plug-in hybrid. The current lithium-ion technology is perfect for use in small handheld devices but it has major drawbacks when applied to fully electric vehicles. Current battery powered vehicles are unable to compete with current motor engine vehicles on power, range, rechargeability and cost. A lithium-ion battery needs to power an electric vehicle for a range of over 500 km on a single charge to compete with petrol or diesel fuelled vehicles.[3] Current lithium-ion technology has insufficient power, capacity and rechargeability to fulfil these requirements.[3] Because of this we must turn to alternative lithium battery technologies. Lithium-air (Li-air) and lithium-oxygen (Li-O_2) batteries are the most promising battery technologies currently under development. Lithium-air and lithium-oxygen batteries use the reaction of lithium with oxygen usually taken from the atmosphere to give an electrical potential of approximately 3 volts.[4–7] As O_2 is not stored inside the battery, this reduces the weight and gives the battery a high specific energy and specific capacity based on the weight of lithium alone.[8] Li-air batteries use the oxygen extracted directly from the air, while Li-O_2 batteries use O_2 provided from an on-board source, such as a cylinder of O_2. Theoretically a lithium-air battery can give a similar specific capacity to petroleum fuel[9–11] and so lithium-air battery powered vehicles could be viable competitors to petrol driven vehicles.

1.1 Lithium Batteries

A battery cell is a device used for converting chemical energy into electrical energy. A single cell consists of two electrodes separated by an electrically insulating, ionically conductive electrolyte.[12,13] The negative electrode is known as the anode during discharge when it is oxidised and donates electrons to the external circuit. The positive electrode is known as the cathode during discharge when it is reduced by accepting electrons from the external circuit. Many cells are usually connected together in series to form a complete battery. During discharge cations move from the anode to the cathode *via* the electrolyte. To counteract the movement of the positively charged cations, negatively charged electrons move from the anode to the cathode *via* the external circuit. This creates a current, used to power the device to which the battery is attached.

The potential of each electrode is given by the Gibbs free energy of the electrochemical reaction as shown in Equation 1.1 where G is the Gibbs free energy in J mol^{-1}, n is the number of electrons transferred, F is the Faraday constant, 96485.3 C mol^{-1} and E is standard potential in volts (V).

$$\Delta G = -nFE \quad \textbf{(1.1)}$$

The greater difference between the potentials of the electrodes, the greater the voltage of the cell.[2] This is given by Equation 1.2, where E is the standard potential in V.

$$E_{Cell} = E_{Anode} - E_{Cathode} \quad \textbf{(1.2)}$$

The theoretical capacity of the cell is a measure of the amount of energy of the cell given in units of ampere-hours (Ah) or coulombs (C). This is determined by the amount of active material in the cell. The theoretical capacity of a cell is usually larger than the actual measured capacity due to inefficiencies in the cell such as internal resistance, the overpotential of the cell and inefficient reaction kinetics.

The theoretical energy of the cell, usually expressed in watt-hours (Wh), is a measure of the total useful energy of the cell as given by Equation 1.3.

$$Watthour\,(\mathrm{Wh}) = voltage\,(\mathrm{V}) \times ampere\text{-}hour\,(\mathrm{Ah}) \qquad \textbf{(1.3)}$$

The specific energy of a cell is a measure of the amount of energy per gram of active material in the cell, given in Wh g^{-1}.

There are many different battery technologies which are currently available or under development for many applications. The specific energies and specific powers of the batteries are shown in the Ragone plot (Figure 1.1).

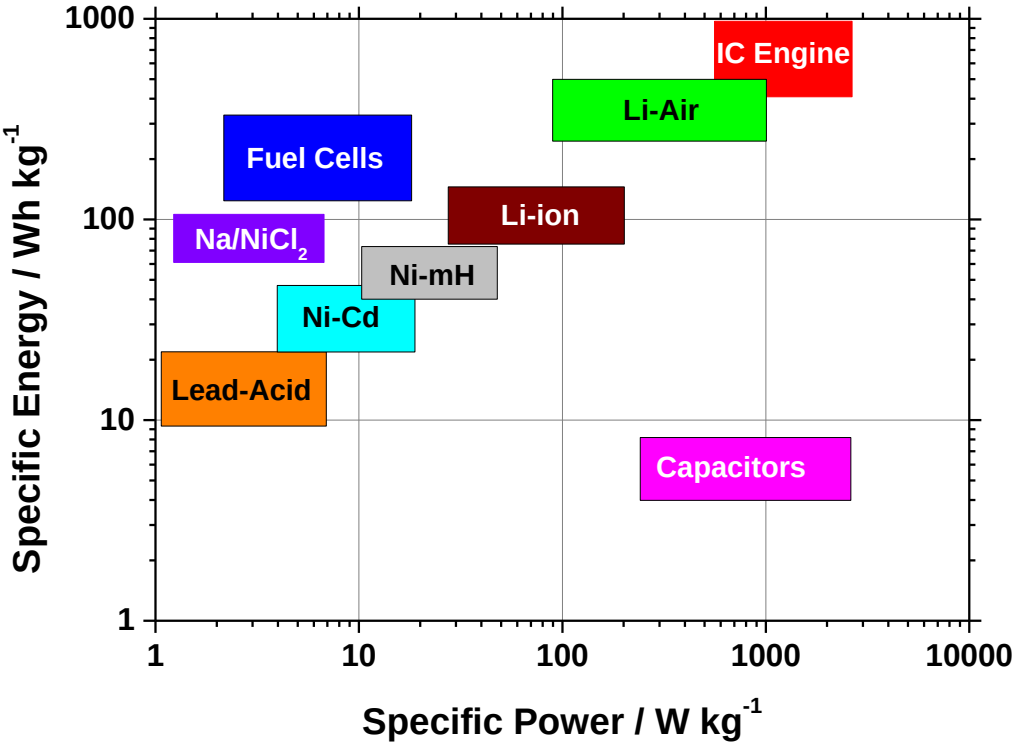

Figure 1.1: Ragone plot showing the specific energies and specific powers of various battery technologies. The values were taken from references.[10,11] IC engine = Internal Combustion Engine.

The lithium-ion battery was first commercially developed in 1991 by Sony and Asahi Kasei using a graphite anode, a lithium cobalt oxide cathode and a carbonate electrolyte.[2,14] Since then lithium-ion batteries have become commonplace in almost all handheld and portable electrical devices.

During discharge, lithium atoms are oxidised and move out of the negative electrode (anode) structure into the electrolyte. The lithium cations move through the electrolyte to the positive electrode (cathode) where they intercalate into the structure and are

reduced. While this occurs, electrons also move from the anode to the cathode *via* the external circuit, powering the device attached to the battery.[1,2] During recharge, an external current is applied to the battery changing the polarity of the electrodes. This causes the lithium to deintercalate from the cathode and travel back through the electrolyte to the anode. This recharges the battery ready for another discharge. This intercalation mechanism is known as the "Rocking chair" mechanism.[1,15,16] A schematic of a general lithium-ion battery is shown in Figure 1.2.

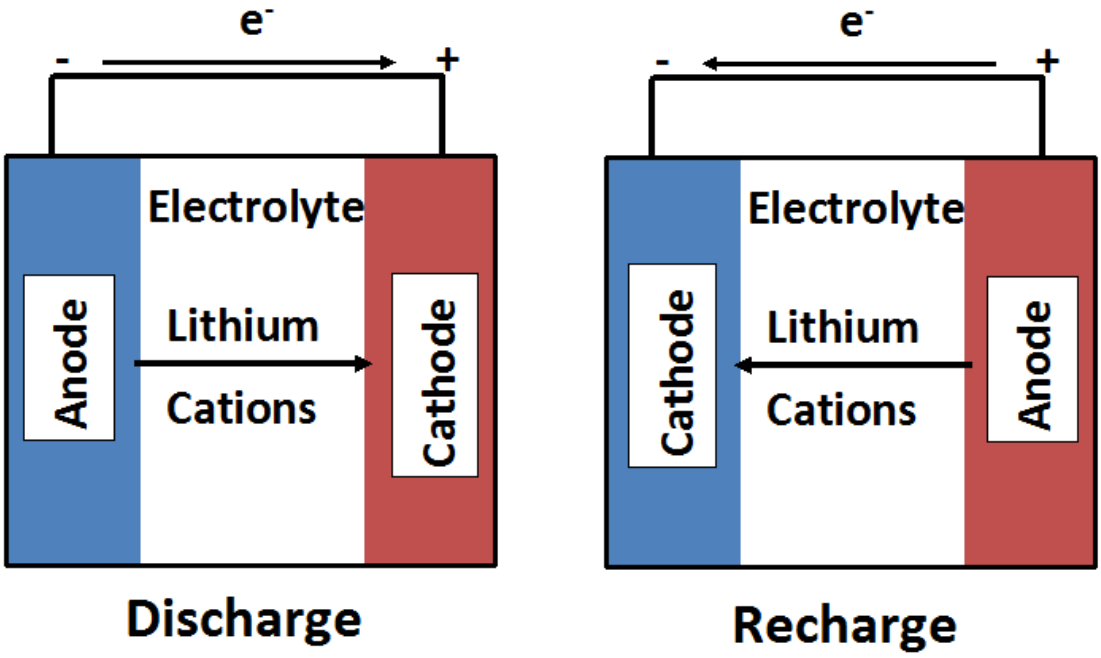

Figure 1.2: schematic of a lithium-ion battery, one of the most commonly used batteries for portable electrical devices.

In lithium-ion cells the negative electrode (anode during discharge) is usually an intercalation compound such as graphite[1,15] containing lithium atoms intercalated into the crystal structure. Silicon has also been investigated for use as an anode material.[3,17] Pure lithium metal would be the ideal candidate for a Li-ion anode as it is easily oxidised and has a very high electropotential per unit mass enabling it to give a high voltage. However, upon repeated cycling, metallic lithium forms mossy needle-shaped growths of lithium known as dendrites.[13,16,18] These are caused by the dissolution of lithium metal from one area of the anode during discharge and its deposition at another area of the same electrode during recharge. These dendrites can occupy volume in the electrolyte, reducing the effectiveness of the discharge and recharge cycles. If dendrites grow long enough they can span across the electrolyte and connect with the cathode

causing a short circuit of the battery[16] and a catastrophic failure as well as a potential fire risk.

Because of dendrites, electrodes such as carbon or silicon have been found to be more suitable for the anode material.[1,3,15,17] When charging, the lithium intercalates inside the graphite structure causing an increase in volume. During discharge the lithium is deintercalated from the structure decreasing the volume. This reaction is seen in Equation 1.4.[19] Carbon is currently the most widely used anode material although silicon anodes with four times the lithium capacity are currently under development.[17]

$$LiC_6 \rightleftarrows Li^+ + e^- + C_6 \quad \textbf{(1.4)}$$

The positive electrode (cathode during discharge) is usually a lithium containing oxide or phosphate crystal structure. This structure usually contains various heavy metals acting as electon donors and acceptors to be oxidised and reduced during charge and discharge.[2] The structures also contain vacancy sites in the cathode for lithium ions to intercalate into. Several structures are in use such as layered oxides (lithium cobalt oxide), spinels (lithium manganese oxide) or olivines such as lithium iron phosphate.[2,19] During discharge the lithium cations intercalate into the crystal structure and intercalate out of the crystal structure during recharge of the cell. A typical cathode reaction is shown in Equation 1.5.[20] The capacity of the battery is affected by the number of lithium cations that can be inserted into the cathode structure, as each lithium cation inserted corresponds to one electron passed through the external circuit.

$$x Li^+ + e^- + Mn^{IV}O_2 \rightleftarrows Li_x Mn^{III}O_2 \quad \textbf{(1.5)}$$

The electrolyte has to be ionically conductive to allow movement of the lithium cations through the cell, yet electronically insulating to avoid short circuit of the cell. The electrolyte material can vary greatly, although aqueous electrolytes are undesirable for use in a lithium battery due to the vigorous chemical reaction of lithium with water. Usually non-aqueous liquid electrolytes such as ethylene carbonate,[16] propylene carbonate[16] or ionic liquids[21,22] are used, with lithium salts such as $LiPF_6$ or lithium bis(trifluoromethylsulfonyl)imide (LiTFSI) added to increase the lithium ion conductivity.[23] However salts containing fluorine such as $LiPF_6$ can decompose to form hydrofluoric acid after repeated cycling or when exposed to water from the air.

This degrades the effectiveness of the battery. Solid electrolytes such as polymers have also been investigated,[2,13] however these are not in widespread use due to the low lithium cation conductivities measured in these electrolytes.[14]

There are many different versions of lithium-ion battery which are currently in use and under development, with a wide range of anodes, cathodes and electrolytes currently available. However none of these technologies has either the capacity or the specific energy to power a small electric vehicle for a range of over 500 km. Currently the most popular electric vehicles such as the Tesla Roadster, use approximately 7000 Li-ion cells and have a current maximum range of 393 km.

As lithium-ion technologies are unable to give the required range for a vehicle alternative battery technologies must be investigated to allow electric vehicles to become competitive with combustion engine vehicles and current electric vehicles.

1.2 Lithium-air Batteries

Lithium-air batteries are one of the potential battery technologies which may be able to compete with current petroleum driven motor vehicles.[6,10,11] Figure 1.1 showed that Li-air batteries have a similar specific energy and specific power to internal combustion engines. First demonstrated in 1996 by Abraham and Jiang,[7] these batteries use the reaction of oxygen and lithium, producing lithium peroxide, to generate energy, as shown in Equation 1.6.[24]

$$2Li + O_2 \rightarrow Li_2O_2 \qquad \textbf{(1.6)}$$

The potential separation between oxygen and lithium gives a voltage of approximately 3V. Oxygen can be taken from the air reducing the mass of the battery that has to be transported as well as the cost of the materials used in the manufacture of the battery. This can give a theoretical specific energy density of up to 11640 Wh. kg^{-1}[6], close to that of gasoline fuel[6,10,11] (13000 Wh. kg^{-1}, most lost as heat. The practical energy density of gasoline is approximately 1700 Wh. kg^{-1}).[9]

In a lithium-air battery the lithium cations move from the lithium anode to the air cathode during discharge. When at the cathode the lithium ions react with oxygen to form lithium peroxide. During recharge the lithium peroxide is reduced at the cathode, oxygen is evolved,[6] and the lithium migrates towards the anode. A schematic of a lithium-air battery is shown in Figure 1.3.

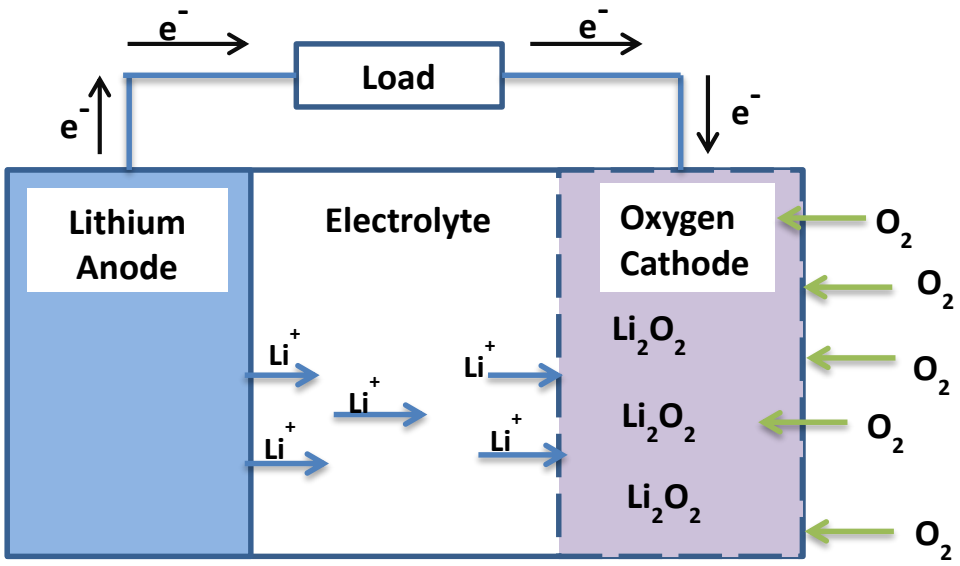

Figure 1.3: schematic of a typical Lithium-air cell during discharge.[25]

There are several types of Li-air cell which are currently under development. Aqueous Li-air cells use an aqueous electrolyte containing a lithium salt and have been investigated by Visco *et al.*[3,26] These cells have several advantages such as high lithium and oxygen diffusion coefficients and oxygen solubilities. The main disadvantage to this system is that metallic lithium reacts extremely violently with water. This requires the lithium anode to have an artificial solid-electrolyte interface (SEI) layer which is a layer required on the anode to separate the anode material from the electrolyte.[27]

Non-aqueous Li-air cells use non-aqueous electrolytes such as ethylene carbonate,[5,10] dimethoxyethane, diglyme[28] or ionic liquids.[29–31] These have a much greater chemical stability towards lithium allowing for a much greater capacity and voltage. Ionic liquids also have a very low volatility,[29,30,32] meaning there is no loss of electrolyte due to evaporation. There are several groups currently investigating non-aqueous electrolytes in the Li-air battery.[29–31]. Nakamoto *et al.* investigated piperidinium based ionic liquids measuring properties such as the diffusion coefficient and solubility of oxygen in the ionic liquids.[29] DeGeorgio *et al.* investigated the effect of lithium ions on oxygen reduction in several pyrrolidinium based ionic liquids as part of the LABOHR project.[30] Kuboki *et al.* used imidazolium based ionic liquid cations with perfluroalkylsulfonyl imide anions as the ionic liquid in a cell which managed to run for 56 days in air.[31]

Hybrid batteries use a mixture of aqueous and non-aqueous electrolytes. The standard template is to use a non-aqueous electrolyte near the anode to increase the chemical stability with an aqueous electrolyte around the oxygen electrode to maximise oxygen diffusion and solubility. These two electrolytes need to be separated by a lithium-permeable membrane which prevents water ingress to the anode preventing a catastrophic failure of the cell.[33]

Polymer electrolyte Li-air batteries use a solid polymer electrolyte. This does not chemically react with the anode, however it has very low oxygen and lithium diffusion coefficients.[7,18]

There are several challenges for lithium-air batteries which need to be overcome before this technology can become commercially viable. One major challenge is electrolyte stability. Lithium metal is chemically unstable in the presence of aqueous electrolytes. Superoxide generated from reduced oxygen can also react with aqueous electrolytes.[34,35] There is also growing evidence that several non-aqueous electrolytes such as ethylene carbonate and propylene carbonate decompose in the presence of superoxide after repeated cycling.[29] This will reduce the cycle life of the battery and makes these electrolytes unsuitable for use in a commercial battery.

Another major problem is contamination of the electrolyte. Because the oxygen is being taken from the atmosphere, the ingress of water, carbon dioxide and nitrogen must be prevented.[3] If water was to enter in the battery and react with lithium this would cause the formation of hydrogen gas which is a potential explosion risk or the formation of hydrogen peroxide which would decrease the efficiency, cycle life and performance of the battery. The ingress of nitrogen would also cause the formation of lithium nitride which would have similar consequences.[36]

A third challenge is the formation of lithium peroxide. Lithium peroxide is insoluble in many solvents[37,38] and so precipitates on the cathode during the discharge cycle. This causes clogging of the pores of the cathode preventing the further ingress of oxygen and lithium ions into the cathode.[37] This would reduce the battery cycle life and performance.

Probably the greatest problem for the Li-air battery is oxygen uptake and transport. A large supply of oxygen towards the cathode is needed to maintain a high discharge rate.

This is dependent upon the solubility of oxygen (c_O) and the diffusion coefficient (D_O) of oxygen in the electrolyte.[11] The diffusion coefficient is a measure of how fast a species diffuses through a solvent. Many of the non-aqueous electrolytes have much lower oxygen solubilities and oxygen diffusion coefficients than water does.[39–41] Finding a suitable electrolyte which can deliver enough oxygen to the cathode is critical to the success of the lithium-air battery.

1.2.1 The LABOHR Project

The Lithium-Air Battery with Split Oxygen Harvesting and Redox processes (LABOHR) Project is a European Commission funded project with the aim to develop a lithium-air battery with the capacity to power a small car to travel over 300 km on a single charge. This battery separates the O_2 harvesting and O_2 reduction processes. O_2 is harvested at the air interface and transported *via* an O_2 transport medium to the air cathode where it is reduced. This decreases the complexity of the battery and replaces a single three-phase electrode-electrolyte-air interface with two two-phase interfaces: an electrolyte-air interface and an electrode-electrolyte interface. A diagram of this battery is shown in Figure 1.4.

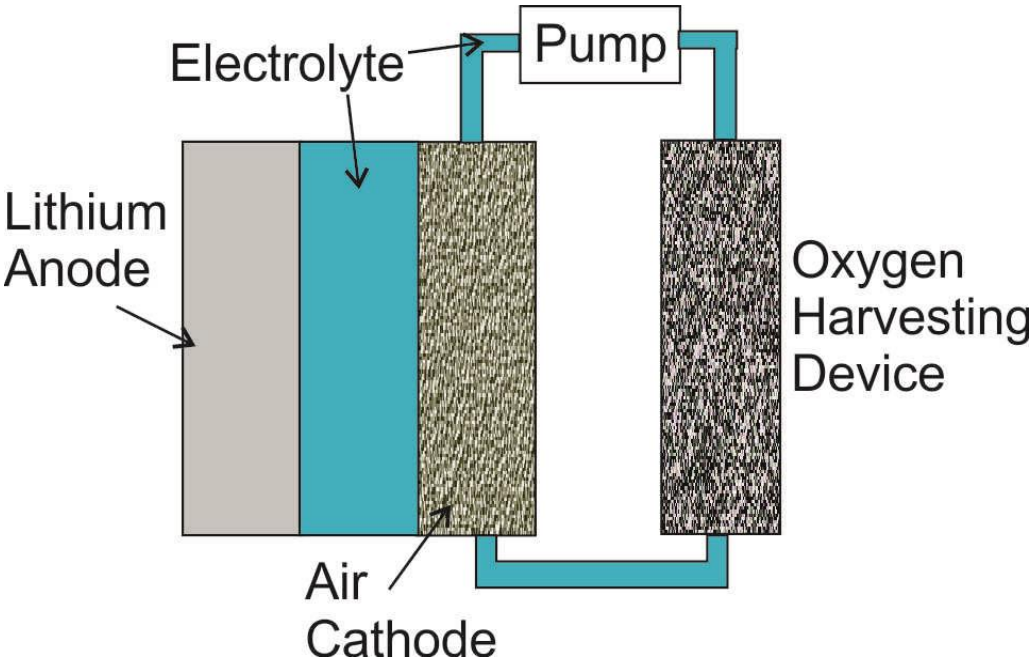

Figure 1.4: schematic of a LABOHR battery showing separated air electrodes and oxygen harvesting device.

Figure 1.4 shows a schematic of the proposed LABOHR battery. The oxygen harvesting device absorbs the oxygen from the atmosphere and dissolves it into the ionic liquid. The pump is able to move the oxygenated ionic liquid towards the cathode where the oxygen is reduced. The lithium metal anode is oxidised and lithium cations move through the ionic liquid electrolyte to the cathode where they react with the oxygen to form lithium peroxide. During recharge the reverse reaction occurs, with lithium cations moving back through the ionic liquid electrolyte to the anode. Oxygen is evolved at the air electrode and dissolves into the ionic liquid. The pump moves the ionic liquid to the oxygen harvesting device where it diffuses back into the atmosphere.

1.3 Ionic Liquids

The LABOHR battery will use room temperature ionic liquids (RTILs) as both the electrolyte and the O_2 transport medium. Ionic liquids are molten salts composed of organic or inorganic anions and cations.[42,43] Ionic liquids are generally liquid at room temperature. The first ionic liquid discovered was ethylammonium nitrate discovered by Paul Walden in 1914.[44] Since then many different RTILs using many combinations of anions and cations have been found. As a result of the large number of combinations of organic and inorganic cations and anions there are a large number of potential RTILs with a variety of properties and potential uses.[42] Due to their ionic nature RTILs generally have a negligible vapour pressure even at low pressure or high temperatures.[42] Because of this they are able to remain liquid in a vacuum with no appreciable evaporation and when heated decompose rather than evaporate. Their lack of vapour pressure makes them non-flammable as well as "green" solvents[42] even though many RTILs contain fluorine. Because of this they are considered safe for use in battery technologies as well as being studied for use in synthetic chemistry, CO_2 capture,[45] gas separation[46] and electrochemical applications such as capacitors.[47] Some RTILs also have a low chemical reactivity allowing them to be stable in the presence of lithium and superoxide. RTILs can also have a higher O_2 solubility than other organic solvents which could be used in a lithium-air battery. RTILs have a very large electrochemical stability window (roughly 5-6 V)[48] allowing them to be used as an electrolyte. Table 1.1 shows the physical properties of several RTILs compared to other commonly used non-aqueous solvents.

Table 1.1: physical properties of several ionic liquids and commonly used solvents.[49,50]

Solvent	PYR_{14} TFSI	PYR_{12O1} TFSI	PYR_{14} BETI	H_2O	MeCN	DMSO	EC	PC
FW **(g mol^{-1})**	422	424	522	18	41.05	78.13	88.06	102.09
m.p (°c)	-6.5	-	8.9	0	-45	19	35	-48.8
b.p (°c)	-	-	-	100	81	189	260.7	242
d **(g cm^{-3})**	1.43	1.46	1.48	1	0.79	1.1	1.32	1.21
η **(cP) RT**	60	38	200	0.89	0.36	1.99	1.9	2.5
σ **(mS cm^{-1}) RT**	3.3	4.2	0.9				91.2	
≈ D_O (x 10^{-6} cm^2 s^{-1})	12[49]	11[49]	3[49]	16[50]	110[50]	21[50]	-	-
≈ c_O (x 10^{-6} mol cm^{-3})	2.9[49]	3[49]	10.7[49]	1.3[50]	8.1[50]	2.1[50]	-	-

The RTILs have extremely high viscosities when compared to water and other commonly used organic solvents. They also have no known boiling point. This is due to the very strong ion-ion interactions which occur between the anions and cations of the ionic liquid. This causes the ionic liquid to have a rather low conductivity and low oxygen diffusion coefficient compared to water. The diffusion coefficient of a substance is normally related to the viscosity *via* the Stokes-Einstein equation (Equation 1.7)[51] where D is the diffusion coefficient of the species in cm^2 s^{-1}, k_B is the Boltzmann constant (1.38×10^{-23} J K^{-1}), T is the temperature in K, η is the viscosity of the solvent through which the species is diffusing in cP and a is the hydrodynamic radius of the species and any attached ions in cm. There is debate as to whether the high ionicity of the RTILs makes the Stokes-Einstein equation applicable to them.[52,53]

$$D = \frac{k_B T}{6\pi\eta a} \qquad \textbf{(1.7)}$$

The values of the solubility (c_O) and the diffusion coefficient (D_O) of oxygen in the ionic liquid are of crucial importance in the LABOHR project with respect to selecting an ionic liquid to be used in the battery. The diffusion coefficient-solubility product ($D_O c_O$) is also of interest as it is directly proportional to the energy produced by the battery.

Most of the literature values for these parameters show little agreement with each other.[38,49,50,54] A wide range of ionic liquids, measurement techniques and experimental conditions have led to large variations in the values obtained by different research groups. The literature related to experimentally determining the diffusion coefficient and solubility of oxygen usually breaks down into values obtained through the use of electrochemical techniques such as cyclic voltammetry and potential step chronoamperometry[38,49,50,54] and non-electrochemical techniques such as pressure drop experiments[55] or measuring diffusion through a membrane.[56]

The large differences in the measurement technique, the RTILs tested, the temperatures and pressures studied and the methods of saturating, purifying and preparing the ionic liquids all lead to large variations in the values of the solubility and the diffusion coefficient of oxygen measured by different groups. One aim of this project is to measure the values of the diffusion coefficient and the solubility of oxygen in several ionic liquids using reliable, reproducible electrochemical methods.

The stability of the ionic liquid is also crucial for the LABOHR project. Some of the most commonly used ionic liquids are protic ionic liquids containing labile protons on the anion.[57] These labile protons may react with superoxide formed during oxygen reduction.[58] This removes the superoxide from the ionic liquid and limits the reversibility of the oxygen reduction reaction. Over repeated cycling this would cause degradation of the ionic liquid and reduce the cycle life of the battery.

1.4 Electrochemical Measurement Techniques

A variety of electrochemical measurement techniques are used in this thesis. These techniques include cyclic voltammetry, potential step chronoamperometry and electrochemical impedance spectroscopy.

1.4.1 Cyclic Voltammetry

Cyclic voltammetry is one of the most useful and widely used techniques in electrochemical and battery research. This technique involves setting the potential of the working electrode to a potential where no electrochemical reaction occurs. The potential is then increased or decreased at a certain sweep rate to a potential where an electrochemical reaction does occur.[59,60] The current is measured as a function of the potential. When an electrochemical reaction occurs, the current increases to show peaks or waves. This is shown in Figure 1.5. Once the potential has reached a certain value the sweep direction is normally reversed allowing the study of the reverse chemical reactions. From this technique we can determine the reactions which occur as well as derive information about the charge passed, the reaction rates, diffusion coefficients and any side reactions of the electrochemical system.

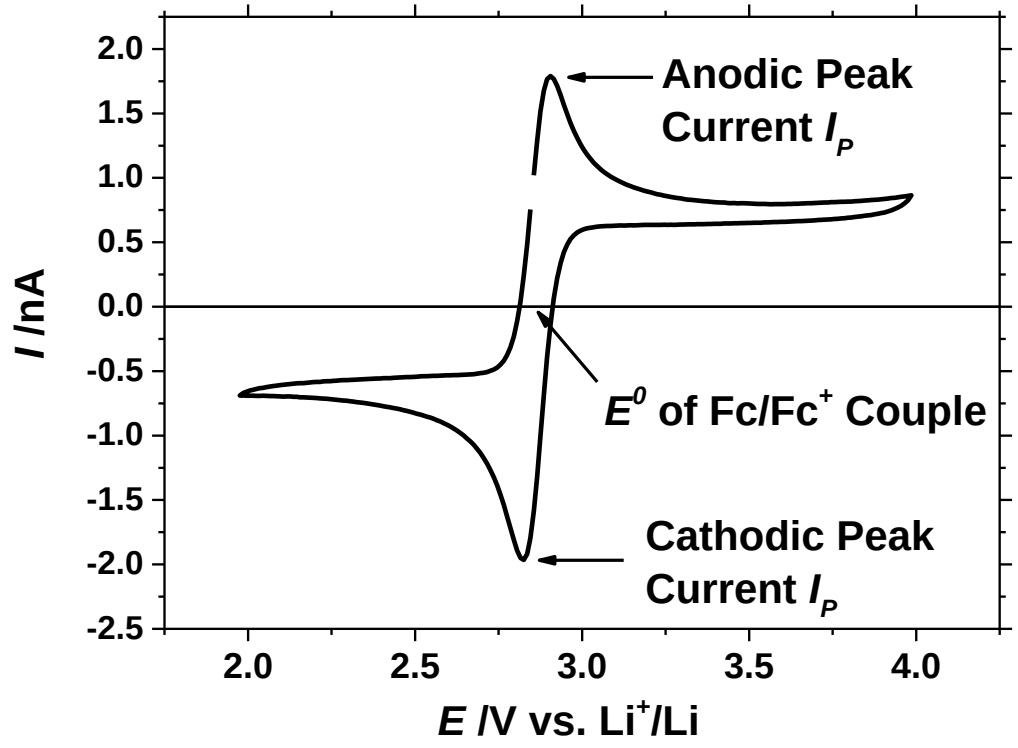

Figure 1.5: sample cyclic voltammogram showing the second scan of 0.1 M ferrocene and 0.1 M ferrocenium tetrafluroroborate in the ionic liquid $PYR_{14}TFSI$ at a 25 µm diameter Au microdisc electrode at a sweep rate of 100 mV s^{-1}. This shows the anodic and cathodic peak currents (I_P) and the standard potential of the Fc/Fc^+ couple (E^0). The gap at 2.9 V *vs*. Li/Li^+ is the switch between cycles.

One of the methods of determining the diffusion coefficient of a species is by doing several cyclic voltammograms at several sweep rates. By taking the current of the reduction peak of a reaction and applying it to the Randles-Sevcik equation (Equation 1.8) the diffusion coefficient of the species can be found.[60] Equation 1.8 is only valid at a temperature of 298 K.

$$I_P = 2.69 \times 10^5 n^{3/2} D^{1/2} c v^{1/2} A \qquad \textbf{(1.8)}$$

In equation 1.8 I_P is the peak current in A, n is the number of electrons transferred, D is the diffusion coefficient in $cm^2\ s^{-1}$, c is the bulk concentration of the reactant in mol cm^{-3} and v is the sweep rate of the cyclic voltammogram in V s^{-1} and A is the surface area of the electrode in cm^2.

This method is very useful and accurate if the concentration of the reactant in the electrolyte is known. However for a gas dissolved in a liquid the concentration is not

easily known. Because of this, cyclic voltammetry must be used in conjunction with other techniques such as potential step chronoamperometry to determine the values of the diffusion coefficient and solubility of oxygen in the ionic liquid.

1.4.2 Potential Step Chronoamperometry

Potential step chronoamperometry (PSCA) is another widely used electrochemical technique. The potential of a cell is stepped from a value where no reaction occurs to a value where an oxidation or reduction reaction occurs. The current response caused by the change in the potential is measured as a function of time. The current response at a disc shaped electrode differs slightly between a macroelectrode and a microelectrode.

For a macrodisc electrode, where the diameter is greater than 100 μm the initial oxidation or reduction of a species close to the electrode causes a large initial current which rapidly decreases as the species is consumed. At longer times molecules of the species diffuse linearly towards the electrode from the bulk solution causing a smaller current. The current can be shown by the Cottrell equation (Equation 1.9) which scales the current with $D^{1/2}c$.[60]

$$I = \frac{nFD^{1/2}cA}{\pi^{1/2}t^{1/2}} \quad \textbf{(1.9)}$$

In the Cottrell equation I is the current of the chronoamperogram in A, n is the number of electrons transferred in the reaction, F is the Faraday constant (96485.3 C mol^{-1}), D is the diffusion coefficient of the reactant in cm^2 s^{-1}, c is the bulk concentration of the reactant in mol cm^{-3}, A is the surface area of the electrode in cm^3 and t is the time since the start of the potential step in seconds.

For a microdisc electrode where the diameter is less than 100 μm, the initial oxidation or reduction also gives an initial current which scales with $D^{1/2}c$ as shown in Equation 1.9. This is shown in the top panel in Figure 1.6 and the large current at short times in Figure 1.7. However at longer times the diffusion field towards the electrode from the bulk solution changes from linear to hemispherical due to the small geometry of the electrode as shown by the middle panel in Figure 1.6. This allows the formation of a quasi-hemispherical, steady state diffusion field causing a steady state current as shown in the bottom panel in Figure 1.6 and the current at long times in Figure 1.7. The value

of the current at long timescales is determined by the Saito equation (Equation 1.10)[55,60] where I is the current of the chronoamperogram in A, n is the number of electrons transferred in the reaction, F is the Faraday constant (96485.3 C mol^{-1}), D is the diffusion coefficient of the reactant in cm^2 s^{-1}, c is the bulk concentration of the reactant in mol cm^{-3} and r is the radius of the microdisc electrode in cm.

$$I = 4nFDcr \qquad \textbf{(1.10)}$$

The radius of the final hemispherical diffusion field is approximately four times greater than the diameter of the microdisc electrode. The times at which the diffusion field changes depend upon the radius of the electrode (r) and the diffusion coefficient of the species diffusing towards the electrode (D). The short timescale linear diffusion field occurs when $Dt/r^2 < 10^{-4}$, the intermediate diffusion field occurs when $Dt/r^2 \approx 10^2$ - 10^{-4} while the long time hemispherical diffusion field occurs at $Dt/r^2 > 10^2$. For a 10 µm diameter microdisc electrode in an ionic liquid where the O_2 diffusion coefficient is approximately 10^6 cm^2 s^{-1} the short timescale occurs at 10^{-5} s after the potential step is applied, the intermediate timescale occurs between 10^4 s and 10 s while the long timescale occurs at times greater than 10s.

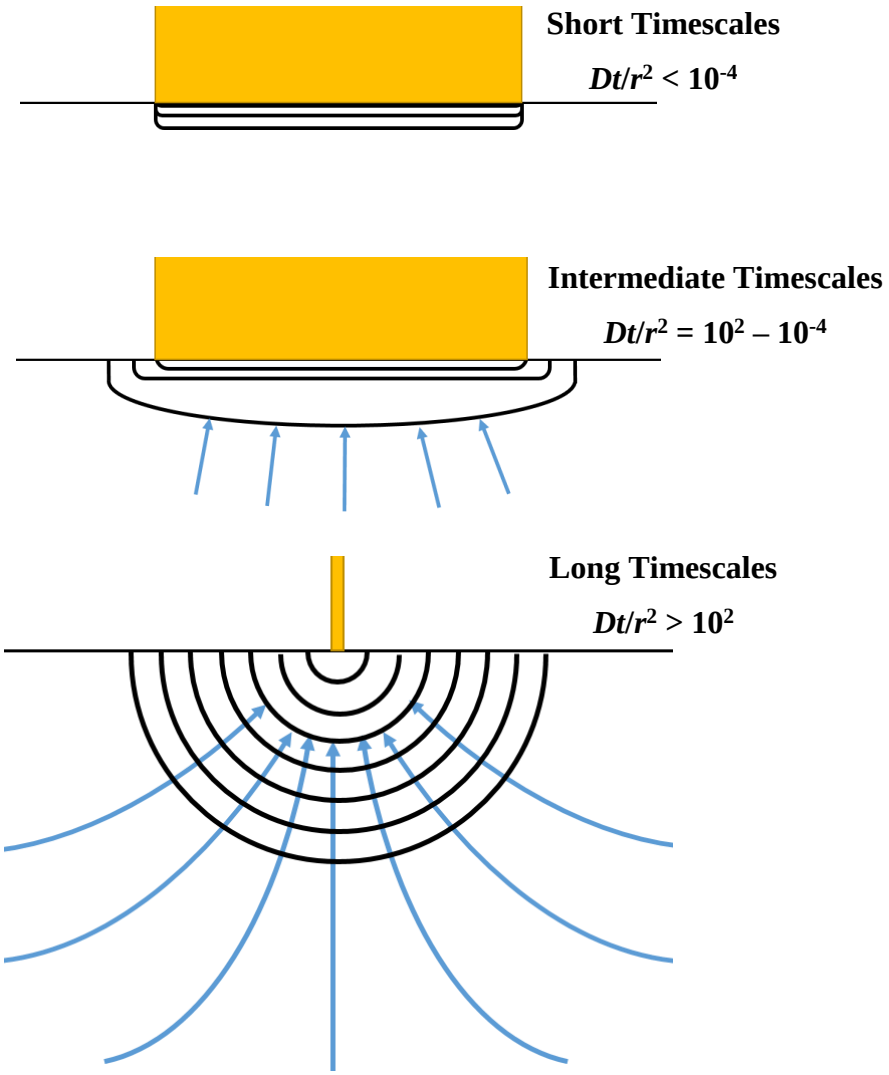

Figure 1.6: this diagram shows the diffusion field (black lines), and the diffusion path from the bulk (blue lines) at a microdisc electrode over time.This shows the diffusion field changing from a linear diffusion field at short times (top diagram), towards an intermediate diffusion field at intermediate times (centre diagram) and then towards a hemispherical diffusion field at long times (bottom diagram).[59,60]

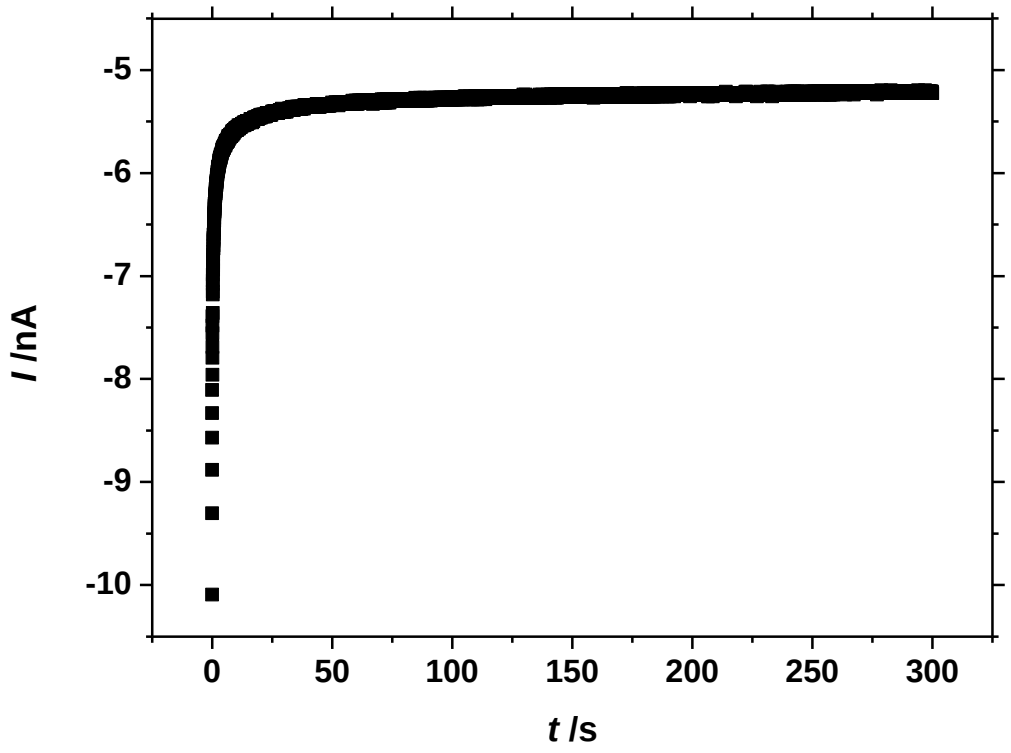

Figure 1.7: sample chronoamperogram showing a potential step to 1.5 V *vs.* Li/Li^+ in oxygenated $PYR_{14}TFSI$ at a 25 μm diameter Pt microdisc electrode at a temperature of 298 K. This shows the reduction of oxygen to superoxide. This shows the large current at short timescales and the steady state current at long timescales.

Because the current scales with $D^{1/2}c$ at short timescales and scales with Dc at long times, a single potential step chronoamperometry measurement at a microdisc electrode can be used to determine the values of D and c of a species when neither are known. There are several methods which can be used to do this. The first method was investigated by Denuault *et al.*[61]which linearises the plot by plotting it as a function of $t^{1/2}$. By combining Equations 1.9 and 1.10, Equation 1.11 is obtained.

$$I = \frac{\pi^{1/2} nF D^{1/2} c r^2}{t^{1/2}} + 4nFDcr \qquad \textbf{(1.11)}$$

By plotting I vs. $t^{-1/2}$ in a Cottrell plot as shown in Figure 1.8 we get Equation 1.12, where I is the current of the chronoamperogram in A, t is the time in s, S is the slope of the plot in A $s^{1/2}$ and C_y is the y-intercept of the plot in A.

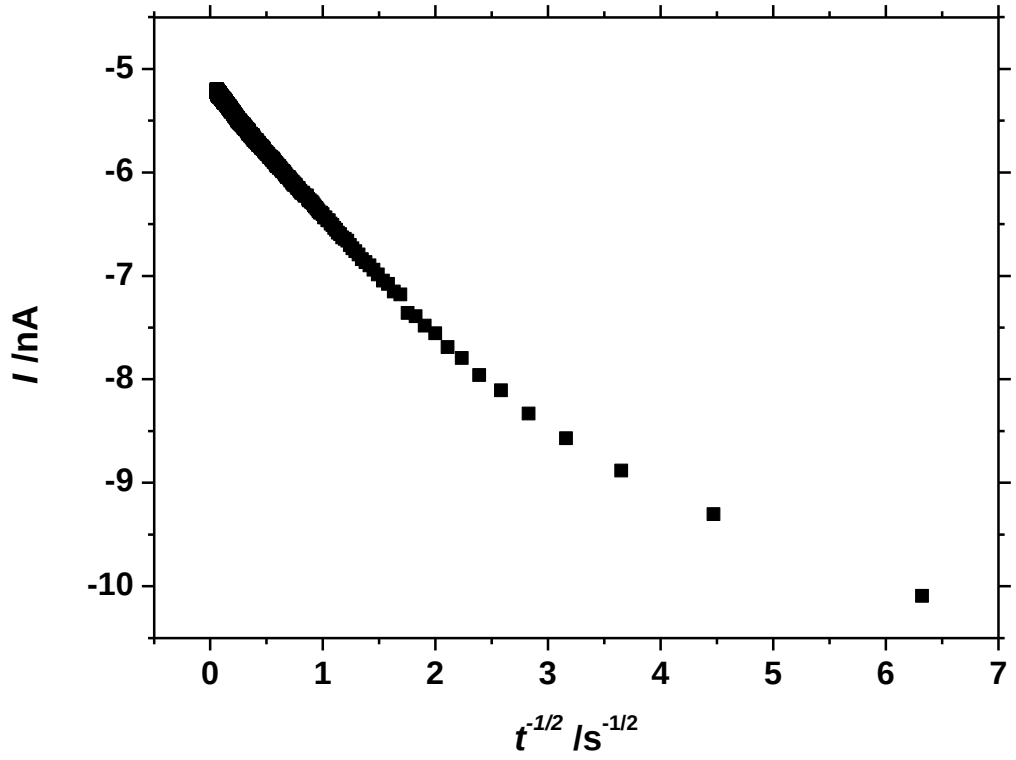

Figure 1.8: Cottrell plot of Figure 1.7 showing the linearised data. The slope of this plot (*S*) can be used to determine the diffusion coefficient of oxygen in $PYR_{14}TFSI$.

$$I = t^{-1/2}S + C_y \quad \textbf{(1.12)}$$

Where:

$$S = nFcr^2(\pi D)^{1/2}$$

and

$$C_y = 4nFDcr$$

The slope and intercept of the resulting straight line plot can be used to find the value of the diffusion coefficient of the measured species as shown in Equation 1.13. Once *D* is known the concentration of the species can be found using Equation 1.14.

$$D = \left(\frac{C_y r\pi^{1/2}}{4S}\right)^2 \quad \textbf{(1.13)}$$

$$c = S/nFr\,(\pi D)^{1/2} \quad \textbf{(1.14)}$$

However this method is only accurate at the short and long timescales. At the intermediate timescales this methods gives an error of up to 6.8%.[61]

Another consideration is that diffusion coefficient of O_2 in ionic liquids is approximately 10^{-5} cm^2 s^{-1} and the microdisc electrodes are in the order of 10 – 25 µm in diameter. This means that at the long timescale hemispherical diffusion field dominates after ≈ 10 seconds. This accounts for most of the time in a 60 second chronoamperogram. Because of this the most appropriate equation is Equation 1.15.

$$I = 4nFDcr + \left(2/\pi^{\frac{3}{2}}\right) r(Dt)^{-1/2} \quad \textbf{(1.15)}$$

Equation 1.15 was used to derive an alternative equation by Shoup and Szabo[62] that claims to be accurate over all timescales. This equation requires nonlinear curve fitting to fit the full chronoamperogram to Equation 1.16. This method gave similar but not identical values for the diffusion coefficient and concentration of the species to the one used by Denuault *et al*.

$$I = -4nFDcr\left(0.7854 + 0.8863\left(\frac{4Dt}{r^2}\right)^{-1/2} + 0.2146\exp\left(-0.7823\left(\frac{4Dt}{r^2}\right)^{-1/2}\right)\right) \quad \textbf{(1.16)}$$

This equation is claimed to be accurate to within 0.6% at all timescales with the greatest error also occurring the intermediate timescales.

Another method by Mahon and Oldham[55] also used curve fitting software and modified versions of Equation 1.16, Equations 1.17 and 1.18, to determine the values of *D* and *c*.

$$\text{If } t \leq 1.281r^2/D$$

$$I = n\pi FDcr\left(\frac{1}{\pi^{1/2}\theta} + 1 + \frac{\theta}{4\pi}^{1/2} - \frac{3\theta}{25} + \frac{3\theta^{3/2}}{226}\right) \quad \textbf{(1.17)}$$

$$\text{If } t \geq 1.281r^2/D$$

$$I = n\pi FDcr\left(\frac{4}{\pi} + \frac{8}{\sqrt{\pi^5\theta}} + \frac{25\theta^{-3/2}}{2792} - \frac{\theta^{-5/2}}{3880} - \frac{\theta^{-7/2}}{4500}\right) \quad \textbf{(1.18)}$$

$$\text{Where: } \theta = Dt/r^2$$

This method also claims to be accurate within 0.5% at all timescales.

All of these methods give identical values of *D* and *c* at the short and long timescales but disagree with each other slightly at intermediate timescales. This is due to differences in the equations used and the methods of accounting for the transition from linear to hemispherical diffusion. For the experiments undertaken in this thesis the method derived by Mahon and Oldham[55] will be used as this is determined to be more accurate over all experimental timescales and allows more accurate information to be derived from the experimental data.

Another alternative method of obtaining the diffusion coefficient is to use the x-intercept of a Cottrell plot (C_x). This method rearranges Equation 1.12 to make $I = 0$:

$$0 = C_x t^{-1/2} S + C_y \qquad \textbf{(1.19)}$$

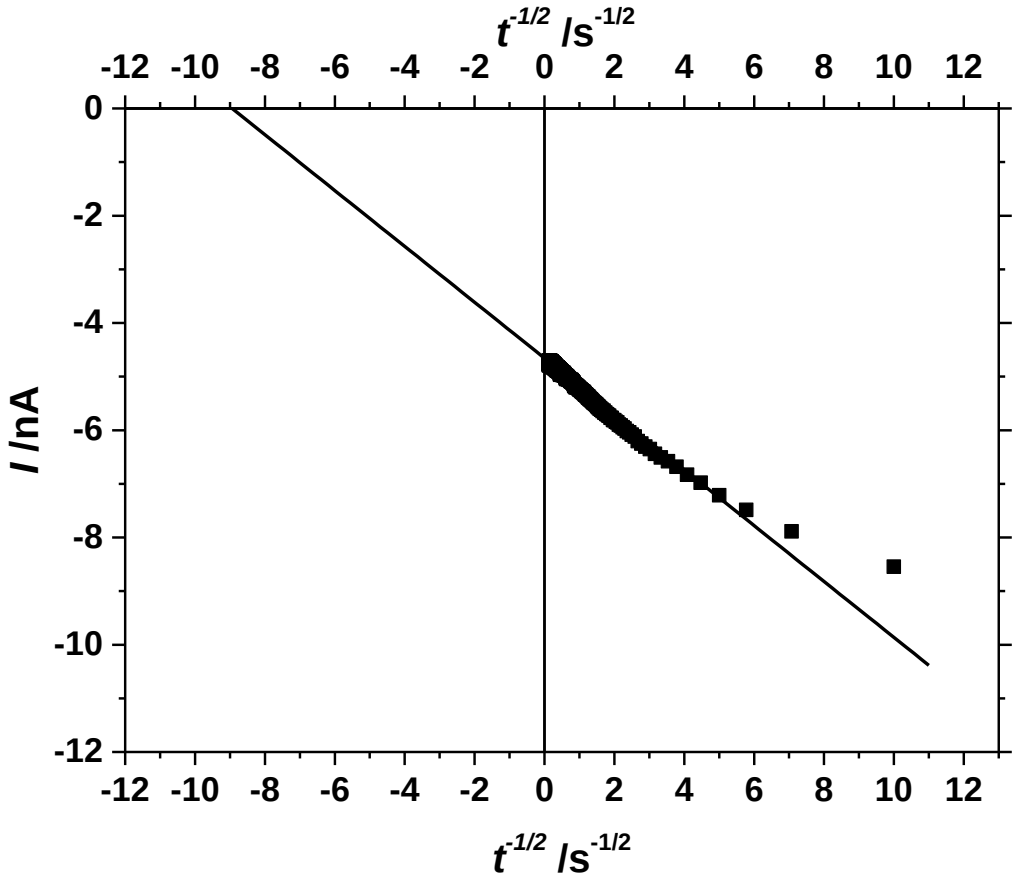

Figure 1.9: plot showing the x-intercept of a Cottrell plot. The slope of this plot can be used to determine the diffusion coefficient and solubility of oxygen in PYR_{14}TFSI. This was a potential step to 1.5 V *vs.* Li/Li^+ in oxygen saturated PYR_{14} TFSI at a 10 µm diameter Pt microdisc electrode.

By rearranging Equation 1.19 we obtain Equation 1.20.

$$C_x = \frac{-4nFDCr}{nFcr^2(\pi D)^{1/2}} \quad \textbf{(1.20)}$$

Simplifying gives:

$$C_x = t^{-1/2} = \frac{-4(D^{1/2})}{r(\pi^{1/2})} \quad \textbf{(1.21)}$$

Rearranging gives:

$$D^{1/2} = \frac{t^{-1/2}\pi^{1/2}r}{-4} \quad \textbf{(1.22)}$$

However the accuracy of this method at all timescales, especially the intermediate timescales, has not been accurately determined, therefore it will not be used to determine the values of *D* and *c* from CAs in this thesis.

1.4.3 Electrochemical Impedance Spectroscopy

Electrochemical Impedance Spectroscopy (EIS) is a versatile analytical technique using an alternating current (AC) to analyse a system. A direct current (DC) is applied to a cell and a small AC potential is overlaid on the DC potential. This AC potential uses a sine wave of 10-25 mV amplitude, applied at various frequencies, and the resulting AC current output is analysed.

In a standard DC voltammetry the resistance of a cell is given by Ohms law where *R* is the resistance in ohms, *E* is the potential in volts and *I* is the current in amps.

$$R = E/I \quad \textbf{(1.23)}$$

The impedance of a cell is the AC equivalent of resistance. The current response to a sinusoidal potential can be phase shifted due to the time constants of the components of the cell. This is shown in Figure 1.10.

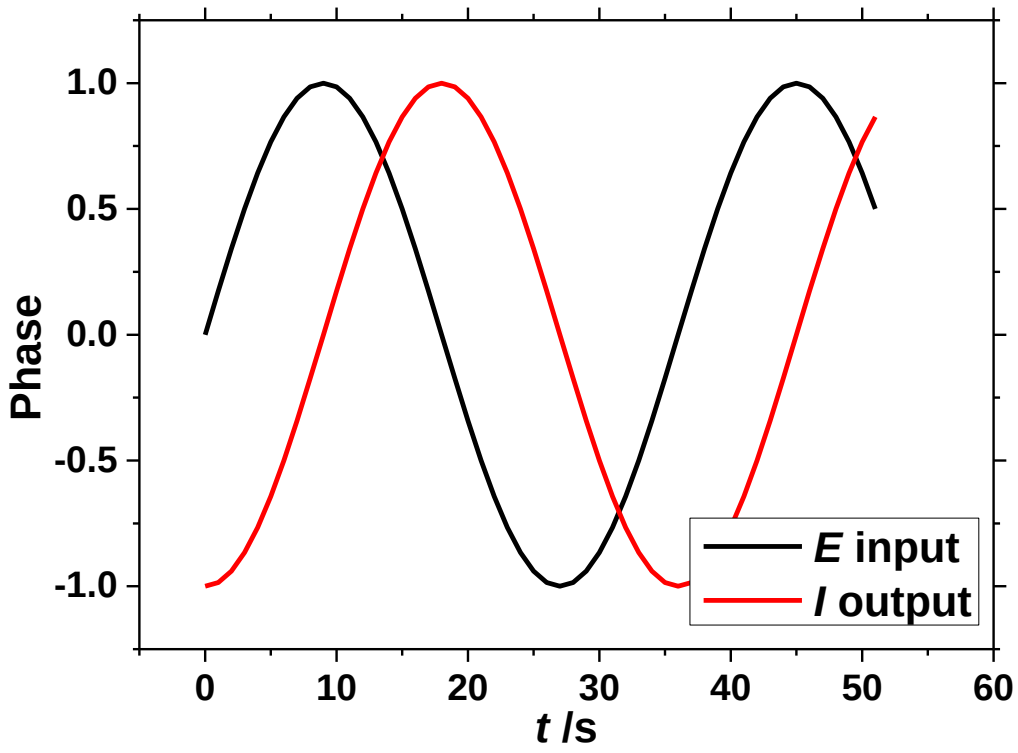

Figure 1.10: figure demonstrating the phase separation between the sine wave voltage input and the current output of a cell.

The phase of the sine wave interacts to give a real and an imaginary part of the impedance. Normally the overpotential is applied and a high frequency sine wave is applied to the overpotential and the current is measured. The frequency of the sine wave is then decreased and the current is measured again. The current is measured at a range of frequencies, usually starting from the highest to the lowest because the time taken to gather data increases as the frequency decreases.

Impedance is most easily analysed by simplifying electrochemical system processes down to simple electrical components, e.g. the resistance caused by a solution corresponds to a resistor, while an electrical double layer caused by a polarised electrode corresponds to a capacitor. Certain processes that occur in a cell have to be modelled with mathematical elements, e.g. diffusion through an electrolyte is modelled by a Warburg element. These components are combined to give an equivalent circuit for the cell.[59]

These simple electrical components have different impedance traces, based on how they are affected by an AC potential. Resistors give an output current which is exactly in-phase with the potential applied. Therefore they have only real components and no

imaginary components giving a real impedance (Z' in Ω) with zero imaginary impedance (Z'' in Ω). The impedance of a resistor is given by Equation 1.24.

$$Z' = E/I, \;\; Z'' = 0 \tag{1.24}$$

Capacitors have a time constant, and so can give a current which is out of phase with the AC potential input. Because of this they have a purely imaginary component.[63] The impedance of a capacitor is given by Equation 1.25 where *f* is the frequency of the sine wave in hertz and *C* is the capacitance in farads.

$$Z' = 0, \;\; Z'' = -1/(2\pi fC) \tag{1.25}$$

A theoretical element known as a Warburg element simulates a diffusion controlled reaction. The Warburg impedance (Z_W in Ω) is given by Equation 1.26.[59,60]

$$Z_W = \sigma 2\pi f^{-1/2} - i\sigma 2\pi f^{-1/2}$$

Where:

$$\sigma = \frac{RT}{2^{1/2} n^2 F^2 A}\left[\frac{1}{c_{\mathrm{Ox}} D_{\mathrm{Ox}}^{1/2}} + \frac{1}{c_{\mathrm{Red}} D_{\mathrm{Red}}^{1/2}}\right] \tag{1.26}$$

In Equation 1.26, *R* is the ideal gas constant (8.314 J K^{-1} mol^{-1}), *T* is the temperature of the solution in K, *n* is the number of electrons transferred in the reaction, *F* is the Faraday constant (96485.3 C mol^{-1}), *A* is the surface area of the working electrode in cm^2, c_{Ox} and c_{Red} are the concentrations of the oxidised and reduced forms of the diffusing species in the solution respectively in mol cm^{-3} and D_{Ox} and D_{Red} are the diffusion coefficients of the oxidised and reduced forms of the diffusion species in cm^2 s^{-1}.

When fitted using computer fitting programmes the Warburg impedance is given by 3 parameters W_{DR}, W_{DT}, W_{DP}. W_{DR} is the resistance at low frequencies in Ω. W_{DT} is a time function equal to L^2/D where *L* is the length of the diffusion field towards the electrode in cm and *D* is the diffusion coefficient of the diffusing species in cm^2 s^{-1}. W_{DP} is a phase parameter which is normally set at 0.5.

One of the most widely used equivalent circuits is the Randles circuit[64]. This circuit combines the uncompensated solution resistance of an electrolyte (R_U), the double layer capacitance of an electrode (C_{DL}), the charge transfer resistance of an electron transfer occurring at the electrode (R_{CT}) and the diffusion of a species through the electrolyte towards the electrode represented by a Warburg (W_D). The Randles circuit is shown in Figure 1.11.

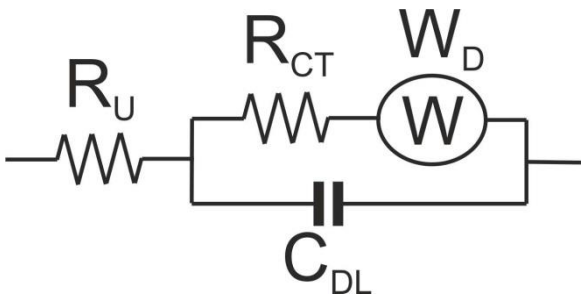

Figure 1.11: Randles circuit R_U = the uncompensated solution resistance, R_{CT} = the charge transfer resistance, C_{DL} = the double layer electrode capacitance, W_D= the Warburg diffusion.

There are several different methods of displaying impedance data which can give different information about the electrochemical cell. A Nyquist plot displays the imaginary impedance against the real impedance. The shape of the trace can give details about the components present in the equivalent circuit. A simulated Nyquist plot for a Randles circuit is shown in Figure 1.12.

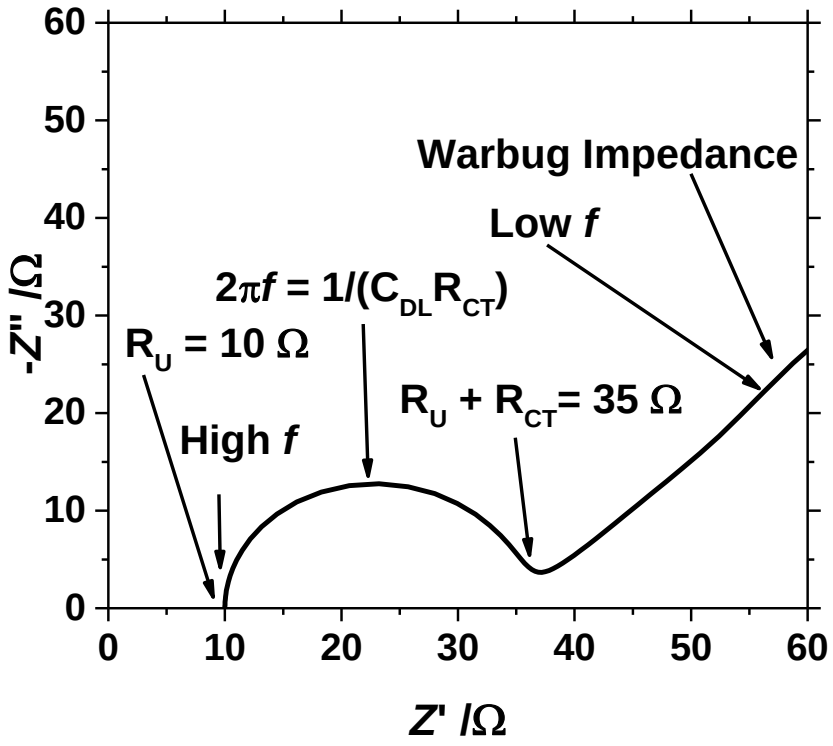

Figure 1.12: simulated Nyquist plot for the Randles circuit. The values of the Randles circuit are R_U = 10 Ω, R_{CT} = 25 Ω, C_{DL} = 0.1 mF, W_{DR} = 100, W_{DT} = 50, W_{DP} = 0.5.

Figure 1.12 shows the simulated Nyquist plot for a Randles circuit. This shows a semicircle, ended by a straight line with a slope of 45 °. The presence of the semicircle indicates that the equivalent circuit contains a resistor and a capacitor in parallel. The size of the semicircle is related to the time constant of the resistor-capacitor pair. The initial solution resistance can be found from the start of the semicircle on the left-hand side. Resistors have no phase shift, and so have no imaginary component. The end of the semicircle can be used to calculate the charge transfer resistance, by subtracting the x-axis intercept of the semicircle from the solution resistance. The maximum height of the semicircle can then be used to calculate the double layer capacitance. The straight 45 ° line is indicative of a Warburg impedance indicating diffusion in the solution. The values of the diffusion coefficient or concentrations of one species in the solution can be found using the x-axis intercept of the Warburg line and Equation 1.25 if the other values of the diffusion coefficient and concentrations of the other species are known.

Another way of displaying impedance data is the Bode plot. This plots the modulus of the impedance and the phase angle of the impedance against the log of the frequency. This gives information into the processes which occur at different frequencies.

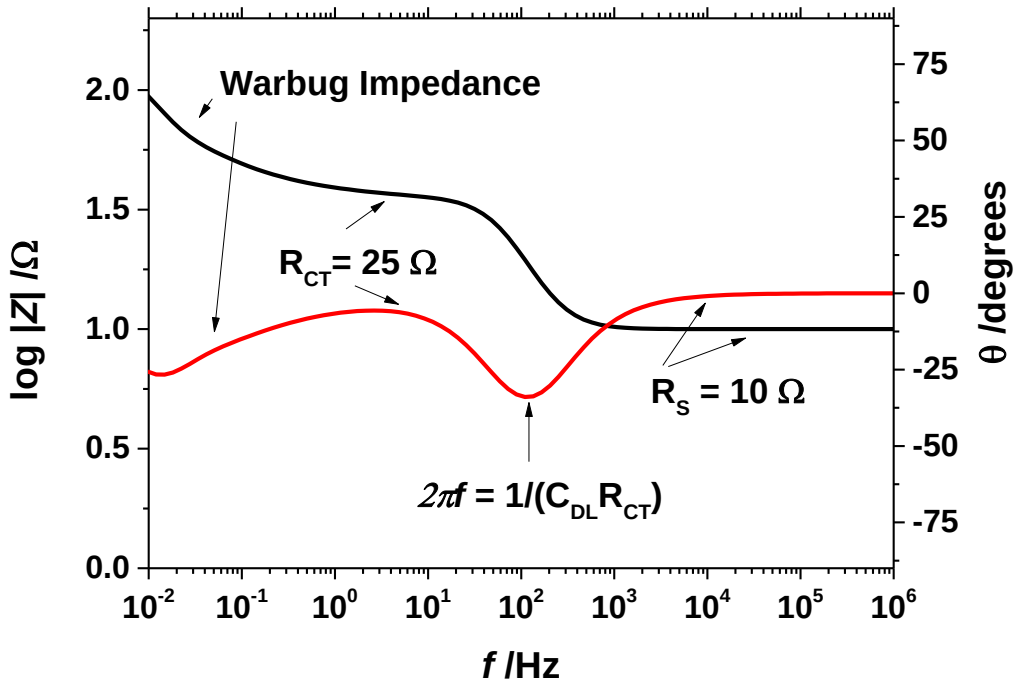

Figure 1.13: simulated Bode plot for the Randles circuit. The values of the Randles circuit are R_S = 10 Ω, R_{CT} = 25 Ω, C_{DL} = 0.1 mF, W_{DR} = 100, W_{DT} = 50, W_{DP} = 0.5. The black line is the log |*Z*| while the red line is the phase (theta - θ).

The Bode plot can be used to determine the values of the components in the equivalent circuit. At the higher frequencies, 10^6 to 10^4 Hz, the |*Z*| shows a flat line at 10 Ω, and the phase angle also shows a flat line at 0. This is caused by the solution resistance. At 10^3 to 10^0 Hz, |*Z*| increases before levelling off at 35 Ω as the phase angle increases to 45 ° before decreasing again to 0. This is caused by the resistor and capacitor combination. The increase in |*Z*| and the peak of the phase are caused by the capacitor, while the levelling off at 35 Ω is caused by the resistor. Below 10^0 Hz, the value of |*Z*| and the phase increase. This is due to the effect of the Warburg impedance.

Staircase potentio-electrochemical impedance spectroscopy (SPEIS) is a technique using multiple impedance measurements at different potentials. Impedance spectroscopy is undertaken at one potential, before the potential is increased or decreased and the impedance measurements repeated. This occurs for several potential steps, repeating the impedance at each potential. This technique is useful to observe the impedance over a range of potentials where different electrochemical reactions could occur.

1.5 Electrochemical Oxygen Reduction

The electrochemical reduction of oxygen is the reaction of greatest interest during the discharge of the lithium-oxygen battery. During the electrochemical reduction molecular oxygen accepts an electron from the cathode to become superoxide.[38,65]

$$O_2 + e^- \rightleftharpoons O_2^{\bullet -} \quad \textbf{(1.27)}$$

In an aqueous electrolyte the superoxide will react with labile protons from the water molecules to form hydrogen peroxide as shown in Equation 1.28.[65]

$$\begin{gathered} O_2^{\bullet -} + H_2O \rightarrow HO_2 + OH^- \\ 2HO_2 \rightarrow O_2 + H_2O_2 \end{gathered} \quad \textbf{(1.28)}$$

However in the absence of labile protons, as in non-aqueous electrolyte, superoxide can be stabilised by adjacent anions such as those present in an ionic liquid.[58] In a solution containing a large amount of lithium cations the superoxide reacts as it would with protons forming insoluble lithium peroxide.[38,66] First the superoxide reacts with lithium to form lithium superoxide (LiO_2). The lithium superoxide then reacts with itself, forming lithium peroxide (Li_2O_2) and evolving molecular oxygen.

$$Li^+ + O_2^{\bullet -} \rightarrow LiO_2 \quad \textbf{(1.29)}$$

$$LiO_2 + LiO_2 \rightarrow Li_2O_2 + O_2 \quad \textbf{(1.30)}$$

In the absence of lithium *i.e.* pure ionic liquid, the superoxide can remain stable long enough to accept another electron. If the potential in the cell is negative enough this allows the superoxide to be reduced to peroxide.[38,65]

$$O_2^{\bullet -} + e^- \rightleftharpoons O_2^{2-} \quad \textbf{(1.31)}$$

The reaction to peroxide appears to be irreversible. Peroxide is less stable than superoxide due to the increased negative charge and therefore it easily reacts or decomposes.[65]

The behaviour of oxygen in room temperature ionic liquids is of paramount importance for a lithium-air battery. Because of the greater charge on the superoxide compared with

molecular oxygen and therefore the greater interaction with the ions in the ionic liquid, the diffusion coefficient of superoxide is approximately a factor of 10 smaller than that of oxygen in the same ionic liquid.[38,67]

1.6 Diffusion and Gas Solubility in Liquids

The profile of diffusion into and through a liquid is governed by Fick's laws of diffusion. Fick's first law (Equation 1.32) states that the flux of a substance into a medium is determined by the diffusion coefficient and the concentration gradient into the medium. In Equation 1.32, J is the flux in mol cm^{-2} s^{-1}, D is the diffusion coefficient in cm^2 s^{-1}, c is the concentration of the diffusing species in mol cm^{-3} while x is the length of the diffusion field in cm.

$$J = -D\frac{\partial c}{\partial x} \quad \textbf{(1.32)}$$

The first law of diffusion states that the flux of a species into the solvent is greatest when the concentration gradient is largest, i.e. when the solvent contains none of the species and the medium outside of the solvent is fully saturated with the species.

$$\frac{\partial c}{\partial t} = D\frac{\partial^2 c}{\partial x^2} \quad \textbf{(1.33)}$$

The second law of diffusion (Equation 1.33) states that diffusion changes the concentration over time (t), with the diffusion into a solution being greatest when there is a large concentration gradient.

The solubility of oxygen in ionic liquids is one of the figures of merit for the lithium-air battery. The solubility of a gas into a liquid at a specific temperature is determined by the Henry constant of the gas (k_H). This is given by Henry's law.[68,69] This states that the concentration of a gas in a liquid (c) is directly proportional to the pressure of that gas over the surface of the liquid (p).

$$k_H = \frac{p}{c} \quad \textbf{(1.34)}$$

There are several versions of Henry's law using mole fractions, pressure and concentrations of gas in the liquid. Because of this k_H can have several different units such as Bar, Pa, Pa mol^{-1} cm^3 or be dimensionless. These units can be converted between each other. [69]

Henry's law is a limiting law which only applies to dilute solutions with a mole fraction less than 0.03.[70] The value of the Henry constant also changes with temperature due to the changes in the solubility of gases.[69,70]

The solubility of a gas in a liquid can be measured using a pressure drop measurement. A known volume of gas is placed into a sealed vessel with a known volume of liquid. The pressure in the vessel is measured as the gas dissolves into the liquid. The pressure drop is related to the total solubility using the ideal gas law.

$$\Delta pV = \Delta nRT \quad \textbf{(1.35)}$$

Where p is the pressure of the cell in kPa, V is the volume of the headspace of the cell in cm^3, n is the number of moles of gas in the volume of the cell in moles, R is the ideal gas constant, 8.314×10^{-3} cm^3 kPa K^{-1} mol^{-1} and T is the temperature of the cell in K.

This pressure drop technique is commonly used to determine the solubility of gases in ionic liquids at various temperatures.

Camper *et al*.[71] have determined the diffusion coefficient of a gas diffusing into an ionic liquid by observing the rate of the decrease in pressure inside the sealed cell as a function of time. The rate of diffusion of a gas into a semi-infinite volume is given by Equation 1.36:

$$M_t = 2c_{x=t=0}\left(\frac{Dt}{\pi}\right)^{1/2} \quad \textbf{(1.36)}$$

Where M_t is the total amount of gas diffused into the solution at time = t in mol cm^{-2}, $c_{x=t=0}$ is the concentration of the gas at the interface at the start of the experiment in mol cm^{-3}, D is the diffusion coefficient of the gas in the solution in cm^2 s^{-1} and t is the time in seconds.

The total amount of gas in a solution can also be related to the change in pressure in the headspace above a solution as a gas dissolves into the solution through the ideal gas law (Equation 1.35). This is shown in Equation 1.37 where A is the surface area of the ionic liquid in cm^2.

$$M_t = \frac{\Delta pV}{RTA} \quad \textbf{(1.37)}$$

By combining Equations 1.36 and 1.37, Equation 1.38 is derived.

$$\Delta p = \frac{RTAM_t}{V} = \frac{RTA}{V} 2c_{t=x=0} \left(\frac{Dt}{\pi}\right)^{1/2} \quad \textbf{(1.38)}$$

By plotting a graph of the change in pressure, Δp, as gas dissolves into a liquid against $t^{1/2}$, a straight line graph is obtained. The slope of this line, m, can be used to determine the diffusion coefficient, as shown in Equation 1.39.

$$m = \frac{RTA}{V} 2c_{t=x=0} \left(\frac{D}{\pi}\right)^{1/2} \quad \textbf{(1.39)}$$

The diffusion coefficient can be found by rearranging Equation 1.39 to get Equation 1.40.

$$D = \frac{mV}{RTA} \frac{\pi^{1/2}}{2c_{t=x=0}} \quad \textbf{(1.40)}$$

This equation assumes that the effect of convection in the solution is negligible. It also assumes that the diffusion of the gas into the solution is a purely physical process with no heterogeneous chemical reactions occurring to remove gas from the cell headspace.

This method could provide an alternative method of determining the diffusion coefficient of gases in liquids that is not dependent on the use of electrodes.

1.7 Oxygen Redox Shuttle Compounds

The diffusion coefficient and solubility of oxygen in the ionic liquid could be improved greatly through the use of a redox shuttle compound.[72] This shuttle compound is able to reduce the oxygen present at the interface between the electrolyte and the atmosphere. The oxidised shuttle compound will then travel towards the air electrode where it will be reduced. The reduced shuttle compound would then travel back towards the air interface to be oxidised again. This prevents molecular oxygen from travelling towards the air electrode and instead uses the shuttle molecule to transfer electrons from the air electrode. This system displaces the oxygen reduction reaction and superoxide formation towards the air interface. This prevents the formation of insoluble lithium peroxide at the air electrode preventing blocking of the air electrode pores. The shuttle system may also be able to increase the current passed to the air electrode if it has a larger concentration or diffusion coefficient in the ionic liquid than oxygen does.

Several research groups have previously investigated the use of shuttles and mediators in Li-ion and Li-O_2 batteries.[3,10,13,72–76]

Ó'Laoire[10] investigated the use of ferrocene as a redox shuttle for overcharge protection in lithium-ion batteries. Chen and Amine[74] investigated the use of a pentaflurophenylboron oxylate compound as a combined redox shuttle and anion receptor for use in lithium-ion batteries. Shanmukaraj[75] *et al.* also investigated the use of boron-based esters as anion carriers and shuttle compounds.

For the lithium-air battery Lacey *et al.*[72] have previously demonstrated that ethyl viologen ditriflate could be used as a mediator and shuttle compound in the discharge reaction of a lithium-oxygen battery, while Chen *et al.*[76] have demonstrated the use of tetrathiafulvalene as a redox mediator to enhance the recharge reaction.

In lithium-air batteries mediators behave similarly to shuttles in that they increase the reaction rate by removing electrons from one molecule or electrode and transferring them to another. Where a shuttle differs from a mediator is in the location of the redox reactions. The mediator would be adjacent to the air electrode and reduce oxygen at the air electrode before being directly reduced by the electrode. A shuttle compound reduces oxygen at the air harvesting interface and then physically travels to the air electrode to be reduced.

One promising potential shuttle compound is ethyl viologen ditriflate (EtV $(OTf)_2$).[72] This compound is useful as its reduced form gives a visible blue colour which turns to colourless when it is oxidised on contact with oxygen. A schematic of this system is shown in Figure 1.14.

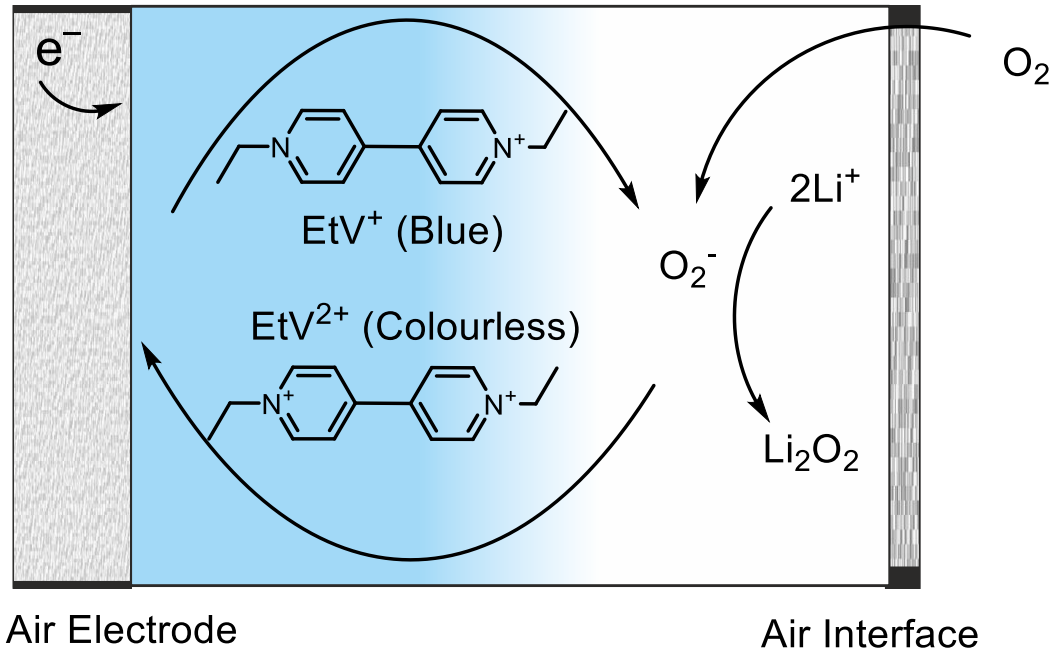

Figure 1.14: schematic of how a redox shuttle compound will work with a lithium-air battery.[72]

The blue reduced viologen ($EtV^{\bullet+}$) would move towards the air interface where it is oxidised by O_2 from the atmosphere. The superoxide formed in this reaction is then able to react with any lithium ions present in the electrolyte to form lithium peroxide. The colourless oxidised viologen (EtV^{2+}) then moves towards the air electrode where it is immediately reduced by the electrode.

This system could potentially increase the rate of diffusion of O_2 into the cell, as oxygen needs to diffuse a shorter distance. This could increase the power of the battery and making lithium-air batteries viable competitors to petrol fuelled engines for use in electric vehicles.

1.8 The Scope of this Thesis

This thesis will examine the electrochemical reduction of oxygen in pyrrolidinium and imidazolium based ionic liquids for use in a lithium-air battery with a focus on the diffusion coefficient and solubility of oxygen in these ionic liquids. The second chapter will study the electrochemical reduction of oxygen in pure 1-butyl-1-methyl pyrrolidinium bis(trifluoromethylsulfonyl)imide (PYR_{14} TFSI) ionic liquid using cyclic voltammetry potential step chronoamperometry to determine the diffusion coefficient and solubility of O_2 in the ionic liquid. The third chapter will study the electrochemical reduction of oxygen in several other pyrrolidinium and imidazolium based ionic liquids. The fourth chapter will investigate the use of electrochemical impedance spectroscopy to study the oxygen reduction reaction in the ionic liquids. The fifth chapter will study the measurement of the diffusion coefficient and solubility of oxygen in pure pyrrolidinium ionic liquids using potential step chronoamperometry. The sixth chapter will study attempts to determine the diffusion coefficient and solubility of oxygen in the ionic liquid containing large amounts of lithium by using perfluorinated additives to the ionic liquid. The final chapter will study the determination of the diffusion coefficient and solubility of oxygen in the ionic liquid through non-electrochemical pressure drop experiments, using the ethyl viologen redox shuttle compound.

1.9 Aims and Objectives

There are several aims which are attempted to be fulfilled in this thesis. The main aim is to investigate the mechanism of electrochemical oxygen reduction in pyrrolidinium and imidazolium based ionic liquids both in the presence and absence of lithium using techniques such as cyclic voltammetry and electrochemical impedance spectroscopy. This is to determine which ionic liquids are the most suitable for use in the LABOHR battery. This will be done in Chapters 2, 3 and 4 in the absence of lithium and Chapters 6 for ionic liquid containing lithium. Another major aim is to accurately determine the diffusion coefficient and solubility of oxygen in various room temperature ionic liquids using potential step chronoamperometry at a microdisc electrode. This is to determine which ionic liquid will give the greatest values of D_O and c_O and so be most suitable to be used in the LABOHR battery. This will be shown in Chapter 5. All of these aims should be able to help determine which ionic liquid is the most chemically suitable for use in the LABOHR battery. Other aims of this thesis are to study the oxygen reduction reaction in PYR_{14} TFSI and C_2MIM TFSI using electrochemical impedance spectroscopy. Another aim is to investigate the addition of ethyl viologen ditriflate to PYR_{14} TFSI and study the effect this has on the diffusion of oxygen into the ionic liquid as well as the solubility of oxygen. This will be shown in Chapter 7.

1.10 References

[1] J.-M. Tarascon, M. Armand, *Nature* **2001**, *414*, 359–367.

[2] M. S. Whittingham, *Chem. Rev.* **2004**, *104*, 4271–4302.

[3] N.-S. Choi, Z. Chen, S. A. Freunberger, X. Ji, Y.-K. Sun, K. Amine, G. Yushin, L. F. Nazar, J. Cho, P. G. Bruce, *Angew. Chem. Int. Ed. Engl.* **2012**, *51*, 9994–10024.

[4] X. Yang, Y. Xia, *J. Solid State Electrochem.* **2009**, *14*, 109–114.

[5] J. Read, *J. Electrochem. Soc.* **2002**, *149*, A1190–A1195.

[6] M. A. Rahman, X. Wang, C. Wen, *J. Appl. Electrochem.* **2013**, *44*, 5–22.

[7] K. M. Abraham, Z. Jiang, *J. Electrochem. Soc.* **1996**, *143*, 1–5.

[8] P. G. Bruce, S. A. Freunberger, L. J. Hardwick, J.-M. Tarascon, *Nat. Mater.* **2012**, *11*, 19–30.

[9] G. Girishkumar, B. McCloskey, A. C. Luntz, S. Swanson, W. Wilcke, *J. Phys. Chem. Lett.* **2010**, *1*, 2193–2203.

[10] C. M. Ó'Laoire, Investigations of Oxygen Reduction Reactions in Non-Aqueous Electrolytes and the Lithium-Air Battery, Northeastern University, **2010**.

[11] R. Padbury, X. Zhang, *J. Power Sources* **2011**, *196*, 4436–4444.

[12] M. Winter, R. J. Brodd, *Chem. Rev.* **2004**, *104*, 4245–4269.

[13] B. Scrosati, J. Garche, *J. Power Sources* **2010**, *195*, 2419–2430.

[14] M. Park, X. Zhang, M. Chung, G. B. Less, A. M. Sastry, *J. Power Sources* **2010**, *195*, 7904–7929.

[15] J.-M. Tarascon, D. Guyomard, *J. Electrochem. Soc.* **1991**, *138*, 2864–2868.

[16] J. R. Owen, *Chem. Soc. Rev.* **1997**, *26*, 259–267.

[17] M. B. Pinson, M. Z. Bazant, *J. Electrochem. Soc.* **2012**, *160*, A243–A250.

[18] F. Li, H. Kitaura, H. Zhou, *Energy Environ. Sci.* **2013**, *6*, 2302–2311.

[19] M. Winter, J. O. Besenhard, M. E. Spahr, P. Novák, *Adv. Mater.* **1998**, *10*, 725–763.

[20] D. Linden, T. B. Reddy, *Handbook of Batteries*, McGraw-Hill, New York, **2002**.

[21] M. Ishikawa, T. Sugimoto, M. Kikuta, E. Ishiko, M. Kono, *J. Power Sources* **2006**, *162*, 658–662.

[22] H. Liu, Y. Liu, J. Li, *Phys. Chem. Chem. Phys.* **2010**, *12*, 1685–1697.

[23] M. Diaw, A. Chagnes, B. Carré, P. Willmann, D. Lemordant, *J. Power Sources* **2005**, *146*, 682–684.

[24] C. O. Laoire, S. Mukerjee, K. M. Abraham, E. J. Plichta, M. A. Hendrickson, *J. Phys. Chem. C* **2010**, *114*, 9178–9186.

[25] A. Débart, A. J. Paterson, J. Bao, P. G. Bruce, *Angew. Chem. Int. Ed. Engl.* **2008**, *47*, 4521–4524.

[26] S. J. Visco, V. Y. Nimon, A. Petrov, K. Pridatko, N. Goncharenko, E. Nimon, L. De Jonghe, Y. M. Volfkovich, D. A. Bograchev, *J. Solid State Electrochem.* **2014**, *18*, 1443–1456.

[27] T. Zhang, N. Imanishi, Y. Takeda, O. Yamamoto, *Chem. Lett.* **2011**, *40*, 668–673.

[28] J. Xiao, W. Xu, D. Wang, J.-G. Zhang, *J. Electrochem. Soc.* **2010**, *157*, A294–A297.

[29] H. Nakamoto, Y. Suzuki, T. Shiotsuki, F. Mizuno, S. Higashi, K. Takechi, T. Asaoka, H. Nishikoori, H. Iba, *J. Power Sources* **2013**, *243*, 19–23.

[30] F. De Giorgio, F. Soavi, M. Mastragostino, *Electrochem. Commun.* **2011**, *13*, 1090–1093.

[31] T. Kuboki, T. Okuyama, T. Ohsaki, N. Takami, *J. Power Sources* **2005**, *146*, 766–769.

[32] J. Dupont, P. A. Z. Suarez, *Phys. Chem. Chem. Phys.* **2006**, *8*, 2441–2452.

[33] J. Christensen, P. Albertus, R. S. Sanchez-Carrera, T. Lohmann, B. Kozinsky, R. Liedtke, J. Ahmed, A. Kojic, *J. Electrochem. Soc.* **2012**, *159*, R1–R30.

[34] E. I. Rogers, X. Huang, E. J. F. Dickinson, C. Hardacre, R. G. Compton, *J. Phys. Chem. C* **2009**, *113*, 17811–17823.

[35] M. C. Buzzeo, O. V. Klymenko, J. D. Wadhawan, C. Hardacre, K. R. Seddon, R. G. Compton, *J. Phys. Chem. B* **2004**, *108*, 3947–3954.

[36] D. R. Simon, Characterization of Li4Ti5O12 and LiMn2O4 Spinel Materials Treated with Aqueous Acidic Solutions, Delft University of Technology, **2007**.

[37] A. Kraytsberg, Y. Ein-Eli, *J. Power Sources* **2011**, *196*, 886–893.

[38] A. W. Lodge, M. J. Lacey, M. Fitt, N. Garcia-Araez, J. R. Owen, *Electrochim. Acta* **2014**, *140*, 168–173.

[39] J. Jacquemin, M. F. Costa Gomes, P. Husson, V. Majer, *J. Chem. Thermodyn.* **2006**, *38*, 490–502.

[40] D. Tromans, *Hydrometallurgy* **1998**, *48*, 327–342.

[41] P. Han, D. M. Bartels, *J. Phys. Chem.* **1996**, *100*, 5597–5602.

[42] M. Armand, F. Endres, D. R. MacFarlane, H. Ohno, B. Scrosati, *Nat. Mater.* **2009**, *8*, 621–629.

[43] Z. Zhang, L. Yang, S. Luo, M. Tian, K. Tachibana, K. Kamijima, *J. Power Sources* **2007**, *167*, 217–222.

[44] H. Olivier-Bourbigou, L. Magna, D. Morvan, *Appl. Catal. A Gen.* **2010**, *373*, 1–56.

[45] T. C. Lourenço, M. F. C. Coelho, T. C. Ramalho, D. van der Spoel, L. T. Costa, *Environ. Sci. Technol.* **2013**, *47*, 7421–7429.

[46] C. Aliaga, C. S. Santos, S. Baldelli, *Phys. Chem. Chem. Phys.* **2007**, *9*, 3683–3700.

[47] T. Sato, G. Masuda, K. Takagi, *Electrochim. Acta* **2004**, *49*, 3603–3611.

[48] G. B. Appetecchi, M. Montanino, M. Carewska, M. Moreno, F. Alessandrini, S. Passerini, *Electrochim. Acta* **2011**, *56*, 1300–1307.

[49] S. Monaco, A. M. Arangio, F. Soavi, M. Mastragostino, E. Paillard, S. Passerini, *Electrochim. Acta* **2012**, *83*, 94–104.

[50] M. C. Buzzeo, C. Hardacre, R. G. Compton, *Anal. Chem.* **2004**, *76*, 4583–4588.

[51] S. Duluard, J. Grondin, J. Bruneel, I. Pianet, A. Grelard, G. Campet, J.-L. Delville, J. Lassegues, *J. Ramen Spectrosc.* **2008**, *39*, 627–632.

[52] M. A. Vorotyntsev, V. A. Zinovyeva, M. Picquet, *Electrochim. Acta* **2010**, *55*, 5063–5070.

[53] T. D. Dolidze, D. E. Khoshtariya, P. Illner, L. Kulisiewicz, A. Delgado, R. van Eldik, *J. Phys. Chem. B* **2008**, *112*, 3085–3100.

[54] Y. Katayama, K. Sekiguchi, M. Yamagata, T. Miura, *J. Electrochem. Soc.* **2005**, *152*, E247–E250.

[55] P. J. Mahon, K. B. Oldham, *Anal. Chem.* **2005**, *77*, 6100–6101.

[56] D. Morgan, L. Ferguson, P. Scovazzo, D. Morvan, *Ind. Eng. Chem. Res.* **2005**, *44*, 4815–4823.

[57] S. B. Capelo, T. Méndez-Morales, J. Carrete, E. López Lago, J. Vila, O. Cabeza, J. R. Rodríguez, M. Turmine, L. M. Varela, *J. Phys. Chem. B* **2012**, *116*, 11302–11312.

[58] A. S. Barnes, E. I. Rogers, I. Streeter, L. Aldous, C. Hardacre, G. G. Wildgoose, R. G. Compton, *J. Phys. Chem. C* **2008**, *112*, 13709–13715.

[59] A. J. Bard, L. R. Faulkner, *ELECTROCHEMICAL METHODS: Fundamentals and Applications*, John Wiley & Sons, Inc., New York, **2001**.

[60] D. Pletcher, *A First Course in Electrode Processes*, Royal Society Of Chemistry, Cambridge, **2009**.

[61] G. Denuault, M. V. Mirkin, A. J. Bard, *J. Electroanal. Chem.* **1991**, *308*, 27–38.

[62] D. Shoup, A. Szabo, *J. Electroanal. Chem.* **1982**, *140*, 237–245.

[63] S. Park, J.-S. Yoo, *Anal. Chem.* **2003**, *75*, 455 A–461 A.

[64] M. Fleischmann, S. Pons, *J. Electroanal. Chem.* **1988**, *250*, 277–283.

[65] Y. Katayama, H. Onodera, M. Yamagata, T. Miura, *J. Electrochem. Soc.* **2004**, *151*, A59–A63.

[66] J. Hou, M. Yang, M. W. Ellis, R. B. Moore, B. Yi, *Phys. Chem. Chem. Phys.* **2012**, *14*, 13487–13501.

[67] R. G. Evans, O. V. Klymenko, S. A. Saddoughi, C. Hardacre, R. G. Compton, *J. Phys. Chem. B* **2004**, *108*, 7878–7886.

[68] A. A. Oliferenko, P. V Oliferenko, K. R. Seddon, J. S. Torrecilla, *Phys. Chem. Chem. Phys.* **2011**, *13*, 17262–17272.

[69] R. Sander, *Atmos. Chem. Phys. Discuss.* **2014**.

[70] J. M. Prausnitz, R. M. Lichtenthaler, E. G. De Azevedo, *Molecular Thermodynamics of Fluid-Phase Equilibria*, Prentice Hall PTR, New Jersey, **1999**.

[71] D. Camper, C. Becker, C. Koval, R. D. Noble, *Ind. Eng. Chem. Res.* **2006**, *45*, 445–450.

[72] M. J. Lacey, J. T. Frith, J. R. Owen, *Electrochem. Commun.* **2013**, *26*, 74–76.

[73] L. F. Li, H. S. Lee, H. Li, X. Q. Yang, X. J. Huang, *Electrochem. Commun.* **2009**, *11*, 2296–2299.

[74] Z. Chen, K. Amine, *Electrochem. Commun.* **2007**, *9*, 703–707.

[75] D. Shanmukaraj, S. Grugeon, G. Gachot, S. Laruelle, D. Mathiron, J.-M. Tarascon, M. Armand, *J. Am. Chem. Soc.* **2010**, *132*, 3055–3062.

[76] Y. Chen, S. A. Freunberger, Z. Peng, O. Fontaine, P. G. Bruce, *Nat. Chem.* **2013**, *5*, 489–94.

2. Electrochemical O_2 Reduction in Pure PYR_{14} TFSI

The experiments undertaken in this chapter will investigate the electrochemical reduction of oxygen in the room temperature ionic liquid PYR_{14} TFSI. The mechanism of O_2 reduction is investigated using cyclic voltammetry at micro and macrodisc electrodes, while the diffusion coefficient and solubility of oxygen in PYR_{14} TFSI are investigated using potential step chronoamperometry at a microdisc electrode.

2.1 Introduction

The most critical reaction in any lithium-air battery is the electrochemical reduction of O_2 to superoxide ($O_2^{\bullet-}$). This reaction was studied in 1-butyl-1-methylpyrrolidinium bis(trifluoromethylsulfonyl)imide (PYR_{14} TFSI) using cyclic voltammetry (CV) and potential step chronoamperometry (PSCA).

In room temperature ionic liquids (RTILs) the reduction of O_2 occurs in two one-electron steps.[1,2] First, the O_2 molecule accepts an electron to be reduced to $O_2^{\bullet-}$. $O_2^{\bullet-}$ is a very nucleophilic species which will react with some ionic liquids,[2–5] making the O_2 reduction reaction irreversible. If the $O_2^{\bullet-}$ is stable in the RTIL it can undergo the second reduction step to be further reduced at lower potentials to peroxide (O_2^{2-}).[1]

Experiments were undertaken to study the mechanism of O_2 reduction in PYR_{14} TFSI using voltammetry and chronoamperometry at a macro and microdisc working electrodes. Simulations of cyclic voltammograms were also undertaken.

The aims of the experiments undertaken in this chapter were to determine the mechanism of oxygen reduction in pure PYR_{14} TFSI ionic liquid using cyclic voltammetry at a microdisc electrode. The aims were also to determine the diffusion coefficient and solubility of oxygen in oxygenated PYR_{14} TFSI using potential step chronoamperometry at a microdisc electrode. This would indicate if ionic liquids were suitable for use as the electrolyte and oxygen transport media in a lithium-air battery.

Parts of this chapter were previously published as Lodge *et al.*[1]

2.2 Experimental

A 3 mm diameter glassy carbon (GC) macrodisc working electrode was used for experiments undertaken using a macrodisc. This was constructed by sealing glassy carbon rods in glass. This GC electrode was polished and placed in a temperature controlled heart-shaped cell similar to that shown in Figure 2.1. A counter electrode of Pt gauze cleaned by flame annealing was used. The electrolytes used in this thesis are non-aqueous ionic liquids meaning that a standard aqueous reference electrode such as a saturated calomel electrode is unsuitable for these experiments. One of the most commonly used reference electrodes for use in RTILs is metallic lithium.[6,7] The reference electrode used in the macrodisc electrodes was Li foil (99.99%, Chemetall GmbH) on stainless steel gauze.

For microdisc CV experiments, a temperature controlled heart-shaped cell was used. The microdisc electrodes were created by sealing gold (99.95%, Alfa Aesar) or platinum (99.99%, Alfa Aesar) wires of the desired thickness in silica glass. A lithium manganese spinel intercalation electrode was used as the counter-reference electrode.[8] This electrode consisted of a $Li_{1.5}Mn_2O_4$ spinel, a mixture of $LiMn_2O_4$ and $Li_2Mn_2O_4$ spinel phases. Lithium intercalates into the spinel structure causing a shift between the phases, as shown in Equation 2.1.

$$LiMn_2O_4 + xLi^+ + xe^- \rightleftharpoons Li_{1+x}Mn_2O_4 \qquad \textbf{(2.1)}$$

The $Li_{1.5}Mn_2O_4$ spinel was made by mixing stoichiometric amounts of $LiMn_2O_4$ (Carus Chemical Company) and LiI (Acros Organics) and heating in a furnace at 120 °C for approximately 17 hours. The resulting spinel was then incorporated into a solution containing 7% w/w $Li_{1.5}Mn_2O_4$, 2% w/w Acetylene black (Chevron Philips Chemical Company LP), 1% w/w PVDF Homopolymer (Solvay Solexis LTD) and 90% w/w cyclopentanone (≥ 99%, Sigma-Aldrich). This solution was then heated and stirred until an ink-like consistency was obtained.

This ink was dip-coated onto platinum wire, which was placed in a fritted glass tube containing a 10 mM solution of LiTFSI (99.95%, Aldrich) in the ionic liquid. This was used as the counter-reference electrode for the experiments. This reference electrode gave a stable potential of +2.96 V *vs.* Li/Li^+.[8]

A picture of a heart-shaped cell used in these experiments is shown in Figure 2.1.

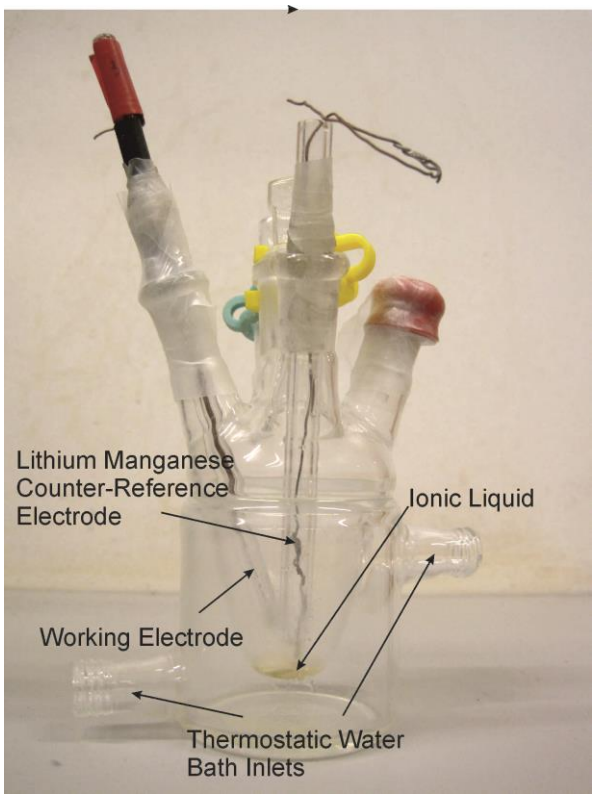

Figure 2.1: photograph of the heart-shaped cell used for these experiments showing a microdisc working electrode and the $Li_{1.5}Mn_2O_4$ counter-reference electrode.

For microdisc PSCA experiments, a cross-shaped cell based on a design by Compton *et al*.[9,10] was used in this experiment. This cell also uses a microdisc working electrode and a $Li_{1.5}Mn_2O_4$ counter-reference electrode. A pipette tip was attached to the microdisc working electrode using heat-shrink tubing. This was used to hold ≈ 0.3 cm^3 of ionic liquid. A photograph of this cell is shown in Figure 2.2.

Both the heart-shaped cell and cross-shaped cell could also be temperature controlled *via* the water bath. A vacuum was applied to the cell to remove any argon, oxygen or water in the ionic liquid before the oxygenation of the ionic liquid was done. O_2 was passed into the ionic liquid by bubbling directly into the ionic liquid *via* a needle.

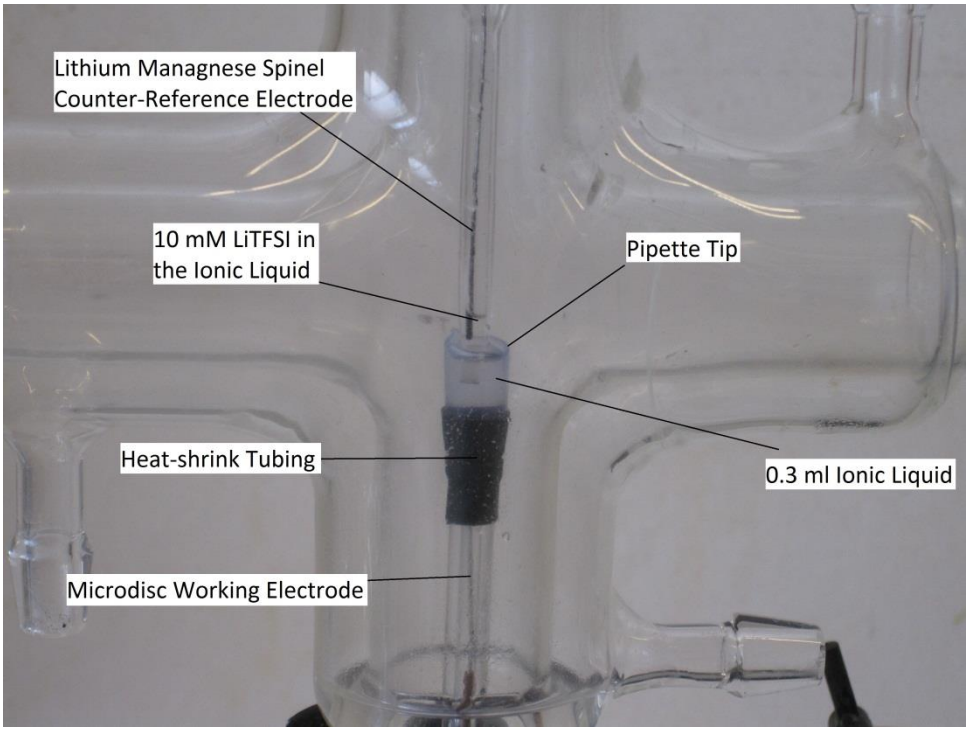

Figure 2.2: photograph of the cell used for these experiments showing the microdisc working electrode and the $Li_{1.5}Mn_2O_4$ counter-reference electrode.

Before doing any experiments using ionic liquids the surface area and diameter of each of the microelectrodes was assessed and measured *via* cyclic voltammetry in an aqueous solution of 0.1 M potassium ferrocyanide ($K_4Fe(CN)_6$**.**$3H_2O$, 99%, BDH Ltd), 0.1 M potassium ferricyanide ($K_3Fe(CN)_6$, 99%, East Anglia Chemicals) and 0.1 M potassium chloride (KCl, 99.0-100.5%, Sigma-Aldrich). The microelectrode was used as the working electrode, a high surface area Pt gauze was used as the counter electrode and a saturated calomel electrode (SCE) was used as the reference electrode. The cyclic voltammogram was swept from 0.5 V to -0.5 V *vs*. SCE at 5 mV s^{-1}, showing the reduction and oxidation of ferricyanide and ferrocyanide. By using the peak current for ferricyanide oxidation and the known diffusion coefficients (7.17×10^{-6} cm^2 s^{-1})[11] and concentrations of ferri/ferrocyanide, the surface area of the microdisc electrode was found using Equation 1.10.

Prior to each experiment the electrodes were polished by first soaking in 10% nitric acid (HNO_3, Fisher Scientific) for approximately 10 minutes to remove any organic contaminants. The electrode was then polished using various grades of alumina slurry (Büehler) on microfiber lapping pads. The electrodes were polished for approximately 10 minutes on 0.3 µm diameter alumina (Büehler), and then on 0.05 µm diameter

alumina (Büehler) for 10 minutes. The electrodes were then sonicated in deionised water (18 MOhm) for approximately 5 minutes to remove any remaining alumina particles.

PYR_{14} TFSI (99% IoLiTec, Ionic Liquid Technologies GmbH, Germany) was prepared and dried by heating at 120 °C under vacuum, while stirring for approximately 18 hours. This removed any oxygen, water and nitrogen from the RTIL. The RTIL was then stored in an argon glovebox (MBraun) where the H_2O concentration was normally less than 0.1 ppm and the O_2 concentration was normally less than 100 ppm. All electrochemical cells were assembled in this glovebox and then sealed airtight against the atmosphere. All electrochemical testing was undertaken outside of the glovebox, as well as the addition of any O_2 or Ar into the RTIL when required. The RTIL was oxygenated by bubbling O_2 directly into the ionic liquid *via* a needle for approximately 15 minutes until the RTIL was fully saturated.

Experiments were undertaken on a Bio-logic VMP 2 variable multichannel potentiostat using EC-lab software, or an Iviumsoft Compactstat potentiostat, using Iviumsoft software. All experiments were conducted in an earthed Faraday cage to eliminate the effects of external electrical noise on the experiment.

All simulations of voltammograms were undertaken using DigiElch 7.FD based on finite difference calculation methods. Initial values for known parameter were inputted along with estimated literature values for the unknown parameters, diffusion coefficient and solubility. Iterative fitting was undertaken until the simulated voltammogram obtained was similar to that determined from the experimental results.

2.3 Cyclic Voltammetry at a GC Macrodisc Electrode

Cyclic voltammetry was done in oxygenated PYR_{14} TFSI at the GC macrodisc electrode from 3.0 V *vs.* Li/Li^+ to 1.5 V *vs.* Li/Li^+ at various scan rates. The results of these experiments are shown in Figure 2.3 and Figure 2.4.

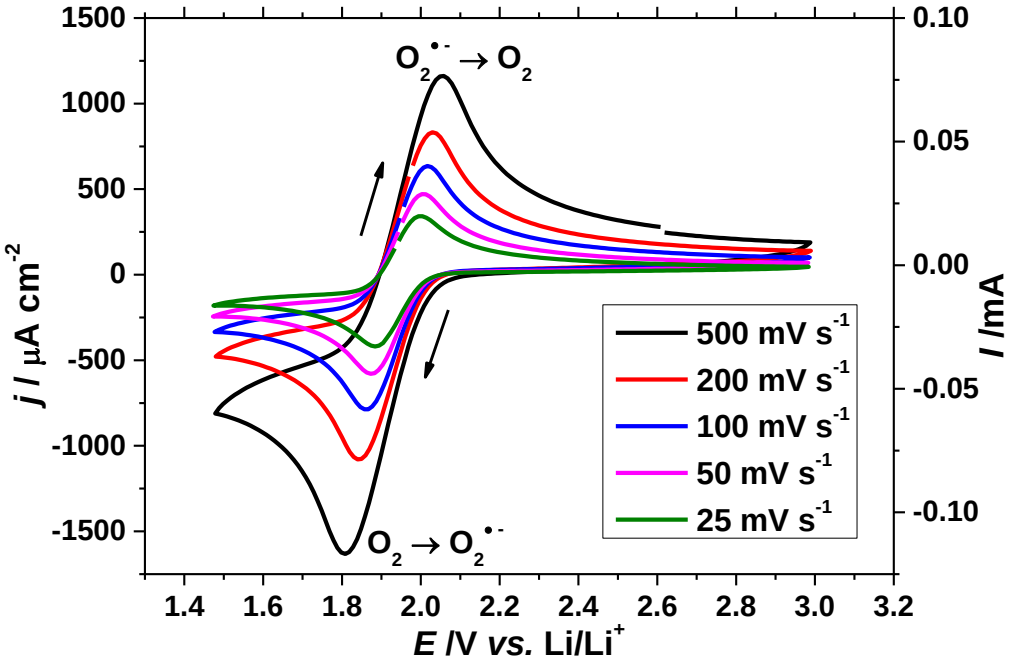

Figure 2.3: the first scans of cyclic voltammograms done at various scan rates from 3.0 V to 1.5 V *vs.* Li/Li^+.[1] This shows the electrochemical reduction of O_2 in oxygenated PYR_{14} TFSI. This experiment was done using a 3 mm diameter GC macroelectrode and a Li foil reference electrode in a heart-shaped cell at room temperature.[1] The ionic liquid was oxygenated by bubbling O_2 into it *via* a needle for approximately 30 minutes.

Figure 2.3 shows a large reduction wave occurring at 1.9 V *vs.* Li/Li^+ corresponding to the one electron reduction of O_2 to $O_2^{\bullet-}$. There is a reverse peak occurring at 2.1 V *vs.* Li/Li^+. This figure gives an $O_2/O_2^{\bullet-}$ formal potential (E^0) of 2.1 V *vs.* Li/Li^+.

[1] Reprinted from Electrochimica Acta, 140, A. W. Lodge, M. J. Lacey, M. Fitt, N. Garcia-Araez and J. R. Owen, Critical appraisal on the role of catalysts for the oxygen reduction reaction in lithium-oxygen batteries, 168-173, Copyright 2014, with permission from Elsevier.

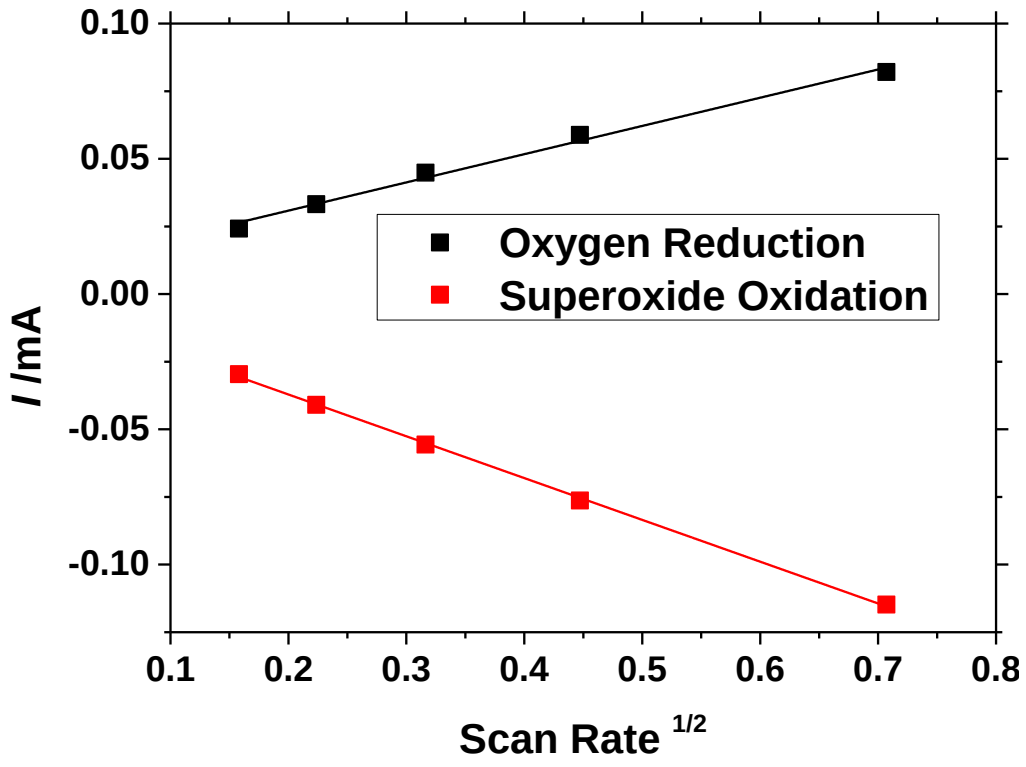

Figure 2.4: the peak current as a function of the scan rate$^{1/2}$ for the data shown in Figure 2.3.

Figure 2.4 shows the peak current as a function of scan rate for the data shown in Figure 2.3. This shows that there is a linear dependence of the scan rate on the peak current. A linear scan rate dependence indicates that the reaction is fully electrochemically reversible. This figure indicates that the reduction of O_2 to $O_2^{\bullet -}$ and the reverse reaction are both fully reversible.

Simulations of the cyclic voltammograms shown in Figure 2.3 were done to determine the values of D_O and c_O for this experiment. These were done using DigiElch 7.FD. The initial values the fitting were E^0 ($O_2/O_2^{\bullet -}$) = 2.1 V *vs.* Li/Li^+, k^0 ($O_2/O_2^{\bullet -}$) = 0.001 cm s^{-1}, $D_O = 12 \times 10^{-6}$ cm^2 s^{-1}, $c_O = 1 \times 10^{-6}$ mol cm^{-3}, $D_{O_2^{\bullet -}} = 1 \times 10^{-6}$ cm^2 s^{-1}.[1] The simulations are shown in Figure 2.5.

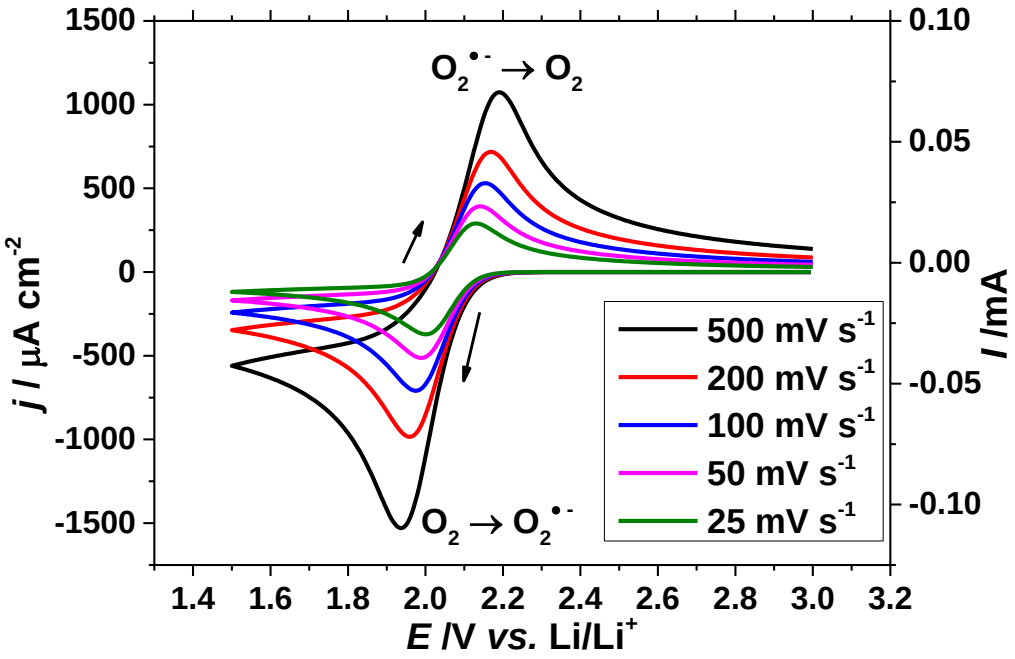

Figure 2.5: simulated cyclic voltammograms for the experiment shown in Figure 2.3 for the reduction of O_2 to $O_2^{\bullet-}$ at a 3 mm diameter GC macrodisc electrode at various scan rates. [2] The simulation parameters were E^0 ($O_2/O_2^{\bullet-}$) = 2.1 V *vs*. Li/Li^+, k^0 ($O_2/O_2^{\bullet-}$) = 0.001 cm s^{-1}, D_O = 12 × 10^{-6} cm^2 s^{-1}, c_O = 1 × 10^{-6} mol cm^{-3}, $D_{O_2^{\bullet-}}$ = 1 × 10^{-6} cm^2 s^{-1}.[1]

The simulated cyclic voltammograms (CVs) in Figure 2.5 show close agreement with the actual CVs in Figure 2.3. This shows peak currents of a similar order of magnitude and identical peak shapes to those seen in Figure 2.3. There are slight differences in the peak potentials. The potentials observed in the simulated data are shifted approximately 0.1 V positive of the potentials observed in Figure 2.3. This could be due to slight errors in the initial parameters used for the simulations or due to other effects such as the resistivity of the ionic liquid that were not accounted for by the simulation.

[2] Reprinted from Electrochimica Acta, 140, A. W. Lodge, M. J. Lacey, M. Fitt, N. Garcia-Araez and J. R. Owen, Critical appraisal on the role of catalysts for the oxygen reduction reaction in lithium-oxygen batteries, 168-173, Copyright 2014, with permission from Elsevier.

2.4 Cyclic Voltammetry at a Pt Microdisc Electrode

Cyclic voltammetry was undertaken in oxygenated PYR_{14} TFSI at a Pt microdisc working electrode from 5 V *vs*. Li/Li^+ to 0 V *vs*. Li/Li^+ at various scan rates. The results of this experiment are shown in Figure 2.6. The cyclic voltammograms shown here were done by undergraduate project student Matt Fitt.

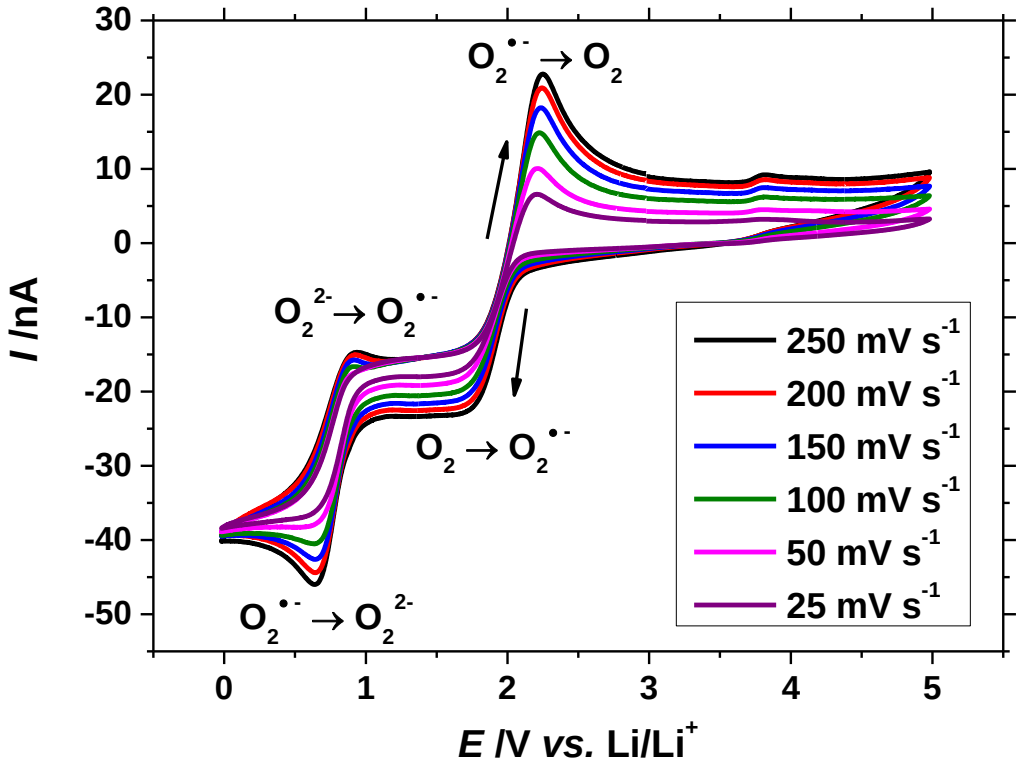

Figure 2.6: the first scan of cyclic voltammograms done in oxygenated PYR_{14} TFSI from 5 to 0 V *vs*. Li/Li^+ at various scan rates.[3] This experiment was done at a 25 µm diameter Pt microdisc working electrode using a $Li_{1.5}Mn_2O_4$ counter-reference electrode in a cross-shaped cell at room temperature.[1] The ionic liquid was saturated by bubbling with O_2 for ≈ 30 minutes. This cyclic voltammogram was done by project student Matt Fitt.

Figure 2.6 shows two electron transfer processes. The first reduction from O_2 to $O_2^{\bullet-}$ occurs at 2.0 V *vs*. Li/Li^+. The current then levels off at a plateau at 1.5 V *vs*. Li/Li^+ before the second reduction from $O_2^{\bullet-}$ to O_2^{2-} occurs at 0.9 V *vs*. Li/Li^+.

[3] Reprinted from Electrochimica Acta, 140, A. W. Lodge, M. J. Lacey, M. Fitt, N. Garcia-Araez and J. R. Owen, Critical appraisal on the role of catalysts for the oxygen reduction reaction in lithium-oxygen batteries, 168-173, Copyright 2014, with permission from Elsevier.

On the reverse scan the first peak at 0.9 V *vs*. Li/Li^+ corresponds to the oxidation of O_2^{2-} to $O_2^{\bullet-}$. This is again followed by a small plateau before the second oxidation peak at 2.2 V *vs*. Li/Li^+ occurs due to the oxidation of $O_2^{\bullet-}$ to O_2.

There are significant differences between the O_2 reduction behaviour on a microelectrode and on a macroelectrode.

The reduction peaks observed at a microelectrode show more wave-like voltammetry than the macroelectrode. This is due to the differences in the diffusion regimes to the microelectrode. On a macroelectrode, the diffusion of O_2 towards the electrode is linear one-dimensional diffusion giving the peak-like voltammetry where the current scales with $D_O^{1/2}c_O$ and scan rate $^{1/2}$. On a microelectrode the diffusion regime changes from linear diffusion at short times to hemispherical two-dimensional steady state diffusion at long times. This gives the distinctive wave-like voltammetry, where the current scales with $D_O c_O$.

Figure 2.6 shows wave-like voltammetry for the forward scan but wave-like voltammetry for the reverse peaks. This is because of the much smaller diffusion coefficient of $O_2^{\bullet-}$, roughly 10 times smaller than that of O_2 in ionic liquids,[1,9,12,13] and the lack of $O_2^{\bullet-}$ in the bulk solution. Because of this the superoxide is unable to form a hemispherical steady state diffusion field and so cannot undergo wave-like voltammetry.[1] This figure shows that O_2 reduction is fast and reversible at a microelectrode.

Simulations were done to simulate the experiment shown in Figure 2.6. The results of these simulations are shown in Figure 2.7.

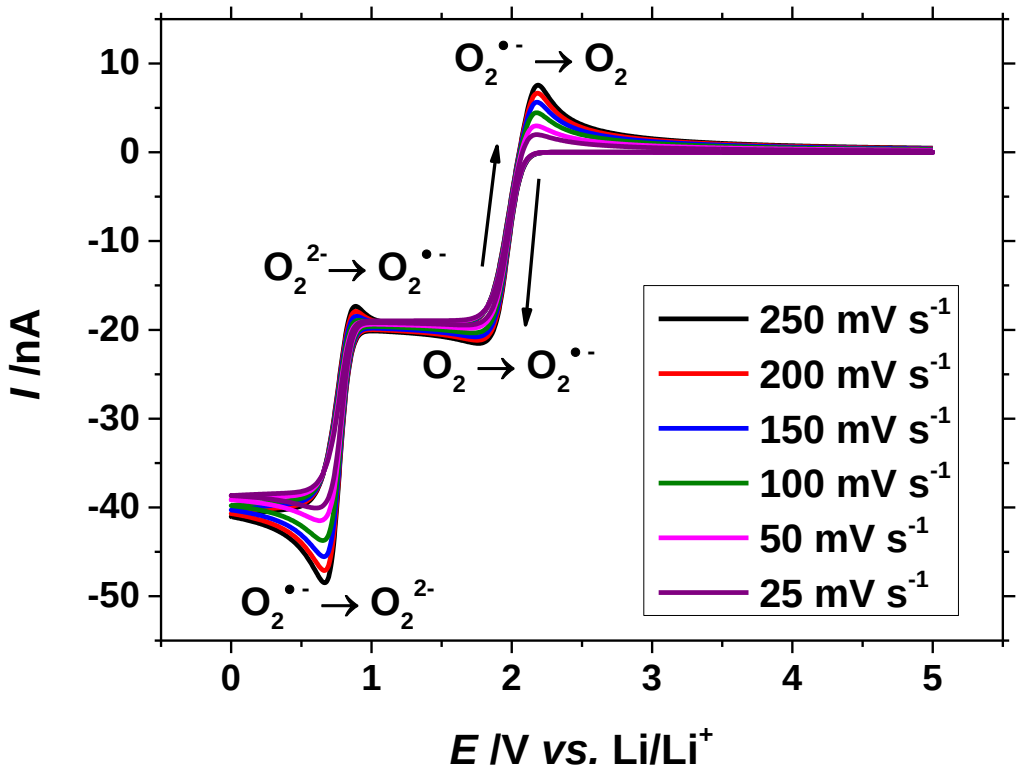

Figure 2.7: simulated cyclic voltammograms for the experiment shown in Figure 2.5 for the reduction of O_2 in PYR_{14} TFSI at a 25 µm diameter Pt microdisc electrode at various scan rates.[4] The simulation parameters were E^0 ($O_2/O_2^{\bullet-}$) = 2.1 V *vs*. Li/Li^+, k^0 ($O_2/O_2^{\bullet-}$) = 0.001 cm s^{-1}, D_O = 12 × 10^{-6} cm^2 s^{-1}, c_O = 1 × 10^{-6} mol cm^{-3}, E^0 ($O_2^{\bullet-}/O_2^{2-}$) = 0.8 V *vs*. Li/Li^+, k^0 ($O_2^{\bullet-}/O_2^{2-}$) = 0.001 cm s^{-1}, $D_{O_2^{\bullet-}}$ = 1 × 10^{-6} cm^2 s^{-1}, $D_{O_2^{2-}}$ = 1 × 10^{-6} cm^2 s^{-1}.[1]

Figure 2.7 shows several differences to Figure 2.6. The main difference is in the current separation between the forwards and reverse scan. This may have been caused by the double layer capacitance of the microdisc electrode which was not accounted for in the simulation. The peak shapes and peak currents are similar to the data shown in Figure 2.6.

[4] Reprinted from Electrochimica Acta, 140, A. W. Lodge, M. J. Lacey, M. Fitt, N. Garcia-Araez and J. R. Owen, Critical appraisal on the role of catalysts for the oxygen reduction reaction in lithium-oxygen batteries, 168-173, Copyright 2014, with permission from Elsevier.

2.5 Chronoamperometry at an Au Microdisc Electrode

Potential step chronoamperometry was undertaken at various temperatures at a 25 µm diameter Au microdisc electrode using the cross-shaped cell. A potential step to the oxygen reduction potential at 1.5 V *vs*. Li/Li^+ for 60 seconds. A sample chronoamperogram is shown in Figure 2.8.

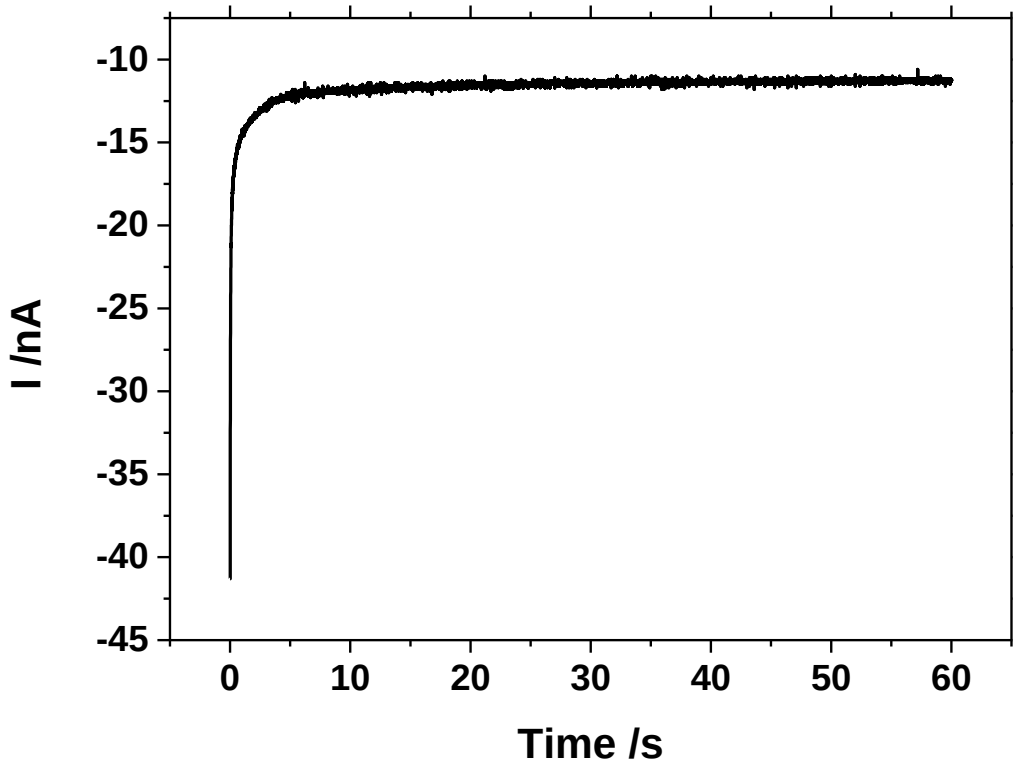

Figure 2.8: sample chronoamperogram showing a potential step to 1.5 V *vs*. Li/Li^+ for 60 seconds in oxygenated PYR_{14} TFSI at a 25 µm diameter Au microdisc working electrode. The experiment was done in a cross-shaped cell at 298 K. The ionic liquid was oxygenated by bubbling *via* a needle with O_2 for 30 minutes.

Figure 2.8 shows a large initial current cause by linear diffusion at short times. This current rapidly decreases as the diffusion field changes to the hemispherical diffusion field at long times.

The chronoamperograms (CAs) were analysed using the method outlined by Mahon and Oldham[14] as described in Chapter 1 to determine the values of D_O and c_O. The values of $D_O c_O$ were determined using the value of the steady state current of the chronoamperogram at long times applied to Equation 1.10. The results of these experiments are shown in Figure 2.9 to Figure 2.11. Each experiment consisted of one

full cell assembly using a fresh sample of ionic liquid. The ionic liquid was oxygenated by bubbling with O_2 for approximately 30 minutes. 3 CAs at each temperature were done at each temperature for each experiment. Three experiments were undertaken, filling the cell with fresh PYR_{14} TFSI each time. The average values of all the CAs from all the experiments for each temperature are shown in Figure 2.9.

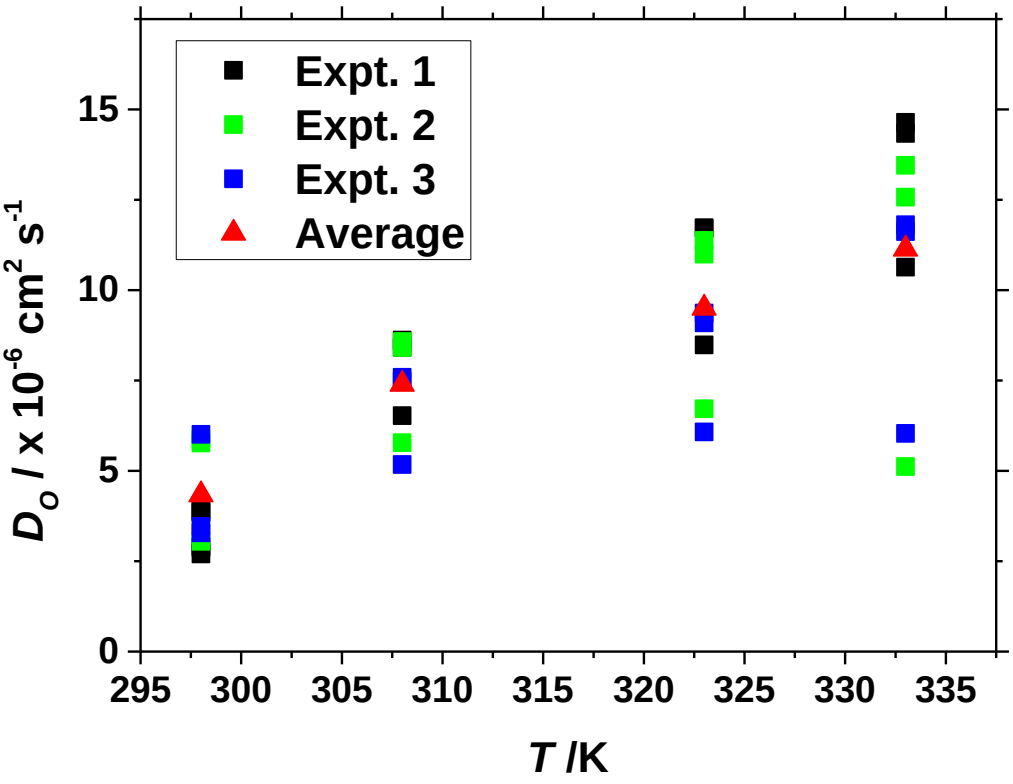

Figure 2.9: values of the diffusion coefficient of O_2 in oxygenated PYR_{14} TFSI at various temperatures measured by potential step chronoamperometry for three experiments. These were measured at a 25 µm diameter Au microdisc working electrode for a potential step to 1.5 V *vs.* Li/Li^+. All potential steps were done for 60 seconds. The ionic liquid was oxygenated by bubbling with O_2 *via* a needle. Each experiment consisted of 3 repeated CAs at each temperature in one sample of PYR_{14} TFSI.

Figure 2.9 shows the values of D_O obtained *via* potential step chronoamperometry. This figure shows that the value of D_O increases as the temperature increases. This is most likely to be due to the decreasing viscosity of the ionic liquid with temperature.[15] This figure shows that there are slight variations in the values of D_O determined for each experiment. This may be due to slight impurities present in the ionic liquid. The largest differences occur between the first CA and the subsequent CAs in an experiment, with

the first CA having a smaller value of D_O. This may be due to the formation of a monolayer on the working electrode during the initial CA.

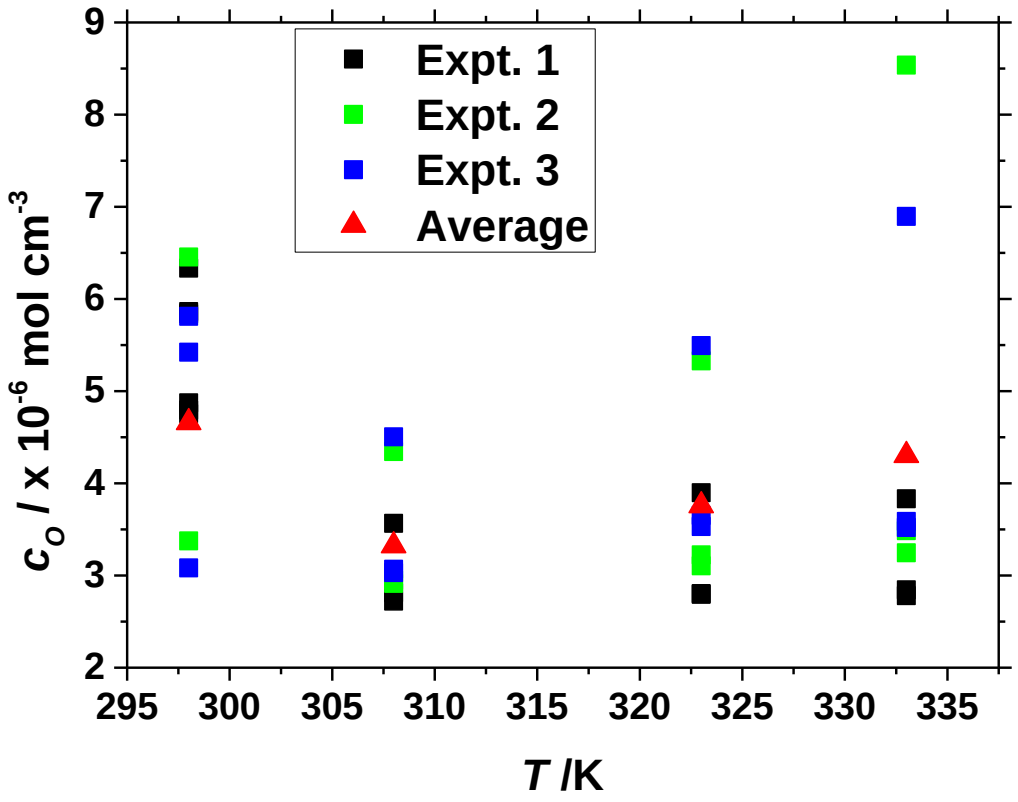

Figure 2.10: values of the solubilities of O_2 in PYR_{14} TFSI at various temperatures measured by potential step chronoamperometry. These were measured at a 25 µm diameter Au microdisc working electrode for PYR_{14} TFSI for a potential step to 1.5 V *vs.* Li/Li^+. All potential steps were done for 60 seconds. The ionic liquid was oxygenated by bubbling with O_2 *via* a needle. Each experiment consisted of 3 repeated CAs at each temperature in one sample of PYR_{14} TFSI.

Figure 2.10 shows the values of c_O at several temperatures for three experiments. This figure shows that the value of c_O decreases with temperature. This is expected as the solubility of gases in liquids generally decreases with temperature. Again Figure 2.10 shows large scattering between the CAs which may be caused by impurities in the ionic liquids.

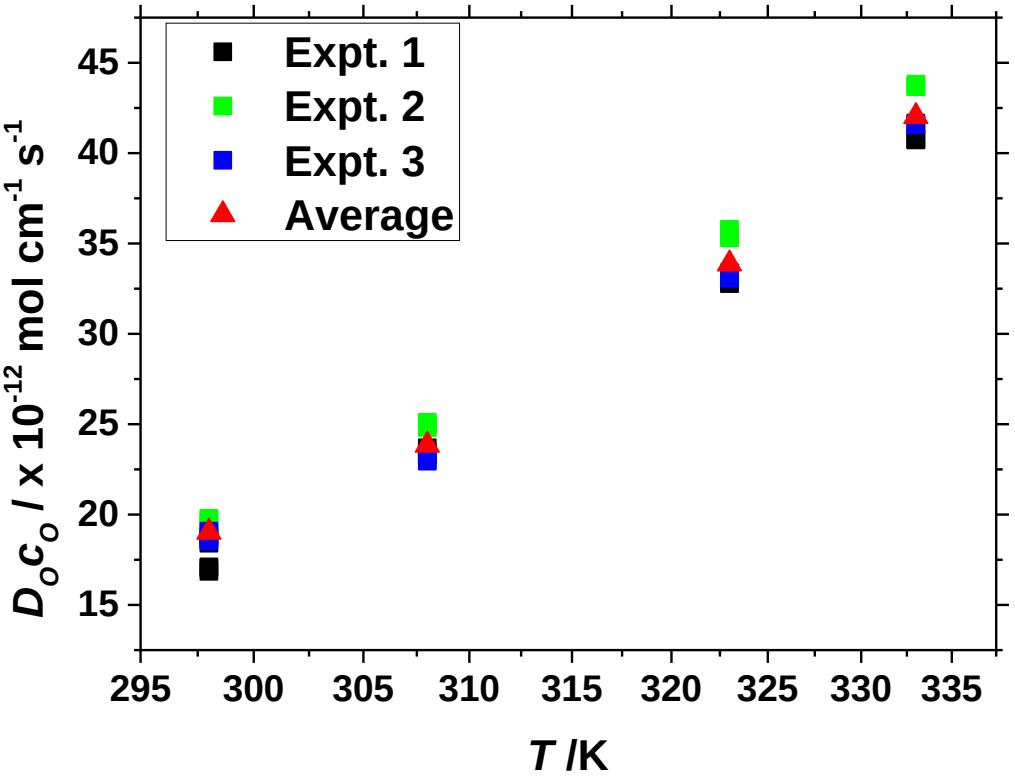

Figure 2.11: values of the diffusion coefficient-solubility products of O_2 in PYR_{14} TFSI at various temperatures measured by potential step chronoamperometry. These were measured at a 25 µm diameter Au microdisc working electrode for PYR_{14} TFSI for a potential step to 1.5 V *vs.* Li/Li^+. All potential steps were done for 60 seconds. The ionic liquid was oxygenated by bubbling with O_2 *via* a needle. Each experiment consisted of 3 repeated CAs at each temperature in one sample of PYR_{14} TFSI.

Figure 2.11 shows the diffusion coefficient-solubility products of O_2 at various temperatures. These values were calculated from the steady state current of the chronoamperogram using the Saito equation (Equation 1.10), however these values were similar to those obtained by combining D_O and c_O. This figure shows that the values of $D_O c_O$ increase as the temperatures increase. This is due to the decreasing viscosity of the ionic liquid increasing the value of D_O. Although the value of c_O decreases as the temperature increases, the D_O increase counteracts this to increase $D_O c_O$ overall.

The values of $D_O c_O$ show less variation between the experiments. This is because the values of $D_O c_O$ are calculated from the steady state current at long timescales, which varies little. However the individual values of D_O and c_O are calculated from the transition between the transient and the steady state diffusion regimes. This transition is

most easily affected by impurities in the ionic liquid, and so gives the largest variations in the values. The values of D_O, c_O and $D_O c_O$ are shown in Table 2.1.

Table 2.1: average values of D_O, c_O and $D_O c_O$ in PYR_{14} TFSI at various temperatures calculated *via* potential step chronoamperometry at a cross-shaped cell using a 25 μm diameter Au microdisc working electrode.

Ionic Liquid	T / K	D_O / × 10^{-6} cm^2 s^{-1}	c_O / × 10^{-6} mol cm^{-3}	$D_O c_O$ / × 10^{-12} mol cm^{-1} s^{-1}
PYR_{14} TFSI	298	4.3	4.6	19
	308	7.4	3.3	24
	323	9.5	3.8	34
	333	11.1	4.3	42

2.6 Comparison with Previously Calculated Values of D_O and c_O

Values of D_O and c_O at 298 K were also calculated by combining the value of $D_O^{1/2}c_O$ derived from the peak current from CVs at the macroelectrode from Figure 2.3 with the values of D_Oc_O calculated from the steady state current of PSCA at a microelectrode from Figure 2.11. The values obtained by this method are $D_O = 11.5 \pm 3.5 \times 10^{-6}$ cm^2 s^{-1} and $c_O = 3 \pm 0.5 \times 10^{-6}$ mol cm^{-2} at 298 K.[1] These values at are of the same order of magnitude as those shown in Figure 2.9 and Figure 2.10. However the value obtained from just PSCA showed a much lower D_O value of 4.3×10^{-6} cm^2 s^{-1}. This difference in the value of D_O may be due to slight passivation of the electrode caused by the presence of Li^+ ions in the solution.

The values obtained by combination of $D_O^{1/2}c_O$ and D_Oc_O are similar to those obtained by other research groups.[16,17] Differences between the values could be caused by different impurities in the ionic liquids, different temperatures and electrode surfaces.

2.6.1 Comparison with Values from Other Research Groups

The values of D_O, c_O and D_Oc_O in PYR_{14} TFSI have been calculated by several other research groups using several different methods. Monaco *et al.*[17] from the Università di Bologna, Italy, were a partner institution on the LABOHR project. This group also received ionic liquids from Westfälische Wilhelms-Universität Münster, Germany. The values of D_O, c_O and D_Oc_O were calculated by combining cyclic voltammograms at a macrodisc working electrode with the steady state currents from a microdisc working electrode. This method was also used in above.

This method was also used by Katayama *et al.*[12] to determine D_O and c_O at various temperatures.

Evans *et al.*[18] used single measurement potential step chronoamperometry. The chronoamperograms were analysed using the formula derived by Shoup and Szabo.[19]

The average values of D_O, c_O and D_Oc_O in PYR_{14} TFSI found in this chapter are compared with the values from other research groups in Figure 2.12 to Figure 2.14.

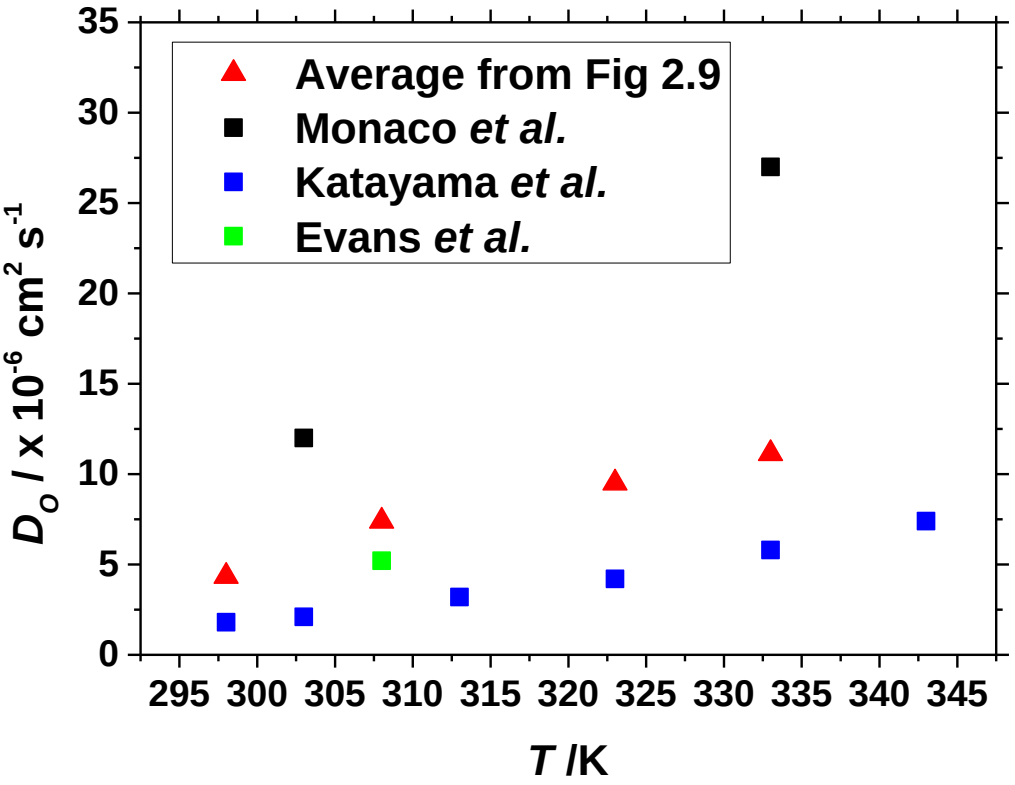

Figure 2.12: average values taken from Figure 2.9 of the diffusion coefficient of O_2 in PYR_{14} TFSI plotted against temperature compared with existing literature values. Literature values are taken from Monaco *et al.*,[17] Katayama *et al.*[12] and Evans *et al.*[18]

Figure 2.12 shows that there is a large variation in the values of D_O between the different sources. All of the sources agree that the diffusion coefficient increases as the temperature increases. However the rest of the variations may be accounted for by the degree of saturation of the ionic liquid and the purity of the ionic liquid. Differences in the methods of calculating D_O could also explain the discrepancy in the values.

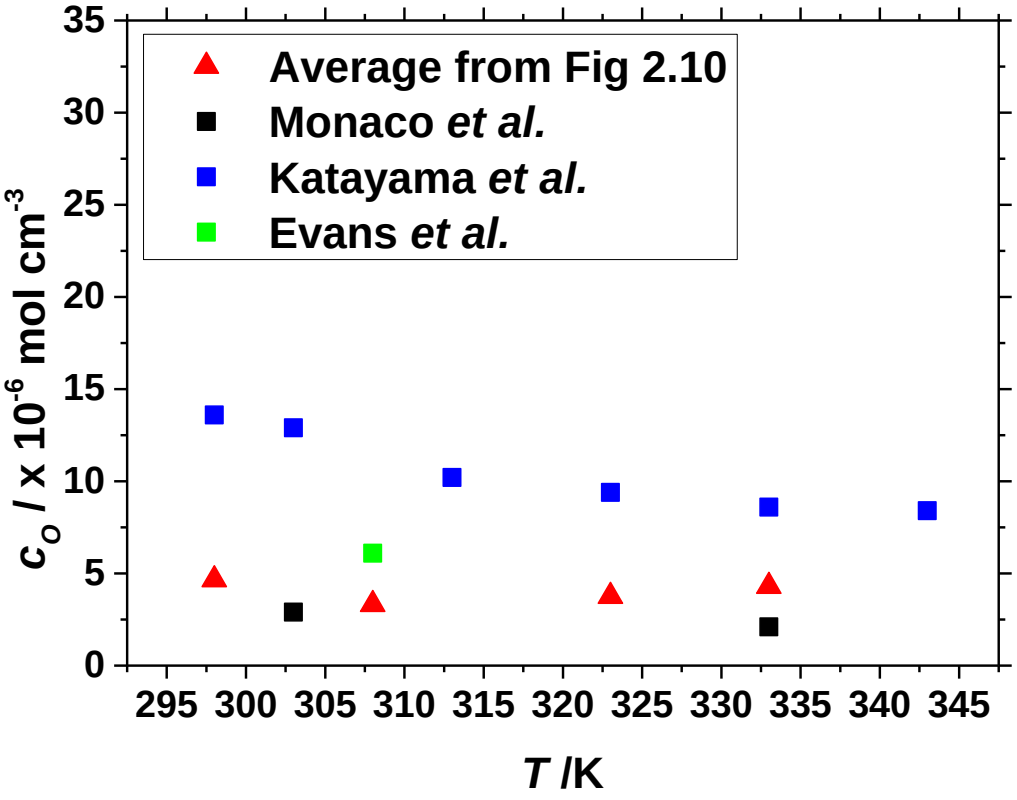

Figure 2.13: average values taken from Figure 2.10 of the solubility of O_2 in PYR_{14} TFSI plotted against temperature compared with existing literature values. Literature values are taken from Monaco *et al.*,[17] Katayama *et al.*[12] and Evans *et al.*[18]

Figure 2.13 shows that all of the experiments indicate that the solubility of O_2 decreases as the temperature increases. However there are large discrepancies in the values obtained from each research group. The values obtained by the experiments shown in this chapter are closest to those obtained by Monaco *et al.*[17] As both of these experiments used the same source of ionic liquid this indicates that the differences between the values from other research groups may be caused by the purity and composition of the ionic liquids.

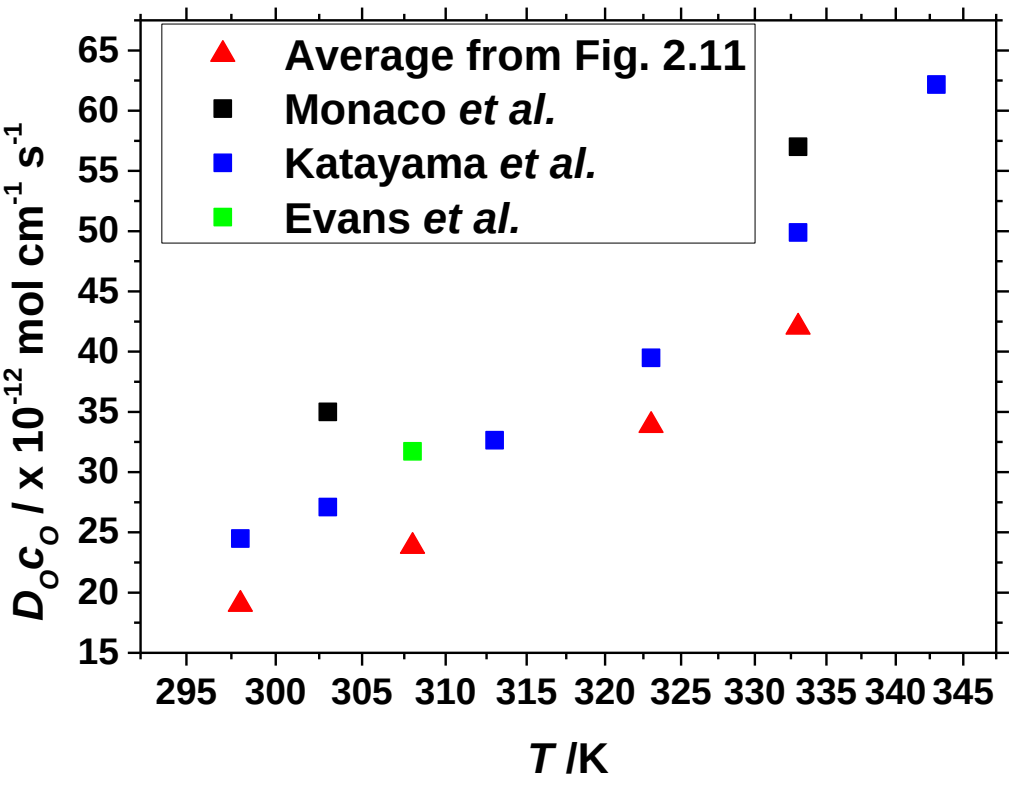

Figure 2.14: average values taken from Figure 2.11 of the diffusion coefficient-solubility product of O_2 in PYR_{14} TFSI plotted against temperature compared with existing literature values. Literature values are taken from Monaco *et al.*,[17] Katayama *et al.*[12] and Evans *et al.*[18]

Figure 2.14 shows that there is much more agreement between the literature values and the values found in this chapter. The literature values all agree that the value of $D_O c_O$ increases as the temperature increases. The slight differences in the values may be due to differences in the purities of the ionic liquids or due to differences in the methods of calculating these values.

Overall the values of D_O, c_O and $D_O c_O$ in PYR_{14} TFSI calculated from PSCA show some agreement with the literature values, however there are some differences which may be caused by differences in the ionic liquid used and the methods of calculating these values. Calculating the values of D_O and c_O individually is also more difficult than calculating $D_O c_O$, hence the larger spread of values of D_O and c_O than values of $D_O c_O$.

2.7 Conclusions

The investigation of O_2 reduction in PYR_{14} TFSI has been undertaken. It was found that O_2 reduction occurs in two one-electron steps, first from O_2 to $O_2^{\bullet-}$ followed by a one electron reduction from $O_2^{\bullet-}$ to O_2^{2-}. It was found that both of the reactions are reversible. However O_2^{2-}seems to be removed from the ionic liquid *via* a degradation reaction, leading to a smaller O_2^{2-} oxidation peak than expected. At a microdisc electrode it was found that the diffusion field towards the electrode was hemispherical, two-dimensional diffusion leading to the wave-like voltammetry observed in Figure 2.6. The values of D_O and c_O of O_2 were found using either a single PSCA measurement at a microelectrode or a combination of both a PSCA measurement at a microelectrode and a CV measurement at a macroelectrode. The values obtained by combined micro and macroelectrode measurements were in agreement with those reported by other groups, especially those for D_O. However the values obtained by a single PSCA measurement show less agreement with each other and the results from other research groups. This may be due to differences in the purity of the ionic liquids between the experiments, causing differences in the chronoamperometry.

The aims of the work undertaken in this chapter were to identify the mechanism of the electrochemical reduction of oxygen using cyclic voltammetry and determine the diffusion coefficient and solubility of oxygen in pure PYR_{14} TFSI using PSCA at a microdisc electrode. All of these aims have been successfully achieved.

The oxygen reduction mechanism in PYR_{14} TFSI has been successfully determined. The next aim is to determine the effect that varying the anion and cation of the ionic liquid has upon the mechanism of oxygen reduction. This is shown in Chapter 3.

2.8 References

[1] A. W. Lodge, M. J. Lacey, M. Fitt, N. Garcia-Araez, J. R. Owen, *Electrochim. Acta* **2014**, *140*, 168–173.

[2] Y. Katayama, H. Onodera, M. Yamagata, T. Miura, *J. Electrochem. Soc.* **2004**, *151*, A59–A63.

[3] M. M. Islam, T. Imase, T. Okajima, M. Takahashi, Y. Niikura, N. Kawashima, Y. Nakamura, T. Ohsaka, *J. Phys. Chem. A* **2009**, *113*, 912–916.

[4] M. M. Islam, T. Ohsaka, *J. Phys. Chem. C* **2008**, *112*, 1269–1275.

[5] E. I. Rogers, X. Huang, E. J. F. Dickinson, C. Hardacre, R. G. Compton, *J. Phys. Chem. C* **2009**, *113*, 17811–17823.

[6] A. Lewandowski, A. Swiderska-Mocek, *J. Appl. Electrochem.* **2009**, *40*, 515–524.

[7] P. C. Howlett, N. Brack, a. F. Hollenkamp, M. Forsyth, D. R. MacFarlane, *J. Electrochem. Soc.* **2006**, *153*, A595–A606.

[8] J.-M. Tarascon, D. Guyomard, *J. Electrochem. Soc.* **1991**, *138*, 2864–2868.

[9] M. C. Buzzeo, O. V. Klymenko, J. D. Wadhawan, C. Hardacre, K. R. Seddon, R. G. Compton, *J. Phys. Chem. A* **2003**, *107*, 8872–8878.

[10] S. R. Belding, E. I. Rogers, R. G. Compton, *J. Phys. Chem. C* **2009**, *113*, 4202–4207.

[11] J. E. Baur, R. M. Wightman, *J. Electroanal. Chem. Interfacial Electrochem.* **1991**, *305*, 73–81.

[12] Y. Katayama, K. Sekiguchi, M. Yamagata, T. Miura, *J. Electrochem. Soc.* **2005**, *152*, E247–E250.

[13] M. Hayyan, F. S. Mjalli, M. A. Hashim, I. M. Alnashef, X. M. Tan, *J. Electroanal. Chem.* **2011**, *657*, 150–157.

[14] P. J. Mahon, K. B. Oldham, *Anal. Chem.* **2005**, *77*, 6100–6101.

[15] S. B. Capelo, T. Méndez-Morales, J. Carrete, E. López Lago, J. Vila, O. Cabeza, J. R. Rodríguez, M. Turmine, L. M. Varela, *J. Phys. Chem. B* **2012**, *116*, 11302–11312.

[16] J. Herranz, A. Garsuch, H. A. Gasteiger, *J. Phys. Chem. C* **2012**, *116*, 19084–19094.

[17] S. Monaco, A. M. Arangio, F. Soavi, M. Mastragostino, E. Paillard, S. Passerini, *Electrochim. Acta* **2012**, *83*, 94–104.

[18] R. G. Evans, O. V. Klymenko, S. A. Saddoughi, C. Hardacre, R. G. Compton, *J. Phys. Chem. B* **2004**, *108*, 7878–7886.

[19] D. Shoup, A. Szabo, *J. Electroanal. Chem.* **1982**, *140*, 237–245.

3. Electrochemical O_2 Reduction in Room Temperature Ionic Liquids

The experiments undertaken in this chapter will investigate the electrochemical reduction of oxygen in pyrrolidinium and imidazolium based ionic liquids using cyclic voltammetry at platinum and gold microdisc electrodes.

3.1 Introduction

The electrochemical reduction of oxygen in several different room temperature ionic liquids has been studied using cyclic voltammetry (CV) at microdisc electrodes. The reduction of O_2 was found to occur in two one-electron reduction steps. The first reduction step occurs from O_2 to superoxide ($O_2^{\bullet -}$) and the second reduction step occurs from superoxide to peroxide (O_2^{2-}).

The aims of the experiments in this chapter were to determine the mechanism of electrochemical oxygen reduction in imidazolium based ionic liquids containing various cations and pyrrolidinium based ionic liquids containing various anions and cations using cyclic voltammetry. This will determine how the mechanism of oxygen reduction is affected by the anions and cations of the ionic liquid. This will enable the determination of which ionic liquids are most suitable for use in the LABOHR battery.

3.2 Experimental

Several imidazolium and pyrrolidinium based room temperature ionic liquids were studied in this investigation. These room temperature ionic liquids (RTILs) were all selected due to their large electrochemical stability windows, approximately 6 V, their relatively high lithium and oxygen diffusion coefficients and solubilities, and their low costs compared to other ionic liquids.[1] Several of these RTILs were purchased commercially from IoLiTec GmbH, Heilbronn, Germany. These had a water and halide content normally less than 100 ppm when received. Eight of the RTILs were synthesised and purified by one of our LABOHR partners, the Passerini Group from Westfälische Wilhelms-Universität (WWU), Münster, Germany. These were reported as being ultrapure RTILs with a negligible H_2O and O_2 content when received.

All of the ionic liquids were dried and deoxygenated using the same method stated in Chapter 2. The RTILs were then stored in the argon glovebox where electrochemical cells were also assembled.

The ionic liquids that were used for these experiments and their physical properties are shown in Table 3.1 while the structures of these ionic liquids are shown in Table 3.2.

Table 3.1: ionic liquids used in these experiments and their physical properties. WWU = Westfälische Wilhelms-Universität, Münster, Germany. Values obtained from references.[2–5]

Ionic Liquid	Acronym	Mr /g mol^{-1}	m.p. /K	ρ /g cm^{-3}	η /cP at 293 K	Source
1-butyl-1-methyl pyrrolidinium bis(trifluoromethylsulfonyl)imide	PYR_{14} TFSI	422	266.5[4]	1.43[3]	60 at 308 K[3]	IoLiTec, WWU
1-ethyl-3-methyl imidazolium bis(trifluoromethylsulfonyl)imide	C_2MIM TFSI	391.3	258.15[2]	1.52[4]	36[4]	IoLiTec
1-butyl-3-methyl imidazolium bis(trifluoromethylsulfonyl)imide	C_4MIM TFSI	419.4	270.2[2]	1.44[2]	44[2]	IoLiTec
1-butyl-3-methyl imidazolium hexafluorophosphate	C_4MIM PF_6	284	283[2]	1.36[2]	312[2]	IoLiTec
1-butyl-1-methyl pyrrolidinium bis(perfluoroethylsulfonyl)imide	PYR_{14} BETI	522	281.9[4]	1.48[4]	350[4]	WWU
1-butyl-1-methyl pyrrolidinium Nonafluorobutylsulfonyl (trifluoromethylsulfonyl)imide	PYR_{14} IM_{14}	572	-	1.51[4]	560[4]	WWU
1-Butyl-1-methyl pyrrolidinium (fluorosulfonyl)imide	PYR_{14} FSI	322	-	-	-	WWU
1- methoxyethyl-1-methyl pyrrolidinium bis(trifluoromethylsulfonyl)imide	PYR_{12O1} TFSI	424	-	1.46[4]	57.6[4]	WWU
1- methoxyethyl -1-methyl pyrrolidinium bis(perfluoroethylsulfonyl)imide	PYR_{12O1} BETI	524	281[5]	-	158.2[5]	WWU
1- methoxyethyl -1-methyl pyrrolidinium Nonafluorobutylsulfonyl (trifluoromethylsulfonyl)imide	PYR_{12O1} IM_{14}	576	-	-	178.8[5]	WWU
1- methoxyethyl -1-methyl pyrrolidinium (fluorosulfonyl)imide	PYR_{12O1} FSI	324	277[5]	-	36.5[5]	WWU

Table 3.2: structures of the ionic liquids used in these experiments.

Acronym	Cation Structure	Anion Structure
PYR_{14} TFSI	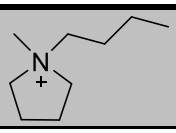	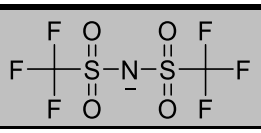
C_2MIM TFSI	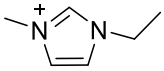	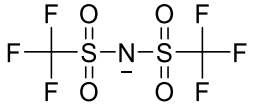
C_4MIM TFSI	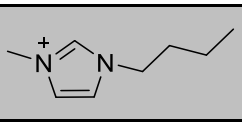	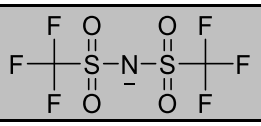
C_4MIM PF_6	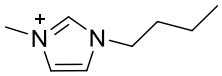	
PYR_{14} BETI	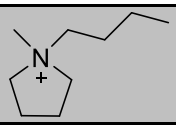	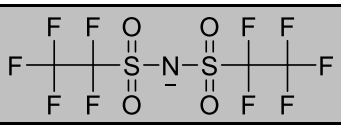
PYR_{14} IM_{14}	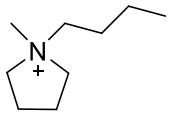	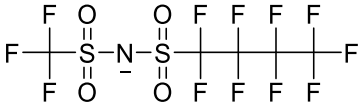
PYR_{14} FSI	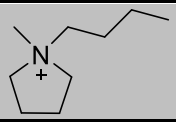	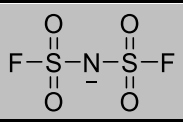
PYR_{12O1} TFSI	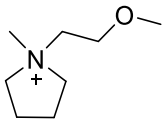	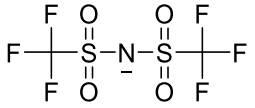
PYR_{12O1} BETI	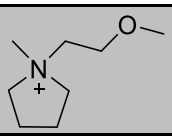	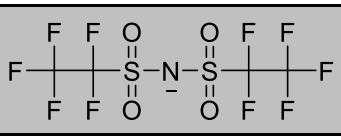
PYR_{12O1} IM_{14}	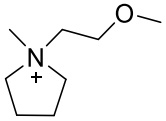	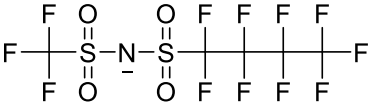
PYR_{12O1} FSI	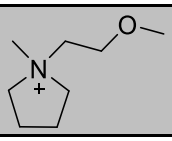	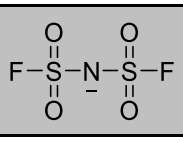

The O_2 reduction reaction in these pure RTILs was analysed using cyclic voltammetry at microdisc electrodes. Gold (99.95%, Alfa Aesar) or platinum (99.95%, Alfa Aesar) wires were sealed in glass rods to make a microdisc electrode. The diameter of these microdisc electrodes was calculated as being 10 µm or 25 µm using ferri/ferrocyanide

solution as described in Chapter 2. The electrodes were polished as previously stated in Chapter 2.

The imidazolium based ionic liquids were analysed using the temperature controlled heart-shaped cell described in Chapter 2 using a Pt microdisc working electrode and a $Li_{1.5}Mn_2O_4$ counter-reference electrode. Pure silver wire (3 mm diameter) was also used as a quasi-reference electrode in several of the imidazolium ionic liquid experiments. This wire had a potential of ≈ +3.8 V *vs.* Li/Li^+. The pyrrolidinium based ionic liquids were analysed using the cross-shaped cell described in Chapter 2 using a Pt or Au microdisc working electrode and a $Li_{1.5}Mn_2O_4$ counter-reference electrode.

Before analysis any extra water, oxygen or nitrogen present in the ionic liquid was removed. For the heart-shaped cell this was done by bubbling argon gas into the ionic liquid *via* a needle inserted through the suba seal for approximately 30 minutes. For the cross-shaped cell a vacuum was applied to one of the stopcocks on the cell and a heating tape applied up to a temperature of 120 °C for approximately 1 hour. All electrochemical measurements were undertaken using a Bio-logic VMP2 potentiostat-galvanostat using EC-Lab software or an Iviumsoft Ivium Portable potentiostat using IviumSoft software.

Oxygen was passed into the ionic liquid by either passing oxygen into the headspace of the cell and allowing it to diffuse into the ionic liquid naturally over several hours, or by bubbling directly into the ionic liquid *via* a needle for approximately 30 minutes.

3.3 Imidazolium Based Ionic Liquids

Initial experiments were undertaken using C_2MIM TFSI, C_4MIM TFSI and C_4MIM PF_6 investigating the electrochemical reduction of O_2 in these ionic liquids using cyclic voltammetry. These ionic liquids were investigated because they are widely used and commercially available. They are also relatively cheap in comparison to other ionic liquids. Heart-shaped cells were assembled as previously stated and argon was bubbled into the ionic liquid for approximately 20 minutes to remove any O_2, H_2O and other volatile impurities. Cyclic voltammetry was then undertaken to successively more positive and more negative potentials to determine the electrochemical stability limits of these ionic liquids where the ionic liquid starts to breakdown due to the large electrical potential applied. This decomposition of the ionic liquid causes a large increase in the current and these measurements are used to determine the safe working limits of the ionic liquids. These voltammograms are shown in Figure 3.1.

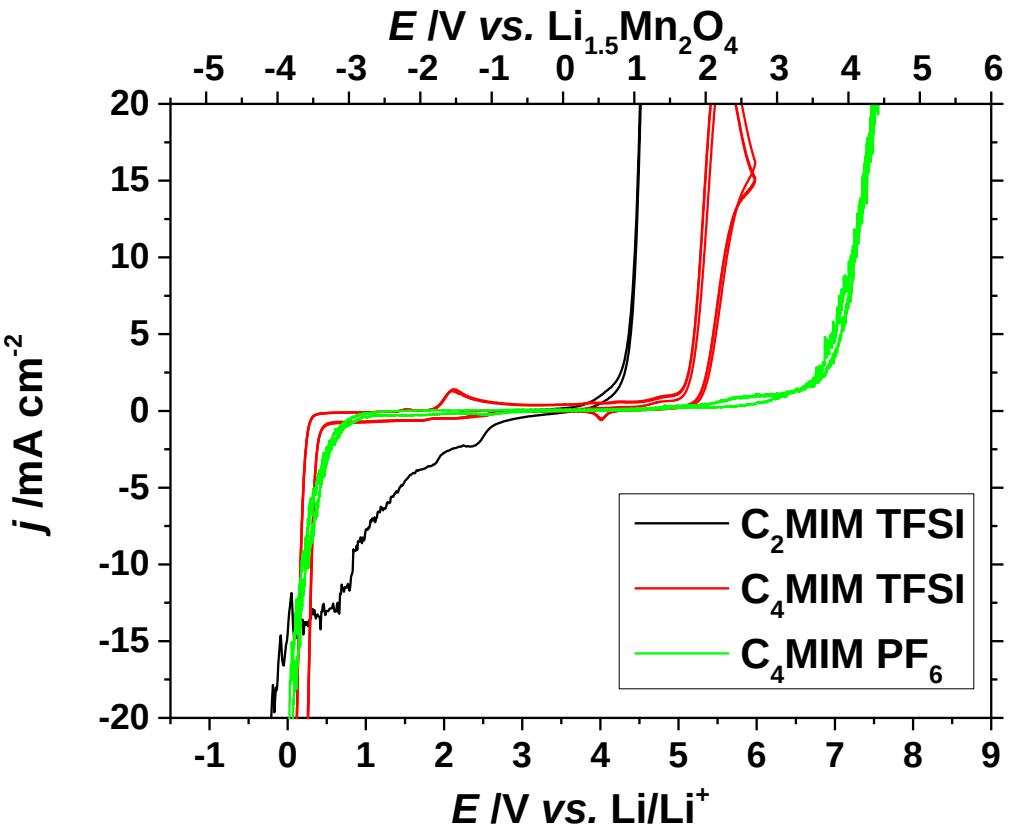

Figure 3.1: cyclic voltammograms showing the electrochemical stability windows of the imidazolium room temperature ionic liquids C_2MIM TFSI (10 µm diameter Pt microelectrode at 50 mV s^{-1}), C_4MIM TFSI (25 µm diameter Au microelectrode at 100 mV s^{-1}) and C_4MIM PF_6 (10 µm diameter Pt microelectrode at 50 mV s^{-1}). The cyclic voltammograms were done using a heart-shaped cell using a $Li_{1.5}Mn_2O_4$ counter-reference electrode.

Figure 3.1 indicates that the imidazolium ionic liquids have rather large stability windows of approximately 5 V, far greater than that of aqueous electrolytes (≈ 2 V).[6] These ionic liquids all appear to show slightly different decomposition potentials, with a cathodic decomposition peak between 0 V and -0.5 V *vs.* Li/Li^+ caused by the decomposition of imidazolium. This indicates that there is little difference in the decomposition potentials of the C_2MIM and C_4MIM. Figure 3.1 shows that the anodic decomposition occurs at 4 to 5 V *vs.* Li/Li^+ for C_4MIM PF_6. This is due to the increased stability of the PF_6 anion compared to the TFSI anion. The voltammogram of C_2MIM TFSI shows an increase in current starting at 2.5 V *vs.* Li/Li^+ on the cathodic sweep. This could be caused by the presence of water in the ionic liquid. The voltammogram of C_4MIM TFSI also shows a small peak at 4 V *vs.* Li/Li^+ on the cathodic sweep as well as peaks at 2 V *vs.* Li/Li^+ and 4.5 V *vs.* Li/Li^+ on the anodic sweep. These small peaks

could be caused by impurities such as oxygen and water present in the ionic liquids. There is significant evidence that impurities such as water affect the electrochemical stability windows of ionic liquids.[7–9] This may explain the TFSI ionic liquids having different anodic stability limits despite having the same anion.

O_2 was bubbled into the ionic liquids for approximately 10 minutes until the ionic liquids were saturated. Cyclic voltammetry was run between 3.7 V and 1.8 V *vs.* Li/Li^+ at various scan rates to study the oxygen reduction reaction. The resulting cyclic voltammograms are shown in Figure 3.2, Figure 3.3 and Figure 3.4.

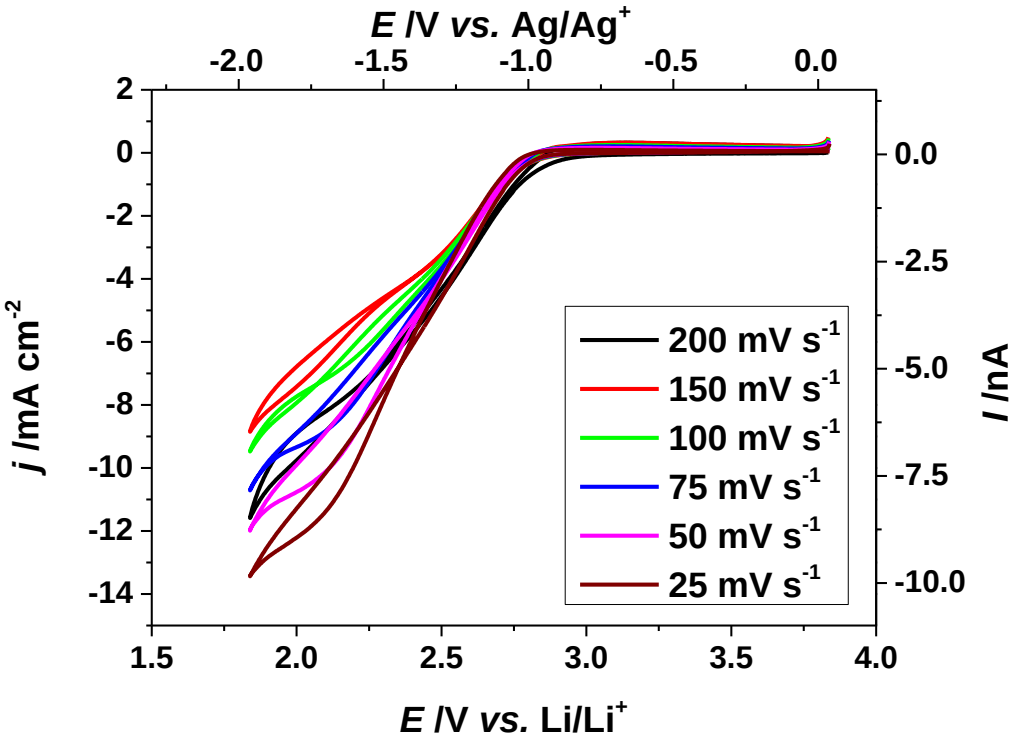

Figure 3.2: cyclic voltammograms showing the electrochemical reduction of oxygen in C_2MIM TFSI. This was done using a cross-shaped cell containing a 10 µm diameter Pt microdisc electrode and an Ag wire counter-reference electrode. The ionic liquid was oxygenated by passing O_2 into the headspace and allowing it to diffuse into the ionic liquid over 12 hours.

Figure 3.2 shows the electrochemical reduction of O_2 at a Pt electrode. This shows a broad slope which begins at 2.75 V *vs.* Li/Li^+ and descends until the end of the cathodic voltammogram sweep. This peak also follows the same path for the anodic reverse scan with no other peak observed. The angle of the slope appears to increase with a decrease in the scan rate. The increase in the current from the baseline indicates that an electrochemical reaction is occurring. The absence of any peak on the reverse scan also

indicates that either the diffusion coefficient of $O_2^{\bullet-}$ is approximately the same as that of O_2 or that $O_2^{\bullet-}$ is not stable in the C_2MIM TFSI. It is generally acknowledged that the diffusion coefficient of $O_2^{\bullet-}$ in ionic liquids is approximately half to thirty times smaller than that of O_2, [10–12] therefore this explanation is unlikely. It is most likely that the superoxide generated by the O_2 reduction is reacting with a species in the solution, removing itself and so not being available to be oxidised on the reverse scan. The most likely and abundant species available for reaction is the imidazolium cation from the ionic liquid. Previous research has noted the reaction of $O_2^{\bullet-}$ with imidazolium cations,[13–16] therefore it is likely that the same reaction is occurring in this experiment. A scheme of this reaction is seen in Equation 3.1.[16] The superoxide anion reacts with the labile proton on the imidazolium cation, forming hydrogen peroxide and a 2-imidazolone. This breaks down the ionic liquid and removes the oxygen from the electrolyte.

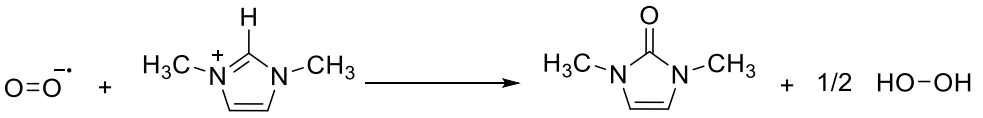

(3.1)

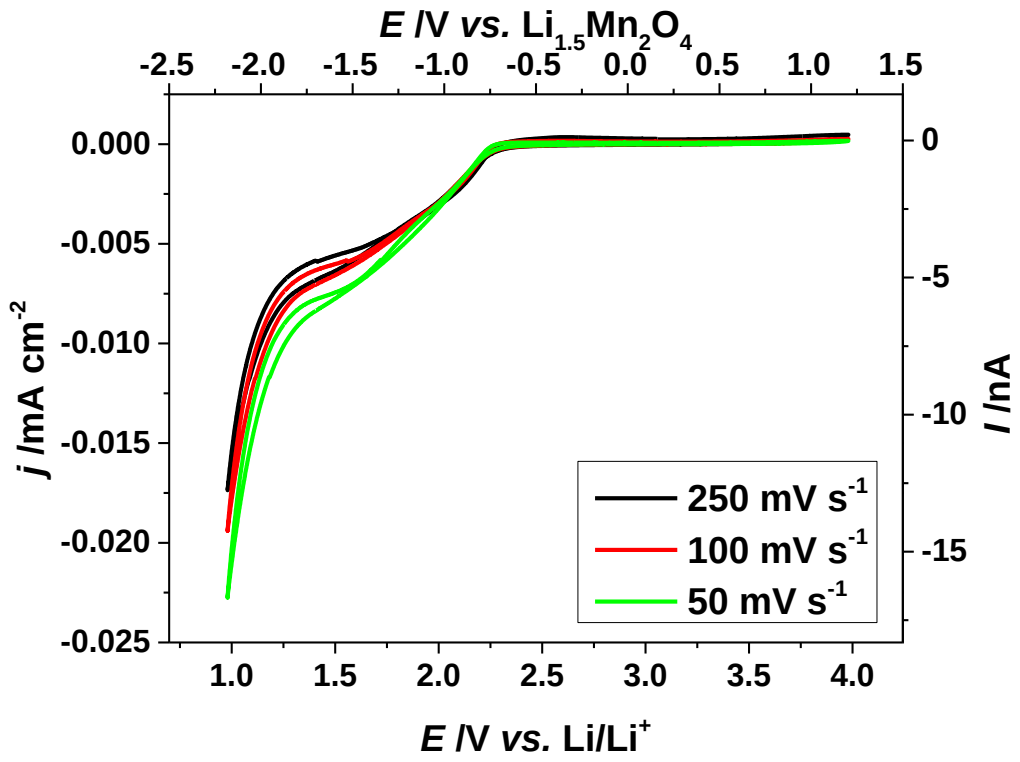

Figure 3.3: cyclic voltammograms showing the electrochemical reduction of oxygen in C_4MIM TFSI. This was done using a cross-shaped cell with a 25 µm diameter Pt microdisc working electrode and a $Li_{1.5}Mn_2O_4$ counter-reference electrode. O_2 was passed into the cell by bubbling with O_2 *via* a needle for approximately 30 mins.

Figure 3.3 shows the electrochemical reduction of oxygen in C_4MIM TFSI ionic liquid at various scan rates. This figure shows that the reduction of O_2 starts to occur at approximately 2.0 V *vs.* Li/Li^+ with the current becoming more negative. This current becomes more negative until almost levelling off at 1.5 V *vs*. Li/Li^+. At 1.25 V *vs*. Li/Li^+ the current becomes much more negative. The magnitude of this change in current indicates the breakdown of the ionic liquid. There are no distinct peaks on the reverse scan, indicating that $O_2^{\bullet-}$ may not be stable in C_2MIM TFSI.

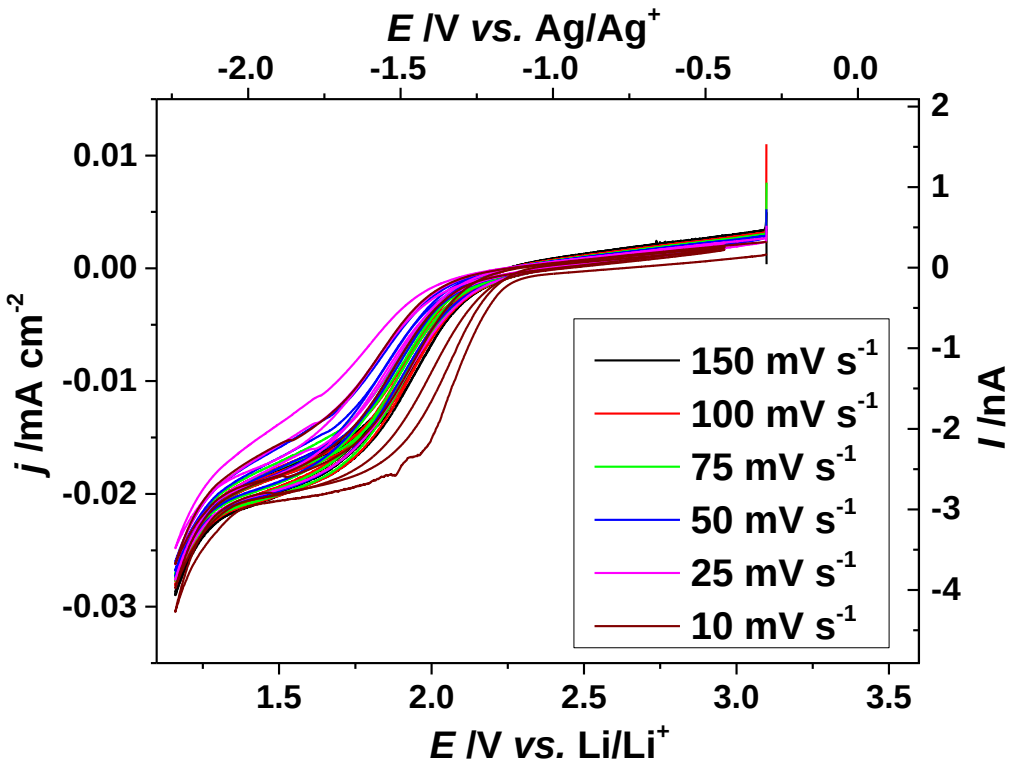

Figure 3.4: cyclic voltammograms showing the electrochemical reduction of O_2 in C_4MIM PF_6.This voltammogram was done using a heart-shaped cell using a 5 µm diameter Pt microdisc working electrode and a $Li_{1.5}Mn_2O_4$ counter-reference electrode. Oxygen was passed into the ionic liquid *via* a needle for approximately 30 minutes to oxygenate the ionic liquid.

Figure 3.4 shows similar electrochemical behaviour to that shown in Figure 3.2. The cathodic sweep shows a reduction wave starting at approximately 2.25 V *vs.* Li/Li^+ and descending until the end of the sweeps at 1.25 V *vs.* Li/Li^+. The reverse sweep shows almost identical behaviour to the forward scan. The lack of oxidation peaks on the reverse, anodic scans indicates that the product formed on the cathodic scan is unstable. The reduction wave shows a slight change in onset potential with scan rate. The reduction wave is caused by the one electron reduction of O_2 to $O_2^{\bullet -}$. However, the lack of a reverse peak or a stable plateau indicates that the superoxide is not stable in this ionic liquid. The superoxide could react with the labile proton on the imidazolium cation, as shown in Equation 3.1, and be removed from the solution.[16] This would explain the lack of the reverse peak and the large reduction wave for the forward peak.

Figure 3.3 and Figure 3.4 show a smaller current density than that of the voltammograms of the other ionic liquids. C_4MIM TFSI and C_4MIM PF_6 show current densities of approximately -0.01 mA cm^{-2} for the O_2 reduction current while C_2MIM

TFSI shows approximately -10 mA cm^{-2} for the O_2 reduction current and PYR_{14} TFSI in Chapter 2 showed approximately -20 mA cm^{-2} for the first O_2 reduction step. All of these ionic liquids were saturated by bubbling with O_2 *via* a needle for approximately 15 minutes. This difference in the current densities is because the greater viscosity of C_4MIM PF_6 decreases the diffusion coefficient of O_2. This means that O_2 diffuses towards the electrode at a slower rate and gives a smaller peak current.

The investigation into the reduction of O_2 in imidazolium ionic liquids indicates that the reduction of oxygen is not reversible. The lack of an oxidation wave on the reverse scan, the long onset of the reduction wave and the lack of stability plateau all indicate that the superoxide anion is unstable in the imidazolium ionic liquids. This lack of stability indicates that the imidazolium ionic liquids are unsuitable for use in a lithium-air battery. If the superoxide is unstable in a working lithium-air battery, O_2 would be permanently removed from the electrolyte instead of forming Li_2O_2, making it unable to be recharged and causing the formation of hydrogen peroxide, which would degrade the battery. Over repeated cycling, the ionic liquid would degrade, causing a loss of capacity of the battery and making it less efficient. Because of this, no further investigation into the use of imidazolium based ionic liquids for a Li-air battery was done.

3.4 Pyrrolidinium Based Ionic Liquids

3.4.1 Electrochemical Stability Limits

Several experiments were undertaken using the pyrrolidinium based ionic liquids shown in Table 3.1 and Table 3.2, varying the anion and keeping the cation constant. Cells were assembled as described previously in the glovebox and any dissolved O_2, N_2 or H_2O was removed. In the case of heart-shaped cells this was done by bubbling with argon. In the case of cross-shaped cells this was done by applying a vacuum. Cyclic voltammograms were undertaken to investigate the electrochemical stability windows of the RTILs. These stability windows are shown in Figure 3.5 and Figure 3.6.

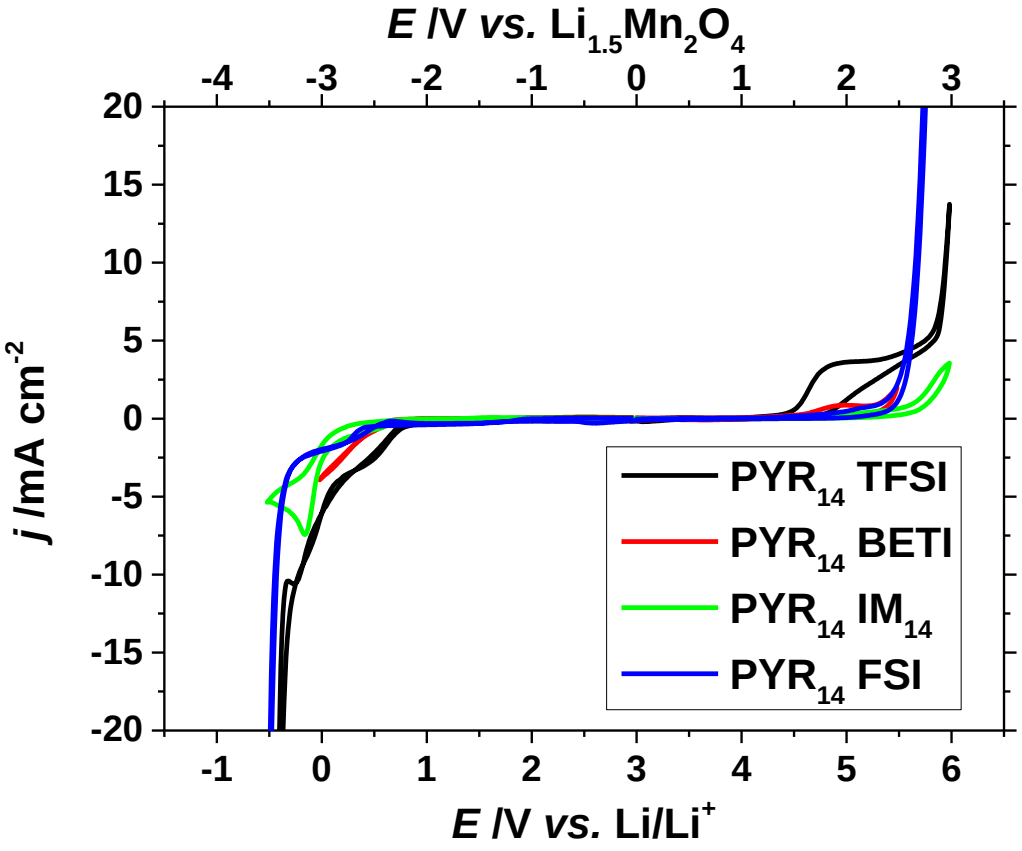

Figure 3.5: cyclic voltammograms showing the electrochemical stability windows of PYR_{14} based ionic liquids PYR_{14} TFSI (10 µm diameter Pt microelectrode, 50 mV s^{-1}), PYR_{14} BETI (25 µm diameter Pt microelectrode, 100 mV s^{-1}), PYR_{14} IM_{14} (10 µm diameter Pt microelectrode, 50 mV s^{-1}) and PYR_{14} FSI (10 µm diameter Pt microelectrode, 50 mV s^{-1}). These experiments were done at 25 °C using a cross-shaped cell with microdisc working electrodes and $Li_{1.5}Mn_2O_4$ counter-reference electrodes.

Figure 3.5 shows that all of the ionic liquids have large electrochemical stability windows of approximately 6 V. This figure also shows that all of the ionic liquids have similar cathodic electrochemical stability limits at approximately 0.5 V *vs.* Li/Li^+. The anodic stability limits vary depending upon the anion present in the ionic liquid. The smallest limits are the BETI and FSI anions at 5.5 V *vs.* Li/Li^+. The next limit is the TFSI anion at approximately 6 V *vs.* Li/Li^+, while the largest anodic stability limit is for the IM_{14} anion at more than 6 V *vs.* Li/Li^+. There are several small prepeaks for all of the ionic liquids at the cathodic stability limit, starting at about 0.75 V *vs.* Li/Li^+ for the PYR_{14} TFSI and starting a 0.5 V *vs.* Li/Li^+ for the rest of the ionic liquids. There is also a peak for the PYR_{14} TFSI anodic sweep at approximately 4.5 V *vs.* Li/Li^+. These peaks are probably due to the presence of H_2O, O_2 or other impurities present in the ionic liquid.

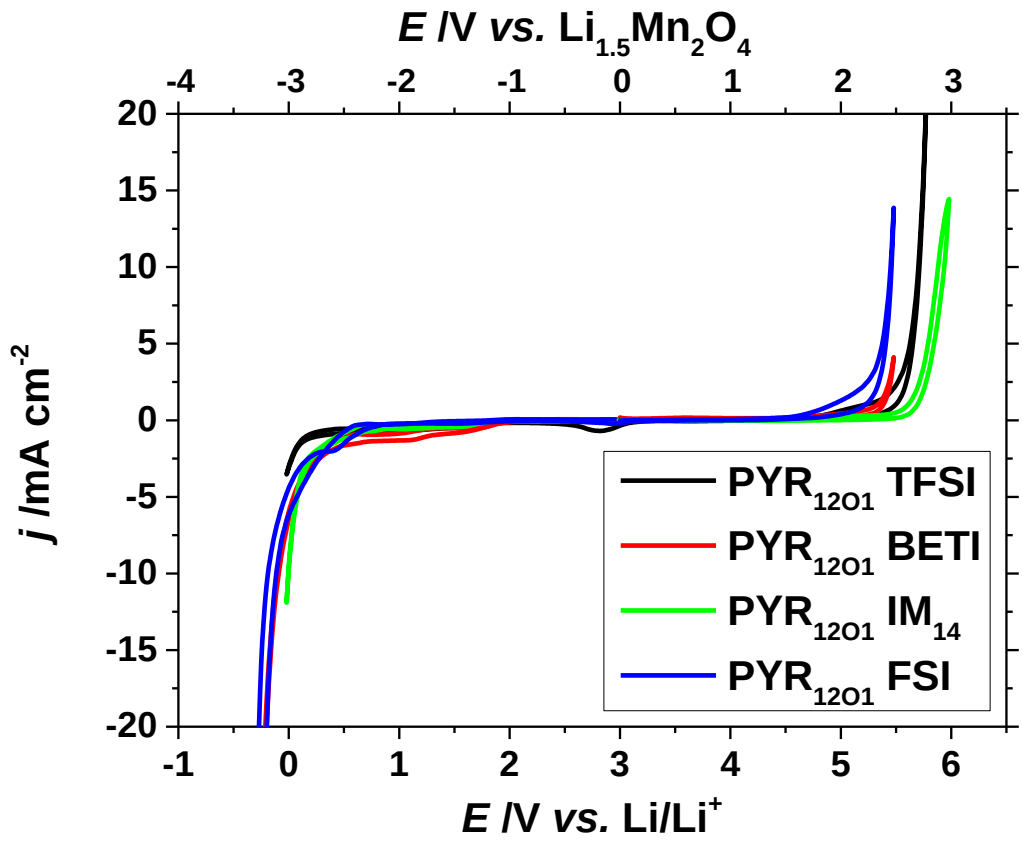

Figure 3.6: cyclic voltammograms showing the electrochemical stability windows of PYR_{12O1} ionic liquids. The cyclic voltammograms were done in cross-shaped cells using a 10 µm diameter Pt microdisc working electrode and a $Li_{1.5}Mn_2O_4$ counter-reference electrode at a scan rate of 50 mV s^{-1}.

Figure 3.6 shows that the PYR_{12O1} based RTILs have an electrochemical stability window of approximately 6 volts. All the ILs have a similar cathodic stability limit at approximately 0.25 V *vs.* Li/Li^+, due to the ionic liquids having the same cation. As with Figure 3.5 the anodic electrochemical stability limit varies slightly for each ionic liquid. The lowest anodic limit is the FSI anion at approximately 5.25 V *vs.* Li/Li^+. The next limit is for BETI at approximately 5.50 V *vs.* Li/Li^+. The next limit is for TFSI at 5.75 V *vs.* Li/Li^+ while the highest stability limit is for the IM_{14} ionic liquid at approximately 6 V *vs.* Li/Li^+. These stability limits follow the same trend as for the PYR_{14} ionic liquids, indicating that the stability limits of these anions are the same for both types of ionic liquid.

There are small peaks in the voltammograms of PYR_{12O1} TFSI and PYR_{12O1} BETI that are likely due to small amounts of oxygen or other impurities present in the RTILs.

3.4.2 Oxygen Reduction in PYR_{14} Based Ionic Liquids

After the electrochemical stability limits of the ionic liquids were determined, O_2 was passed into the ionic liquids, either by passing into the headspace of the cell and allowing it to diffuse into the ionic liquid, or by bubbling *via* a needle for approximately 30 minutes. Once the ionic liquids were fully saturated, cyclic voltammograms were undertaken at various scan rates to study the electrochemical reduction of O_2. The cyclic voltammograms are shown in Figure 3.7 to Figure 3.9. The cyclic voltammograms of PYR_{14} TFSI were shown previously in Chapter 2.

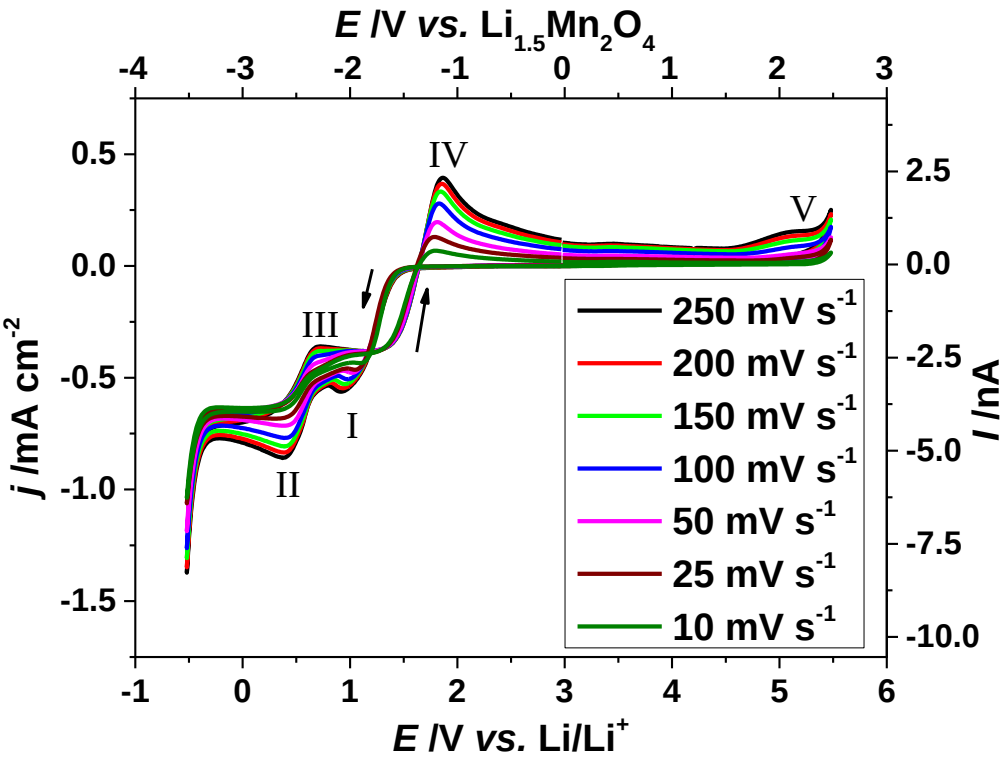

Figure 3.7: cyclic voltammograms showing the electrochemical reduction of oxygen in PYR_{14} BETI. This experiment used a cross-shaped cell with a 10 µm diameter Pt microdisc electrode and a $Li_{1.5}Mn_2O_4$ counter-reference electrode. The ionic liquid was oxygenated by passing O_2 into the cell cavity and allowing it to diffuse into the ionic liquid over approximately 18 hours.

Figure 3.7 shows the electrochemical reduction of oxygen in PYR_{14} BETI. These cyclic voltammograms show similar behaviour to the voltammograms of oxygenated PYR_{14} TFSI shown in Chapter 2.This shows that O_2 reduction occurs in two steps. The first O_2 reduction wave occurs at 1.25 V *vs.* Li/Li^+ (peak I) as a steady state wave voltammogram. The second reduction step occurs almost immediately at 0.75 V *vs.*

Li/Li^+ (peak II). The first reduction step corresponds to the one-electron reduction of O_2 to $O_2^{\bullet-}$, while the second reduction wave corresponds to the one-electron reduction of $O_2^{\bullet-}$ to O_2^{2-}. On the anodic reverse scan the first small oxidation peak occurs at 0.75 V *vs.* Li/Li^+ (peak III) corresponding to the oxidation of O_2^{2-} to $O_2^{\bullet-}$. A second larger oxidation peak occurs at 1.75 V *vs.* Li/Li^+ (peak IV). This peak corresponds to the one-electron oxidation of $O_2^{\bullet-}$ to O_2. There is also a small oxidation peak at 3.5 V *vs.* Li/Li^+ (peak V). This may correspond to the formation of platinum oxide on the electrode by taking it up to a high potential.

There is a crossing over of the forward and reverse scans occurring between 1.25 V and 1.75 V *vs.* Li/Li^+. This crossover is present on the voltammograms that used platinum working electrodes but is not present on the voltammograms done using gold working electrodes. This crossover may be due to the presence of water on the working electrode, indicating that there were impurities of water present in the ionic liquid. A similar crossover is also observed for oxygen reduction on platinum electrodes in aqueous solutions. Other than this crossover no discernible differences in the peak shape, position or current magnitude were observed between the reduction of O_2 on gold and platinum electrodes.

These cyclic voltammograms show similar behaviour to that of the reduction of O_2 in PYR_{14} TFSI, with two wave-shaped forward, cathodic reduction peaks and one large reverse, anodic oxidation peak. This indicates that the mechanism of O_2 reduction in PYR_{14} BETI is similar to that in PYR_{14} TFSI, with a one-electron reduction of O_2 to $O_2^{\bullet-}$ followed by the one-electron reduction of $O_2^{\bullet-}$ to O_2^{2-}.

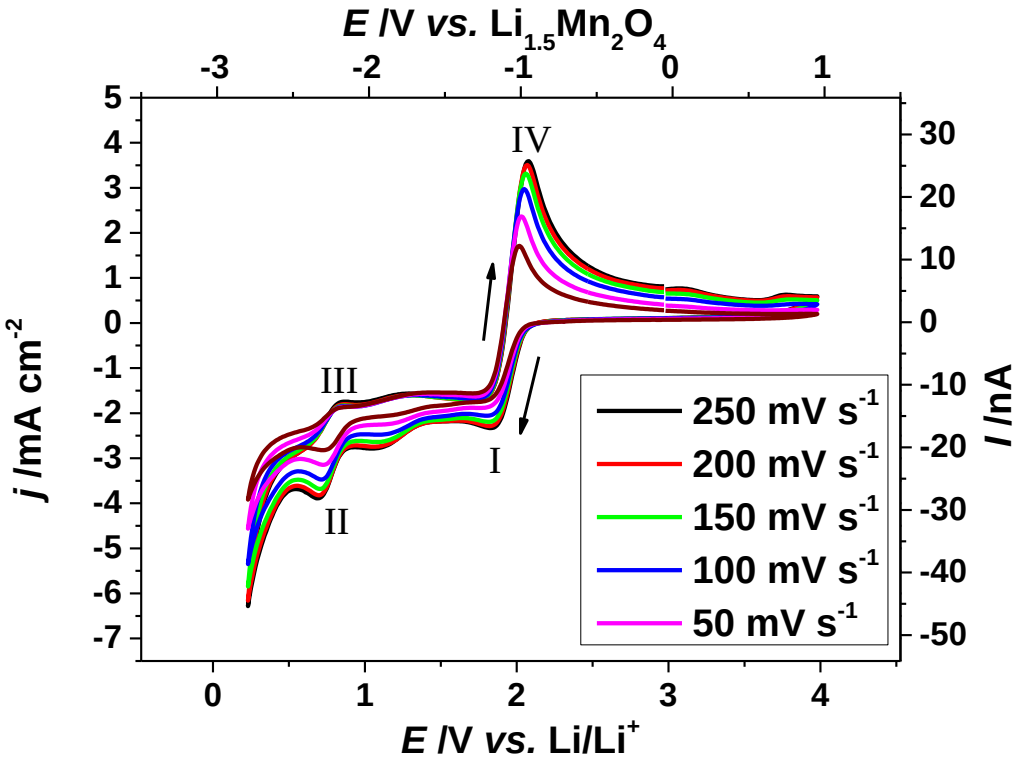

Figure 3.8: cyclic voltammograms showing the electrochemical reduction of oxygen in $PYR_{14}IM_{14}$. This experiment is done using a cross-shaped cell with a 25 µm diameter Au microdisc working electrode and a $Li_{1.5}Mn_2O_4$ counter-reference electrode. The ionic liquid was oxygenated *via* bubbling with a needle.

Figure 3.8 shows the electrochemical reduction of oxygen in $PYR_{14}IM_{14}$ ionic liquid at various scan rates. These voltammograms show that the reduction of oxygen occurs in two one-electron steps similar to that seen in the other PYR_{14} ionic liquids. Figure 3.8 shows that the first reduction for O_2 to $O_2^{\bullet-}$ occurs at approximately 2 V *vs.* Li/Li^+ (peak I). This is followed by a stable plateau between 1.75 V and 0.75 V *vs.* Li/Li^+ before the second reduction curve for $O_2^{\bullet-}$ to O_2^{2-} occurs at 0.75 V *vs.* Li/Li^+ (peak II). The final curve occurring at 0.5 V *vs.* Li/Li^+ is due to the decomposition of the ionic liquid. On the reverse, anodic scan, the O_2^{2-} oxidation peak occurs at 0.75 V *vs.* Li/Li^+ (peak III) while the $O_2^{\bullet-}$ oxidation peak occurs at 1.8 V *vs.* Li/Li^+ (peak IV). As with the other PYR_{14} ionic liquids, the oxidation of $O_2^{\bullet-}$ to O_2 gives a more peak shaped current, due to the smaller diffusion coefficient of $O_2^{\bullet-}$.

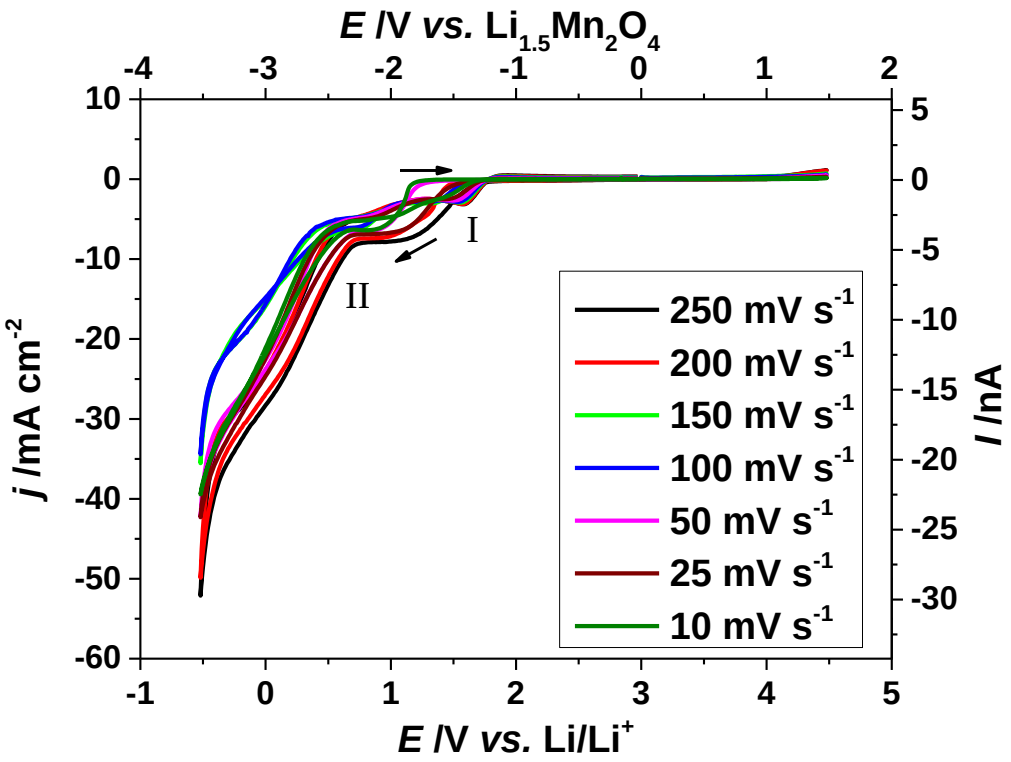

Figure 3.9: cyclic voltammograms showing the electrochemical reduction of oxygen in PYR_{14} FSI. This experiment was done using a cross-shaped cell with a 10 µm diameter Pt microdisc electrode and a $Li_{1.5}Mn_2O_4$ counter-reference electrode. The ionic liquid was oxygenated by passing O_2 into the headspace of the cell and allowing it to diffuse into the ionic liquid over approximately 18 hours.

Figure 3.9 shows the electrochemical reduction of oxygen in PYR_{14} FSI ionic liquid at various scan rates. These voltammograms show a marked difference from those of the other PYR_{14} ionic liquids. The initial O_2 reduction to $O_2^{\bullet-}$ occurs at 1.75 V *vs.* Li/Li^+ (peak I). This reduction wave curves down to a plateau before following down to a large reduction wave starting at 1.25 V *vs.* Li/Li^+ (peak II). This reduction wave may be due to the electrochemical reduction of $O_2^{\bullet-}$ to O_2^{2-} or may be caused by the reduction of the FSI anion. The reverse scan shows no peaks. This may be due to the superoxide or peroxide reacting with the FSI anion. This would remove the superoxide from the RTIL, therefore no superoxide oxidation peak would be seen. This indicates that the PYR_{14} FSI ionic liquid is unsuitable for use in a lithium-air battery due to it being unstable in the presence of superoxide.

3.4.3 Oxygen Reduction in PYR_{12O1} Based Ionic Liquids

Cyclic voltammetry was also done in the PYR_{12O1} equivalents of the PYR_{14} ionic liquids investigated above.

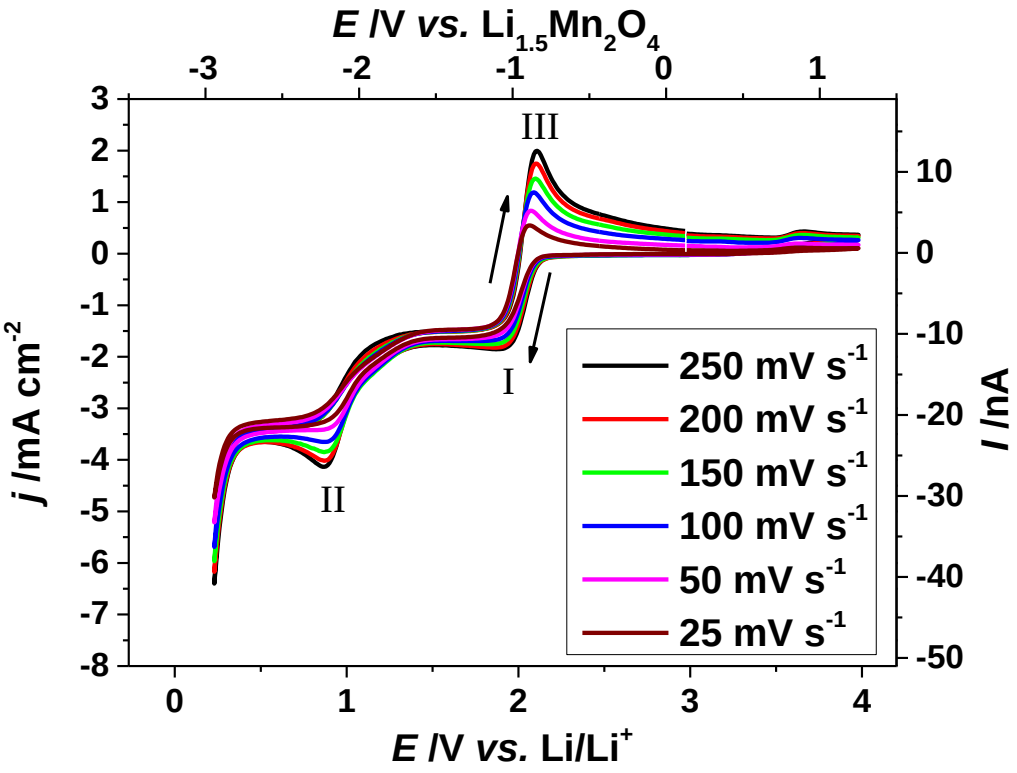

Figure 3.10: cyclic voltammograms showing the electrochemical reduction of oxygen in PYR_{12O1} TFSI. This experiment was done using a cross-shaped cell with a 25 µm diameter Au microdisc working electrode and a $Li_{1.5}Mn_2O_4$ counter-reference electrode. The ionic liquid was oxygenated by bubbling O_2 into the ionic liquid *via* a needle.

Figure 3.10 shows the electrochemical reduction of oxygen in PYR_{12O1} TFSI ionic liquid. These voltammograms show that O_2 reduction occurs in a similar fashion to that seen in most of the PYR_{14} based ionic liquids. On the forward cathodic scan, the first reduction wave from O_2 to $O_2^{\bullet-}$ occurs at 2.0 V *vs.* Li/Li^+ (peak I), followed by a small plateau from 2.0 V to 1.25 V *vs.* Li/Li^+. The second wave, corresponding to the reduction of $O_2^{\bullet-}$ to O_2^{2-} occurs at approximately 1.25 V *vs.* Li/Li^+ (peak II). There is a sharp increase in the current at 0.25 V *vs.* Li/Li^+ due to the breakdown of the RTIL. On the reverse cathodic scan, the only oxidation peak observed is at 2.25 V *vs.* Li/Li^+ (peak III). This peak is due to the oxidation of $O_2^{\bullet-}$ to O_2. As was previously observed with the

PYR_{14} ILs, the oxidation reaction gives a transient peak due to the smaller diffusion coefficient of superoxide.

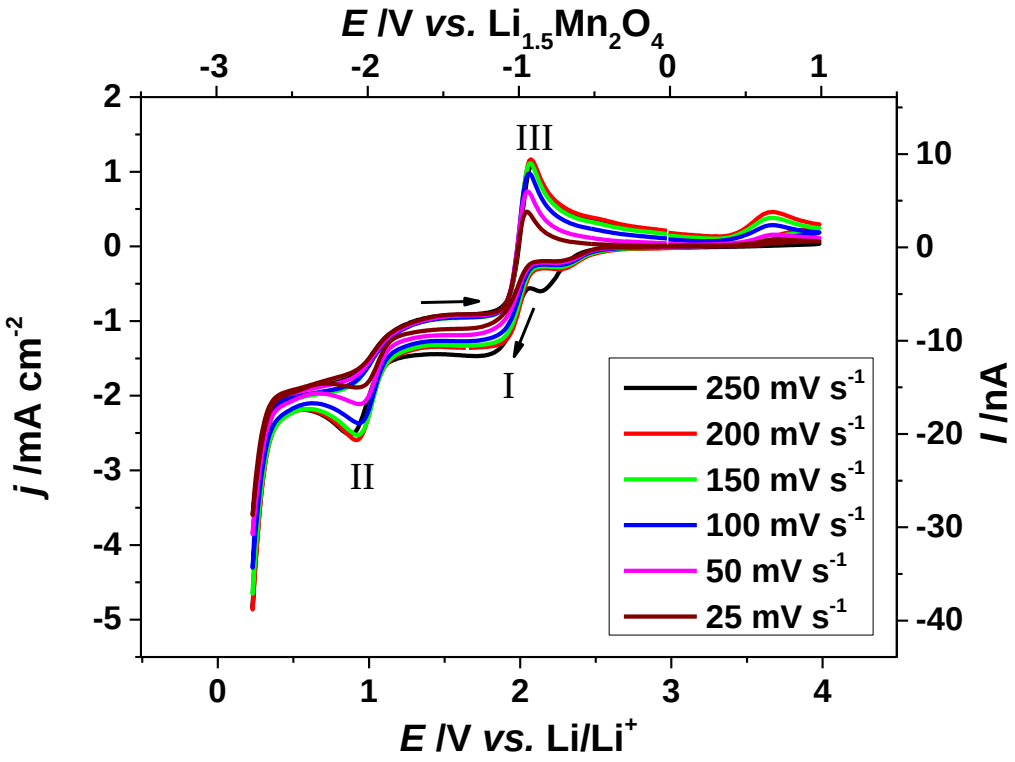

Figure 3.11: cyclic voltammograms showing the electrochemical reduction of oxygen in PYR_{12O1} BETI. This experiment was done using a cross-shaped cell with a 25 µm diameter Au microdisc working electrode and a $Li_{1.5}Mn_2O_4$ counter-reference electrode. The ionic liquid was oxygenated by bubbling O_2 into the ionic liquid *via* a needle.

Figure 3.11 shows the electrochemical reduction of oxygen in pure PYR_{12O1} BETI. This figure also shows that the reduction of O_2 to $O_2^{\bullet-}$ occurs at 2.0 V *vs.* Li/Li^+ (peak I), followed by a plateau until 1.0 V *vs.* Li/Li^+ when the second reduction wave from $O_2^{\bullet-}$ to O_2^{2-} occurs (peak II). On the cathodic reverse scan the only visible oxidation wave occurs at 2.0 V *vs.* Li/Li^+ (peak III) corresponding to the oxidation of $O_2^{\bullet-}$ to O_2. As with the other ionic liquids this oxidation wave is peak shaped due to the much smaller diffusion coefficient of superoxide.

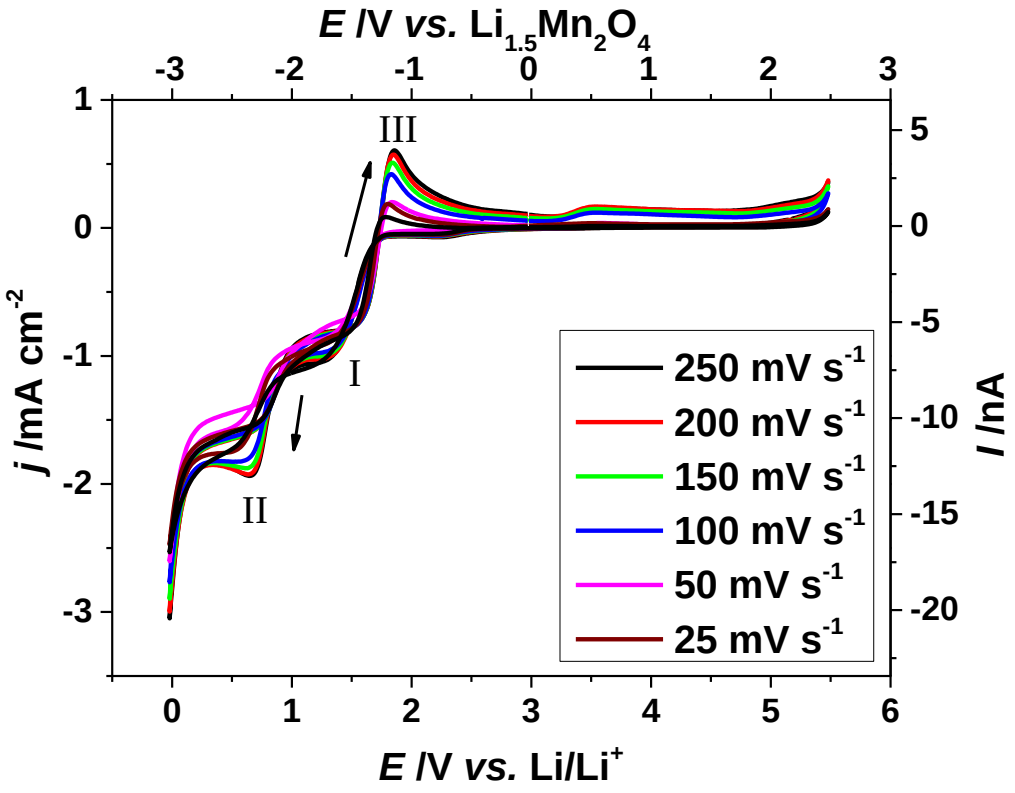

Figure 3.12: cyclic voltammograms showing the electrochemical reduction of oxygen in PYR_{12O1} IM_{14}. This experiment was done using a cross-shaped cell using a 25 µm diameter Pt microdisc working electrode and a $Li_{1.5}Mn_2O_4$ counter-reference electrode. The ionic liquid was oxygenated by passing O_2 into the cell cavity and allowing it to diffuse into the ionic liquid over 18 hours.

Figure 3.12 shows the electrochemical reduction of oxygen in PYR_{12O1} IM_{14}. This figure shows that the reduction of oxygen also occurs in two one-electron oxygen reductions. The first reduction occurs at 1.75 V *vs.* Li/Li^+ (peak I) due to the reduction of O_2 to $O_2^{\bullet-}$ with the second reduction from $O_2^{\bullet-}$ to O_2^{2-} occurring at 0.75 V *vs.* Li/Li^+ (peak II). On the anodic reverse scan the only oxidation peak occurs at 1.5 V *vs.* Li/Li^+ (peak III) corresponding with oxidation of $O_2^{\bullet-}$ to O_2. This peak is also transient in behaviour indicating a smaller diffusion coefficient for superoxide than oxygen in PYR_{12O1} IM_{14} ionic liquid.

A large amount of crossing over of the forward and reverse scans is observed. As this is a Pt microelectrode, this indicates the presence of trace amount of water in the ionic liquid, again showing that the ionic liquids contained trace amount of impurities.

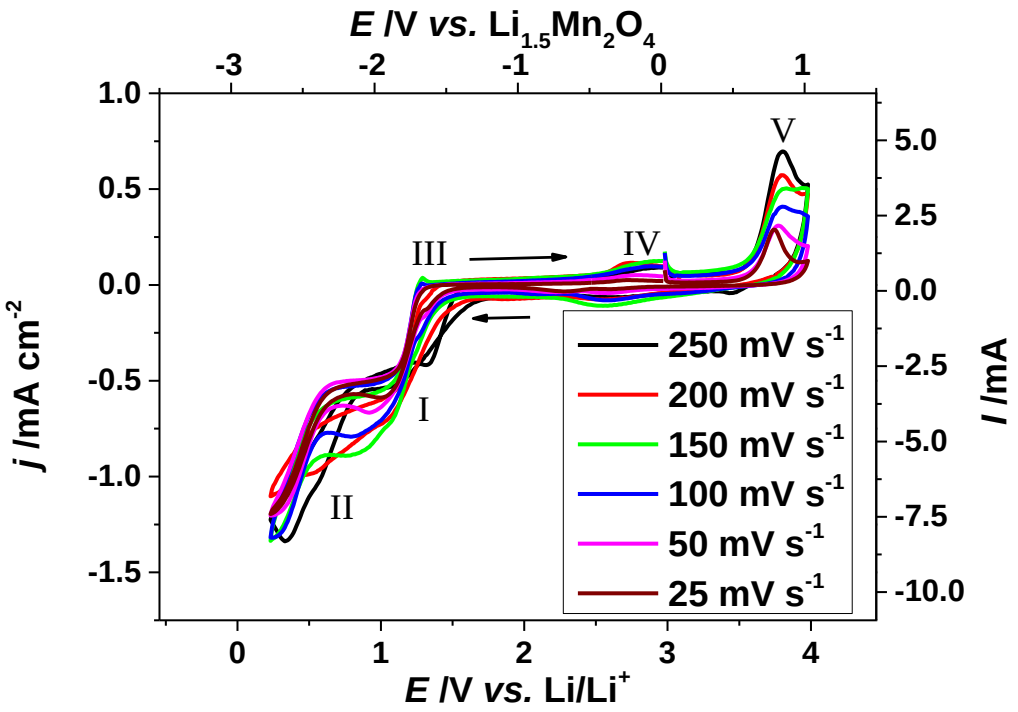

Figure 3.13: cyclic voltammograms showing the electrochemical reduction of oxygen in PYR_{12O1} FSI. This experiment was done using a cross-shaped cell with a 25 µm diameter Au microdisc working electrode and a $Li_{1.5}Mn_2O_4$ counter-reference electrode. The ionic liquid was oxygenated by passing O_2 into the cell headspace and allowing it to diffuse into the ionic liquid over 18 hours.

Figure 3.13 shows the electrochemical reduction of O_2 in PYR_{12O1} FSI at various scan rates. These scans show several similarities with those presents in the PYR_{14} FSI voltammograms (Figure 3.9). Both voltammograms show that the first reduction (peak I) occurs at 1.25 V *vs.* Li/Li^+ due to the one-electron reduction of O_2 to $O_2^{\bullet-}$. The second reduction occurs at 0.5 V *vs.* Li/Li^+ (peak II). This is due to the one-electron reduction of $O_2^{\bullet-}$ to O_2^{2-}. On the reverse scan there is a small reverse peak (peak III) at 1.25 V *vs.* Li/Li^+ which occurs at 150 and 100 mV s^{-1}. This very small peak is due to the oxidation of $O_2^{\bullet-}$ to O_2 and is only present at certain scan rates. This indicates that $O_2^{\bullet-}$ is not stable in the PYR_{12O1} FSI. These voltammograms also seem to be overlapping, with little reproducibility between the scan rates. This indicates that the $O_2^{\bullet-}$ may be reacting with the FSI anion, removing the FSI from the solution. Alternatively this could indicate the presence of impurities such as water in the ionic liquids. There is a small peak at 2.5 to 3 V *vs.* Li/Li^+ (peak IV) on both the forward and the reverse scans of the voltammograms. This may be caused by the decomposition products of the reaction

between peroxide and the FSI anion. The peak at 3.75 V *vs*. Li/Li^+ (peak V) is caused by the formation of gold oxide on the working electrode due to the potential being swept to very positive potentials. This gold oxide could also be the reason for peak IV.

3.5 Conclusions

These experiments show that the electrochemical reduction of O_2 occurs differently in imidazolium based ionic liquids compared to pyrrolidinium based ionic liquids. In imidazolium based ionic liquids, the oxygen is reduced to superoxide in a one-electron reduction reaction. It is likely that the superoxide is reacting with the labile proton on the imidazolium cation as shown in Equation 3.1.[16]

The cyclic voltammograms of oxygen reduction in pyrrolidinium ionic liquids show considerable differences to those of the reduction of oxygen in imidazolium based ionic liquids. In pyrrolidinium ionic liquids, the reduction of O_2 occurs in two stages. First, a one-electron reduction of O_2 to $O_2^{\bullet-}$ occurs causing the formation of stable $O_2^{\bullet-}$. This reduction occurs at a value between 1.5 – 2.0 V *vs.* Li/Li^+.

After the first reduction peak there is a small plateau for approximately 0.5 V where the $O_2^{\bullet-}$ is stable. This may be due to the $O_2^{\bullet-}$ being stabilised through some intermolecular reaction between the superoxide and the pyrrolidinium of the ionic liquid.

After the plateau, there is evidence of a second, one-electron reduction at between 1.25 V and 0.5 V *vs.* Li/Li^+ due to the reduction of superoxide to peroxide.

The reverse scan shows that there is no peak for the peroxide oxidation. This indicates that the peroxide may not be stable in pyrrolidinium ionic liquids as it may be reacting with the ionic liquid, being consumed and removed from the ionic liquid. This may also indicate that the diffusion coefficient of peroxide is similar to the diffusion coefficient of oxygen, however it is generally accepted that the diffusion coefficient of superoxide is a factor of ten smaller than that of oxygen [10–12], while the simulated values of the diffusion coefficient of peroxide used in Figure 2.5 and Figure 2.7 was 1×10^{-6} cm^2 s^{-1}.

The reverse scan shows a peak due to superoxide oxidation to oxygen. This indicates that the superoxide is stable in the presence of pyrrolidinium ionic liquids, allowing the reduction of oxygen to be fully reversible in pyrrolidinium based ionic liquids. This was previously observed in PYR_{14} TFSI in Chapter 2.

The cyclic voltammograms show no discernible differences between oxygen reduction in PYR_{14} ionic liquids and PYR_{12O1} ionic liquids.

The FSI ionic liquids show several differences compared to the other pyrrolidinium based ionic liquids. These ionic liquids show no $O_2^{\bullet-}$ oxidation peak, indicating that the superoxide may react with the FSI anion. This indicates that the $O_2^{\bullet-}$ anion is unstable and should not be used in a Li-air battery.

The voltammograms show that there is little difference in the reduction of O_2 at a platinum or a gold microelectrode in either current shape, potential or current magnitude. The only major difference is a crossing-over of the forward and reverse scans that occurs only on platinum electrode. This is caused by the presence of water impurities in the ionic liquid, indicating that the ionic liquids are not fully dried. The water adsorbs to the Pt electrode, causing a crossing over on the forward and reverse scans.

The aims of the experiments in this chapter were to determine the mechanism of O_2 reduction in various imidazolium and pyrrolidinium based ionic liquids. It has been determined that imidazolium based ionic liquids are unsuitable for use in the LABOHR battery due to the instability of the superoxide ion. It has also been determined that pyrrolidinium based ionic liquids are suitable candidates for use as electrolytes and oxygen transport media in the LABOHR battery.

Further experiments could be undertaken with regards to the electrochemical reduction of O_2. Experiments could be undertaken using different electrode materials to further investigate the adsorption of O_2 onto the microelectrode surface. If possible, investigation could be done into generation of $O_2^{\bullet-}$ in the bulk ionic liquid, allowing further investigation of the $O_2^{\bullet-}$ oxidation and O_2^{2-} formation.

One further technique that could be applied to determine more information about the oxygen reduction reaction is electrochemical impedance spectroscopy. This will be shown in Chapter 4.

3.6 References

[1] G. B. Appetecchi, M. Montanino, D. Zane, M. Carewska, F. Alessandrini, S. Passerini, *Electrochim. Acta* **2009**, *54*, 1325–1332.

[2] S. Zhang, N. Sun, X. He, X. Lu, X. Zhang, *J. Phys. Chem. Ref. Data* **2006**, *35*, 1475–1517.

[3] S. Monaco, A. M. Arangio, F. Soavi, M. Mastragostino, E. Paillard, S. Passerini, *Electrochim. Acta* **2012**, *83*, 94–104.

[4] G. B. Appetecchi, M. Montanino, M. Carewska, M. Moreno, F. Alessandrini, S. Passerini, *Electrochim. Acta* **2011**, *56*, 1300–1307.

[5] J. Reiter, E. Paillard, L. Grande, M. Winter, S. Passerini, *Electrochim. Acta* **2013**, *91*, 101–107.

[6] C. Wessells, R. Ruffo, R. A. Huggins, Y. Cui, *Electrochem. Solid-State Lett.* **2010**, *13*, A59–A61.

[7] S. Randström, M. Montanino, G. B. Appetecchi, C. Lagergren, A. Moreno, S. Passerini, *Electrochim. Acta* **2008**, *53*, 6397–6401.

[8] L. E. Barrosse-Antle, C. Hardacre, R. G. Compton, *J. Phys. Chem. B* **2009**, *113*, 2805–2809.

[9] S. Randström, G. B. Appetecchi, C. Lagergren, A. Moreno, S. Passerini, *Electrochim. Acta* **2007**, *53*, 1837–1842.

[10] M. C. Buzzeo, O. V. Klymenko, J. D. Wadhawan, C. Hardacre, K. R. Seddon, R. G. Compton, *J. Phys. Chem. B* **2004**, *108*, 3947–3954.

[11] M. C. Buzzeo, O. V. Klymenko, J. D. Wadhawan, C. Hardacre, K. R. Seddon, R. G. Compton, *J. Phys. Chem. A* **2003**, *107*, 8872–8878.

[12] Y. Katayama, K. Sekiguchi, M. Yamagata, T. Miura, *J. Electrochem. Soc.* **2005**, *152*, E247–E250.

[13] M. M. Islam, T. Imase, T. Okajima, M. Takahashi, Y. Niikura, N. Kawashima, Y. Nakamura, T. Ohsaka, *J. Phys. Chem. A* **2009**, *113*, 912–916.

[14] Y. Katayama, H. Onodera, M. Yamagata, T. Miura, *J. Electrochem. Soc.* **2004**, *151*, A59–A63.

[15] E. I. Rogers, X. Huang, E. J. F. Dickinson, C. Hardacre, R. G. Compton, *J. Phys. Chem. C* **2009**, *113*, 17811–17823.

[16] I. M. Alnashef, M. A. Hashim, F. S. Mjalli, M. Q. A. Ali, M. Hayyan, *Tetrahedron Lett.* **2010**, *51*, 1976–1978.

4. Electrochemical Impedance Spectroscopy

The experiments undertaken in this chapter will study the use of electrochemical impedance spectroscopy at various potentials to investigate the oxygen reduction reaction in oxygenated PYR_{14} TFSI and C_2MIM TFSI.

4.1 Introduction

Electrochemical impedance spectroscopy is a versatile technique which can be used to determine properties such as the resistance, capacitance and the diffusion ongoing in a system. Oxygenated solutions of PYR_{14} TFSI and C_2MIM TFSI were studied using electrochemical impedance spectroscopy applied at various potentials to study the onset of the oxygen reduction reaction. The impedance data was plotted in Nyquist and Bode plots as previously described in Chapter 1.

The conductivity of a solution can be found from the resistance of the electrolyte using Newmans formula.[1]

$$R = \frac{1}{4\kappa r} \tag{4.1}$$

Where R is the resistance of the electrolyte in Ω, κ is the conductivity of the cell in S cm^{-1} and r is the radius of the microdisc electrode. By rearranging this formula we can obtain the conductivity of the solution. This is shown in Equation 4.2.

$$\kappa = \frac{1}{4Rr} \tag{4.2}$$

Warburg diffusion impedance (Z_W) can be used to determine the diffusion coefficient of a species in the solution. This technique uses the slope of the Warburg element on the Nyquist plot (σ) and Equation 4.3[2,3] to determine the diffusion coefficient of the reduced or oxidised species as long as the values of the concentrations of both species and the diffusion coefficient of the other species are known.

$$Z_W = \sigma 2\pi f^{-1/2} - i\sigma 2\pi f^{-1/2}$$

Where:

$$\sigma = \frac{RT}{2^{1/2} n^2 F^2 A}\left[\frac{1}{c_{\mathrm{Ox}} D_{\mathrm{Ox}}^{1/2}} + \frac{1}{c_{\mathrm{Red}} D_{\mathrm{Red}}^{1/2}}\right] \tag{4.3}$$

If the Warburg element does not easily show a straight line on a Nyquist plot the value of σ can also be calculated from the impedance when the phase angle is 1 rad s^{-1} using Equation 4.4.

$$\sigma = \frac{Z}{\sqrt{2}} \quad \textbf{(4.4)}$$

The size of the diffusion field (L) towards the working electrode can also be determined from the W_T function as is shown in Equation 4.5.

$$W_T = \frac{L^2}{D} \quad \textbf{(4.5)}$$

A large amount of information can be determined using electrochemical impedance spectroscopy. A full analysis and fitting of all the information obtained *via* SPEIS is beyond the scope of this thesis.

That aims of the experiments in this chapter are to further investigate the electrochemical reduction of oxygen in PYR_{14} TFSI and C_2MIM TFSI ionic liquids, as well as to investigate the application of electrochemical impedance spectroscopy at microelectrodes to ionic liquids.

4.2 Experimental

Staircase potentio-electrochemical impedance spectroscopy (SPEIS) was undertaken in oxygenated PYR_{14} TFSI and oxygenated C_2MIM TFSI. These experiments were done using a 10 µm diameter platinum microdisc working electrode and a $Li_{1.5}Mn_2O_4$ counter-reference electrode in the cross-shaped cell shown in previous chapters. The ionic liquids were oxygenated by passing O_2 into the cell cavity and allowing it to diffuse into the ionic liquid overnight. The experiments were done using a Bio-logic VMP2 potentiostat using EC-Lab software. All experiments were done in an earthed Faraday cage to protect against external electrical interference.

Earlier experiments were attempted using a 3 mm diameter GC working electrode. However over the timescale of the experiment all of the oxygen dissolved in the ionic liquid was reduced to superoxide, making the experiment unable to be completed. Because of this these experiments were done using a microelectrode to prevent bulk electrolysis of the O_2 in the ionic liquids.

A bias potential was applied to the cell and an AC amplitude of 25 mV was applied at frequencies from 200 kHz to 2 mHz, using 6 frequencies per decade. The bias potential was changed from 2.9 V *vs.* Li/Li^+ to 0.5 V *vs.* Li/Li^+ using 0.1 V potential steps. This enabled the study of the impedance at different reaction potentials in the same experiment. Each potential took approximately 35 minutes to be analysed at all frequencies.

The data received from the SPEIS experiments were fitted to equivalent circuits using Scribner Associates inc. ZView 2 (Version 2.8) fitting software. The data were fitted to equivalent circuits and the values of the charge transfer resistance, double layer capacitance and Warburg diffusion parameters were able to be estimated using these fittings.

4.3 Results and Discussion

4.3.1 Impedance of Oxygenated PYR_{14} TFSI

The impedances taken at each potential in oxygenated PYR_{14} TFSI were plotted as a Nyquist plot showing the real impedance (*Z'*) and the imaginary impedance (*Z''*). These impedances are shown in Figure 4.1. The information displayed in the Nyquist plot can also be displayed as a Bode plot showing the impedance (*Z*) as a function of the frequency (*f*). This is shown in Figure 4.2.

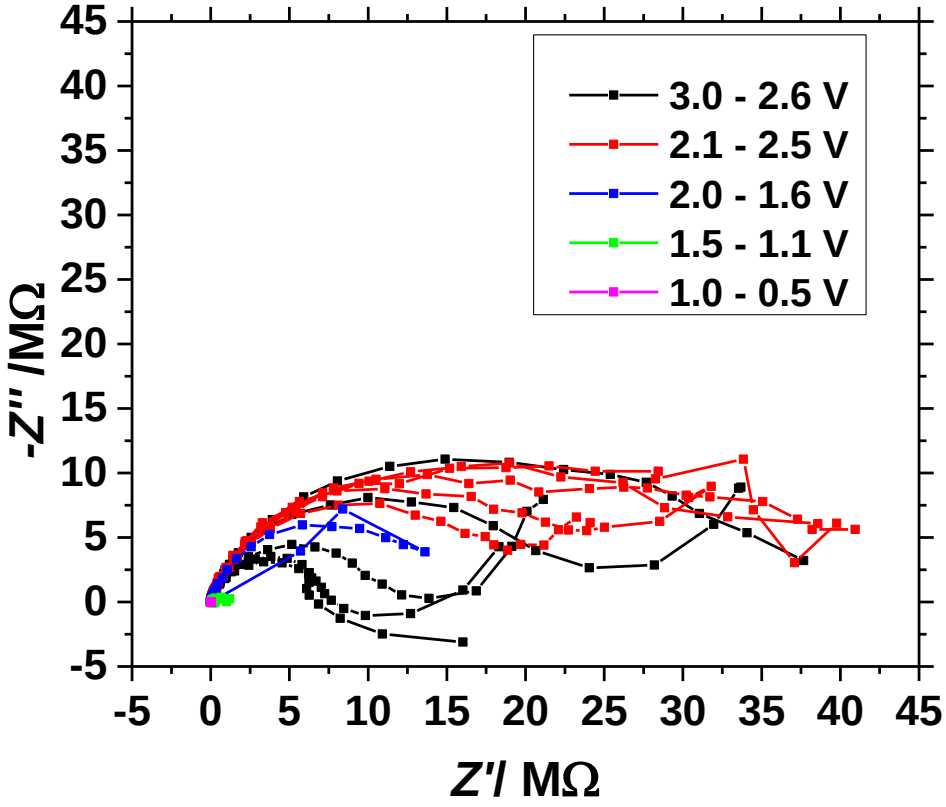

Figure 4.1: Nyquist plot showing the imaginary impedance *vs*. real imaginary impedance for each potential *vs*. Li/Li^+ during the SPEIS measurement of oxygenated PYR_{14} TFSI. The frequency range used was 200 kHz to 2 mHz, using 6 frequencies per decade with an amplitude of 25 mV. The experiment was done using a 10 µm diameter Pt microelectrode working electrode and a $Li_{1.5}Mn_2O_4$ counter-reference electrode in a cross-shaped cell. The ionic liquid was oxygenated by allowing oxygen to diffuse into the ionic liquid over a period of approximately 18 hours.

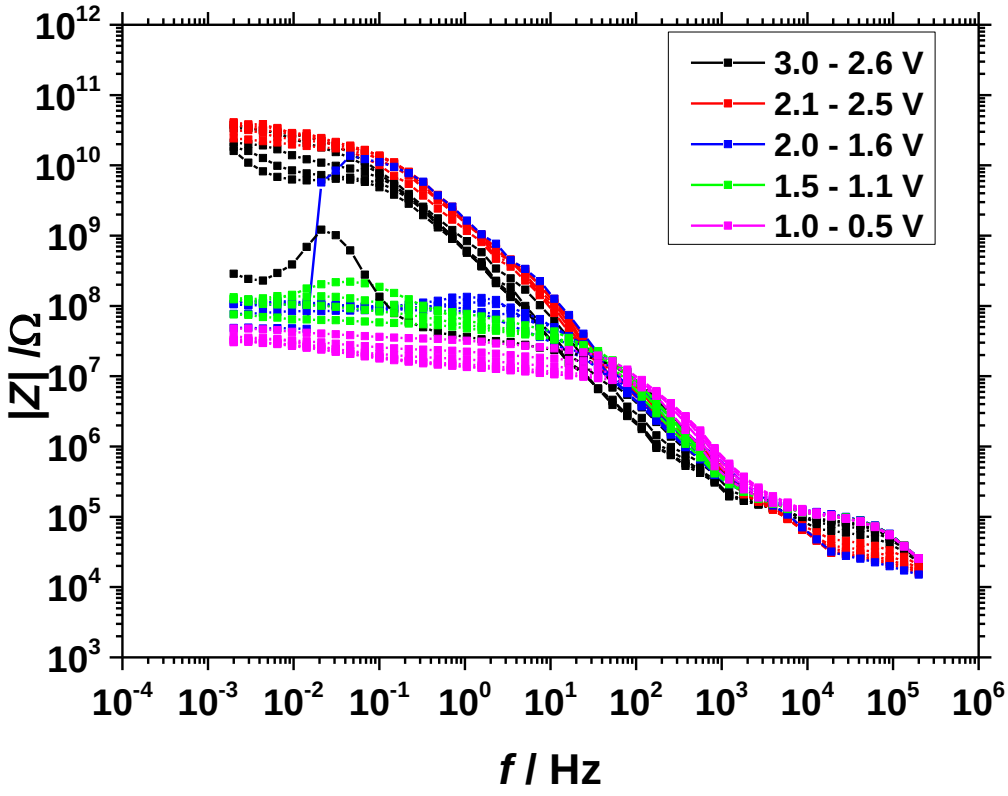

Figure 4.2: Bode plot showing the frequency *vs*. the modulus of the impedance for each potential *vs*. Li/Li^+ during the SPEIS measurement of oxygenated PYR_{14} TFSI. The frequency range used was 200 kHz to 2 mHz, using 6 frequencies per decade with an amplitude of 25 mV. The experiment was done using a 10 µm diameter Pt microelectrode working electrode and a $Li_{1.5}Mn_2O_4$ counter-reference electrode in a cross-shaped cell. The ionic liquid was oxygenated by allowing oxygen to diffuse into the ionic liquid over a period of approximately 18 hours.

Figure 4.1 shows the impedance measured at each potential between 3.0 V and 0.5 V *vs*. Li/Li^+ during the SPEIS measurement in oxygenated PYR_{14} TFSI. Figure 4.1 and Figure 4.2 indicate that the behaviour of the cell changes depending upon the potential the impedance was undertaken. At potentials above 2.0 V *vs*. Li/Li^+ the impedance at the low frequencies, below 10^{-1} Hz, is of the order of 10^{10} Ω. However at 2.0 V *vs*. Li/Li^+ the impedance at low frequencies decreases greatly to approximately 10^8 Hz. This decrease may be due to the onset of the O_2 reduction reaction. This suggests that it is possible to determine the onset potential of the O_2 reduction reaction using electrochemical impedance spectroscopy.

An alternative way of displaying the impedance is as a function of the potential. This is shown in Figure 4.3.

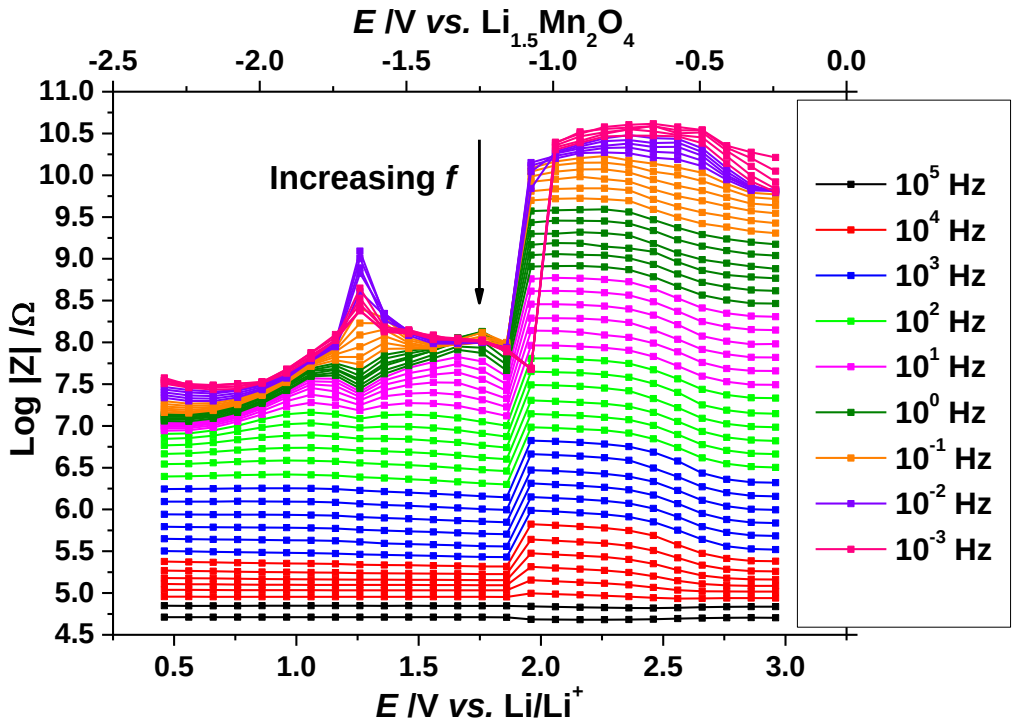

Figure 4.3: log of the modulus of the impedance of oxygenated PYR_{14} TFSI at different potentials. Each line represents a different frequency. The frequency range used was 200 kHz to 2 mHz, using 6 frequencies per decade with an amplitude of 25 mV. The experiment was done using a 10 µm diameter Pt microelectrode working electrode and a $Li_{1.5}Mn_2O_4$ counter-reference electrode in a cross-shaped cell. The ionic liquid was oxygenated by allowing oxygen to diffuse into the ionic liquid over a period of approximately 18 hours.

Figure 4.3 shows the onset potential of the oxygen reduction reaction much more visibly than the previous figures. This shows a sharp drop in the impedance at the low frequencies at 2.0 V *vs*. Li/Li^+ corresponding to the onset of the oxygen reduction reaction from O_2 to $O_2^{\bullet-}$. This figure also shows a small increase in the low frequency impedance at 1.3 V *vs*. Li/Li^+ which may correspond to the onset of the second electrochemical reduction reaction of $O_2^{\bullet-}$ to O_2^{2-}.

The impedances measured were fitted to different equivalent circuits depending upon the bias potential of the impedance. Potentials above 2.0 V *vs*. Li/Li^+ were attempted to be fitted to a resistor, followed by a resistor and a capacitor in parallel. This circuit (Circuit 1)[3] is shown in Figure 4.4.

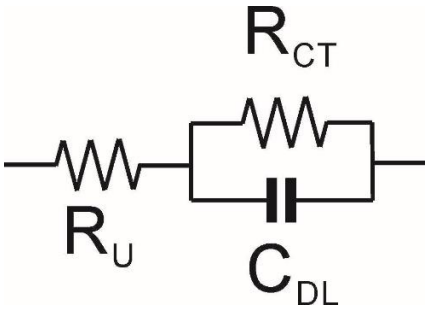

Figure 4.4: the equivalent circuit (Circuit 1) that should theoretically fit potentials between 3.0 V and 2.0 V *vs*. Li/Li$^+$. R_U = Uncompensated resistance, R_{CT} = Charge transfer resistance, C_{DL} = Double layer capacitance.

This circuit would account for the uncompensated solution resistance, charge transfer resistance and double layer capacitance that occurs when a potential is applied. As the potential is above 2.0 V *vs*. Li/Li$^+$, the oxygen reduction onset potential, the diffusion of oxygen does not need to be accounted for. Although this circuit does explain the features seen in impedance measurements above 2.0 V *vs*. Li/Li$^+$, the fitting program was unable to fit the data exactly to this equivalent circuit. The fitting would only occur if the R_U element was removed. The value of R_U was determined from the high frequency end of the semicircle in the Nyquist plot. The examples of the fitting are shown in Figure 4.5 and Figure 4.6.

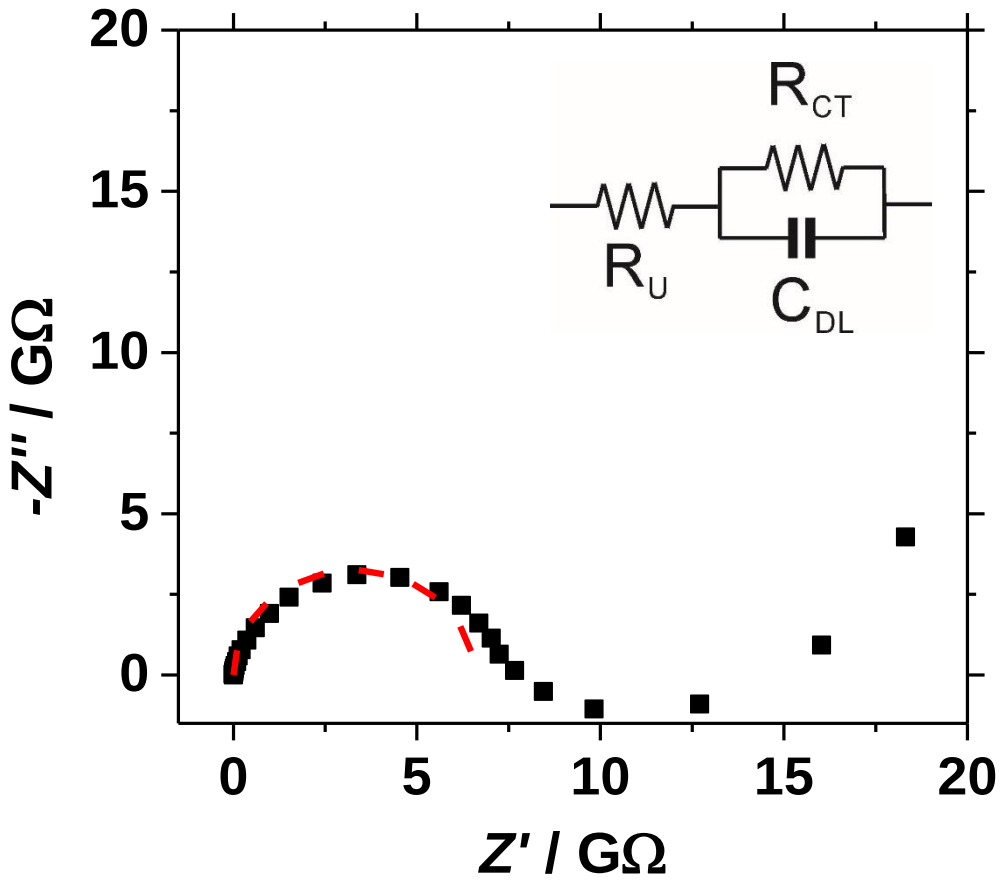

Figure 4.5: Nyquist plot for impedance at oxygenated PYR_{14} TFSI at 2.8 V *vs.* Li/Li^+. The frequency range used was 200 kHz to 2 mHz, using 6 frequencies per decade with an amplitude of 25 mV. The experiment was done using a 10 µm diameter Pt microelectrode working electrode and a $Li_{1.5}Mn_2O_4$ counter-reference electrode in a cross-shaped cell. The ionic liquid was oxygenated by allowing oxygen to diffuse into the ionic liquid over a period of approximately 18 hours. The red dashed line shows a best fit to a resistor and capacitor in parallel. The parameters used for fittings are $R_{CT} = 6.64 \times 10^9$ Ω, $C_{DL} = 6.66 \times 10^{-11}$ F. $R_U = 1 \times 10^5$ Ω but was not calculated by fitting. This data is taken from Figure 4.1.

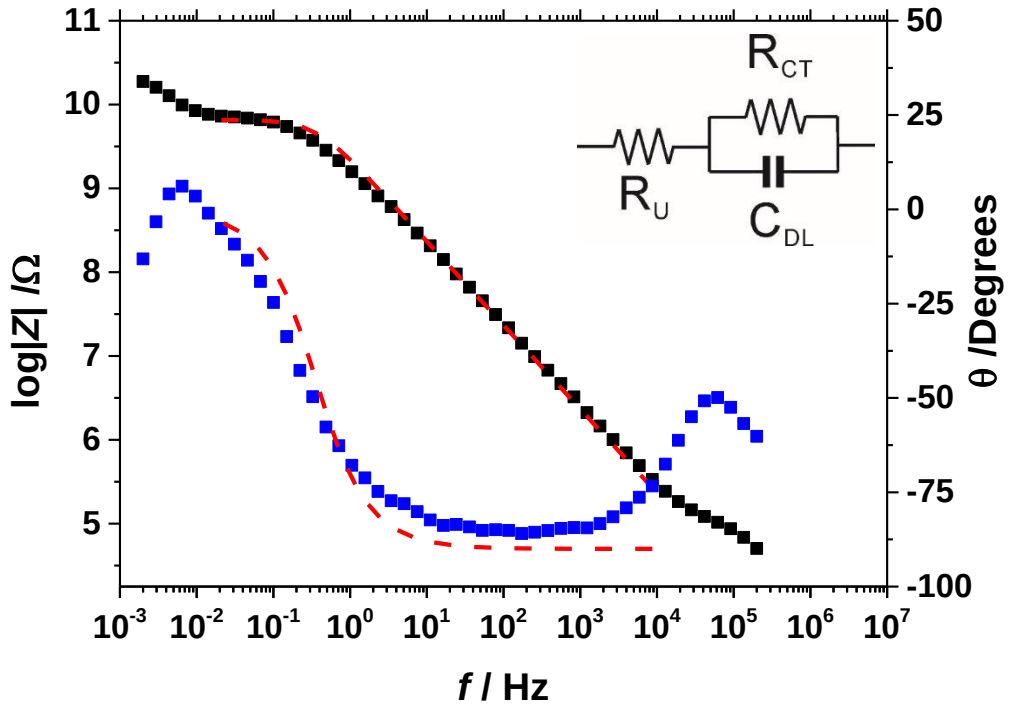

Figure 4.6: Bode plot for impedance at oxygenated PYR_{14} TFSI at 2.8 V *vs.* Li/Li^+. The frequency range used was 200 kHz to 2 mHz, using 6 frequencies per decade with an amplitude of 25 mV. The experiment was done using a 10 µm diameter Pt microelectrode working electrode and a $Li_{1.5}Mn_2O_4$ counter-reference electrode in a cross-shaped cell. The ionic liquid was oxygenated by allowing oxygen to diffuse into the ionic liquid over a period of approximately 18 hours. The black line is the log |Z|. The blue line is the phase value. The red dashed line shows a best fit to a resistor and capacitor in parallel. The parameters used for fittings are $R_{CT} = 6.64 \times 10^9$ Ω, $C_{DL} = 6.66 \times 10^{-11}$ F. $R_U = 1 \times 10^5$ Ω but was not calculated by fitting. This data is taken from Figure 4.2.

From 3.0 V to 2.0 V *vs.* Li/Li^+ the Nyquist plots show large semicircle, indicative of a charge transfer resistance (R_{CT}) in parallel with the double layer capacitance (C_{DL}) of the microdisc electrode. At the higher frequencies, the capacitance is out of phase with the period of the AC sine wave and so becomes blocking. This causes the impedance to move up the imaginary axis of the Nyquist plot. As the frequency decreases, it moves in phase with the time constant of the capacitor and the Nyquist plot curves to become a semicircle. As the frequency decreases further the period of the sine wave moves out of phase with the capacitor, and the double layer capacitance once again becomes blocking, this causes the charge transfer resistance to dominate, causing the Nyquist plot to curve down to the *Z'* axis and complete the semicircle.

When the capacitor in the equivalent circuit is replaced with a constant phase element for fitting, the phase of the constant phase element is approximately 0.95. This is non-ideal, indicating that the surface of the working electrode may be slightly roughened and imperfect. This would give a charge transfer resistance that varies at different points on the surface of the working electrode.

The values of the capacitance obtained in the fitting can be used to determine the double layer capacitance occurring at the working electrode. This is calculated to be 85 μF cm^{-2}. This is similar in value to other values of the double layer capacitance previously measured in other ionic liquids using different electrodes.[4]

At very low frequencies, e.g. below 10^{-1} Hz, the Nyquist plots start to show anomalous behaviour such as inductances and negative resistances. This could be caused by the presence of a trace impurity, such as lithium, being present in the solution. This could also be caused by the convection of the ionic liquid at very long timescales. Another plausible explanation is that the anomalous behaviour is caused by instrumental artefacts occurring in the potentiostat.

The charge transfer resistance calculated for each potential is shown in Figure 4.7.

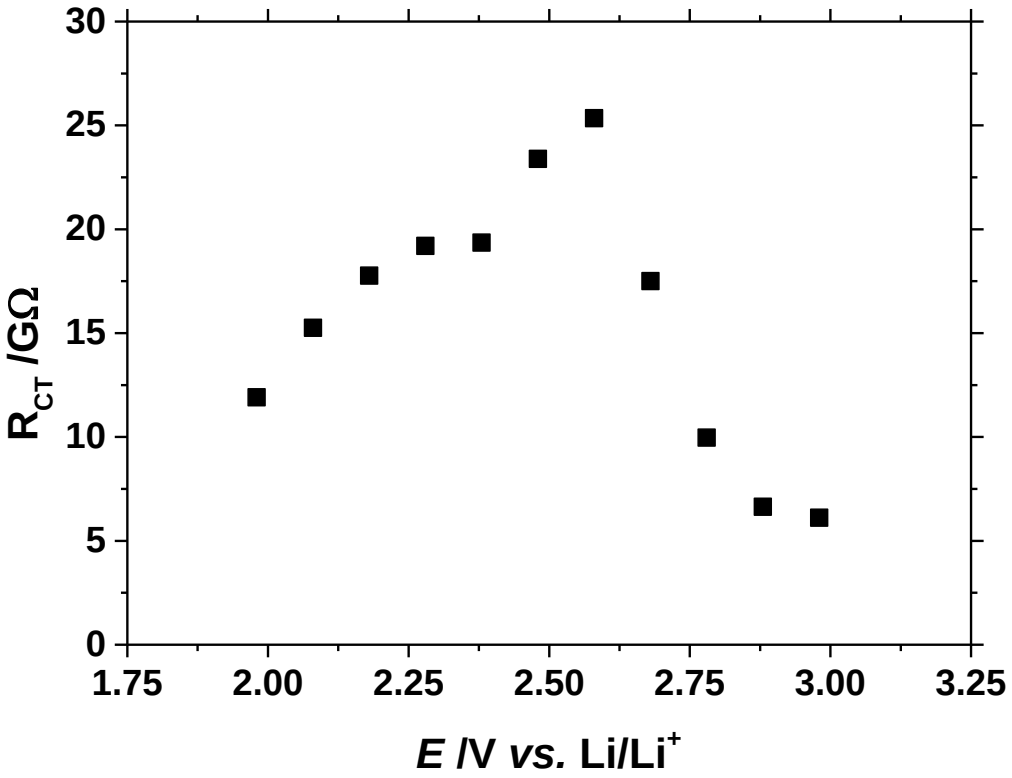

Figure 4.7: plot showing the charge transfer resistance *vs*. potential of oxygenated PYR_{14} TFSI. The data shown are calculated from the data shown in Figure 4.1 and Figure 4.2 by the fitting to Circuit 1 (Figure 4.4).

Figure 4.7 shows that the charge transfer resistance increases slightly until 2.6 V *vs*. Li/Li^+ as the bias potential of the impedance decreases. This is most probably caused by the build-up of a film of impurities forming on the working electrode. Below 2.6 V *vs*. Li/Li^+ the charge transfer resistance decreases, this may be due to the early onset of the oxygen reduction reaction.

The conductivity of the ionic liquid can be found using Newmans formula applied to the solution resistance measured at the high frequency. From the Nyquist plot the solution resistance was found to be 93248 Ohm. Using Equation 4.1 the conductivity of the solution was estimated to be approximately 5.36 mS cm^{-1}. This is of the same order of magnitude of the values previously measured in other ionic liquids.[5]

At a potential of 2.0 V *vs*. Li/Li^+, the value of R_{CT} decreases by a factor of 100. This is most easily seen on the Bode plot of the impedance at 2.0 V *vs*. Li/Li^+.

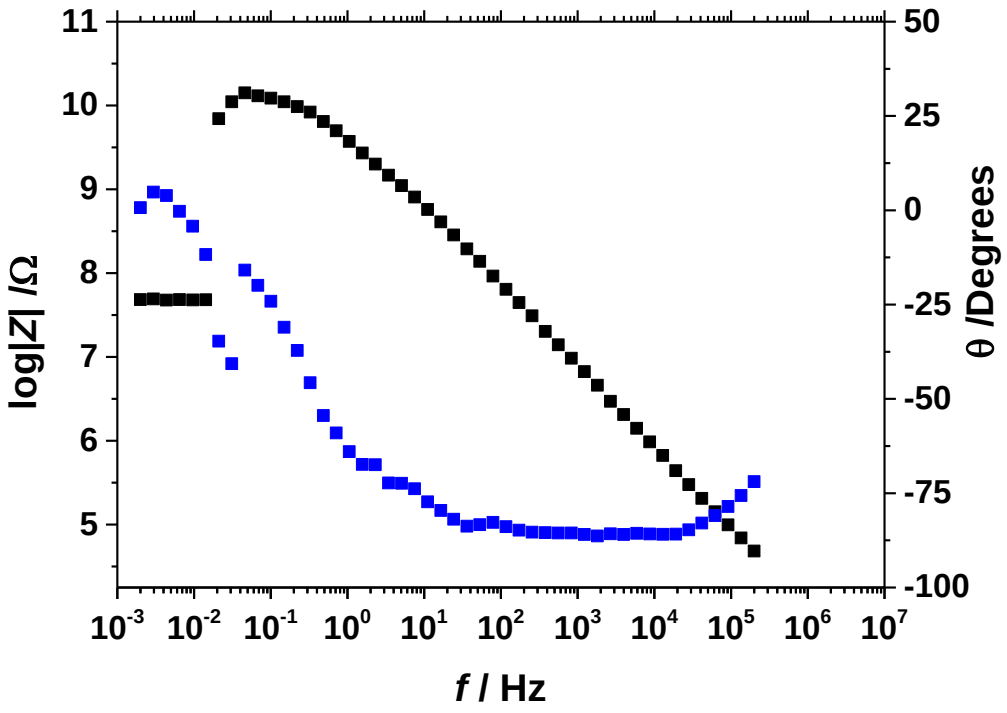

Figure 4.8: Bode plot for impedance at oxygenated PYR_{14} TFSI at 2.0 V *vs.* Li/Li^+. The frequency range used was 200 kHz to 2 mHz, using 6 frequencies per decade with an amplitude of 25 mV. The experiment was done using a 10 µm diameter Pt microelectrode working electrode and a $Li_{1.5}Mn_2O_4$ counter-reference electrode in a cross-shaped cell. The ionic liquid was oxygenated by allowing oxygen to diffuse into the ionic liquid over a period of approximately 18 hours. The black line is the log |Z|. The blue line is the phase value. This data is from Figure 4.2.

Figure 4.8 shows that at the high frequencies, the Bode plot shows similar behaviour to that seen in the previous impedances at the high potentials. At 10^{-1} Hz the impedance suddenly decreases from 10^{10} Ω to 10^8 Ω. The bias potential applied corresponds to the onset potential of the first oxygen reduction reaction from O_2 to superoxide. The decrease in the impedance occurs after the bias potential has been applied for some time instead of occurring at a higher frequency. This indicates that the onset of the reaction may require nucleation of oxygen on the working electrode to initiate oxygen reduction at that potential. This would explain the impedance dropping from 10^{10} Ω to 10^8 Ω at a long time after the bias potential was applied.

At potentials below 2.0 V *vs.* Li/Li^+ the onset of the O_2 reduction reaction decreases the charge transfer resistance greatly decreasing the size of the semicircle observed on the Nyquist plot. This also changes the equivalent circuit that the impedance data can be

fitted to. This could theoretically be fitted to a Randles circuit for a microelectrode which is shown in Figure 4.9. This circuit accounts for the diffusion of oxygen towards the microdisc electrode by adding a Warburg element.[2,3,6,7]

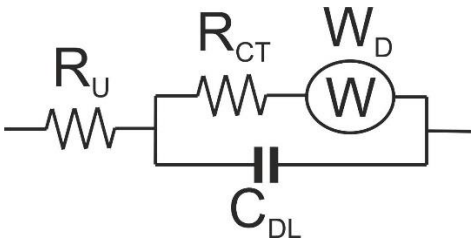

Figure 4.9: the Randles circuit that theoretically should fit potentials between 2.0 V and 0.5 V *vs*. Li/Li$^+$. R_U = Uncompensated solution resistance, R_{CT} = Charge transfer resistance, C_{DL} = Double layer Capacitance, W_D = Warburg diffusion element.

The actual data was not able to be successfully fitted to this circuit using the fitting programme. This could be due to incorrect initial values being used for the fitting, or due to the data being abnormal so that the Randles circuit was no longer a good approximation. It was found through iterative fitting and repeated modification of the elements in the Randles circuit that the equivalent circuit that gave the best fit was two resistor-capacitor parallel pairs in series with a Warburg element and an uncompensated resistance. This fitted circuit is shown in Figure 4.10.

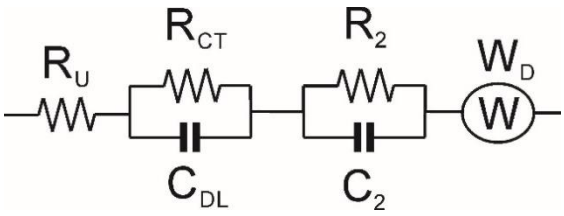

Figure 4.10: the circuit (Circuit 2) that was able to fit potentials between 2.0 V and 0.5 V *vs*. Li/Li$^+$. R_U = Uncompensated solution resistance, R_{CT} = Charge transfer resistance, C_{DL} = Double layer capacitance, W_D = Warburg diffusion element. R_2 = SEI resistance, C_2 = SEI capacitance.

As with Figure 4.5 and Figure 4.6 the R_U value was unable to be determined by fitting. This could be due to the large magnitude differences between the value of R_U and the values of R_{CT} and R_2. Instead R_U was determined from the high frequency end of the semicircle in the Nyquist plot.

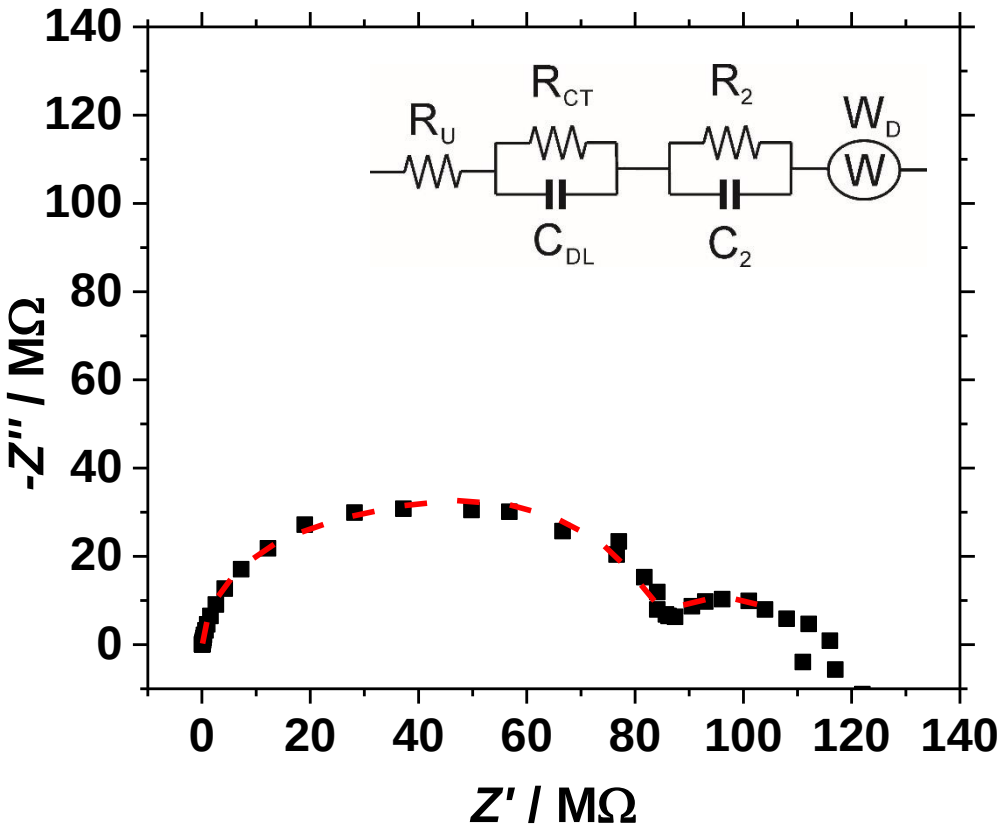

Figure 4.11: Nyquist plot for impedance at oxygenated PYR_{14} TFSI at 1.6 V *vs.* Li/Li^+. The frequency range used was 200 kHz to 2 mHz, using 6 frequencies per decade with an amplitude of 25 mV. The experiment was done using a 10 µm diameter Pt microelectrode working electrode and a $Li_{1.5}Mn_2O_4$ counter-reference electrode in a cross-shaped cell. The ionic liquid was oxygenated by allowing oxygen to diffuse into the ionic liquid over a period of approximately 18 hours. The red dashed line shows a best fit to Circuit 2. The parameters used for fittings are $R_{CT} = 2.96 \times 10^7$ Ω, $C_{DL} = 1.29 \times 10^{-10}$ F, $R_2 = 5.22 \times 10^7$ Ω, $C_2 = 3.83 \times 10^{-10}$ F, $W_{D\text{-}R} = 8.46 \times 10^6$ Ω, $W_{D\text{–}T} = 6.509$ s, $W_{D\text{-}P} = 0.31$. $R_U = 1 \times 10^5$ Ω but was not determined by fitting. This data is from Figure 4.1.

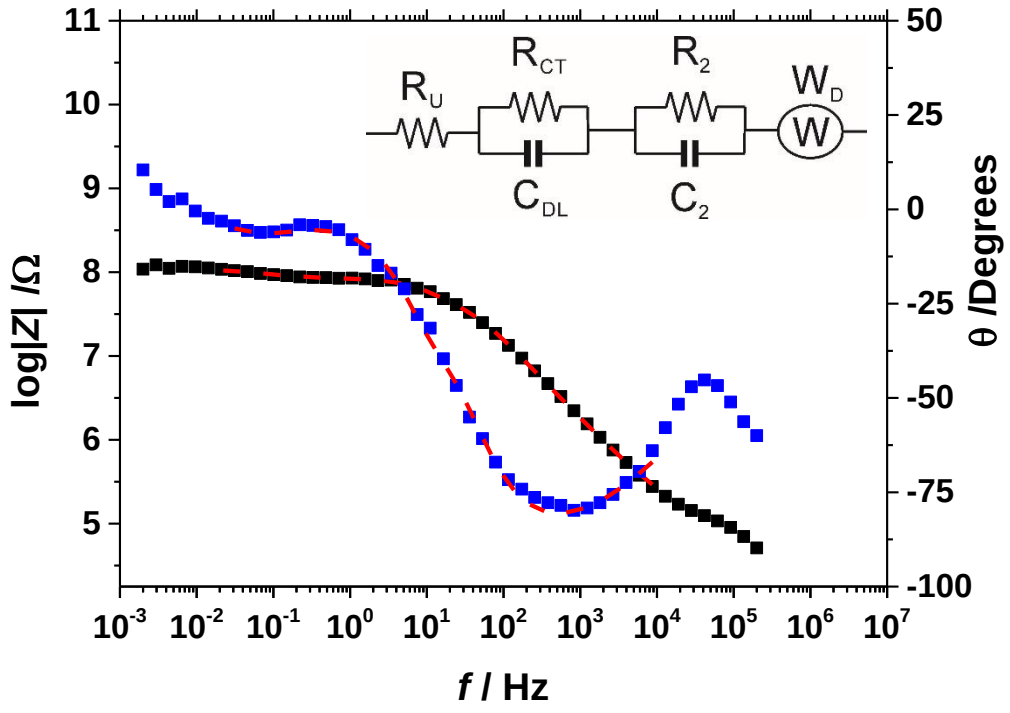

Figure 4.12: Bode plot for impedance at oxygenated PYR_{14} TFSI at 1.6 V *vs.* Li/Li^+. The frequency range used was 200 kHz to 2 mHz, using 6 frequencies per decade with an amplitude of 25 mV. The experiment was done using a 10 µm diameter Pt microelectrode working electrode and a $Li_{1.5}Mn_2O_4$ counter-reference electrode in a cross-shaped cell. The ionic liquid was oxygenated by allowing oxygen to diffuse into the ionic liquid over a period of approximately 18 hours. The black line is the log |Z|. The blue line is the phase value. The red dashed line shows a best fit to Circuit 2. The parameters used for fittings are $R_{CT} = 2.96 \times 10^7$ Ω, $C_{DL} = 1.29 \times 10^{-10}$ F, $R_2 = 5.22 \times 10^7$ Ω, $C_2 = 3.83 \times 10^{-10}$ F, $W_{D\text{-}R} = 8.46 \times 10^6$ Ω, $W_{D\text{–}T}$ = 6.509 s, $W_{D\text{-}P} = 0.31$. $R_U = 1 \times 10^5$ Ω but was not determined by fitting. This data is from Figure 4.2.

Figure 4.11 and Figure 4.12 were successfully fitted to a different equivalent circuit to that seen at 3.0 V to 2.0 V *vs.* Li/Li^+. The equivalent circuit shown contains two resistor and capacitor parallel combinations followed by a Warburg impedance.

At the high frequencies there is an initial uncompensated solution resistance of approximately 10^5 Ω. This was unable to be successfully fitted using computer fitting but can be seen by eye looking at the data. This is followed by a resistor and capacitor combination corresponding to the charge transfer resistance (R_{CT}) and the double layer capacitance (C_{DL}). As the frequency decreases further this is then followed by the second resistor (R_2) and capacitor (C_2) combination. This may be caused by the formation of a solid-electrolyte interface (SEI) layer on the working electrode. This SEI

layer has a similar capacitance and interfacial transfer resistance as the electrode itself. Because of this, the first semicircle on the Nyquist plot is actually an overlapping of the semicircles for the two resistor/capacitor combinations. This explains its depressed curve. At the lower frequencies, the effect of Warburg diffusion can be observed by the final semicircle, indicating a Short or Finite Warburg. This indicates a finite length hemispherical diffusion field with a transmissive boundary caused by the diffusion of O_2 towards the working electrode. O_2 diffuses towards the working electrode from the bulk ionic liquid in a hemispherical manner, giving a hemispherical diffusion field. When the frequency applied to the bias potential coincides with the time taken for an O_2 molecule to move through the diffusion field Warburg shows as a straight line with a phase angle of 45 degrees. As the frequency decreases further the amplitude becomes out of phase with the time taken for O_2 to move through the diffusion field. Because of this the Warburg acts like a resistor, moving down to the x-axis of the Nyquist plot to form a semicircle.

This Warburg gives a W_T value of approximately 6 s. By using Equation 4.5 and a diffusion coefficient of O_2 of 5.7×10^{-6} cm^2 s^{-1} this corresponds to a diffusion layer thickness of approximately 0.0058 cm (58 µm). This agrees with the microelectrode theory that the diffusion layer will be 8-10 times the radius of the microelectrode (5 µm).

The Short Warburg can also be used to determine the values of $D^{1/2}c$ from the slope of the Warburg in the Nyquist plot. The value of σ estimated for Figure 4.11 is approximately 70 MΩ s$^{-1/2}$. This value can be applied to Equation 4.3 to determine the value of $D_O^{1/2}c_O$ as being approximately 3.4×10^{-9} mol cm^{-2} s$^{-1/2}$. This is of the same order of magnitude as that determined by other research groups using the Randles-Sevcik equation,[8] and the same order of magnitude as data obtained in Chapter 5.

Figure 4.3 shows that at 1.3 V *vs.* Li/Li$^+$ there is a small increase in the impedance at the low frequencies. This corresponds to the onset potential of the second reduction reaction from superoxide to peroxide.

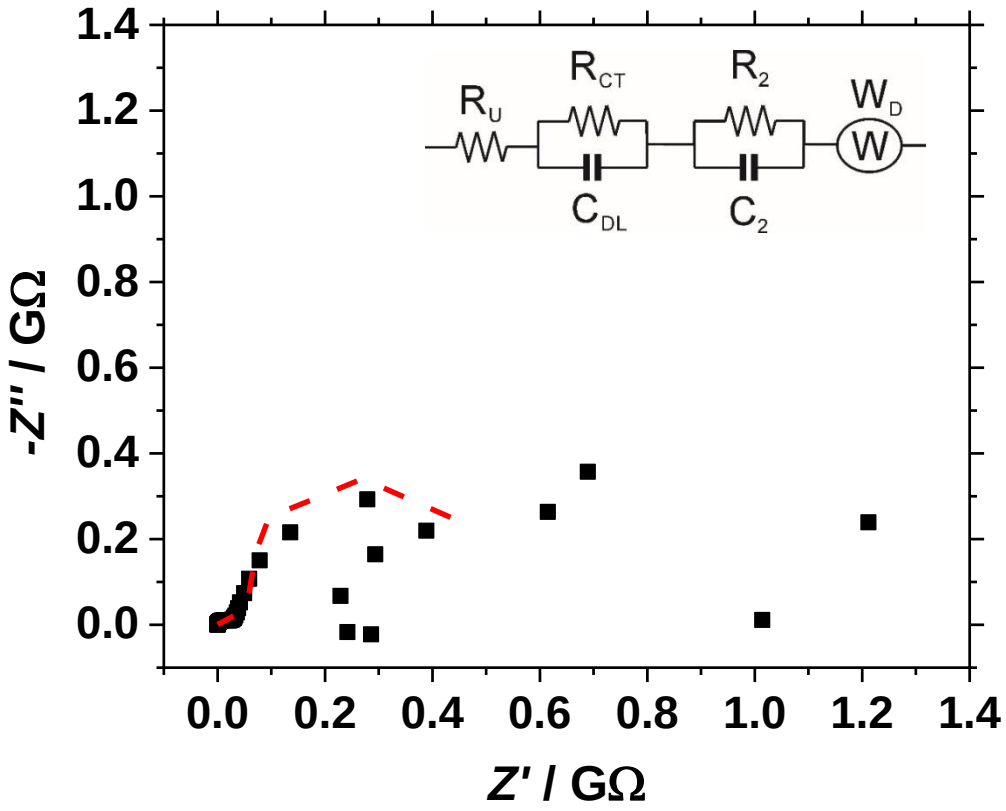

Figure 4.13: Nyquist plot for impedance at oxygenated PYR_{14} TFSI at 1.3 V *vs.* Li/Li^+. The frequency range used was 200 kHz to 2 mHz, using 6 frequencies per decade with an amplitude of 25 mV. The experiment was done using a 10 µm diameter Pt microelectrode working electrode and a $Li_{1.5}Mn_2O_4$ counter-reference electrode in a cross-shaped cell. The ionic liquid was oxygenated by allowing oxygen to diffuse into the ionic liquid over a period of approximately 18 hours. The red dashed line shows a best fit to Circuit 2. The parameters used for fittings are $R_{CT} = 1.66 \times 10^7$ Ω, $C_{DL} = 1.07 \times 10^{-10}$ F, $R_2 = 5.67 \times 10^7$ Ω, $C_2 = 7.01 \times 10^{-8}$ F, $W_{D\text{-}R} = 1.05 \times 10^8$ Ω, $W_{D\text{–}T} = 5.803$ s, $W_{D\text{-}P} = 0.65$. $R_U = 1 \times 10^5$ Ω but was not determined by fitting. This data is from Figure 4.1.

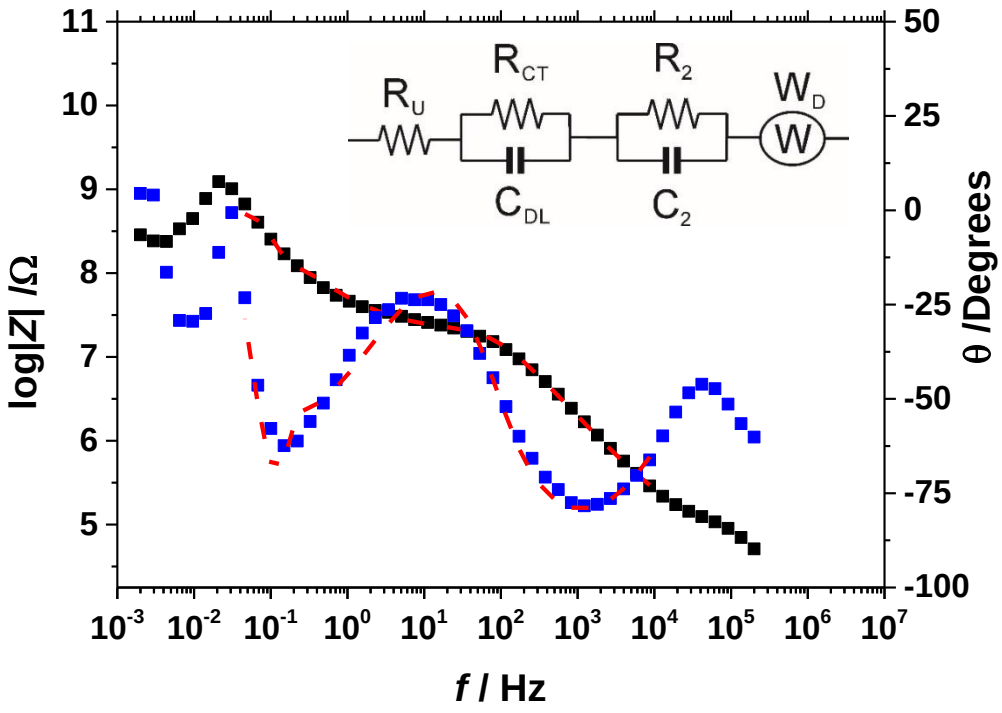

Figure 4.14: Bode plot for impedance at oxygenated PYR_{14} TFSI at 1.3 V *vs.* Li/Li^+. The frequency range used was 200 kHz to 2 mHz, using 6 frequencies per decade with an amplitude of 25 mV. The experiment was done using a 10 µm diameter Pt microelectrode working electrode and a $Li_{1.5}Mn_2O_4$ counter-reference electrode in a cross-shaped cell. The ionic liquid was oxygenated by allowing oxygen to diffuse into the ionic liquid over a period of approximately 18 hours. The black line is the log |Z|. The blue line is the phase value. The red dashed line shows a best fit to Circuit 2. The parameters used for fittings are $R_{CT} = 1.66 \times 10^7$ Ω, $C_{DL} = 1.07 \times 10^{-10}$ F, $R_2 = 5.67 \times 10^7$ Ω, $C_2 = 7.01 \times 10^{-8}$ F, $W_{D\text{-}R} = 1.05 \times 10^8$ Ω, $W_{D\text{-}T}$ = 5.803 s, $W_{D\text{-}P} = 0.65$. $R_U = 1 \times 10^5$ Ω but was not determined by fitting. This data is from Figure 4.2.

As with the previous Figure 4.11 and Figure 4.12, Figure 4.13 and Figure 4.14 do not easily fit to a Randles circuit. Instead they fit to the same equivalent circuit used for Figure 4.11 and Figure 4.12. Again the value of R_U was unable to be determined by fitting so had to be determined by observation. The fitting is also further complicated by a large negative resistance which occurs at high frequencies. Because of this the fitting can be described as unreliable. The real impedances which are seen in these figures at low frequencies are of an order of magnitude greater than that seen in the previous impedances at similar potentials. This increase in the magnitude of the impedance may be caused by the onset of the superoxide reduction to peroxide. Initially during the SPEIS experiment the potential was shifted to more and more negative potentials,

successively reducing more oxygen and forming superoxide. Each full impedance measurement took approximately 28 minutes per potential. The generated superoxide is stable in the ionic liquid and over the timescale of the experiment may have diffused into the bulk of the solution. At this potential, superoxide begins to be reduced to peroxide. Because of this the superoxide in the bulk of the solution diffuses towards the electrode in the same manner as the oxygen. This causes a spherical diffusion field for superoxide, overlapping with the existing diffusion field of oxygen. This may cause an increase in the impedance at low frequencies as a Warburg for superoxide. This was seen in Figure 4.3. As the amount of superoxide in the bulk is much smaller than the amount of O_2, the superoxide is depleted during this impedance measurement so that for the later impedance measurements at potentials lower than 1.3 V *vs*. Li/Li^+, the only source of superoxide is that generated by oxygen reduction at the microelectrode. Because this superoxide is formed near the electrode, it does not need to diffuse towards the electrode to be reduced, and so the impedance in potentials below 1.3 V *vs*. Li/Li^+ reduces in size to similar to that seen between 2.0 V and 1.4 V *vs*. Li/Li^+ where no superoxide reduction occurs.

Much further investigation could be undertaken to study the reduction of O_2 in PYR_{14} TFSI using SPEIS techniques. Further investigation could be attempted into the onset potential of the O_2 reduction as well as the onset of the superoxide reduction reaction.

4.3.2 Impedance of Oxygenated C_2MIM TFSI

SPEIS was also undertaken using oxygenated C_2MIM TFSI ionic liquids. The impedance at each potential was plotted in Nyquist and Bode plots as shown in Figure 4.15 and Figure 4.16.

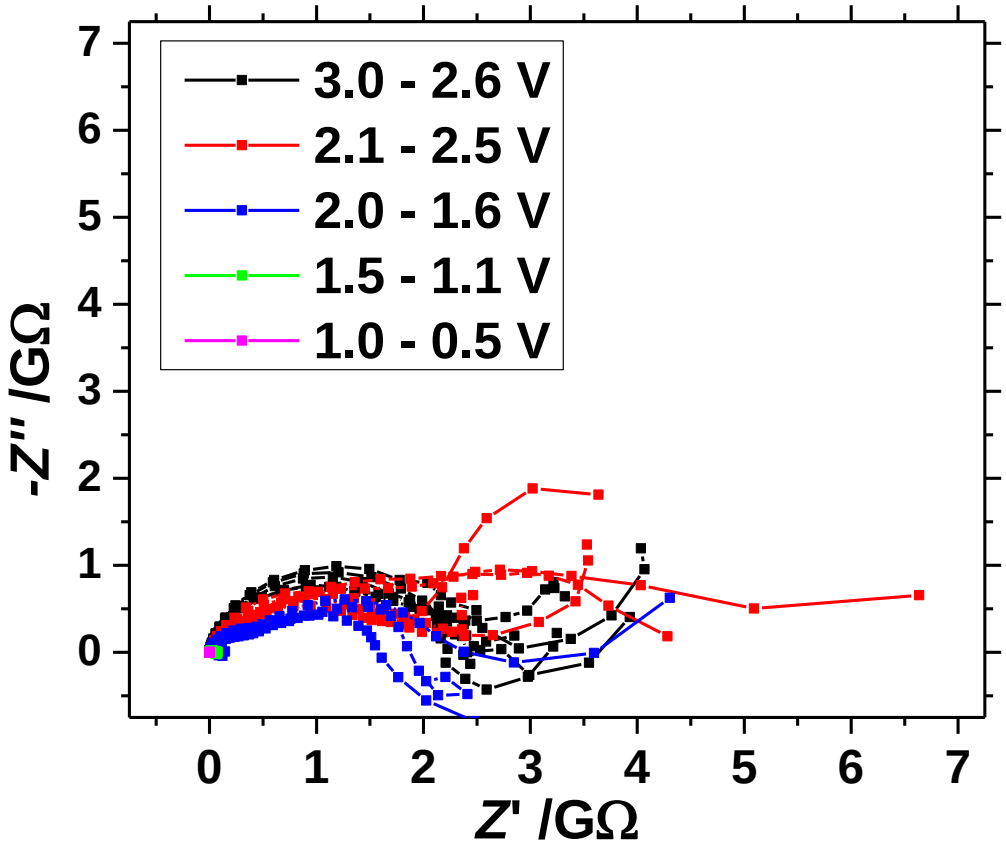

Figure 4.15: Nyquist plot showing the real impedance *vs*. the imaginary impedance for each potential during the SPEIS measurement of oxygenated C_2MIM TFSI. The experiment was done from 3.0 V to 0.5 V *vs*. Li/Li$^+$. The frequency range used was 200 kHz to 2 mHz, using 6 frequencies per decade with an amplitude of 25 mV. The experiment was done using a 10 µm diameter Pt microelectrode working electrode and a $Li_{1.5}Mn_2O_4$ counter-reference electrode in a cross-shaped cell. The ionic liquid was oxygenated by allowing oxygen to diffuse into the ionic liquid over a period of approximately 18 hours.

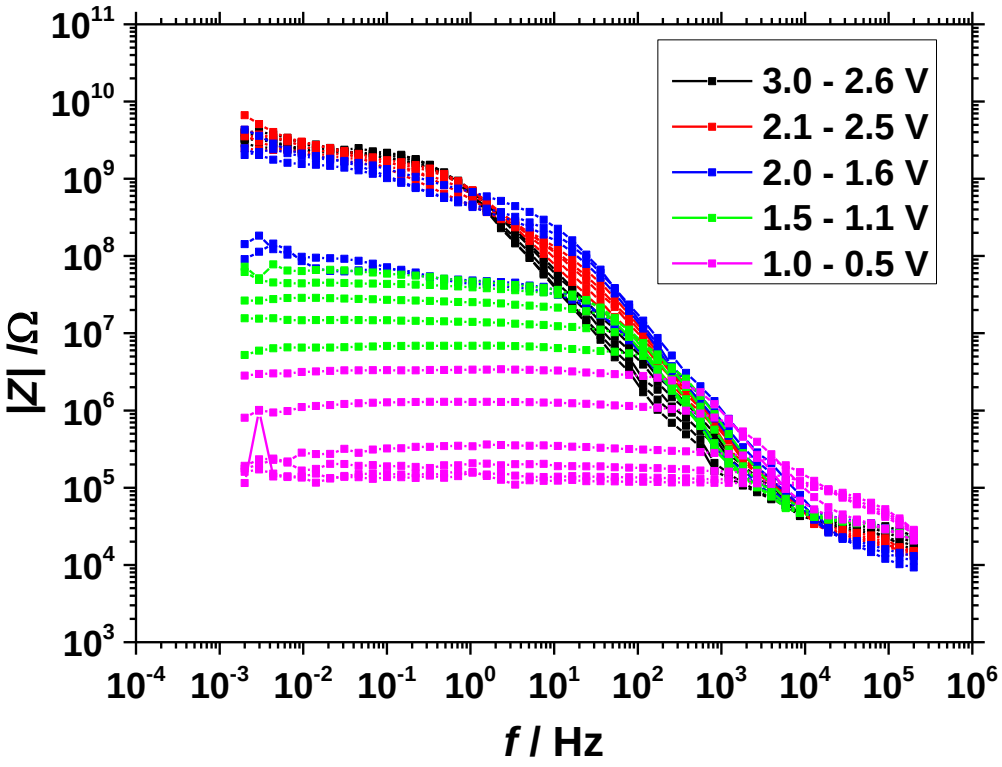

Figure 4.16: Bode plot showing the frequency *vs*. the modulus of the impedance for each potential during the SPEIS measurement of oxygenated C_2MIM TFSI. The frequency range used was 200 kHz to 2 mHz, using 6 frequencies per decade with an amplitude of 25 mV. The experiment was done using a 10 µm diameter Pt microelectrode working electrode and a $Li_{1.5}Mn_2O_4$ counter-reference electrode in a cross-shaped cell. The ionic liquid was oxygenated by allowing oxygen to diffuse into the ionic liquid over a period of approximately 18 hours.

As was seen in the PYR_{14} TFSI, the impedance changes with the bias potential applied to the cell. At the higher potentials, 3.0 V to 1.8 V *vs*. Li/Li^+, the Nyquist and Bode plots were fitted to a solution resistance in series with a double layer capacitance and charge transfer resistance (Circuit 1). As was previously seen in PYR_{14} TFSI the charge transfer resistance at potential where no O_2 reduction occurs was of the order of GΩ. The double layer capacitance and the uncompensated resistances observed were also similar to those observed in oxygenated PYR_{14} TFSI. When the capacitor in the fitting is replaced by a constant phase element, the phase value of the double layer capacitance was approximately 0.9 indicating that the working electrode may be slightly roughened.

Between 1.8 V and 1.7 *vs*. Li/Li^+, the impedance decreases greatly at the lower frequencies, as was previously seen in oxygenated PYR_{14} TFSI. This is due to the onset

of the first oxygen reduction reaction from O_2 to 1.8 V to 1.7 V *vs.* Li/Li$^+$. This can be seen more easily in seen in Figure 4.17.

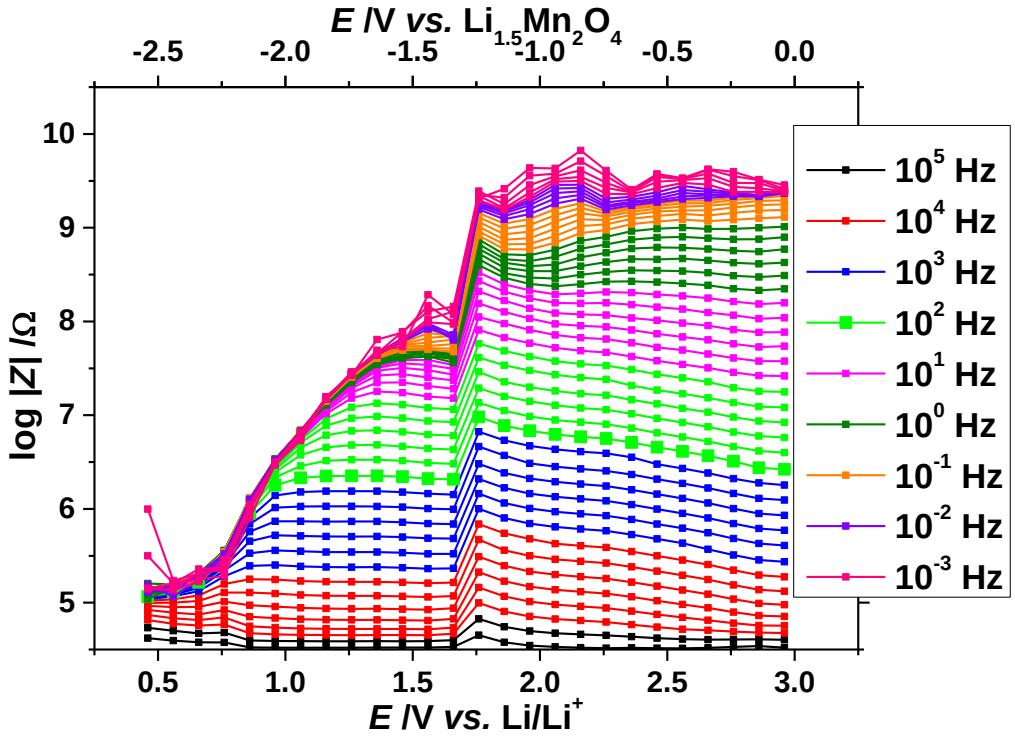

Figure 4.17: log of the modulus of the impedance of oxygenated C_2MIM TFSI at different potentials. Each line represents a different frequency. The frequency range used was 200 kHz to 2 mHz, using 6 frequencies per decade with an amplitude of 25 mV. The experiment was done using a 10 µm diameter Pt microelectrode working electrode and a $Li_{1.5}Mn_2O_4$ counter-reference electrode in a cross-shaped cell. The ionic liquid was oxygenated by allowing oxygen to diffuse into the ionic liquid over a period of approximately 18 hours.

Figure 4.17 shows that the impedance at the lower frequencies decreases at 1.8 V *vs.* Li/Li$^+$ due to the onset of the first O_2 reduction reaction. The impedance then continues to decrease at higher and higher frequencies as the potential becomes more negative. There seems to be no further increases in impedance. This indicates that there is no peak for the second electron reduction of $O_2^{\bullet-}$ to O_2^{2-}. This could be due to $O_2^{\bullet-}$ being removed from the system by reacting with the imidazolium cation in the C_2MIM TFSI. This confirms that the superoxide ion is not stable in C_2MIM TFSI.

The impedance measurements done at 1.5 V *vs.* Li/Li$^+$ where O_2 reduction occurs are shown in Figure 4.18 and Figure 4.19. These were fitted to Circuit 2 shown in Figure 4.10. The fittings for C_2MIM TFSI were much less accurate than the fittings for PYR_{14}

TFSI. Because of this these fittings should be deemed to be less reliable than those given previously. As with the previous fittings the value for R_U had to be determined manually from the Nyquist plots.

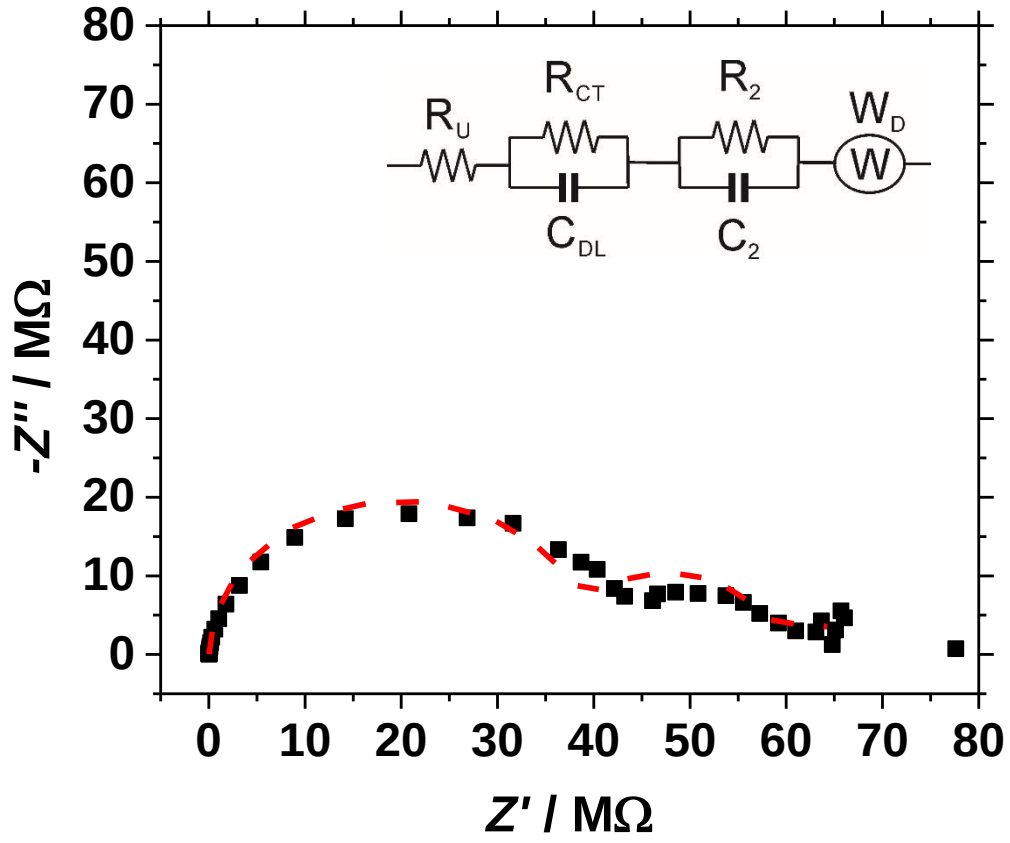

Figure 4.18: Nyquist plot for an impedance experiment done in oxygenated C_2MIM TFSI at 1.5 V *vs*. Li/Li$^+$. The frequency range used was 200 kHz to 2 mHz, using 6 frequencies per decade with an amplitude of 25 mV. The experiment was done using a 10 µm diameter Pt microelectrode working electrode and a $Li_{1.5}Mn_2O_4$ counter-reference electrode in a cross-shaped cell. The ionic liquid was oxygenated by allowing oxygen to diffuse into the ionic liquid over a period of approximately 18 hours. The fitting to Circuit 2 is the red dashed line. The parameters used for fittings are $R_{CT} = 3.80 \times 10^7$ Ω, $C_{DL} = 9.72 \times 10^{-11}$ F, $R_2 = 1.71 \times 10^7$ Ω, $C_2 = 9.77 \times 10^{-9}$ F, $W_{D\text{-}R} = 1.09 \times 10^7$ Ω, $W_{D\text{–}T} = 24.11$ s, $W_{D\text{-}P} = 0.35$. $R_U = 1 \times 10^5$ Ω but was not calculated *via* fitting. This plot was taken from Figure 4.15.

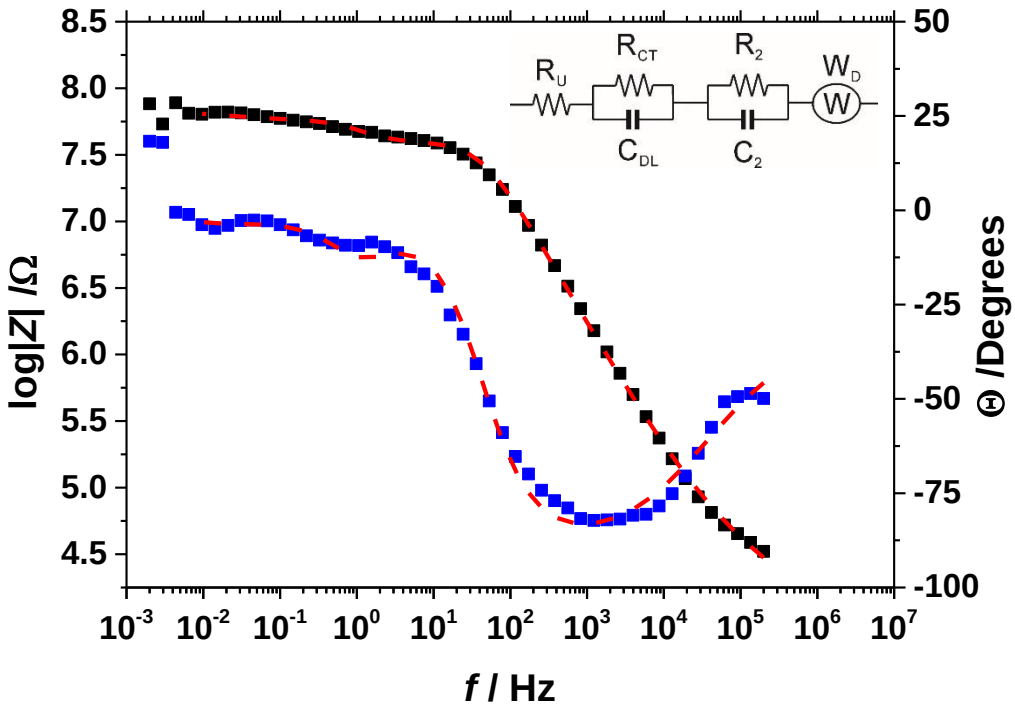

Figure 4.19: Bode plot for an impedance experiment done in oxygenated C2MIM TFSI at 1.5 V vs. Li/Li^+. The frequency range used was 200 kHz to 2 mHz, using 6 frequencies per decade with an amplitude of 25 mV. The experiment was done using a 10 µm diameter Pt microelectrode working electrode and a $Li_{1.5}Mn_2O_4$ counter-reference electrode in a cross-shaped cell. The ionic liquid was oxygenated by allowing oxygen to diffuse into the ionic liquid over a period of approximately 18 hours. The black line is the log $|Z|$. The blue line is the phase angle. The red lines are the fittings to Circuit 2. The parameters used for fittings are R_{CT} = 3.80 × 10^7 Ω, C_{DL} = 9.72 × 10^{-11} F, R_2 = 1.71 × 10^7 Ω, C_2 = 9.77 × 10^{-9} F, $W_{D\text{-}R}$ = 1.09 × 10^7 Ω, $W_{D\text{–}T}$ = 24.11 s, $W_{D\text{-}P}$ = 0.35. R_U = 1 x 10^5 Ω but was not calculated *via* fitting. This plot was taken from Figure 4.16.

Figure 4.18 and Figure 4.19 shows many similarities to the Nyquist and Bode plots shown for PYR_{14} TFSI. These plots are able to be fitted to Circuit 2. At the high frequency there is a small uncompensated solution resistance which was not calculated *via* fitting but could be calculated *via* measuring the high frequency intercept of the semicircle on the Nyquist plot. The value of the solution resistance calculated from the Nyquist plot can be used to determine the conductivity of C_2MIM TFSI using Newmans formula. The value of the conductance calculated is 14.3 mS cm^{-1}. This value is approximately double that of oxygenated PYR_{14} TFSI. This increased conductance may be due to the slightly lower viscosity of C_2MIM TFSI, 36 cP[9] *vs.* 60 cP for PYR_{14} TFSI.[8]

As the frequency decreases there occurs the first capacitor/resistor parallel combination. This corresponds to the double layer capacitance and the charge transfer resistance. The value of the double layer capacitance is approximately 9.72×10^{-11} F. This corresponds to 125 μF cm^{-2}. This value is similar to the value determined for PYR_{14} TFSI.

As $O_2^{\bullet-}$ is unstable in C_2MIM TFSI, and reacts with the labile protons on the imidazolium cation this means that no $O_2^{\bullet-}$ reduction to O_2^{2-} is observed. This is seen in Figure 4.17 by the low frequency impedance dropping at 1.7 V *vs*. Li/Li^+, due to O_2 reduction, followed by the impedance decreasing more and more rapidly until it reaches a minimum at approximately 0.75 V *vs*. Li/Li^+. This indicates that the onset potential of the O_2 reduction reaction is 1.7 V *vs*. Li/Li^+. This method appears to be a more accurate method of determining the onset potential of the O_2 reduction reaction in C_2MIM than cyclic voltammetry.

The C_2MIM TFSI shows a smaller uncompensated resistance, but a similar charge transfer resistance and double layer capacitance as PYR_{14} TFSI. This indicates that most of the electrochemical properties of the two ionic liquids are similar. This also indicates that the reduction of O_2 is an electrochemical reaction, while the reaction of the superoxide with the imidazolium cation is a chemical reaction. If the reaction of the superoxide and imidazolium cation were an electrochemical reaction, the charge transfer resistance would be significantly decreased.

4.4 Conclusions

The aims of the experiments in this chapter were to investigate SPEIS in oxygenated PYR_{14} TFSI and C_2MIM TFSI using electrochemical impedance spectroscopy. This has been achieved. These results show that the impedance of the oxygenated ionic liquid changes depending upon the potential applied. At the potentials where no O_2 reduction occurs the impedance shows only a large charge transfer resistance and a double layer capacitance. As the potential decreases and O_2 reduction starts to occur, the charge transfer resistance decreases and a hemispherical finite length diffusion Warburg occurs. This fits to two resistor/capacitor parallel pairs, corresponding to charge transfer resistance, double layer capacitance and an SEI layer combined with the Warburg diffusion of O_2 towards the working electrode. This circuit is not normally used to model diffusion at a microelectrode but the standard Randles circuit did not fit for unknown reasons.

These results indicate that reaction of $O_2^{\bullet -}$ with the imidazolium cation on C_2MIM TFSI is a chemical reaction and not an electrochemical reaction. This is consistent with the results seen in Chapter 3.

A full and thorough analysis of the impedance data shown here is beyond the scope of this thesis. A considerable amount of further analysis and fitting could be undertaken with the data obtained. This could be done by improving the fitting and by undertaking further analysis of the diffusion of O_2 towards the working electrode. Further experimentation could also be undertaken such as using different ionic liquids and different electrode materials. Further investigation of the onset of the O_2 reduction reaction using smaller bias potential steps could also be undertaken.

4.5 References

[1] J. Newman, *J. Electrochem. Soc.* **1966**, *113*, 501.

[2] D. Pletcher, *A First Course in Electrode Processes*, Royal Society Of Chemistry, Cambridge, **2009**.

[3] A. J. Bard, L. R. Faulkner, *ELECTROCHEMICAL METHODS: Fundamentals and Applications*, John Wiley & Sons, Inc., New York, **2001**.

[4] F. Silva, C. Gomes, M. Figueiredo, R. Costa, A. Martins, C. M. Pereira, *J. Electroanal. Chem.* **2008**, *622*, 153–160.

[5] M. Kanakubo, K. R. Harris, N. Tsuchihashi, K. Ibuki, M. Ueno, *Fluid Phase Equilib.* **2007**, *261*, 414–420.

[6] M. Fleischmann, S. Pons, *J. Electroanal. Chem.* **1988**, *250*, 277–283.

[7] P. G. Bruce, A. Lisowska-Oleksiak, P. Los, C. A. Vincent, *J. Electroanal. Chem.* **1994**, *367*, 279–283.

[8] S. Monaco, A. M. Arangio, F. Soavi, M. Mastragostino, E. Paillard, S. Passerini, *Electrochim. Acta* **2012**, *83*, 94–104.

[9] G. B. Appetecchi, M. Montanino, M. Carewska, M. Moreno, F. Alessandrini, S. Passerini, *Electrochim. Acta* **2011**, *56*, 1300–1307.

5. The Diffusion Coefficient and Solubility of O_2 in Room Temperature Ionic Liquids

The experiments undertaken in this chapter will study the determination of the diffusion coefficient and solubility of oxygen in pyrrolidinium based ionic liquids using potential step chronoamperometry at platinum and gold microdisc electrodes.

5.1 Introduction

The most critical parameters for the development of the LABOHR cell are the diffusion coefficient (D_O) and solubility (c_O) of oxygen in room temperature ionic liquids. The diffusion coefficient of a substance is a measure of the rate at which the substance diffuses through a medium, in this case the room temperature ionic liquid (RTIL). This is an important measure as the ionic liquid with the greatest diffusion coefficient for O_2 will allow O_2 to move towards the cathode fastest, allowing a greater amount of O_2 to be reduced and giving a larger current for the battery. The ionic liquid with the greatest O_2 solubility will also absorb more O_2 from the atmosphere and transport more O_2 to the cathode, allowing more O_2 to be reduced further increasing the current of the battery.

The most accurate method of determining D_O and c_O in a room temperature ionic liquid using a single measurement is through the use of potential step chronoamperometry at a microdisc electrode. Microelectrode chronoamperometry has been widely used by many groups, either as a standalone technique by Compton *et al.*,[1–5] or in conjunction with cyclic voltammetry at a macrodisc electrode by Katayama *et al.*[6] and Monaco *et al.*[7] as well as other groups, to determine the values D_O and c_O in many ionic liquids. The standalone chronoamperometry technique was chosen because it requires only a single measurement to determine the value of D_O and c_O and it requires only a single electrode, reducing the chances for error in the measurement.

The aims of the experiments undertaken in this chapter are to determine the diffusion coefficient and solubility of oxygen in various pyrrolidinium based room temperature ionic liquids at gold and platinum microdisc electrodes. The experiments will also investigate the effect that the method of oxygenating the ionic liquid has on the oxygen concentration.

5.2 Experimental

5.2.1 Experimental Setup

Four of the ionic liquids previously investigated in Chapter 2 were selected to be investigated using potential step chronoamperometry. Ultrapure PYR_{14} TFSI, PYR_{14} BETI, PYR_{14} IM_{14} and PYR_{12O1} TFSI were synthesised by our LABOHR partners (Passerini group, Westfälische Wilhelms-Universität, Münster). Before use any volatile components such as O_2, N_2 or H_2O were removed by applying a vacuum to the ionic liquid whilst stirring and heating at 120 °C for approximately 18 hours. The ionic liquids were then stored inside the argon atmosphere glovebox as previously described in Chapter 2.

The cell used for these experiments was the cross-shaped cell derived from a design by Compton *et al.*,[3,4] previously described in Chapter 2. A small pipette tip was used to hold approximately 0.25 cm^3 of the ionic liquid. 10 µm diameter Pt or 25 µm diameter Au microdisc electrodes used in experiments in Chapter 2 were used as the working electrodes. The $Li_{1.5}Mn_2O_4$ reference electrode previously described in Chapter 2 was used as the counter-reference electrode. The working electrodes were polished before use using the same method described in Chapter 2.

The cross-shaped cell was assembled in the glovebox, with the ionic liquid being added and the cell sealed against the atmosphere. The cell was removed from the glovebox and a vacuum was applied to the cell *via* the stopcock inlets on the cross-shaped cell. This vacuum removed all dissolved argon from the ionic liquid, as there is significant evidence that argon can affect the diffusion coefficient of substances in ionic liquids.[2] The vacuum was applied for approximately 60 minutes. Heating tape was also wound around the cross-shaped cell and heated to 120 °C for approximately 30 minutes during vacuuming. This increased the temperature of the ionic liquid, increasing the volatility of dissolved compounds, and increasing its purity.

The cross-shaped cell was then attached to the temperature-controlled water bath set to 25 °C (298 K) and cyclic voltammetry was done to test for any electro active impurities in the ionic liquid. For the experiments involving the Pt microelectrode the ionic liquid was oxygenated by passing O_2 into the headspace of the cell and allowing it to diffuse

into the ionic liquids overnight. For the experiments involving the Au microelectrode the solution was oxygenated by bubbling O_2 directly into the ionic liquid *via* a needle for approximately 15 minutes. After the ionic liquid was saturated, cyclic voltammograms (CVs) were done at various scan rates to determine the mechanism of O_2 reduction. These CVs were analysed previously in Chapter 2 and Chapter 3.

Potential step chronoamperometry (PSCA) was done on the cross-shaped cell by giving an open circuit potential period for 60 seconds to relax the cell from the cyclic voltammetry. Next, a potential step to 3 V *vs.* Li/Li^+, where no O_2 reduction reaction occurred, was done for 60 seconds to ensure that the next potential step started from the same potential. Finally, the potential was stepped to the O_2 reduction potential for 60 seconds to measure D_O and c_O. This sequence was done a total of 3 times at each temperature to test for repeatability.

The temperature of the cell was then increased to study the effect of temperature on the solubility and the diffusion coefficient. The potential steps were repeated at 35 °C (308 K), 50 °C (323 K) and 60 °C (333 K). For the experiments where the ionic liquid was saturated by bubbling *via* a needle the ionic liquid was bubbled with O_2 whilst the cell was undergoing heating to each temperature to ensure that the ionic liquid was fully saturated with O_2.

The PSCA was undertaken using an Iviumsoft Iviumstat potentiostat with the automatic current range disabled. The experiments were done in an earthed Faraday cage to remove interference from external electrical sources. The CAs were analysed using the method determined by Mahon and Oldham[8] as described in Chapter 1.

5.3 Chronoamperometry at a Platinum Microdisc Electrode with Ionic Liquid Saturated with O_2 *via* Headspace Filling

Initial experiments were undertaken using PSCA at a 10 µm diameter platinum microdisc working electrode. The ionic liquids were saturated by filling the cell headspace with O_2 and allowing the O_2 to diffuse into the ionic liquid over a period of approximately 18 hours. The ionic liquids PYR_{14} TFSI, PYR_{14} BETI, PYR_{14} IM_{14}, and PYR_{12O1} TFSI were studied using this experimental method. These ionic liquids were chosen to determine the effect of varying the anion and cation with respect to PYR_{14} TFSI. The current-time plots obtained from the chronoamperometry were linearized and the values for D_O and c_O were found using the method determined by Mahon and Oldham[8] The results of these experiments are shown in Figure 5.1 to Figure 5.4. Several consecutive experiments were done for each ionic liquid.

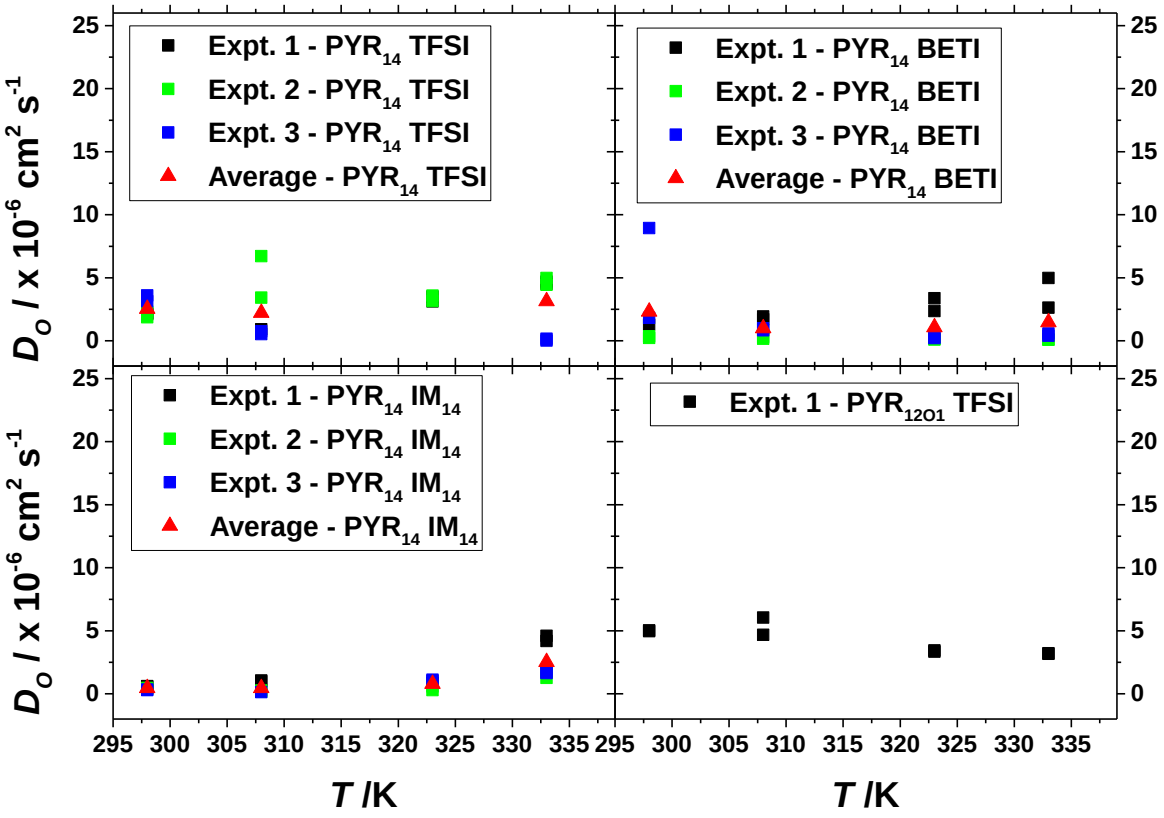

Figure 5.1: values of the diffusion coefficient of O_2 at various temperatures measured by potential step chronoamperometry at a 10 µm diameter Pt microdisc working electrode for PYR_{14} TFSI (Step to 1.0 V *vs.* Li/Li^+), PYR_{14} BETI (Step to 1.0 V *vs.* Li/Li^+), PYR_{14} IM_{14} (Step to 1.0 V *vs.* Li/Li^+) and PYR_{12O1} TFSI (Step to 1.25 V *vs.* Li/Li^+) ionic liquids. All potential steps were done for 60 seconds and the ionic liquids were oxygenated by allowing O_2 to diffuse into the ionic liquid over approximately 18 hours.

Figure 5.1 shows the values of D_O in several ionic liquids, calculated from the Cottrell plots for potential steps at the platinum microdisc electrode. This figure shows that, for all of the ionic liquids tested, D_O increases as the temperature increases. This may be caused by the viscosity of the ionic liquids decreasing with increasing temperature, allowing the O_2 to move through the ionic liquid more easily.

This figure shows that there is considerable variation in the values of D_O obtained between different experiments using the same ionic liquid and between different potential steps at the same temperature within the same experiment. These variations are caused by differences in the curve of the CAs at intermediate timescales. An example of these differences is shown in Figure 5.2. This shows two sequential potential steps which have different curves in the intermediate region between the transient short time

behaviour and the steady state long time behaviour. The first potential step shows a gentler curve than the second potential step. When the data is translated onto a Cottrell plot the gentler curve gives a steeper gradient. When fitted the diffusion coefficient obtained is 2.63×10^{-6} cm^2 s^{-1}, while the concentration of O_2 is 3.23×10^{-5} mol cm^{-3}. The sharper curve of potential step 2, shown by the red line, has a Cottrell plot slope of 0.0856 and an oxygen diffusion coefficient of 4.98×10^{-6} cm^2 s^{-1} and an O_2 concentration 1.69×10^{-5} mol cm^{-3}. Both potential steps gave identical steady state currents at long timescales and the Cottrell plots gave almost identical y-axis intercepts.

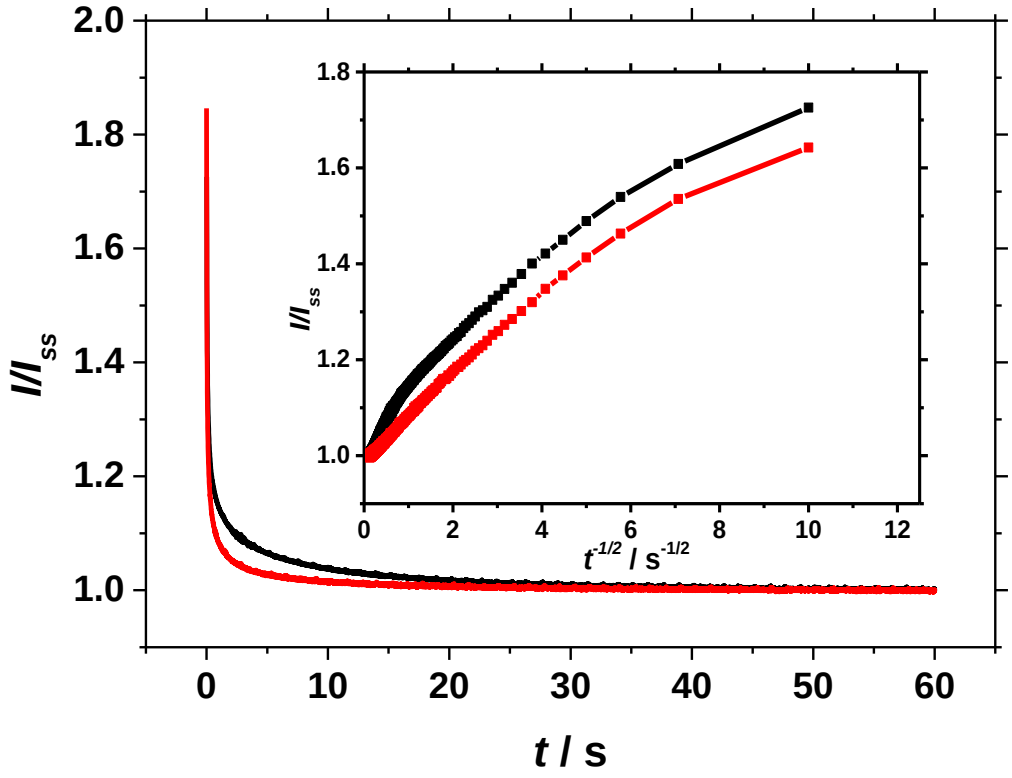

Figure 5.2: current/steady state current (I_{ss}) *vs.* time plots and Cottrell plots (inset) of two successive potential steps at the Pt microdisc working electrode at 333 K for PYR_{14} BETI. Potential step 1 (Black trace) has a Cottrell plot slope of 0.1214 s$^{1/2}$, $D_O = 2.63 \times 10^{-6}$ cm^2 s^{-1}, $c_O = 3.23 \times 10^{-5}$ mol cm^{-3}. Potential step 2 (Red trace) has a Cottrell plot slope of 0.0856 s$^{1/2}$, $D_O = 4.98 \times 10^{-6}$ cm^2 s^{-1}, $c_O = 1.69 \times 10^{-5}$ mol cm^{-3}.

The differences which occur between potential steps of the same temperature of the same experiment show that the first potential step gives a smaller diffusion coefficient, but larger O_2 concentration than the second potential step. These differences may be due to the formation of a film of lithium peroxide on the surface of the microdisc electrode during the initial potential step, which is still present but not deposited on the

subsequent potential step due to all the lithium ions in the vicinity of the electrode being consumed during the first potential step. A small amount of lithium ions may be present in the ionic liquid, having diffused from the counter-reference electrode into the bulk ionic liquid *via* the glass frit of the counter-reference electrode.

Alternatively this difference in the curves of the potential steps may be caused by the adsorption of oxygen onto the microdisc electrode during the initial potential step or by the removal of trace amounts of water or other electroactive impurities present in the ionic liquid, which were not removed during vacuuming of the cell.

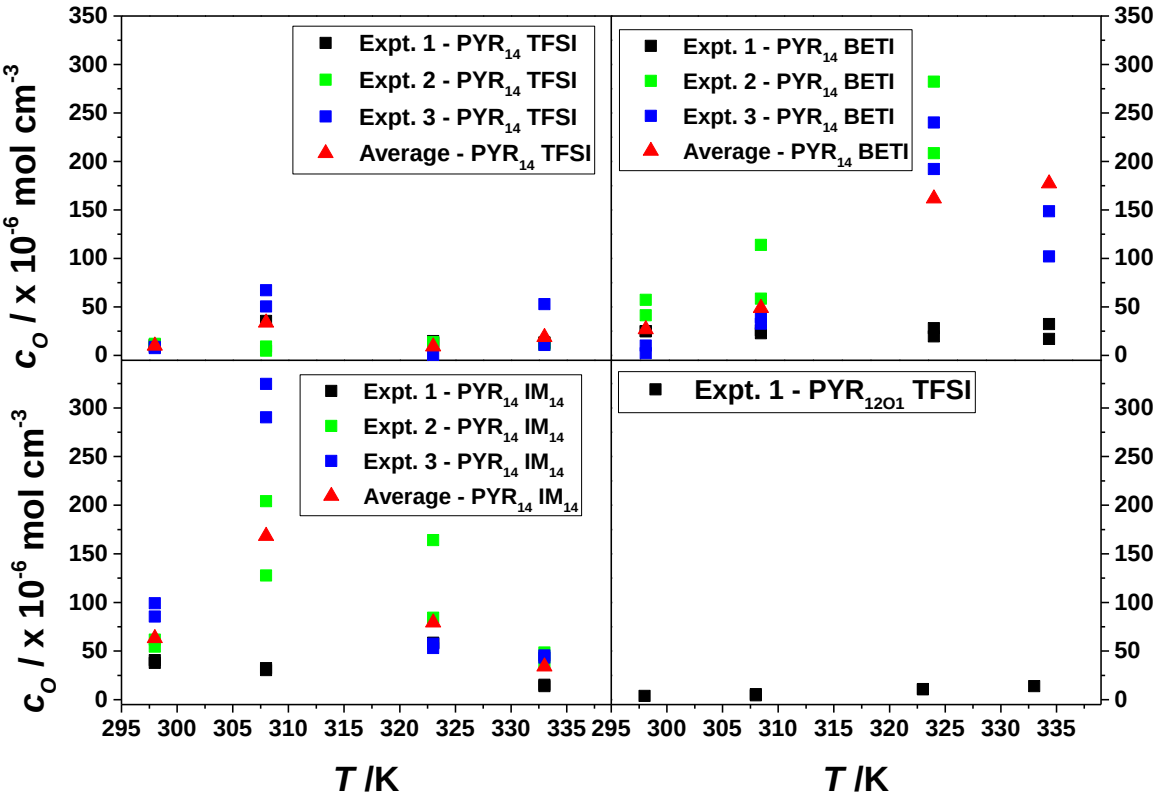

Figure 5.3: values of the concentrations of O_2 at various temperatures measured by potential step chronoamperometry at a 10 µm diameter Pt microdisc working electrode for PYR_{14} TFSI (Step to 1.0 V *vs.* Li/Li^+), PYR_{14} BETI (Step to 1.0 V *vs.* Li/Li^+), PYR_{14} IM_{14} (Step to 1.0 V *vs.* Li/Li^+) and PYR_{12O1} TFSI (Step to 1.25 V *vs.* Li/Li^+) ionic liquids. All potential steps were done for 60 seconds and the ionic liquids were oxygenated by allowing O_2 to diffuse into the ionic liquid over approximately 18 hours.

Figure 5.3 shows c_O in the ionic liquids, measured in the same potential steps as Figure 5.1. This figure shows no clear trend for c_O with temperature. It also shows that there is a large amount of variation in the values of c_O measured between experiments on the same ionic liquid and between potential steps at the same temperature within the same

experiment. The variation between experiments for the same ionic liquid could be caused by the amount of O_2 in the ionic liquid. Each ionic liquid was saturated by filling the headspace of the cross-shaped cell with O_2 and allowing it to diffuse into the cell over a period of approximately 18 hours. This method of oxygenation may not give the same degree of saturation each time and may not guarantee that the ionic liquids were fully saturated for each experiment. This would lead to variation in c_O in each ionic liquid, which would give different values for each experiment shown in Figure 5.3.

Another drawback of this method is that it may not allow enough time for the O_2 to diffuse out of the ionic liquid when the temperature was increased. As the temperature of a liquid increases the solubility of a gas in the liquid decreases. Because the diffusion coefficient of the O_2 in the ionic liquid is very small it would therefore take a long time for the O_2 to diffuse out of the ionic liquid naturally. The ionic liquid was heated to each temperature and left to thermally equilibrate before the experiment was done. However there may not have been enough time to allow O_2 to diffuse out of the ionic liquid before the experiment was started. This may mean that the concentration of oxygen in the ionic liquid at each temperature was not the equilibrium concentration of oxygen in the ionic liquid.

The differences between potential steps at the same temperature within the same experiment show that the first potential step gives a different value to the second potential step, with the first potential step giving a greater value for c_O than the subsequent potential step. This may be due to the formation of Li_2O_2 at the working electrode during the first potential step, giving a different value of c_O for the second potential step.

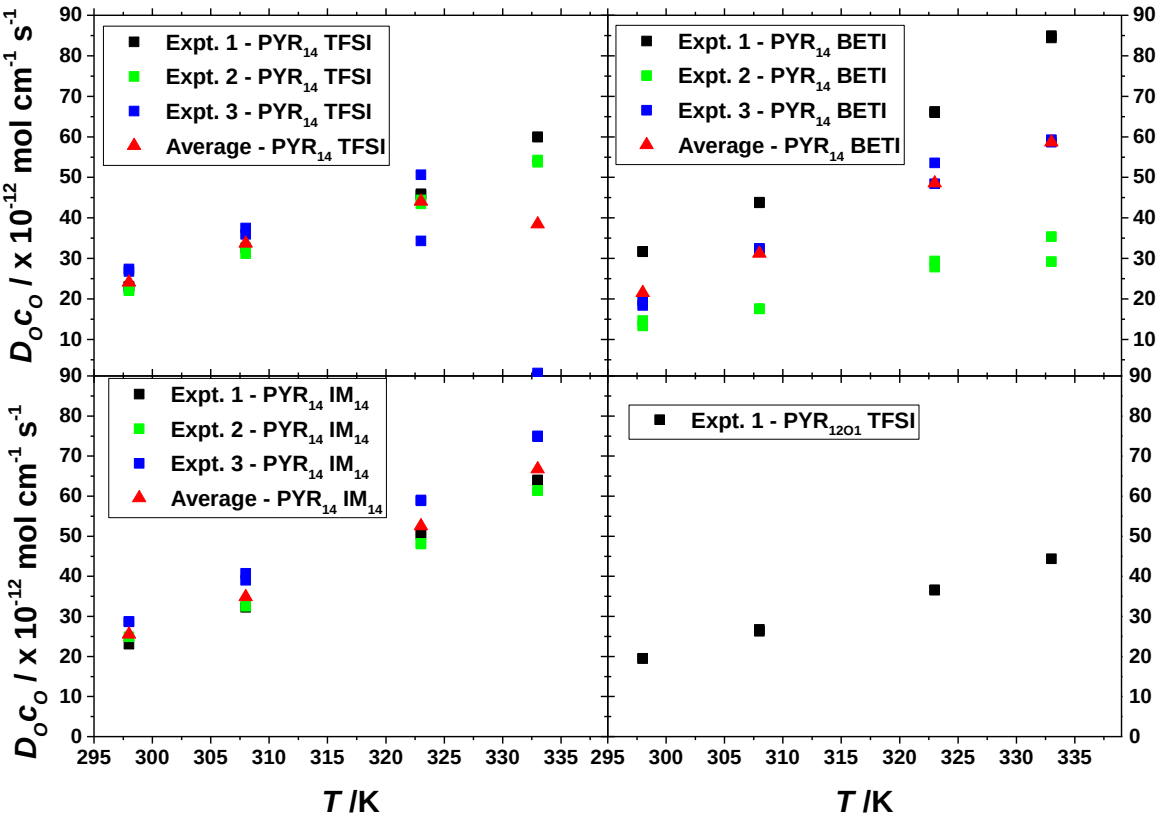

Figure 5.4: values of the diffusion coefficient-solubility product of O_2 at various temperatures measured by potential step chronoamperometry at a 10 µm diameter Pt microdisc working electrode for PYR_{14} TFSI (Step to 1.0 V *vs*. Li/Li^+), PYR_{14} BETI (Step to 1.0 V *vs*. Li/Li^+), PYR_{14} IM_{14} (Step to 1.0 V *vs*. Li/Li^+) and PYR_{12O1} TFSI (Step to 1.25 V *vs*. Li/Li^+) ionic liquids. All potential steps were done for 60 seconds and the ionic liquids were oxygenated by allowing O_2 to diffuse into the ionic liquid over approximately 18 hours.

Figure 5.4 shows the $D_O c_O$ values of O_2 in the ionic liquids, measured at several temperatures using the 10 µm diameter Pt microdisc working electrode. This figure shows that for all the ionic liquids the $D_O c_O$ value increases as the temperature increases. This is due to the increasing diffusion coefficient caused by the decreasing viscosity of the ionic liquid at higher temperatures. This figure also shows that the $D_O c_O$ values for each ionic liquid are much more in agreement with each other than the individual values for D_O and c_O. Figure 5.4 shows no appreciable difference in the values of $D_O c_O$ between potential steps at the same temperature of the same experiment. This is because the differences in D_O and c_O between potential steps of the same experiment are due to the differences in the slope of the Cottrell plot, due to the change from transient to steady state behaviour and not due to differences in the final steady state current.

Figure 5.4 also shows that there are differences in the $D_O c_O$ values between different experiments in the same ionic liquids. This may be caused by differences in the amount of O_2 which diffused into the ionic liquid, which would cause differences in the steady state current. Alternatively these differences may be caused by impurities in the ionic liquids which may affect the diffusion coefficient of O_2 through the ionic liquids.

Overall the results for potential step chronoamperometry at a Pt microdisc electrode show large variations between the values obtained for each experiment. Because of these large uncertainties, no certain conclusions can be made as regards to the absolute values of D_O, c_O and $D_O c_O$ in each ionic liquid.

These experiments were repeated and improved using a larger Au microdisc working electrode to give a larger surface area that is less likely to be passivated with Li_2O_2 deposits. The experiments were also improved by changing the bubbling of the RTIL with O_2 *via* a needle to ensure that the ionic liquid was fully saturated with O_2.

5.4 Chronoamperometry at a Gold Microdisc Electrode with Ionic Liquid Saturated with O_2 *via* a Needle

Potential step chronoamperometry was done on the aforementioned ionic liquids using the 25 µm diameter gold microdisc working electrodes using the cross-shaped cell.

The electrode material was changed from platinum to gold to reduce any effects of adsorption of water as seen in the CVs on Pt in Chapter 3. It was also suspected that the method of saturation the ionic liquid with oxygen by passing oxygen into the cell cavity and allowing it to diffuse into the ionic liquid did not fully saturate the ionic liquid. Because of this the method of oxygenating the ionic liquid was changed to bubbling the ionic liquid with oxygen *via* a needle to ensure that the ionic liquid was fully saturated with oxygen for each experiment.

The cross-shaped cell was assembled in the glovebox and the vacuum and heating tape were used to remove argon and any other volatile impurities. Oxygen was passed into the ionic liquid *via* a needle bubbling directly into the ionic liquids. The temperature was controlled *via* the temperature controlled water bath, with potential step chronoamperometry being done at 298, 308, 323 and 333 K. As the temperature was being increased to the next interval the ionic liquid was bubbled with oxygen to ensure that it remained saturated with oxygen at each temperature.

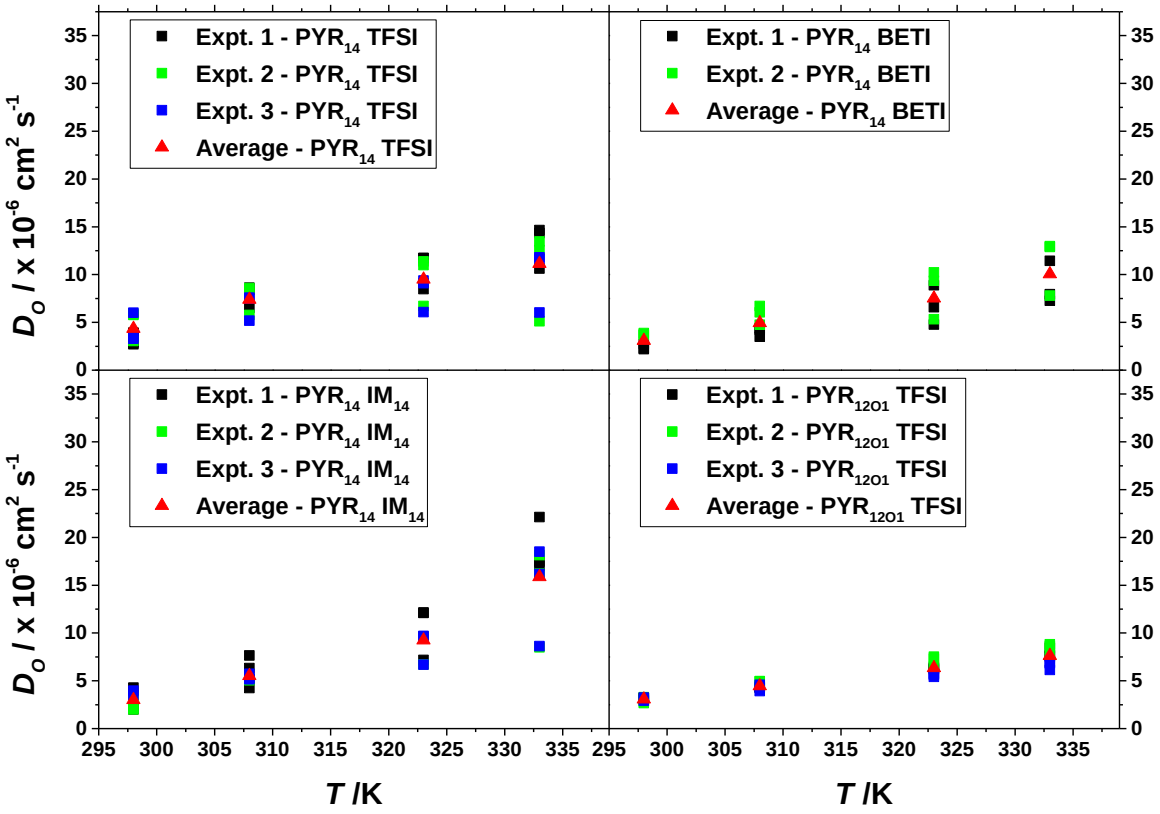

Figure 5.5: values of the diffusion coefficient of O_2 at various temperatures measured by potential step chronoamperometry at a 25 µm diameter Au microdisc working electrode for PYR_{14} TFSI (Step to 1.5 V *vs*. Li/Li^+) (values taken from Figure 2.9), PYR_{14} BETI (Step to 1.25 V *vs*. Li/Li^+), PYR_{14} IM_{14} (Step to 1.5 V *vs*. Li/Li^+) and PYR_{12O1} TFSI (Step to 1.5 V *vs*. Li/Li^+) ionic liquids. All potential steps were done for 60 seconds and the ionic liquids were oxygenated by bubbling oxygen directly into the ionic liquids *via* a needle.

Figure 5.5 shows the values of D_O in the ionic liquids measured through chronoamperometry at a 25 µm Au microdisc working electrode. This figure shows that the D_O increases with temperature for all of the ionic liquids. This is most probably due to the decrease in the viscosity of the ionic liquid as the temperature increases. This trend is much more defined in these results than was seen for the Pt microdisc electrode, indicating that the data obtained from these experiments is more reliable.

Figure 5.5 shows that there are differences between the first potential step in an experiment and the subsequent potential steps. This variation was also seen for the experiments done at a Pt microdisc electrode. This may be caused by the formation of Li_2O_2 at the electrode during the initial potential step, giving a different slope from that of the second and third potential steps.

This figure also shows that there are variations in the values obtained between different experiments. This variation may be caused by the differences in the purity of the ionic liquids. The ionic liquids may be contaminated by trace amounts of argon or water present in the ionic liquids, which was not removed *via* the vacuuming. There is evidence that substances such as argon can cause differences in the diffusion coefficient of oxygen in ionic liquids.

The values of D_O are far more reproducible for a gold microdisc electrode than for a platinum microdisc electrode. The values seem to agree with each other to a greater degree than in the Pt electrode experiments. This may be due to the larger surface area of the gold electrode being less susceptible to fouling than the smaller platinum electrode. Alternatively there may be fewer impurities in the ionic liquid which has been oxygenated by bubbling *via* a needle. This would create a convective movement of the ionic liquid causing the displacement and removal of any volatile components from the ionic liquid.

There are no extreme differences in the spread of results between the ionic liquids. All of the ionic liquids give values of D_O which are the same order of magnitude. To find the differences between the ionic liquids, the averages of these values should be used.

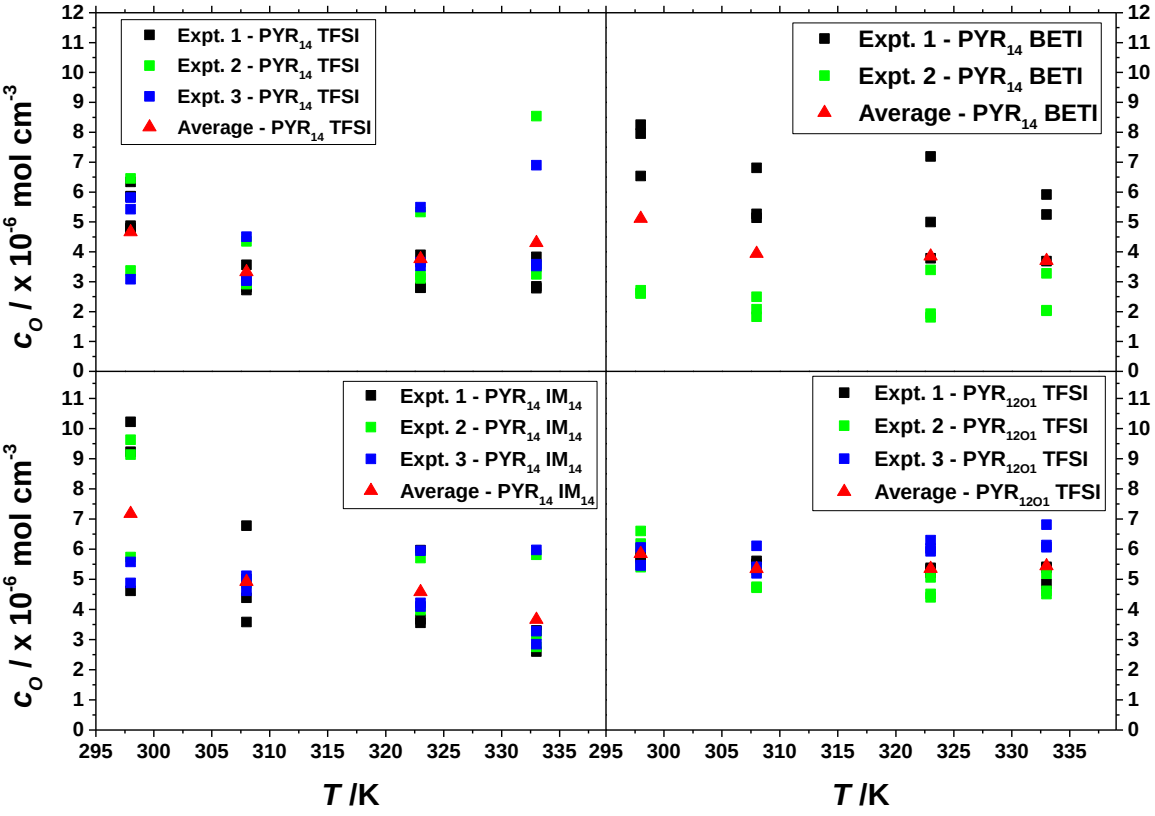

Figure 5.6: values of the solubility of O_2 at various temperatures measured by potential step chronoamperometry at a 25 µm diameter Au microdisc working electrode for PYR_{14} TFSI (Step to 1.5 V *vs.* Li/Li^+) (values taken from Figure 2.10), PYR_{14} BETI (Step to 1.25 V *vs.* Li/Li^+), PYR_{14} IM_{14} (Step to 1.5 V *vs.* Li/Li^+) and PYR_{12O1} TFSI (Step to 1.5 V *vs.* Li/Li^+) ionic liquids. All potential steps were done for 60 seconds and the ionic liquids were oxygenated by bubbling oxygen directly into the ionic liquids *via* a needle.

Figure 5.6 shows the values of c_O measured *via* chronoamperometry at a gold microdisc working electrode for all of the ionic liquids. This figure shows that all of the ionic liquids show a general trend where c_O decreases as the temperature increases. This may be due to O_2 becoming less soluble in a liquid as the temperature of the liquid increases.

The values of c_O seen above show much greater agreement with each other than the values seen at the Pt microdisc electrode. There are still some differences between the values obtained for different experiments and for the values obtained within each experiment. The differences between experiments may be caused by the degree to which the ionic liquid was saturated with O_2 before the measurements were started. Bubbling the ionic liquid with O_2 saturates the ionic liquid to a greater degree than allowing oxygen to simply diffuse into the ionic liquid. However there may have been

differences in the flow rate at which the ionic liquid was bubbled which may have caused slight differences in the concentration of O_2 between the experiments.

Within each experiment, the largest differences are observed between the first potential step and subsequent potential steps. This may be due to the formation of a layer of lithium peroxide on the initial potential step, which is then not formed on the subsequent potential steps due to the lithium being depleted on the first potential step. The lithium may have leaked from the reference electrode compartment solution into the main RTIL solution.

This figure shows that all of the ionic liquids have similar O_2 solubilities at each temperature, all of them following the same trends. The average values of c_O will be used to distinguish between the ionic liquids.

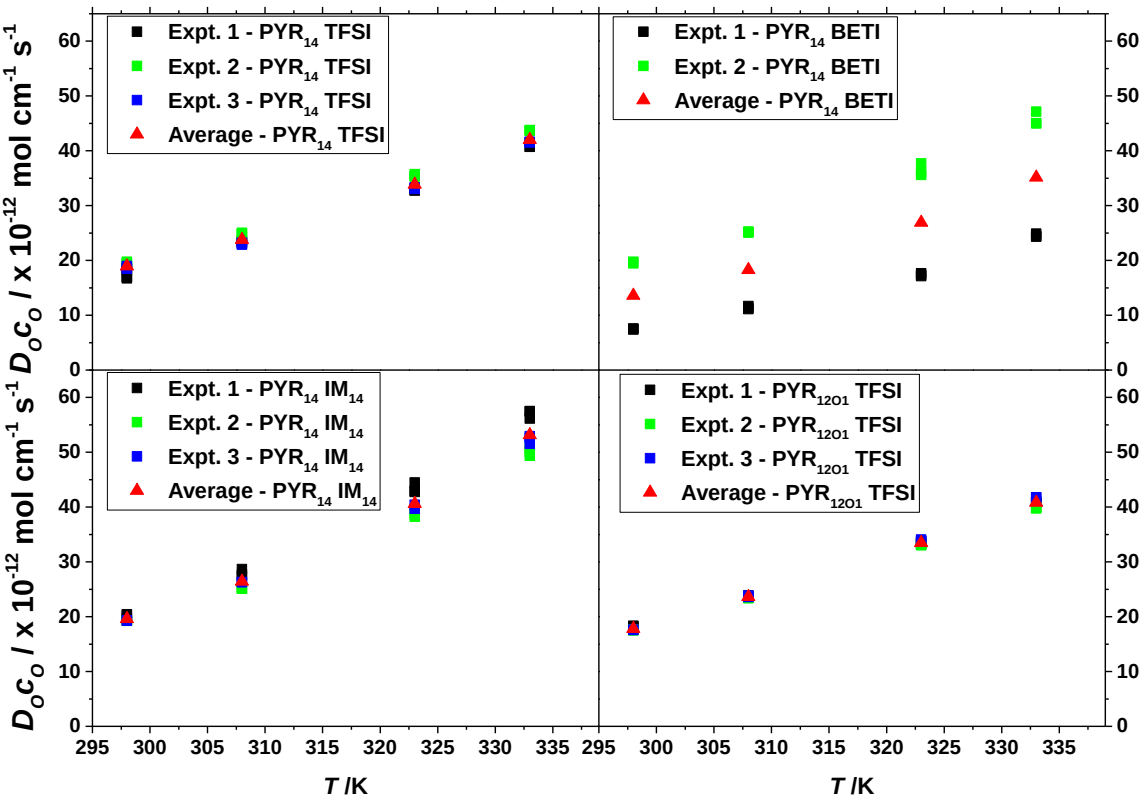

Figure 5.7: values of the diffusion coefficient-solubility product of O_2 at various temperatures measured by potential step chronoamperometry at a 25 µm diameter Au microdisc working electrode for PYR_{14} TFSI (Step to 1.5 V *vs*. Li/Li^+) (values taken from Figure 2.11), PYR_{14} BETI (Step to 1.25 V *vs*. Li/Li^+), PYR_{14} IM_{14} (Step to 1.5 V *vs*. Li/Li^+) and PYR_{12O1} TFSI (Step to 1.5 V *vs*. Li/Li^+) ionic liquids. All potential steps were done for 60 seconds and the ionic liquids were oxygenated by bubbling oxygen directly into the ionic liquids *via* a needle.

Figure 5.7 shows the values of D_OC_O for each ionic liquid calculated from chronoamperometry at the gold microdisc electrode. This figure shows that for all of the ionic liquids the D_OC_O values increase as the temperature increases. This is due to the increasing diffusion coefficient, caused by the decreasing viscosity of the ionic liquid, allowing O_2 molecules to move through the ionic liquid more rapidly. These results show greater agreement between the values of D_OC_O for each experiment for each ionic liquid, than those obtained at the Pt electrode. The only major differences occur for PYR_{14} BETI where Experiment 1 gives a much lower D_OC_O value than Experiment 2. This may be caused by the electrode being polished incorrectly for Experiment 1, giving a smaller surface area and therefore a smaller steady state current. Alternatively the ionic liquid in Experiment 1 may not have been fully saturated with O_2, giving the

slightly lower O_2 solubility for Experiment 1 than for Experiment 2 as was seen in Figure 5.6.

The values in Figure 5.7 also show no difference between the values of $D_O c_O$ from the first potential step and the subsequent potential steps for each experiment. This indicates that the differences between the first potential steps and the subsequent potential steps may occur in the transient region of the chronoamperogram, at short timescales, but have little effect at long timescales in the steady state region.

The greatest variation in the $D_O c_O$ values between experiments on the same ionic liquid is seen for PYR_{14} BETI. These large variations may be caused by impurities in the ionic liquid for one of the experiments or by differences in the degree of saturation of the ionic liquid with O_2 between the experiments.

In conclusion, all of the results obtained from the gold microdisc working electrode show much greater repeatability and reproducibility than the results obtained using the platinum microdisc electrode. These results should be more trusted than the results obtained from the platinum microdisc electrode. Because of this, it is possible to compare the average values of D_O, c_O and $D_O c_O$ for the ionic liquids. The average values of D_O, c_O and $D_O c_O$ were determined for each of the ionic liquids tested and plotted as a function of time. These values are shown in Figure 5.8 to Figure 5.10.

5.5 Average Values of D_O, c_O and D_Oc_O for each Ionic Liquid

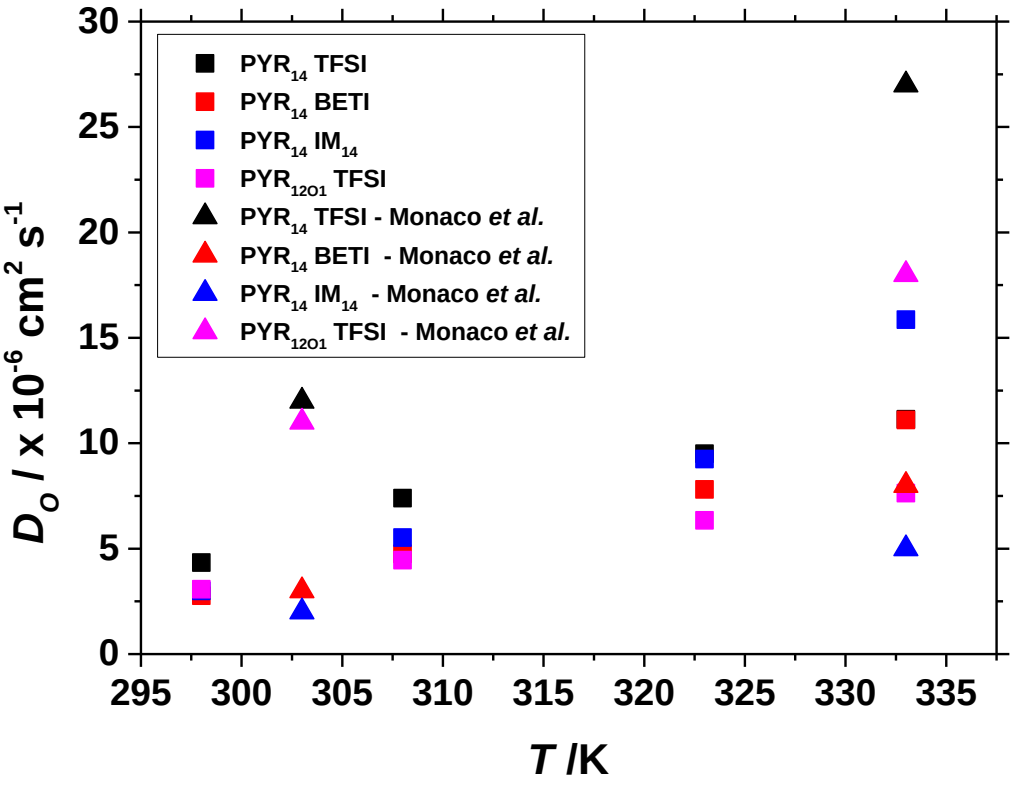

Figure 5.8: average diffusion coefficients of O_2 at various temperatures in the ionic liquids measured *via* potential step chronoamperometry at a 25 µm diameter Au microdisc working electrode. The average values are taken from Figure 5.5. The literature values are from Monaco *et al.*[7]

Figure 5.8 shows the average diffusion coefficients of O_2 in the ionic liquids tested above. These values confirm that the diffusion coefficient of O_2 increases as the temperature increases for each of the ionic liquids. The trend for D_O at 298 K roughly follows that of the viscosity of the ionic liquids. At 298 K the highest D_O belongs to PYR_{14} TFSI, which has a viscosity of 60 cP. The lowest D_O belong to PYR_{14} IM_{14} and PYR_{14} BETI with viscosities of 290 and 200 cP respectively. PYR_{12O1} TFSI has a recorded viscosity of 57.6 cP, similar to that of PYR_{14} TFSI, yet it has a smaller D_O for O_2 similar to PYR_{14} BETI and PYR_{14} IM_{14}. This may be due to the oxygen on the pyrrolidinium molecule interacting with the O_2 molecule and reducing its mobility inside the ionic liquid.

At higher temperatures the trend appears to hold. Although there is no viscosity data for most of these ionic liquids at 333 K, the diffusion coefficient measurements indicate that PYR_{12O1} TFSI gives the smallest O_2 mobility, probably due to the increased interaction with O_2 and the oxygen atom on the pyrrolidinium ion. Unexpectedly, PYR_{14} IM_{14} gives the largest diffusion coefficient of any ionic liquid at 333 K. As the LABOHR battery will be designed to run at 333 K for greater power output, this indicates that PYR_{14} IM_{14} would be most suitable for that battery based on the diffusion coefficient alone.

The values obtained from Monaco *et al.*[7] show a similar trend of increasing with temperature. They also show that the TFSI ionic liquids have the highest D_O while the BETI and IM_{14} ionic liquid have the lowest D_O. However the actual values obtained vary from those found in this chapter. This may be due to differences in the method of determining D_O, as Monaco *et al.*[7] used a combination of cyclic voltammetry at a macrodisc electrode and chronoamperometry at a microdisc electrode to find D_O.

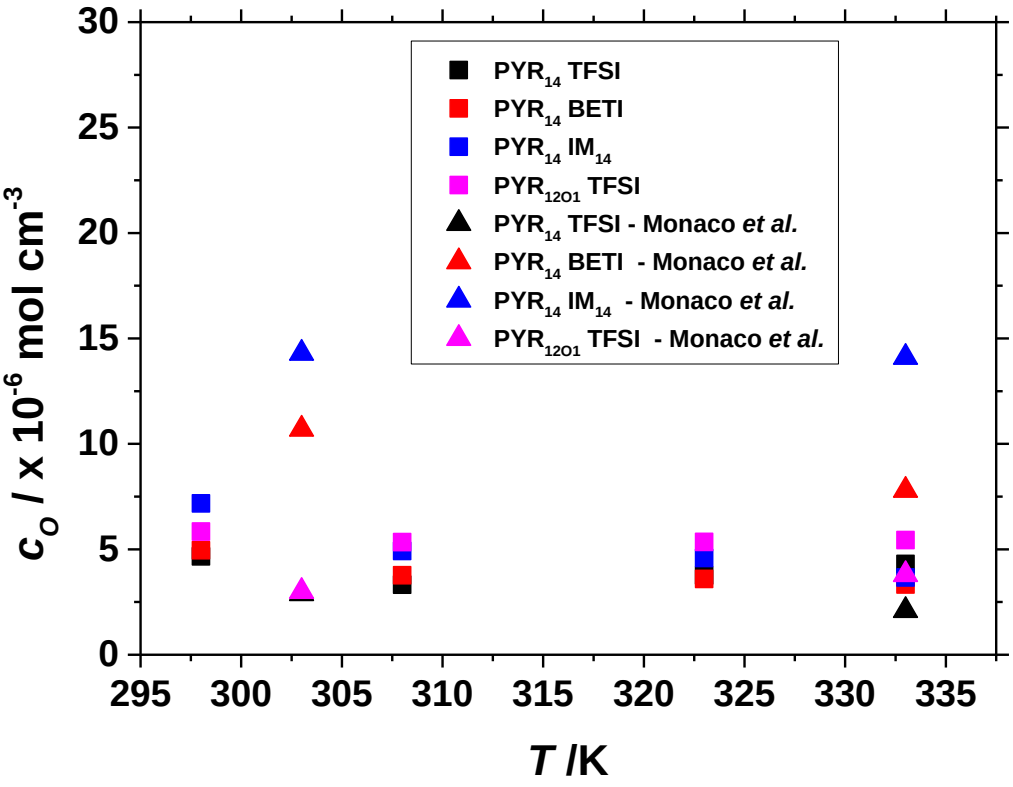

Figure 5.9: average concentrations of oxygen at various temperatures in the ionic liquids measured *via* potential step chronoamperometry at a 25 µm diameter Au microdisc working electrode. The average values are taken from Figure 5.6. The literature values are from Monaco *et al.*[7]

Figure 5.9 shows the average values of c_O in several O_2 saturated room temperature ionic liquids. This figure confirms that, for all of the ionic liquids, c_O decreases as the temperature increases. This is due to Henry's law whereby the solubility of a gas in a liquid decreases as the temperature of the liquid increases. As the LABOHR battery will be operated at 333 K, where the ionic liquids have a decreased O_2 solubility, the decreasing solubility with temperature may cause a problem with respect to the power generated from the battery. At 298 K, PYR_{14} TFSI has the smallest O_2 solubility of the ionic liquids tested. The fluorinated ionic liquids PYR_{14} BETI and PYR_{14} IM_{14} have slightly higher oxygen solubilities. At 308 K the greatest oxygen solubility belongs to the PYR_{12O1} TFSI. This may be due to the oxygen atom in the pyrrolidinium group increasing the free volume available in the ionic liquid for oxygen to dissolve into it. At higher temperatures the greatest solubility belongs to PYR_{12O1} TFSI.

The values obtained from Monaco *et al.* show similar trends to the data obtained in this chapter. However the values of c_O are much greater than the ones obtained here. This may be due to differences in the oxygenation of the ionic liquid, or due to differences in the method of calculating c_O.

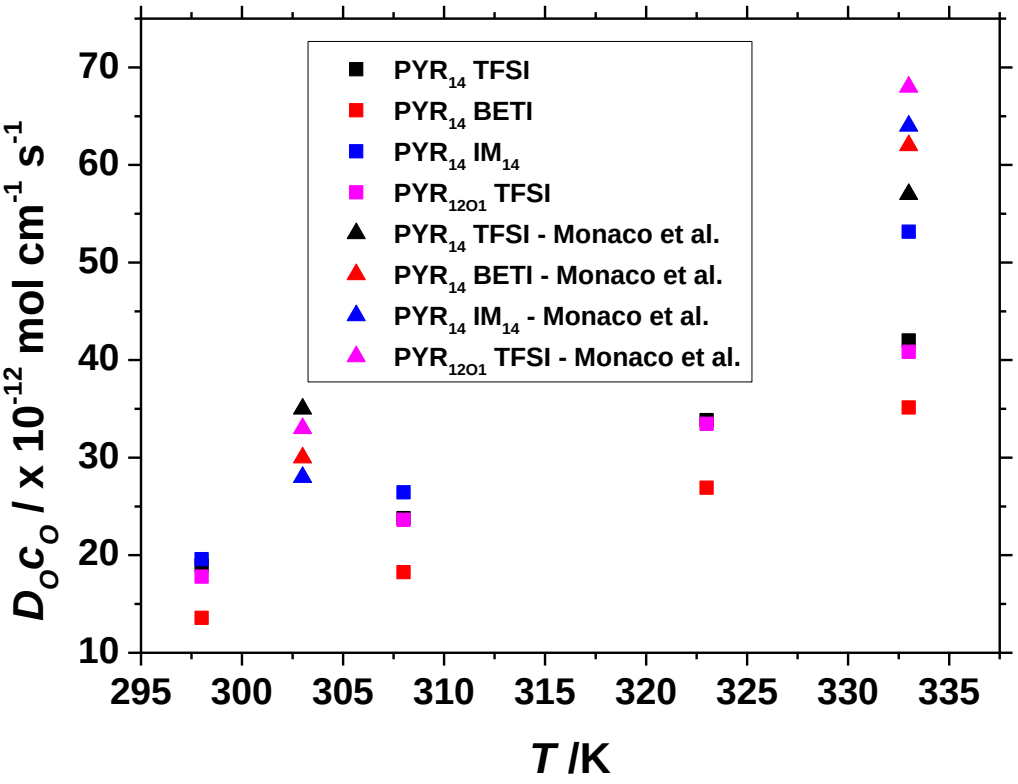

Figure 5.10: average diffusion coefficient-solubility products of oxygen at various temperatures in the ionic liquids measured *via* potential step chronoamperometry at a 25 µm diameter Au microdisc working electrode. The average values are taken from Figure 5.7. The literature values are from Monaco *et al.*[7]

Figure 5.10 shows the average diffusion coefficient-stability products of the ionic liquids at various temperatures. These values show that the $D_O c_O$ values increase as the temperature increases. This is due to the increased diffusion coefficient due to the decreased viscosity of the ionic liquid. Even though the c_O value in the ionic liquids decreases as the temperature increases, the increase in D_O counteracts this to increase the $D_O c_O$ value overall. This figure shows that at all temperatures PYR_{14} IM_{14} gives the greatest $D_O c_O$ value. As the $D_O c_O$ value is directly related to the current given by the battery, this indicates that PYR_{14} IM_{14} would be the most suitable ionic liquid for use in the LABOHR battery.

This figure shows that PYR_{14} BETI gives the lowest $D_O c_O$ value and that there is no appreciable difference between the $D_O c_O$ values for PYR_{14} TFSI and PYR_{12O1} TFSI. The low value for PYR_{14} BETI is due to the small diffusion coefficient while the identical values of PYR_{14} TFSI and PYR_{12O1} TFSI indicate that the added oxygen atom

on the pyrrolidinium cation has little effect on $D_O c_O$, increasing the solubility of oxygen but reducing the diffusion coefficient.

The values obtained by Monaco *et al.*[7] confirm that $D_O c_O$ does increase with temperature. However the values obtained are greater than the ones calculated here and the most suitable ionic liquid appears to be PYR_{12O1} TFSI at 60 °C. This difference may be caused by differences between the two experimental setups. Both experiments may have oxygenated and degassed the ionic liquids in different ways, as well as calculated the values using different methods. Monaco *et al.* used a rotating disc electrode which is unable to be used with an enclosed air-tight cell. However O_2 was bubbled through the cell for approximately 30 seconds between each experiment. The experiments done in this chapter were done in a fully airtight cell but the ionic liquid was bubbled with O_2 only prior to the experiment and not between each measurement. This difference in the oxygenation of the ionic liquid between the experiments may account for the differences in D_O, c_O and $D_O c_O$. The values of D_O, c_O and $D_O c_O$ for the ionic liquids at different temperatures are shown in Table 5.1.

Table 5.1: the values of the diffusion coefficient, solubility and diffusion coefficient-solubility product of O_2 at various temperatures in various ionic liquids.

Ionic Liquid	T / K	D_O / × 10^{-6} cm^2 s^{-1}	c_O / × 10^{-6} mol cm^{-3}	$D_O c_O$ / × 10^{-12} mol cm^{-1} s^{-1}
PYR_{14} TFSI	298	4.3	4.7	18.9
	308	7.4	3.3	23.8
	323	9.5	3.8	33.8
	333	11.1	4.3	42.0
PYR_{14} BETI	298	2.8	5.0	13.6
	308	4.8	3.8	18.2
	323	7.8	3.6	26.9
	333	11.1	3.3	35.1
PYR_{14} IM_{14}	298	3.0	7.2	19.6
	308	5.5	4.9	26.4
	323	9.3	4.6	40.6
	333	15.9	3.7	53.1
PYR_{12O1} TFSI	298	3.1	5.8	17.8
	308	4.5	5.3	23.6
	323	6.3	5.4	33.5
	333	7.6	5.4	40.8

The diffusion coefficient of O_2 in the ionic liquid can be used to calculate the activation energy of diffusion *via* an Arrhenius plot. By plotting ln D_O *vs.* 1/T a straight line graph is obtained, the slope of which can be used to determine the activation energy of diffusion when applied to the Arrhenius equation (Equation 5.1).[9]

$$D_O = D_{0K} e^{-E_a/RT} \qquad \textbf{(5.1)}$$

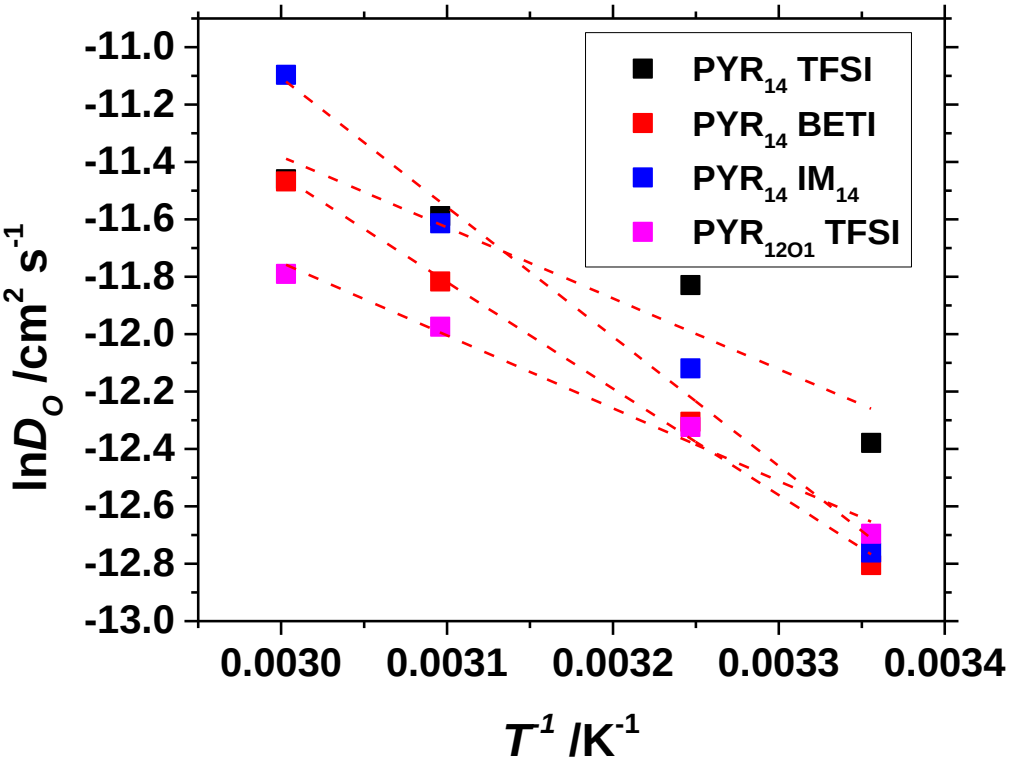

Figure 5.11: an Arrhenius plot showing the ln D_O *vs*. 1/*T* used to calculate the activation energy of diffusion of the ionic liquids. The values are taken from Figure 5.8.

Figure 5.11 shows the Arrhenius plot used to calculate the activation energy of diffusion in the ionic liquids. The values of the activation energy calculated are shown in Table 5.2. These values show that the activation energy of diffusion increases as the viscosity of the ionic liquid increases. This is to be expected as O_2 molecules dissolved in a more viscous ionic liquid would be expected to overcome a larger energy barrier to diffuse through the liquid. This also follows the similar trend to that of D_O of O_2 at 298 K. The PYR_{14} TFSI and PYR_{12O1} TFSI have the lowest activation energies and the greatest diffusion coefficients, while the more viscous PYR_{14} BETI and PYR_{14} IM_{14} have greater activation energies and lower D_O values. This confirms that the diffusion coefficient is related to the viscosity of the ionic liquid.

Table 5.2: the values of the activation energy of diffusion of the ionic liquids, calculated from Figure 5.11.

Ionic Liquid	Slope of Arrhenius plot / K	Intercept	E_a /kJ mol^{-1}	η at 298 K /cP	D_O at 298 K/ × 10^{-6} cm^2 s^{-1}
PYR_{14} TFSI	-2469	-3.4	20.5	60	4.3
PYR_{14} BETI	-3710	-0.31	30.8	200	2.8
PYR_{14} IM_{14}	-4511	2.43	37.5	290	3.0
PYR_{12O1} TFSI	-2538	-4.14	21.1	57.6	3.1

5.6 Conclusions

In conclusion, the diffusion coefficients and concentrations of O_2 were measured in four different ionic liquids, at four different temperatures, using potential step chronoamperometry at 25 µm diameter gold and 10 µm diameter platinum microdisc electrodes. The values which were obtained at the Pt microdisc electrode showed large uncertainties and variations, with no clear trends apparent and no direct comparison between the ionic liquids was possible. This was assumed to be due to the O_2 saturation regime of passing O_2 into the headspace and allowing it to diffuse naturally into the ionic liquid. This may have led to the ionic liquids not being fully saturated. Because of this the values obtained from potential step chronoamperometry at the Pt microdisc electrode are deemed to be unreliable.

The data obtained from PSCA at the Au microdisc working electrode shows much smaller uncertainties and much greater reliability than the values obtained from the Pt microdisc working electrode. This may be due to differences in bubbling the RTIL with O_2. The experiments using the Au microdisc electrode were saturated with O_2 by bubbling *via* a needled at each temperature. This ensured that the RTIL was fully saturated with O_2. The values obtained showed that D_O increased as the temperature of the ionic liquid increased, due to the decreased viscosity of the ionic liquids. The results also showed that c_O decreased slightly as the temperature increased.

The diffusion coefficient-solubility product values showed that the values of $D_O c_O$ increased as the temperature was increased. This is due to the greater diffusion coefficient of oxygen counteracting the decreasing solubility of oxygen.

From these results it was possible to calculate the average values of D_O, c_O and $D_O c_O$ for each ionic liquid and the most suitable ionic liquid to be used in the LABOHR battery at 333 K, based on O_2 solubility and diffusion alone, is PYR_{14} IM_{14}. The activation energy of diffusion for each ionic liquid was also calculated.

The aims of this chapter were to determine the value of D_O, c_O and $D_O c_O$ *via* potential step chronoamperometry at a microdisc electrode for several pyrrolidinium based ionic liquids. The values of D_O, c_O and $D_O c_O$ were successfully determined for four ionic liquids at various temperatures. These aims were achieved.

Further research could be done to improve these experiments and refine the results. The vacuum applied to the ionic liquids to remove any volatile components could be applied for longer or to a lower pressure to ensure that all contaminants are removed. The experiments could be repeated at different temperatures, to gain more reliable data and more insight into the effects of temperature. The experiments could also be repeated on another microelectrode material such as vitreous carbon or using a counter-reference electrode which does not contain lithium to prevent contamination of the ionic liquid by lithium.

5.7 References

[1] R. G. Evans, O. V. Klymenko, P. D. Price, S. G. Davies, C. Hardacre, R. G. Compton, *Chemphyschem* **2005**, *6*, 526–533.

[2] L. E. Barrosse-Antle, L. Aldous, C. Hardacre, A. M. Bond, R. G. Compton, *J. Phys. Chem. C* **2009**, *113*, 7750–7754.

[3] S. R. Belding, E. I. Rogers, R. G. Compton, *J. Phys. Chem. C* **2009**, *113*, 4202–4207.

[4] M. C. Buzzeo, O. V. Klymenko, J. D. Wadhawan, C. Hardacre, K. R. Seddon, R. G. Compton, *J. Phys. Chem. A* **2003**, *107*, 8872–8878.

[5] E. I. Rogers, X. Huang, E. J. F. Dickinson, C. Hardacre, R. G. Compton, *J. Phys. Chem. C* **2009**, *113*, 17811–17823.

[6] Y. Katayama, K. Sekiguchi, M. Yamagata, T. Miura, *J. Electrochem. Soc.* **2005**, *152*, E247–E250.

[7] S. Monaco, A. M. Arangio, F. Soavi, M. Mastragostino, E. Paillard, S. Passerini, *Electrochim. Acta* **2012**, *83*, 94–104.

[8] P. J. Mahon, K. B. Oldham, *Anal. Chem.* **2005**, *77*, 6100–6101.

[9] D. Camper, C. Becker, C. Koval, R. D. Noble, *Ind. Eng. Chem. Res.* **2006**, *45*, 445–450.

6. The Diffusion Coefficient and Solubility of O_2 in Ionic Liquids Containing LiTFSI

The experiments undertaken in this chapter will investigate attempts to determine the diffusion coefficient and solubility of O_2 in room temperature ionic liquids containing LiTFSI. The experiments will also investigate attempts to increase the solubility of lithium peroxide using tris(pentafluorophenyl)borane.

6.1 Introduction

In the previous chapters the determination of the diffusion coefficient (D_O) and solubility (c_O) of O_2 in pure room temperature ionic liquids (RTILs) was discussed. However the ionic liquid that is used in the LABOHR battery contains large concentrations of lithium salt. There is evidence that the addition of lithium salts to ionic liquids affects the viscosity, and therefore the diffusion coefficients of oxygen in ionic liquid.[1] The aim of the experiments done in this chapter was to determine the diffusion coefficient (D_O) and solubility of oxygen (c_O) in ionic liquid containing varying concentrations of LiTFSI.

These experiments were made more challenging through the passivation of the microdisc working electrode, which occurs when Li ions react with the superoxide formed during O_2 reduction to form lithium superoxide (LiO_2). The lithium superoxide then disproportionates to form lithium peroxide (Li_2O_2). The Li_2O_2 is insoluble and electronically insulating in the ionic liquid. Li_2O_2 passivates on the working electrode and makes it less electrically conductive. This affects the values of the current obtained from any potential step chronoamperometry measurements and makes the accurate determination of D_O and c_O impossible using this method.

Methods of reducing the passivation of the electrode and increasing the solubility of the lithium peroxide were investigated. There is some evidence that compounds such as tris(pentafluorophenyl)borane (TPFPB) can bind to and increase the solubility of lithium oxides and peroxides.[2–6] TPFPB is a strong Lewis acid that can bind to Li_2O_2, increasing its solubility. As TPFPB is a heavily fluorinated compound, it may also be useful to improve the solubility of O_2 in the ionic liquid[7–10] as perfluorocarbons have been investigated for use as potential blood substitutes.[10–12]

The aims of the experiments in this chapter were to study the mechanism of oxygen reduction in PYR_{14} TFSI containing various amounts of LiTFSI using cyclic voltammetry. Further aims were to determine the values of D_O, c_O and $D_O c_O$ in PYR_{14} TFSI containing various amounts of LiTFSI at various temperatures using potential step chronoamperometry at a microdisc electrode.

Parts of this chapter were published as Lodge *et al.*[13]

6.2 Experimental Methods

These experiments were done using a temperature controlled heart-shaped cell used in Chapter 2. A 25 µm diameter Au microdisc electrode previously used for experiments in Chapters 2, 3 and 5 was used as the working electrode. A $Li_{1.5}Mn_2O_4$ counter reference electrode was used.

PYR_{14} TFSI (99.95%, IoLiTec GmbH, Heilbronn, Germany) was used as the electrolyte in this cell. Varying amounts of LiTFSI (99.95%, Sigma-Aldrich) and TPFPB (95%, Sigma-Aldrich) were dissolved in PYR_{14} TFSI inside an argon atmosphere glovebox. The structure of TPFPB is shown in Figure 6.1.

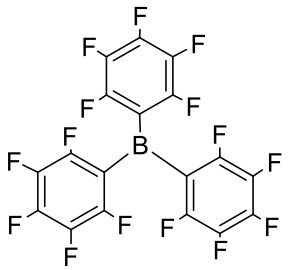

Figure 6.1: structure of tris(pentafluorophenyl)borane (TPFPB) used in these experiments.

The cell was assembled and the solution added to the cell in the glovebox and sealed against the atmosphere. The cell was removed from the glovebox and attached to the temperature controlled water bath to control the temperature of the cell. O_2 (99.99%, BOC) was passed into the cell by bubbling directly into the ionic liquid *via* a needle. The convection of the solution caused by the movement of the O_2 bubbles fully saturated the solution in under 15 minutes.

Cyclic voltammetry was done at various scan rates in solutions containing various concentrations of TPFPB and LiTFSI in PYR_{14} TFSI The cyclic voltammetry was done using an Iviumsoft Iviumstat portable potentiostat inside a Faraday cage to reduce the effect of external electrical noise on the measurements.

6.3 Results and Discussion

6.3.1 O_2 Reduction in PYR_{14} TFSI Containing LiTFSI

Cyclic voltammetry was undertaken to study the effect of LiTFSI on the electrochemical reduction of O_2 in PYR_{14} TFSI. A 0.1 M solution of LiTFSI/PYR_{14} TFSI was created in the argon atmosphere glovebox. Initial cyclic voltammetry was done to determine the purity of the ionic liquid. The ionic liquid was then oxygenated by bubbling *via* a needle for approximately 20 minutes. Cyclic voltammetry was then repeated at various scan rates to investigate the effect of LiTFSI on the electrochemical reduction of oxygen in PYR_{14} TFSI.

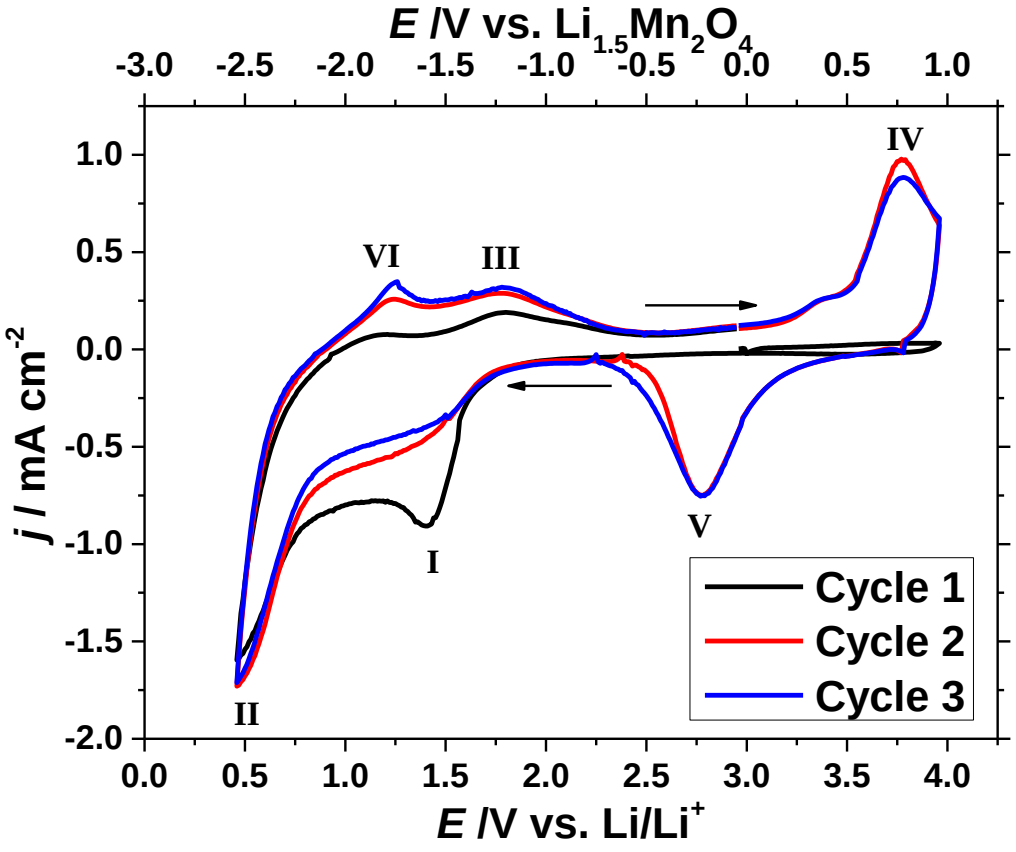

Figure 6.2: cyclic voltammograms at 1 V s^{-1} of the electrochemical reduction of O_2 in 0.1 M LiTFSI in PYR_{14} TFSI. This voltammogram was done at 298 K at a 25 µm diameter Au microdisc working electrode using a $Li_{1.5}Mn_2O_4$ counter reference electrode in a heart-shaped cell. The ionic liquid was oxygenated by bubbling with O_2 for approximately 10 minutes *via* a needle.

Figure 6.2 shows cyclic voltammograms showing the electrochemical reduction of O_2 in 0.1 M LiTFSI/PYR_{14} TFSI at a scan rate of 1 V s^{-1}. These were the initial cyclic voltammograms done immediately after the solution had been oxygenated. This figure shows considerable differences between the first cycle and the subsequent cycles. The first cycle shows a peak at 1.5 V *vs*. Li/Li^+ (peak I) followed by a small plateau, then a second peak starting at 0.75 V *vs*. Li/Li^+ (peak II). On the reverse scan there is a small peak at 1.75 V *vs*. Li/Li^+ (peak III). This is followed by a large peak at 3.75 V *vs*. Li/Li^+ at the start of the second cycle (peak IV). The second and third cycles are considerably different from the initial cycle. On the forward scan there is a peak at 2.75 V *vs*. Li/Li^+ (peak V) followed by peak I at 1.5 V *vs*. Li/Li^+, which is much smaller than the peak I on the first scan. On the reverse sweeps for the second and thirds scans there is a peak at 1.25 V *vs*. Li/Li^+ (peak IV), followed by peaks III and IV.

The first cycle and the subsequent cycles show differing voltammetry. This indicates that different processes occur on the first cycle than the subsequent cycles. On the first cycle O_2 reduction to superoxide starts to occur at peak I. Peak II occurs due to the breakdown of PYR_{14} TFSI. The superoxide then chemically reacts with the Li^+ ions present in the ionic liquid to form lithium superoxide (LiO_2). The LiO_2 is chemically unstable and reacts with other LiO_2 molecules to form Li_2O_2 and O_2.

On the reverse scan peak IV corresponds to the formation of gold oxide at high potentials. On the second and third scans, peak V corresponds to the removal of the gold oxide layer. This is confirmed by the similar peak areas of peak IV and V.

O_2 reduction does occur at peak I, however the lower current density indicates that less O_2 in being reduced to superoxide at each consecutive cycle. This is due to the passivation of Li_2O_2 on the electrode surface. This would decrease the surface area of the microelectrode, causing the current to decrease.

Because of this, after repeated cycling or chronoamperometry at a microdisc electrode in an ionic liquid containing a high Li^+ concentration, the electrode becomes fully passivated with Li_2O_2. This makes it impossible to do potential step chronoamperometry at a microdisc electrode in these solutions and gain any reliable

data that could be used to determine the values of the diffusion coefficient and solubility of oxygen in these ionic liquids.

6.3.2 The Effect of TPFPB on O_2 Reduction in PYR_{14} TFSI.

Tris(pentafluorophenyl)borane was investigated as an additive to the ionic liquid to increase the solubility of Li_2O_2. A solution of 0.1 M TPFPB in PYR_{14} TFSI was made in the argon atmosphere glovebox. Cyclic voltammetry at the Au microdisc electrode was undertaken before and after applying a vacuum to the cell for approximately 15 minutes to remove any argon, oxygen or water present in the ionic liquid. These CVs are shown in Figure 6.3.

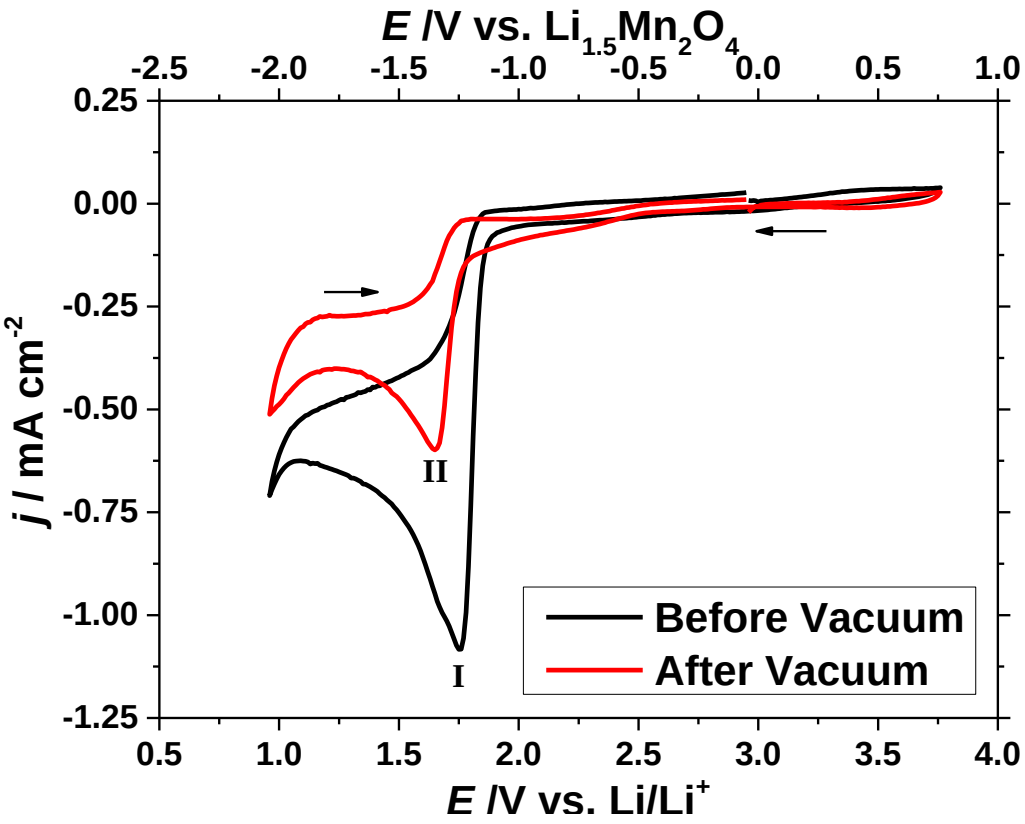

Figure 6.3: cyclic voltammograms at 100 mV s^{-1} showing the effect of a vacuum on a solution of 0.1 M TPFPB in PYR_{14} TFSI. The cyclic voltammograms were recorded at 100 mV s^{-1} at 298 K using a 25 µm diameter Au microdisc working electrode using a $Li_{1.5}Mn_2O_4$ counter reference electrode in a heart-shaped cell.

Figure 6.3 shows that TPFPB has a large peak at 1.75 V *vs.* Li/Li^+ (peak I). This may be due to the TPFPB being reduced or due to impurities in the TPFPB which are being

reduced on the forward scan. There does not seem to be any oxidation peak on the reverse scan, indicating that this reaction is irreversible.

This CV shows that peak I is larger than peak II. This indicates that the application of vacuum to the cell reduces the reduction peak current density. This may indicate that TPFPB is easily volatilised and may be removed from the ionic liquid *via* the application of vacuum or bubbling the ionic liquid with a gas. Although TPFPB has a boiling point of 126.0 °C (399.0 K) at room pressure, highly fluorinated compounds are known to be very volatile and evaporate rapidly when exposed to vacuum e.g. C_6F_{14} has a boiling point of 58.9 °C (331.9 K).[14]

O_2 was bubbled into the ionic liquid for approximately 10 minutes and CVs were undertaken at various scan rates to study the effect of TPFPB on O_2 reduction in PYR_{14}TFSI.

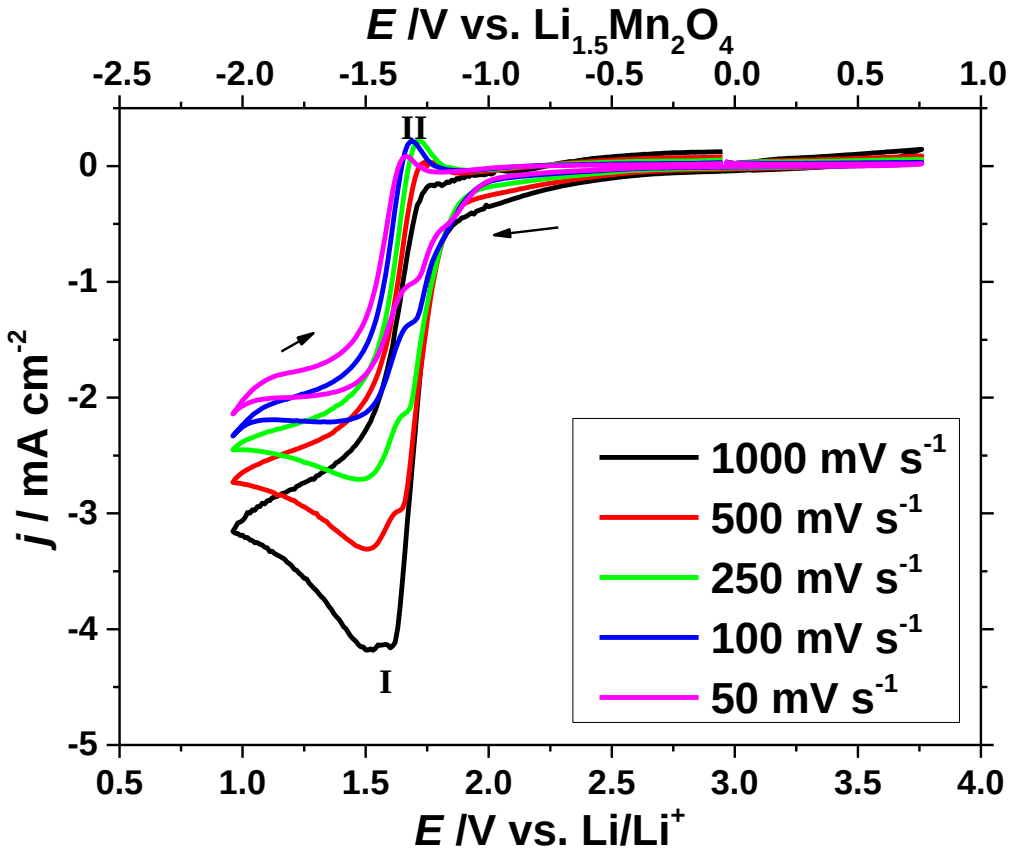

Figure 6.4: cyclic voltammograms showing O_2 reduction in a solution of 0.1 M TPFPB in PYR_{14} TFSI. The cyclic voltammograms were done at 298 K using a 25 µm diameter Au microdisc working electrode using a $Li_{1.5}Mn_2O_4$ counter reference electrode in a heart-shaped cell. The ionic liquid was oxygenated by bubbling with O_2 for approximately 10 minutes *via* a needle. Arrows show the sweep direction.

Figure 6.4 shows a reduction wave that occurs at 1.75 V *vs*. Li/Li^+ (peak I) in 0.1 M TPFPB/PYR_{14} TFSI solutions. This wave corresponds to the electron reduction of O_2 to superoxide. This figure also shows a small oxidation peak at 1.75 V *vs*. Li/Li^+ (peak II) corresponding to the oxidation of superoxide to O_2. This figure shows some similarities with the CVs of the reduction of O_2 in pure PYR_{14} TFSI. This figure shows the same wave like reduction peak for the reduction of oxygen to superoxide, as well as a small plateau at the lower scan rates. However Figure 6.4 has a much smaller superoxide oxidation peak, peak II, than was previously observed in pure PYR_{14} TFSI (Figure 2.6). This indicates that the superoxide is being removed from the solution before it can be oxidised. The superoxide may be reacting with the TPFPB in the ionic liquid. This may indicating that the TPFPB is unstable in the ionic liquid.

Potential step chronoamperometry was undertaken at the gold microdisc electrode, stepping the potential to the O_2 reduction potential at 1.5 V *vs*. Li/Li^+ for 60 seconds. The values of D_O, c_O and $D_O c_O$ in the ionic liquid were calculated using the method used by Mahon and Oldham used in Chapters 2 and 5.

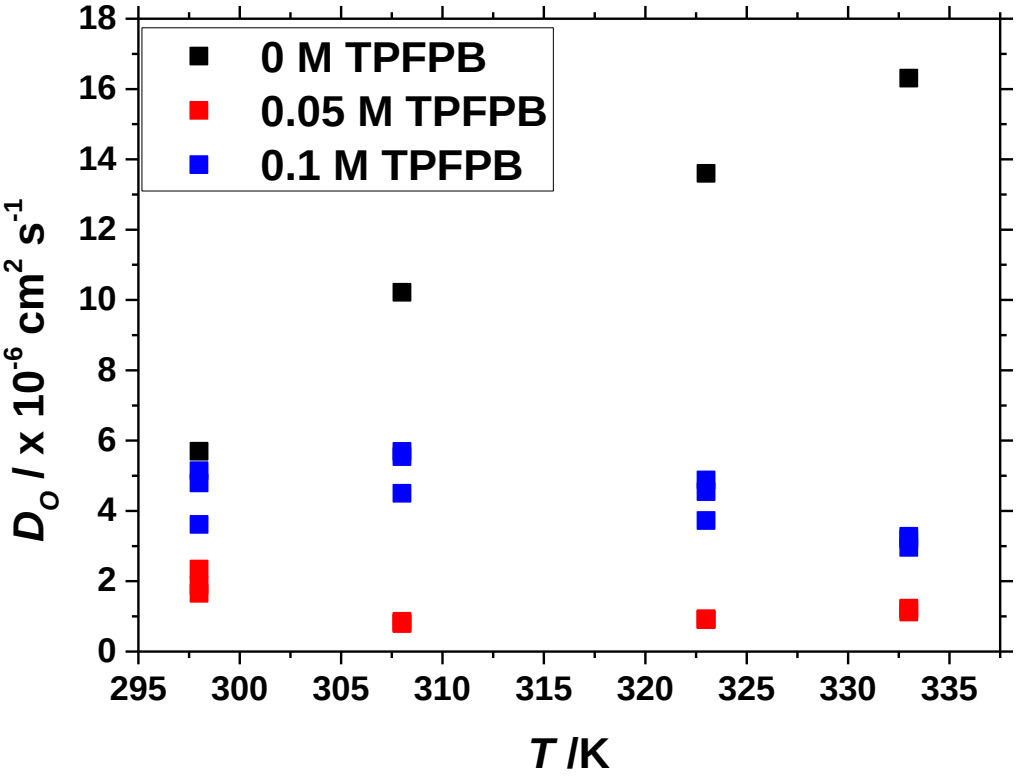

Figure 6.5: diffusion coefficients of O_2 in PYR_{14} TFSI containing various amounts of TPFPB at various temperatures. These values were calculated from potential step chronoamperometry at a 25 µm diameter gold microdisc working electrode to -1.5 V *vs*. Li/Li^+ for 60 seconds.

Figure 6.5 shows that D_O of O_2 in pure PYR_{14} TFSI increases as the temperature increases. This is expected and was confirmed in Chapter 5. Upon the addition of TPFPB the value of D_O decreases across all temperatures. This may be due to the TPFPB causing the viscosity of the ionic liquid to increase.

Figure 6.5 also shows that the value of D_O is greater for the ionic liquid containing 0.1 M TPFPB than for the solution containing 0.05 M TPFPB. This does not seem to fit the expected trend. It would be expected that the values of D_O would be smaller for the greater concentration of TPFPB. These deviations from the expected trend may be caused by TPFPB evaporating from the ionic liquid during bubbling of the ionic liquid

with O_2. The high volatility of TPFPB makes it difficult to determine its true concentration in the ionic liquid once the solution has been bubbled with O_2. Because of this, there may be more TPFPB remaining in the 0.05 M TPFPB solution than the 0.1 M TPFPB solution after bubbling with O_2, leading to a higher viscosity and lower diffusion coefficient for the 0.05 M TPFPB solution.

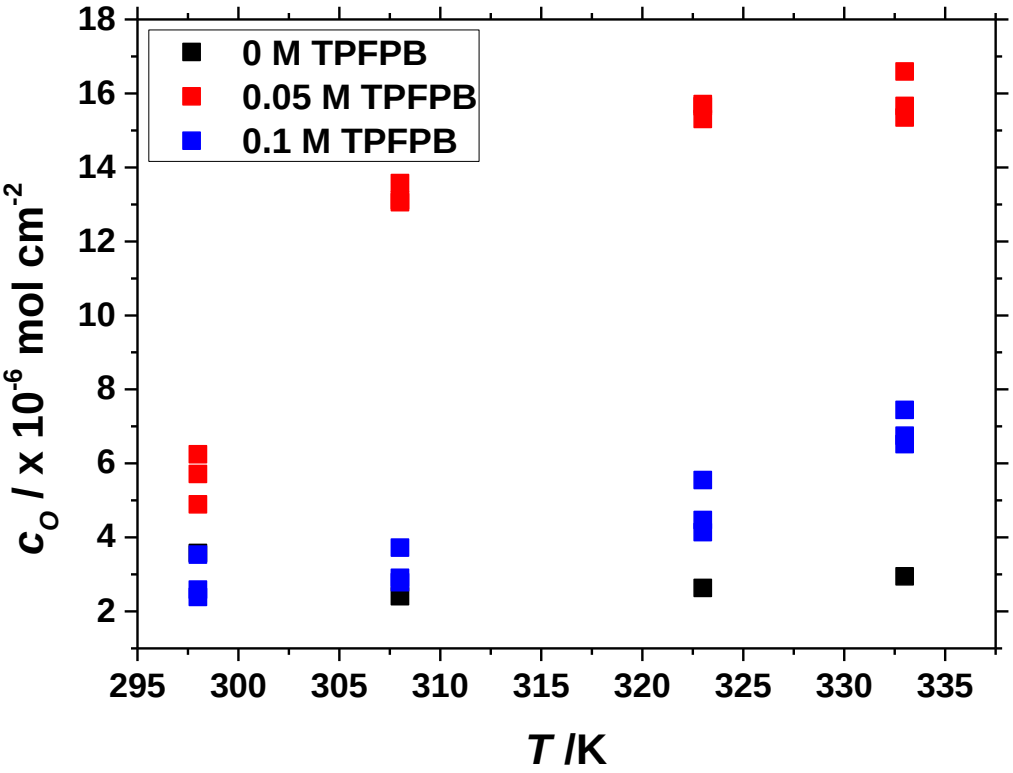

Figure 6.6: concentrations of oxygen in PYR_{14} TFSI containing various amounts of TPFPB at various temperatures. These values were calculated from potential step chronoamperometry at a 25 µm diameter gold microdisc working electrode to -1.5 V *vs*. Li/Li^+ for 60 seconds.

Figure 6.6 shows that the values of c_O increase as the concentration of TPFPB increases. There has been significant evidence that highly fluorinated compounds have high oxygen solubilities. This figure indicates that TPFPB may dramatically increase the solubility of O_2 in the ionic liquid.

In this figure the 0.05 M TPFPB solution has a higher O_2 solubility than the 0.1 M TPFPB solution. This again does not follow the expected trend. The expected trend is that the c_O value should increase as the TPFPB concentration increases. The difference may be due to differences in the actual TPFPB concentration in the solution caused by

TPFPB being removed from the solution when O_2 bubbling was undertaken. This further indicates that the true concentration of TPFPB is difficult to ascertain once the ionic liquid has been saturated with oxygen.

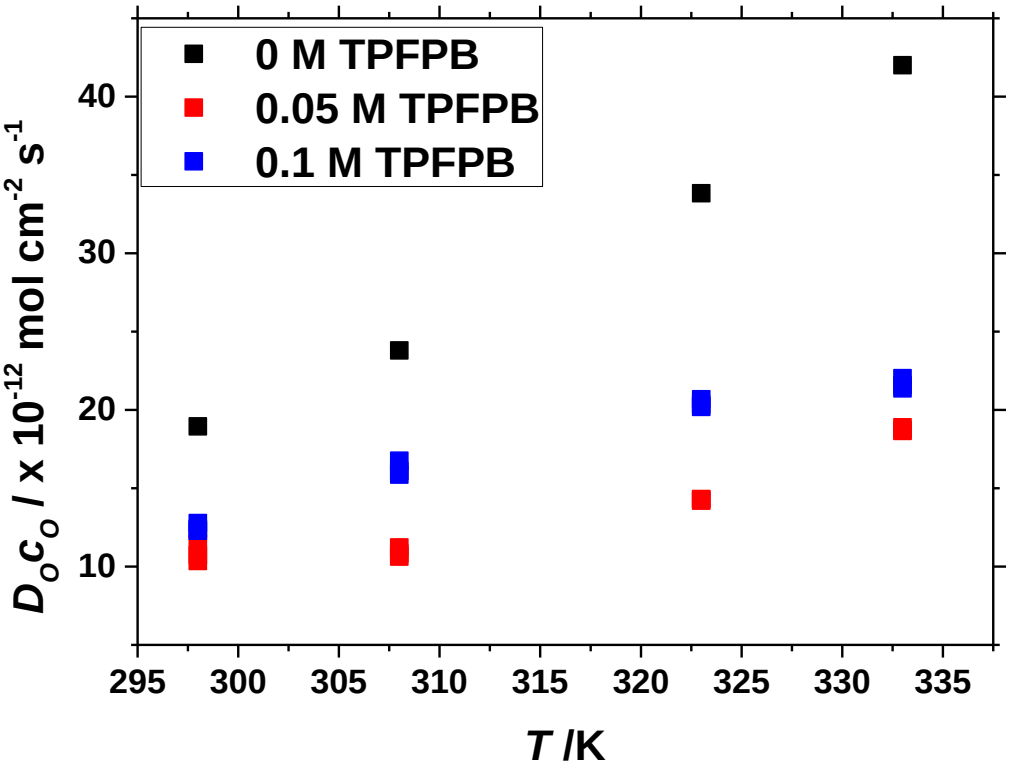

Figure 6.7: diffusion coefficient-solubility product of oxygen in PYR_{14} TFSI containing various amounts of TPFPB at various temperatures. The values are calculated from potential step chronoamperometry at a 25 µm diameter gold microdisc working electrode to -1.5 V *vs*. Li/Li^+ for 60 seconds.

Figure 6.7 shows that the $D_O c_O$ value of the ionic liquid decreases as the concentration of TPFPB increases. The higher c_O of ionic liquid containing TPFPB is counteracted by the much smaller diffusion coefficient of ionic liquid containing TPFPB.

These results indicate that TPFPB does affect the values of the D_O and c_O of O_2 in the ionic liquid. These results also indicate that TPFPB is very volatile and can be removed from the ionic liquid during bubbling with O_2.

6.3.3 The solubility of Li_2O_2 in PYR_{14} TFSI

Figure 6.2 indicates that lithium peroxide is easily formed during oxygen reduction in the presence of Li ions. The superoxide ion reacts with lithium to form lithium superoxide. The lithium superoxide then quickly reacts with other LiO_2 molecules forming Li_2O_2. This means the formation of lithium peroxide is a two-electron process.

The differences in the stability of the $O_2^{\bullet-}$ and LiO_2 can be demonstrated using a Frost diagram, Figure 6.8, plotting the product of the oxidation number and the standard potential relative to that of O_2 *vs*. the oxidation number.

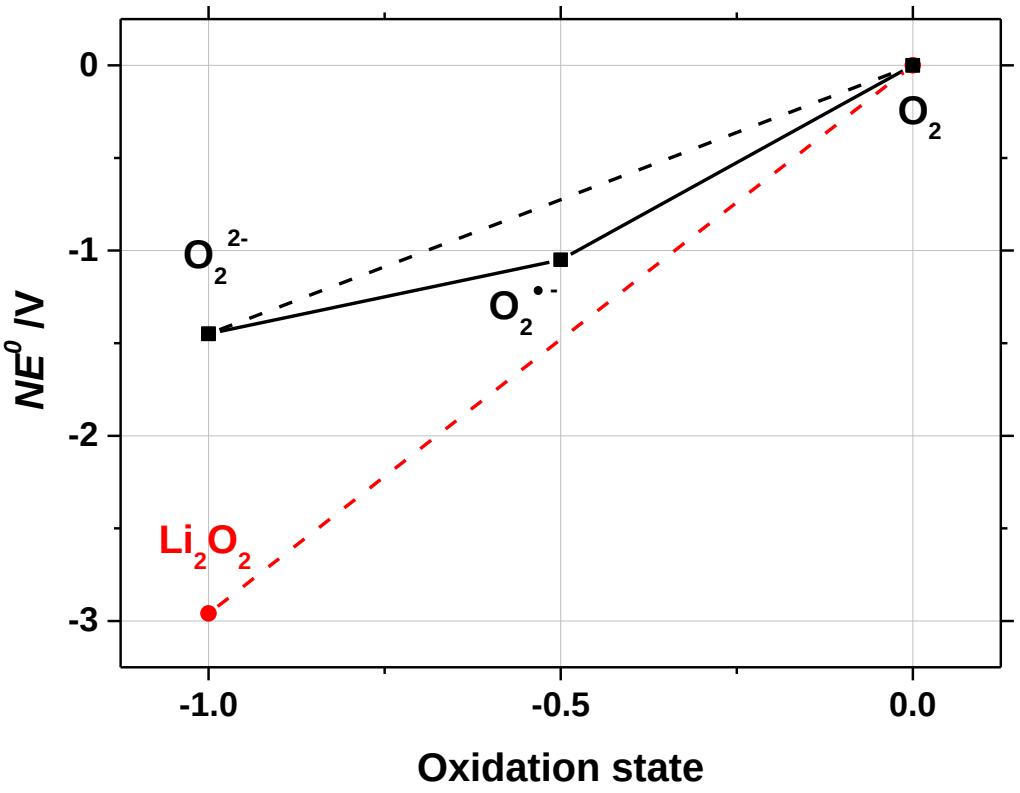

Figure 6.8: Frost diagram for O_2 reduction in the presence and absence of LiTFSI.[5] This shows the oxidation number, *N*, multiplied by E^0 *vs*. the oxidation state.[13] A version of this figure was previously published in Lodge *et al.*[13]

[5] Reprinted from Electrochimica Acta, 140, A. W. Lodge, M. J. Lacey, M. Fitt, N. Garcia-Araez and J. R. Owen, Critical appraisal on the role of catalysts for the oxygen reduction reaction in lithium-oxygen batteries, 168-173, Copyright 2014, with permission from Elsevier.

Figure 6.8 shows that for solutions not containing lithium, the value of NE^0 decreases as the oxidation state decreases. This figure also shows that the superoxide exists at a valley where it is thermodynamically stable when no lithium is present. Lithium peroxide has a much lower value of NE^0 than O_2^{2-} and is more stable than LiO_2. This indicates that LiO_2 easily disproportionate into the much more stable Li_2O_2 and O_2 due to the much lower E^0 of Li_2O_2 compared to O_2^{2-}.[13]

The difference in the value of E^0 between Li_2O_2 and O_2^{2-} is due to the Gibbs free energy change (ΔG) that occurs during the precipitation of Li_2O_2 out of the ionic liquid. This is calculated from Equation 6.1[13] where F is the Faraday constant (96485 C mol^{-1}) and E^0 is the standard potential of the couple.

$$\Delta G = -2F\left(E^0_{O_2/LiO_2} - E^0_{O_2/O_2^{\bullet-}}\right) \quad \textbf{(6.1)}$$

$$\Delta G = -2F(2.959\ V - 1.45\ V) \approx \text{-290 kJ mol}^{-1} \quad \textbf{(6.2)}$$

This Gibbs free energy value can be used to calculate the solubility constant product (K_S) for Li_2O_2 using Equation 6.3.[13]

$$K_S = \exp\left(\frac{\Delta G}{RT}\right) = \exp\left(\frac{-290\ \text{kJ mol}^{-1}}{RT}\right) \approx 10^{-51} \quad \textbf{(6.3)}$$

The value of the solubility constant product is very small, approximately 10^{-51}. This explains why lithium peroxide is extremely insoluble in the ionic liquid and easily precipitates on the surface of the working electrode.

6.3.4 The Effect of TPFPB on the Solubility of Li_2O_2 in PYR_{14} TFSI.

Various concentrations of TPFPB and 0.05 M LiTFSI were dissolved in PYR_{14} TFSI in the argon atmosphere glovebox and placed into heart-shaped cells. These ionic liquids were bubbled with O_2 and cyclic voltammetry was done at various scan rates to determine the effect of TPFPB on the build-up of Li_2O_2 at the working electrode. These results are shown in Figure 6.9.

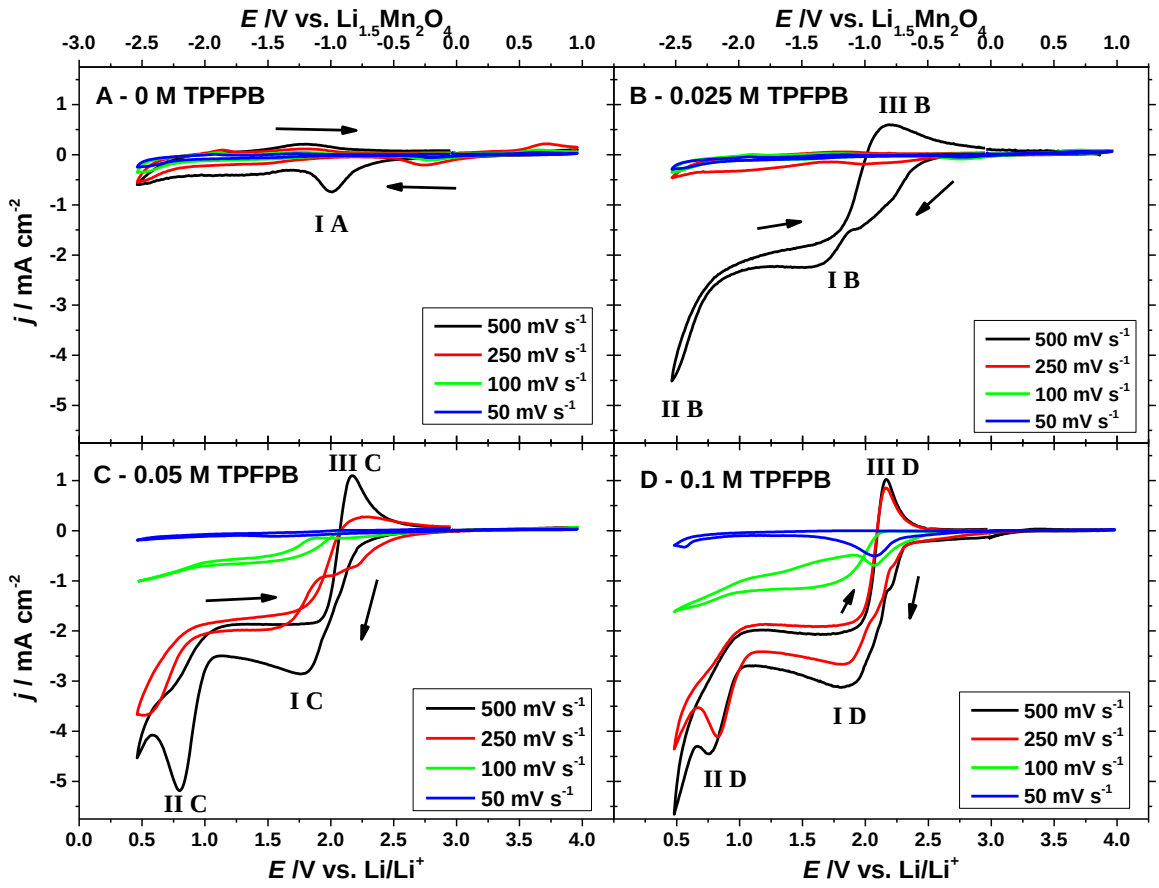

Figure 6.9: cyclic voltammograms at various scan rates showing O_2 reduction in PYR_{14} TFSI containing 0.05 M LiTFSI and varying concentrations of TPFPB. All the experiments were done at 298 K using a 25 µm diameter gold microdisc working electrode and a heart-shaped cell. A = 0 M TPFPB, 0.05 M LiTFSI in PYR_{14} TFSI. B = 0.025 M TPFPB, 0.05 M LiTFSI in PYR_{14} TFSI, C = 0.05 M TPFPB 0.05 M LiTFSI in PYR_{14} TFSI, D = 0.1 M TPFPB, 0.05 M LiTFSI in PYR_{14} TFSI.

Figure 6.9 shows the oxygen reduction occurring in solutions of PYR_{14} TFSI containing 0.05 M LiTFSI and increasing concentrations of TPFPB. Graph A shows a solution containing no TPFPB. The cyclic voltammograms show similar behaviour to Figure 6.2, with only one large O_2 reduction peak during the first cycle at 500 mV s^{-1}, peak I A, and with the subsequent lower scan rate voltammograms showing the oxidation and reduction of Li_2O_2. The current density obtained by these voltammograms is approximately -0.5 mA cm^{-2}.

Graph B shows the cyclic voltammograms for O_2 reduction in a solution containing 0.025 M TPFPB and 0.05 M LiTFSI. This graph shows that the first CV done at the highest scan rate of 500 mV s^{-1} shows wave-like behaviour similar to the reduction of

O_2 in pure PYR_{14} TFSI. This CV shows O_2 reduction to superoxide (peak I B), followed by a plateau at 1.5 V *vs*. Li/Li^+. A second peak at 1.0 V *vs*. Li/Li^+ (peak II B) corresponding to the reduction of superoxide to peroxide. On the reverse scan there is a superoxide oxidation peak (peak III B) at 2.25 V *vs*. Li/Li^+. However at the lower scan rates, 250 to 50 mV s^{-1}, the voltammetry shows behaviour similar to that in graph A, showing the reduction of Li_2O_2. The current density at the higher scan rates is as large as -4 mA cm^{-2}. However at the lower scan rates the current density decreases to approximately -0.5 mA cm^{-2}. This indicates that the electrode has passivated with Li_2O_2 at the lower scan rates.

Graph C shows the CVs for O_2 reduction in a solution containing 0.05 M TPFPB. The higher scan rate CVs at 500 and 250 mV s^{-1} show behaviour similar to the reduction of O_2 in pure ionic liquid with large wave like behaviour (peak I C) followed by a stability plateau. On the reverse scan there is a superoxide oxidation peak (peak III C). The highest peak current reached during this voltammogram is -5.5 mA cm^{-2}. However the CV at 50 mV s^{-1} shows Li_2O_2 behaviour with a greatly decreased current density of -0.25 mA cm^{-2}. The CV at 100 mV s^{-1} shows intermediate behaviour between the two regimes. This CV also shows a maximum current density of -1.0 mA cm^{-2}. This indicates that the TPFPB is inhibiting the passivation of Li_2O_2 on the electrode at the higher scan rates, but not at the lower scan rates.

Graph D shows the CVs for O_2 reduction in a solution containing 0.1 M TPFPB. Again this graph shows that the higher scan rates at 500 and 250 mV s^{-1} show O_2 reduction behaviour and maximum current densities of -6 mA cm^{-2}. The lowest scan rate at 50 mV s^{-1} shows Li_2O_2 passivation behaviour and a maximum current density of -1.0 mA cm^{-2}, with the 100 mV s^{-1} showing similar intermediate behaviour to Graph C.

These results all indicate that as the TPFPB concentration is increased, the scan rate at which pure O_2 reduction is seen is decreased and the current density of the CVs increases. This indicates that the TPFPB does increase the solubility of the lithium peroxide. At the higher scan rates the sweep remains in the lithium peroxide forming potential region for a small amount of time, forming only a small amount of Li_2O_2 which is easily solubilised by the TPFPB. However at the lower scan rates the CV remains in the Li_2O_2 forming region for longer causing production of more Li_2O_2. Not

all of this Li_2O_2 can be solubilised by the TPFPB to prevent passivation of the microelectrode.

The diffusion coefficient of TPFPB is expected to be smaller than the diffusion coefficient of O_2 in PYR_{14} TFSI, due to the much greater size of the TPFPB molecule. This would limit the amount of TPFPB that is able to move towards the working electrode to solubilise any Li_2O_2 formed at that location, requiring an extremely high TPFPB concentration for O_2-like voltammetry to be seen at low scan rates or during potential step chronoamperometry. The amount of TPFPB required to do this would increase the viscosity of the ionic liquid dramatically and make it impossible to gain an accurate value of D_O in the ionic liquid containing LiTFSI *via* potential step chronoamperometry. Because of this no further investigation was undertaken into the use of TPFPB.

6.4 Conclusions

These results showed that the reduction of O_2 in LiTFSI-containing ionic liquids is hampered by the formation of lithium oxides and peroxides which deposit on the working electrode and passivate the electrode. The solubility of the lithium peroxides can be enhanced through the addition of tris(pentafluorophenyl)borane to the ionic liquid. However it has been found that the TPFPB increases the viscosity of the ionic liquid dramatically. It is also volatile, as bubbling the ionic liquid with O_2 can decrease its concentration. The addition of TPFPB to PYR_{14} TFSI containing LiTFSI does allow O_2 reduction to occur at high scan rates. However passivation of the electrode still occurs at lower scan rates. This indicates that the use of potential step chronoamperometry to determine D_O and c_O in the ionic liquid containing LiTFSI is unreliable. The concentration of TPFPB required for successful chronoamperometry in a high lithium concentration solution would severely increase the viscosity of the ionic liquid and may be above the maximum solubility of TPFPB in the ionic liquid. However further research into the use of TPFPB may prove useful for other lithium-air applications in the future.

One of the aims of the experiments undertaken in this chapter was to understand the electrochemical reduction of oxygen in PYR_{14} TFSI containing various concentrations of LiTFSI. This objective has been achieved. Another aim was to determine the values of D_O, c_O and $D_O c_O$ in PYR_{14} TFSI containing various concentrations of LiTFSI. This aim was unable to be completed due to the fouling of the microelectrode with Li_2O_2, even with high concentrations of TPFPB.

6.5 References

[1] M. J. Monteiro, F. F. C. Bazito, L. J. A. Siqueira, M. C. C. Ribeiro, R. M. Torresi, *J. Phys. Chem. B* **2008**, *112*, 2102–2109.

[2] F. De Giorgio, F. Soavi, M. Mastragostino, *Electrochem. Commun.* **2011**, *13*, 1090–1093.

[3] N.-S. Choi, G. Jeong, B. Koo, Y.-W. Lee, K. T. Lee, *J. Power Sources* **2013**, *225*, 95–100.

[4] D. Shanmukaraj, S. Grugeon, G. Gachot, S. Laruelle, D. Mathiron, J.-M. Tarascon, M. Armand, *J. Am. Chem. Soc.* **2010**, *132*, 3055–3062.

[5] B. Xie, H. S. Lee, H. Li, X. Q. Yang, J. McBreen, L. Q. Chen, *Electrochem. Commun.* **2008**, *10*, 1195–1197.

[6] L. J. Hardwick, P. G. Bruce, *Curr. Opin. Solid State Mater. Sci.* **2012**, *16*, 178–185.

[7] L. Ju, J. F. Lee, W. B. Armiger, *Biotechnol. Prog.* **1991**, *7*, 323–329.

[8] C. A. Fraker, A. J. Mendez, C. L. Stabler, *J. Phys. Chem. B* **2011**, *115*, 10547–10552.

[9] A. M. A. Dias, M. G. Freire, J. A. P. Coutinho, I. M. Marrucho, *Fluid Phase Equilib.* **2004**, *222-223*, 325–330.

[10] K. C. Lowe, *J. Fluor. Chem.* **2001**, *109*, 59–65.

[11] R. E. Barlag, H. B. Halsall, W. R. Heineman, *Electroanalysis* **2007**, *19*, 1139–1144.

[12] R. Ferreira, M. Blesic, J. Trindade, I. Marrucho, J. N. C. Lopes, L. P. N. Rebelo, *Green Chem.* **2008**, *10*, 918–928.

[13] A. W. Lodge, M. J. Lacey, M. Fitt, N. Garcia-Araez, J. R. Owen, *Electrochim. Acta* **2014**, *140*, 168–173.

[14] M. G. Freire, A. G. M. Ferreira, I. M. A. Fonseca, I. M. Marrucho, J. A. P. Coutinho, *J. Chem. Eng. Data* **2008**, *53*, 538–542.

7. Investigating O_2 in PYR_{14} TFSI Using Non-Electrochemical Methods

The experiments in this chapter will investigate the determination of the diffusion coefficient and solubility of O_2 in PYR_{14} TFSI containing LiTFSI and ethyl viologen ditriflate using non-electrochemical methods such as pressure drop measurements and one-dimensional diffusion experiment.

7.1 Introduction

As was discussed in Chapter 6, the determination of the diffusion coefficient (D_O) and solubility (c_O) of O_2 in ionic liquids containing significant concentrations of lithium ions *via* electrochemical methods was unsuccessful, due to the fouling of the microelectrode surface by lithium peroxide (Li_2O_2). Because of this, alternative methods of determining c_O and D_O must be investigated.

One potential technique which could be used to solve this problem was investigated by Camper *et al.*[1] This method uses a known volume of ionic liquid in a sealed vessel of known volume. A gas such as O_2 is passed into the headspace of the vessel and is allowed to diffuse into the ionic liquid over a period of time. The pressure inside the vessel is measured, and the drop in pressure caused by O_2 diffusing into the ionic liquid is used to calculate the diffusion coefficient and the solubility of oxygen in the ionic liquid.

Other groups such as Husson-Borg *et al.*[2] have used methods to determine the Henry constants of several gases in various ionic liquids using the total pressure drop in a sealed cell.[3–7] This technique could also be used to study the effect of an oxygen redox shuttle compound on the rate of oxygen absorption into the ionic liquid. A redox shuttle compound, such as ethyl viologen ditriflate ($EtV(OTf)_2$) could be used to enhance the rate of diffusion of O_2 into the ionic liquid.[8] As was previously introduced in Chapter 1, a redox shuttle compound $O_2^{\bullet-}$ is an aromatic compound which is reversibly oxidised and reduced. The $EtV^{\bullet+}$ can be easily oxidised by O_2 to form the EtV^{2+} ion and superoxide as shown in Equation 7.1. If there is a source of lithium ions present in the solution, the superoxide will react with it to form lithium peroxide.

$$EtV^{\bullet+} + O_2 \leftrightharpoons EtV^{2+} + O_2^{\bullet-} \qquad \textbf{(7.1)}$$

The blue $EtV^{\bullet+}$ ion will reduce O_2 to O_2^- at the air interface to form the colourless EtV^{2+} ion. This ion would travel through the ionic liquid to the cathode where it will be reduced back to $EtV^{\bullet+}$ before it travels back to the air interface. This would separate the oxygen reduction and the electron transfer steps as well as prevent the build-up of lithium peroxide at the cathode. This is shown in Figure 7.1. If the EtV^{2+} has a greater

diffusion coefficient and solubility than O_2, it may transfer electrons from the cathode faster than O_2 would, giving a greater battery power.

Ionic liquids containing reduced viologen (blue) were also placed in the sealed vessel and the diffusion coefficient and solubility of oxygen in these solutions was also determined.

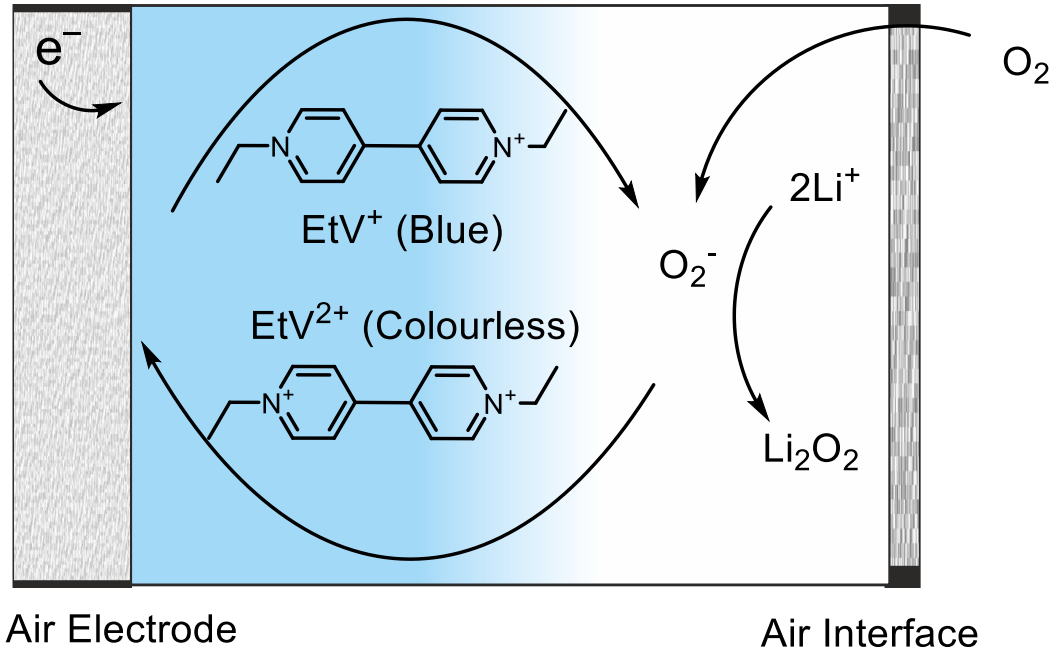

Figure 7.1: schematic of how a redox shuttle compound would work in a Li-O_2 battery.

Another technique was also used to determine the diffusion coefficient of O_2 in ionic liquid using reduced viologen as an indicator. A thin film of ionic liquid containing $EtV^{\bullet+}$ is placed between two glass microscope slides. One end of this film is exposed to pure O_2 and the O_2 diffusion along the film is observed by the decolourisation of the $EtV^{\bullet+}$. The rate of movement of this front is used to determine the diffusion coefficient of O_2 in the ionic liquid.

The aims of the experiments undertaken in this were to study the effect of ethyl viologen on the diffusion of oxygen into PYR_{14} TFSI. The aims of the experiments also included to determine the values of D_O, c_O and D_Oc_O of O_2 in PYR_{14} TFSI containing various amounts of LiTFSI using a non-electrochemical pressure drop technique as an alternative to the electrochemical methods used in previous chapters. Another aim is to determine the diffusion coefficient of O_2 by observing the decolourisation of $EtV^{\bullet+}$caused by O_2 progressing through a thin layer of PYR_{14} TFSI.

7.2 Experimental

7.2.1 Experiments Measuring the Pressure Drop in a Sealed Vessel

A sealed pressure measurement rig was built from oxygen safe, stainless steel piping. This rig consisted of two pressure and temperature sensors, a vacuum pump and a sealed pressure measurement vessel. The vessel consisted of a custom made glass vial attached to part of a commercial lithium-air test cell (ECC-Air test cell, EL-Cell GmbH, Hamburg, Germany) using a commercially available air-tight silicone sealant. A stirrer bar was placed in this cell and it was connected to the measurement rig using polyether ether ketone (PEEK) tubing. The entire setup was pressure tight. The internal volume of the pressure measurement vessel was measured using water displacement, while the volume of the rig was measured using pressure differences. The volume of the pressure measurement vessel was found to be 6.8 cm^3. A photo of the pressure measurement vessel is shown in Figure 7.2 while a schematic of the pressure measurement rig is given in Figure 7.3.

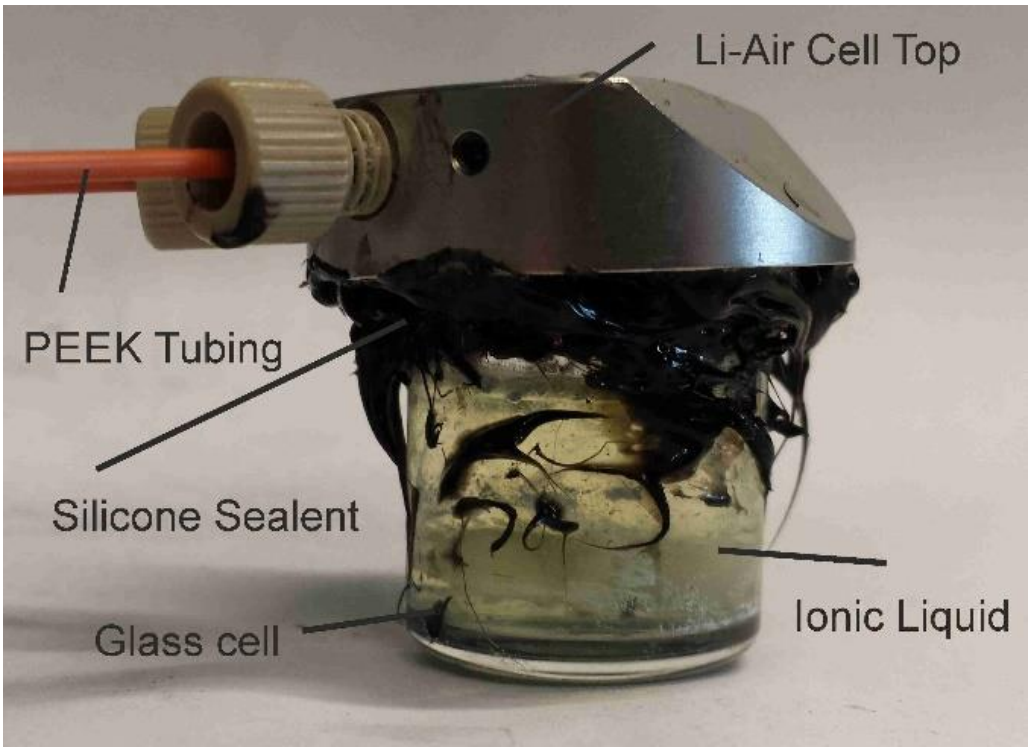

Figure 7.2: photo of the pressure measurement vessel used for these experiments.

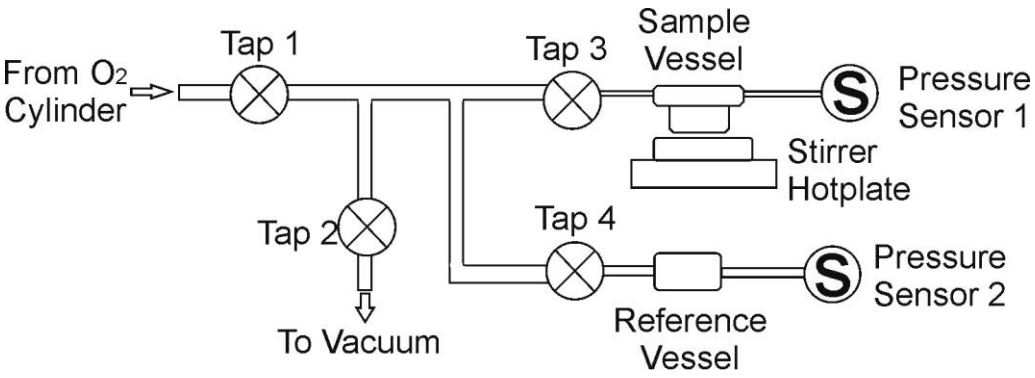

Figure 7.3: schematic of the pressure drop experiment rig used for these experiments.

The pressure measurement vessel was assembled outside the glovebox by placing a stirrer bar into the glass vial and by attaching the top of the cell using silicone sealant. Once the sealant was dry the sample chamber was placed in the argon glovebox.

LiTFSI (99.95%, Aldrich) was dissolved in PYR_{14} TFSI (99%, IoLiTec GmbH, Heilbronn, Germany) solutions of 0.05 M and 0.1 M LiTFSI. Ethyl viologen ditriflate was made by addition of stoichiometric amount of Li $(OTf)_2$ (99.995%, Sigma-Aldrich) to EtV I_2 (99%, Sigma-Aldrich). Lithiated lithium titanate was synthesised by adding n-butyl lithium (1.6 M in hexane, Aldrich) to $Li_4Ti_5O_{12}$ (>99%, sigma-Aldrich) to form $Li_{6.8}Ti_5O_{12}$.

For solutions containing ethyl viologen ditriflate, the correct amount of EtV $(OTf)_2$ was dissolved in the solution. The EtV^{2+} was then reduced to $EtV^{\bullet+}$ by the addition of a stoichiometric amount of lithiated lithium titanate ($Li_{6.8}Ti_5O_{12}$), as shown in Equation 7.2.

$$2.8\ EtV^{2+} + Li_{6.8}Ti_5O_{12} \longrightarrow 2.8\ EtV^{\bullet+} + Li_4Ti_5O_{12} + 2.8\ Li^+ \qquad \textbf{(7.2)}$$

The solution was placed into the sample vessel by being injected through the oxygen inlet *via* a needle. 4 cm^3 of ionic liquid was used in the vessel giving a headspace above the ionic liquid of 2.8 cm^3. Once the desired amount of ionic liquid had been added to the sample vessel, the inlets to the sample vessel were sealed and it was removed from the glovebox and attached to the pressure measurement apparatus.

Prior to the experiment, a vacuum was applied to the rig and the ionic liquid was stirred for approximately 3-4 hours to remove any argon, nitrogen, oxygen or water present in the ionic liquid which could affect the diffusion coefficient of oxygen. Taps 2, 3 and 4

were opened while Tap 1 remained closed. The pressure in the sample vessel and the rig was recorded as being at below 0.01 bar. When the experiment started, the stirring of the ionic liquid was stopped and Taps 2 and 3 were closed before opening Tap 1 and allowing pure oxygen (99.95%, BOC) into the apparatus to a pressure of approximately 1.5 bar. Tap 1 was then closed, leaving a fixed amount of O_2 in the apparatus. Tap 3 was then opened, allowing O_2 into the sample chamber to a pressure of approximately 1.45 bar, before being closed. The amount of O_2 that passed in the sample chamber was calculated from the increase in the pressure at Sensor 1 and the decrease in pressure at Sensor 2. The ionic liquid was held as a stagnant solution for the first 30 minutes of the experiment to allow O_2 to naturally diffuse into the ionic liquid while the decrease in pressure in the sample vessel was measured. The rate of pressure decrease was used to calculate the D_O in PYR_{14} TFSI. After a period of approximately 30 minutes natural convection may have occurred which would have influenced the results obtained by increasing the movement of O_2 through the solution at a faster rate. Because of this the ionic liquid was stirred to rapidly saturate it with O_2. The total pressure drop was measured to calculate c_O in the ionic liquid. A sample of a pressure trace of a typical experiment is shown in Figure 7.4.

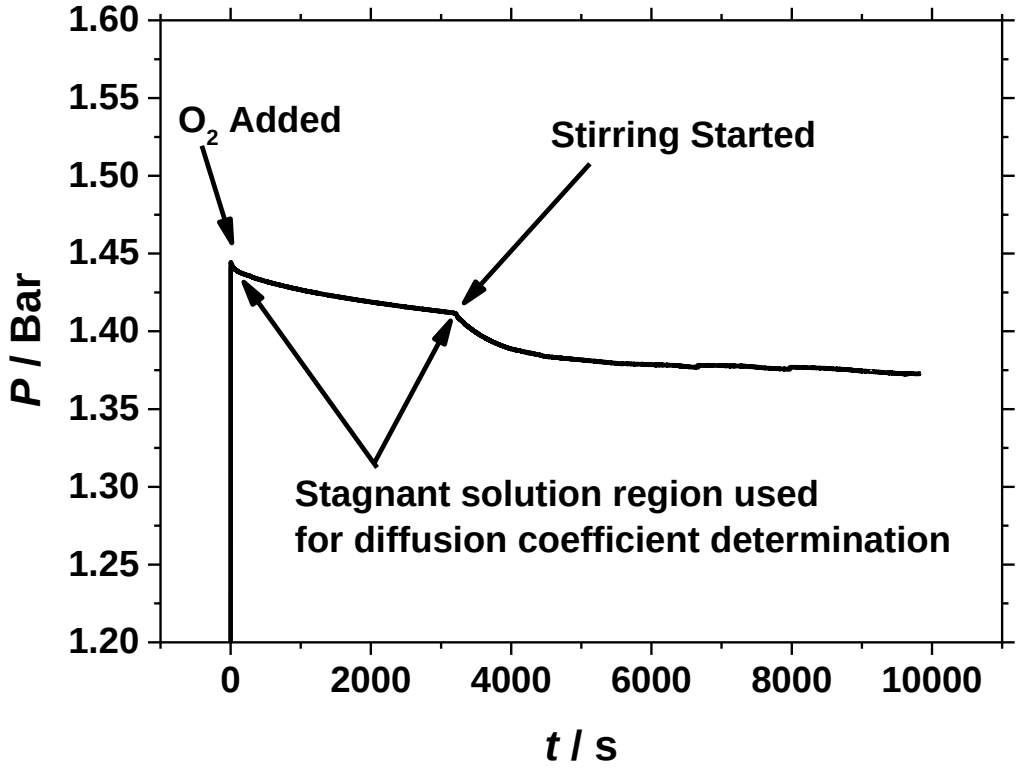

Figure 7.4: sample graph showing the pressure drop measurement over the timescale of a typical pressure drop experiment.

Figure 7.4 shows the pressure trace as a function of time. At $t = 0$, O_2 was added to the pressure cell to 1.45 Bar. The pressure then decreased as the cell was left stagnant as O_2 diffused naturally into the ionic liquid. At 3000 seconds the solution was stirred, increasing the movement of the solution and increasing the rate of diffusion into ionic liquid and decreasing the pressure.

7.2.2 Calculating the Diffusion Coefficient and Solubility of O_2 in Ionic Liquids from Pressure Data

The change in the amount of O_2 in the headspace above the ionic liquid, and therefore the amount of oxygen dissolved in the ionic liquid, is related to the pressure of the oxygen in the headspace by the ideal gas law (Equation 7.3) where P is the pressure in kPa, V is the volume of the headspace in cm^3, n is the number of moles of O_2 in mol, R is the ideal gas constant, 8314 m^3 kPa K^{-1} mol^{-1} and T is the temperature in K.

$$\Delta PV = \Delta nRT \qquad \textbf{(7.3)}$$

After the initial addition of oxygen, the ionic liquid was left unstirred over a period of time to allow the oxygen to diffuse into the ionic liquid. The decrease in pressure over this timescale was recorded. Camper *et al.*[1] determined that the total amount of oxygen that had diffused into the ionic liquid at a certain time (M_t) in mol cm^{-2} was related to the diffusion coefficient (D) in cm^2 s^{-1} of O_2 that diffused into the ionic liquid. This is shown in Equation 7.4 where t is the time in s and $c_{x=t=0}$ is the concentration at the ionic liquid interface at t = 0 in mol cm^{-3}.

$$M_t = 2c_{x=t=0}\left(\frac{Dt}{\pi}\right)^{1/2} \quad \textbf{(7.4)}$$

In this experiment the total amount of oxygen that had diffused into the ionic liquid could be calculated by the change in pressure since the start of the experiment. This is shown in Equation 7.5 where A is the surface area of the ionic liquid interface in cm^2.

$$M_t = \frac{\Delta PV}{RTA} \quad \textbf{(7.5)}$$

By rearranging Equation 7.5 and combining it with Equation 7.4 we get Equation 7.6

$$\Delta P = \frac{RTAM_t}{V} = \frac{RTA}{V}2c_{t=x=o}\left(\frac{Dt}{\pi}\right)^{1/2} \quad \textbf{(7.6)}$$

This equation means that the diffusion coefficient can be calculated by plotting the change in pressure (ΔP) against $t^{1/2}$ to give a straight line plot as shown in Figure 7.5. The slope of this straight lined plot, m in bar s$^{-1/2}$ or kPa s$^{-1/2}$, is related to the diffusion coefficient as shown in Equation 7.7.

$$m = \frac{RTA}{V}2c_{t=x=o}\left(\frac{D}{\pi}\right)^{1/2} \quad \textbf{(7.7)}$$

Rearranging gives:

$$D = \frac{mV}{RTA}\frac{\pi^{1/2}}{2c_{t=x=0}} \quad \textbf{(7.8)}$$

Using this method, the diffusion coefficient of oxygen in the ionic liquid was found using only the slope of a plot of the change in pressure inside the cell against $t^{1/2}$ as shown in Figure 7.5.

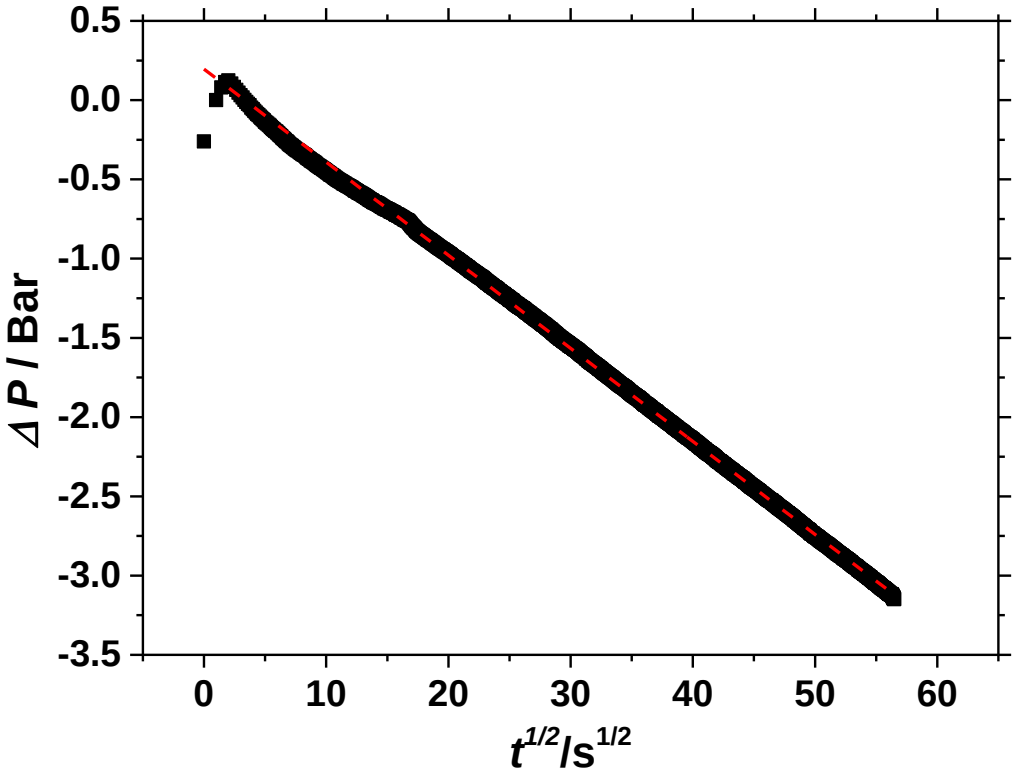

Figure 7.5: graph showing the change in pressure against the $t^{1/2}$ for the diffusion limited section of the pressure drop experiment. The dotted red line is the slope used in Equation 7.7.

The solubility of O_2 in the ionic liquid was found using the total pressure drop when the pressure in the cell has decreased to a slow rate, using the ideal gas law. The total solubility of the ionic liquid can also be used to find the Henrys law constant for O_2 in the ionic liquid. This constant is related to the pressure of the gas above the surface of a liquid and the concentration of the gas dissolved in the liquid. Henrys law only applies to dilute solutions[9] and the values of Henrys law constant also change with temperature[9]. Henry's law is shown in Equation 7.9 where k_H is the Henrys law constant in kPa mol^{-1} cm^3, P is the pressure of O_2 above the ionic liquid in kPa and c is the concentration of O_2 dissolved in the ionic liquid in mol cm^{-3}. k_H can also have other units such as Bar, or Pa per unit of volume depending upon the units of P and c used.

$$k_H = \frac{P}{c} \qquad \textbf{(7.9)}$$

7.2.3 Experiments Using One-Dimensional Diffusion

The experiments measuring the movement of oxygen through a thin film of ionic liquid used low concentrations of reduced ethyl viologen ditriflate, 5 and 10 mM dissolved in ionic liquids containing various concentrations of LiTFSI. These solutions were created in an argon atmosphere glovebox in an identical manner to those used for the pressure drop experiments as previously described.

The thin film of the ionic liquid was created by taking two microscope slides and sandwiching a thin layer of parafilm between them. The parafilm had a small section removed in the centre. The slides were glued together, leaving a void at the edge where the section of parafilm was removed. The void between the two microscope slides was filled with the ionic liquid in the argon atmosphere glovebox. A scale accurate to a range of 0.1 mm was attached to the top of the slide to enable accurate measurement of the oxygen through the ionic liquid. The slides were placed in a modified, airtight, transparent centrifuge tube with a gas inlet and outlet attached to the lid of the tube. The tube was then removed from the glovebox and placed under a microscope (Olympus BH 2) and the gas inlets were attached to an oxygen cylinder and a pressure sensor. A vacuum was first applied to the tube for approximately two minutes to remove the argon present in the centrifuge tube. Oxygen was then passed into the centrifuge tube and the tube was sealed.

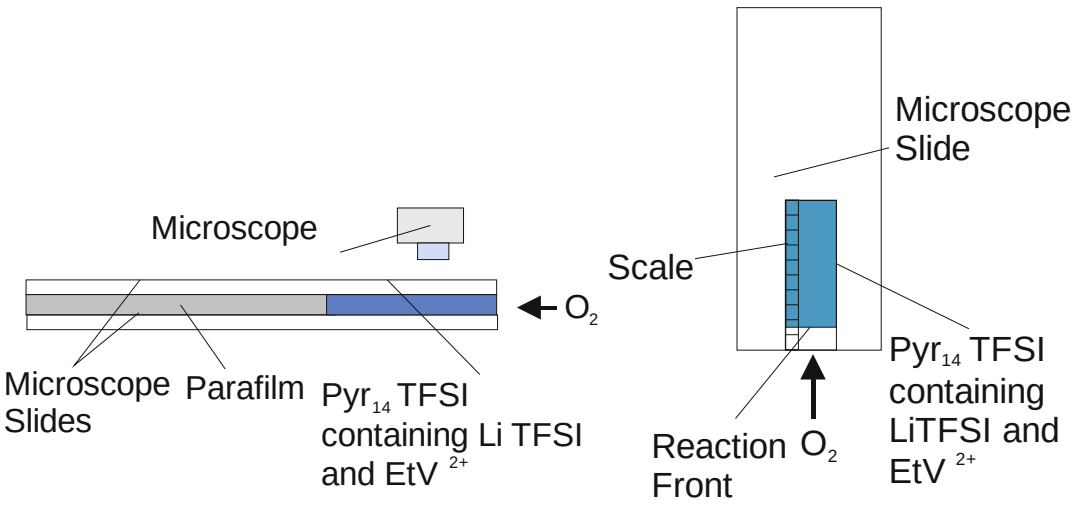

Figure 7.6: schematic of the slide setup used for the one-dimensional diffusion experiments.

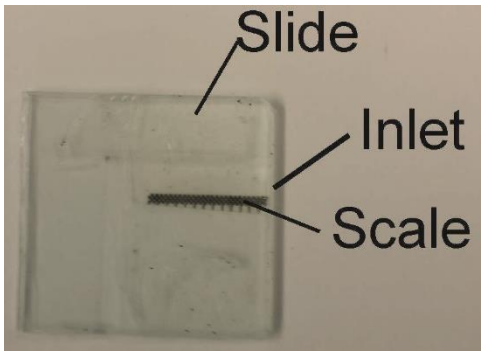

Figure 7.7: photo of one of the slides used for the one-dimensional diffusion experiments.

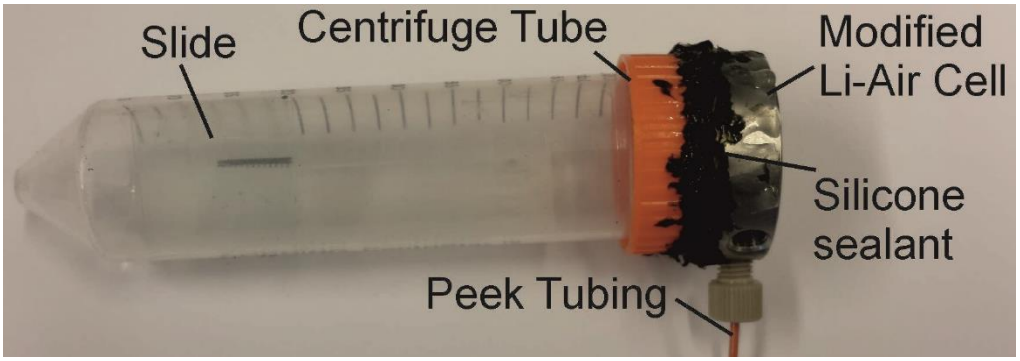

Figure 7.8: photo of the slide enclosed in the modified centrifuge tube used for the one-dimensional diffusion experiments.

O_2 diffused into the ionic liquid between the microscope slides *via* the inlet between the slides. As O_2 diffused through the ionic liquid, it oxidised the $EtV^{\bullet+}$ present in the ionic liquid, causing a colour change from blue to white. This colour change was easily observed through the microscope as a reaction front. The distance and speed of the reaction front as it moved away from the ionic liquid/oxygen interface was measured and was used to calculate the diffusion coefficient of oxygen in the ionic liquid.

7.3 Pressure Drop Experiments Results and Discussions

The pressure drop experiments were done both with and without ethyl viologen ditriflate dissolved in the ionic liquid. The values of the diffusion coefficient were determined through the method previously described, using the rate of pressure drop in the cell, while the total amount of oxygen dissolved in the ionic liquid was measured using the total pressure drop at long times.

7.3.1 Ionic Liquid Containing No Ethyl Viologen Ditriflate

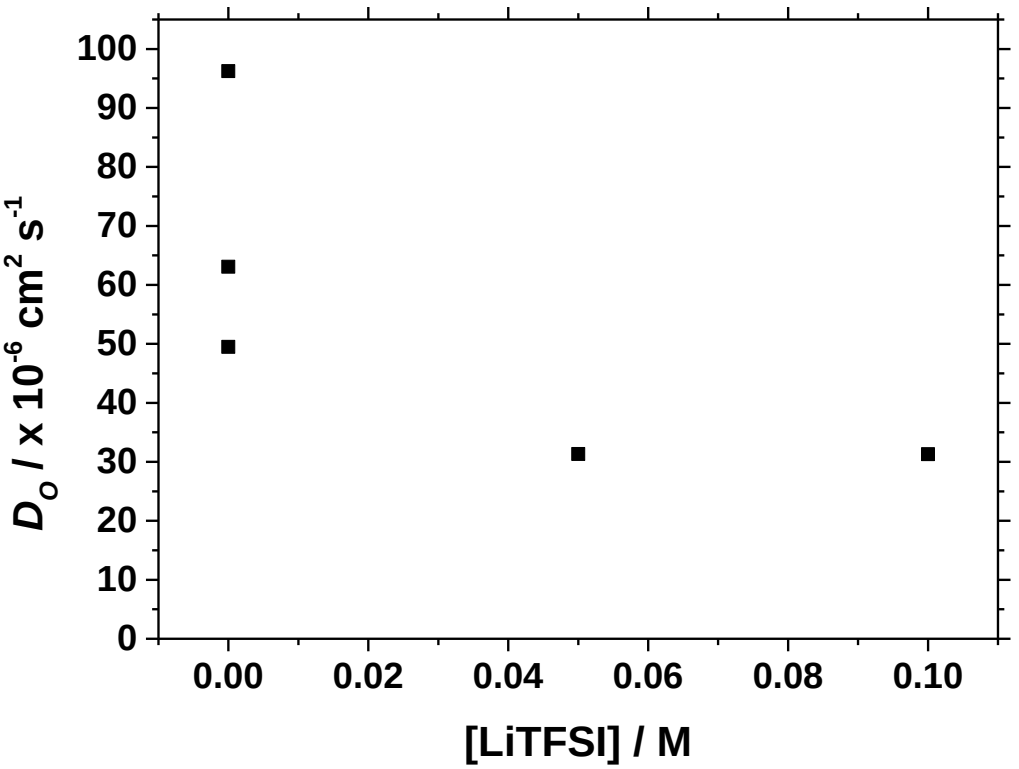

Figure 7.9: diffusion coefficients of O_2 in PYR_{14} TFSI *vs*. LiTFSI concentration for five experiments with PYR_{14} TFSI solutions containing no EtV $(OTf)_2$ and various amounts of LiTFSI. These values were determined using the pressure drop in a stagnant solution at room temperature. The diffusion coefficients were calculated using Equation 7.8. The cell was vacuumed for approximately 3-4 hours before the experiment. The O_2 was passed into the cell and the ionic liquid held stagnant for 30 minutes to determine these values.

Figure 7.9 shows the diffusion coefficients of O_2 as a function of the concentration of LiTFSI dissolved in the ionic liquid. This shows that D_O decreases as the LiTFSI concentration increases. This is probably due to the viscosity increasing as the LiTFSI

concentration increases. It has been seen that the viscosity of the ionic liquid increases as the concentration of LiTFSI in the ionic liquid is increased. The Stokes-Einstein equation states that the diffusion coefficient of a substance decreases as the viscosity increases. Figure 7.9 shows a significant variability in the values obtained for pure PYR_{14} TFSI. This may be due to differences in the temperature of the ionic liquid or due to not all of the argon being removed from the ionic liquid before the O_2 was passed into the cell.

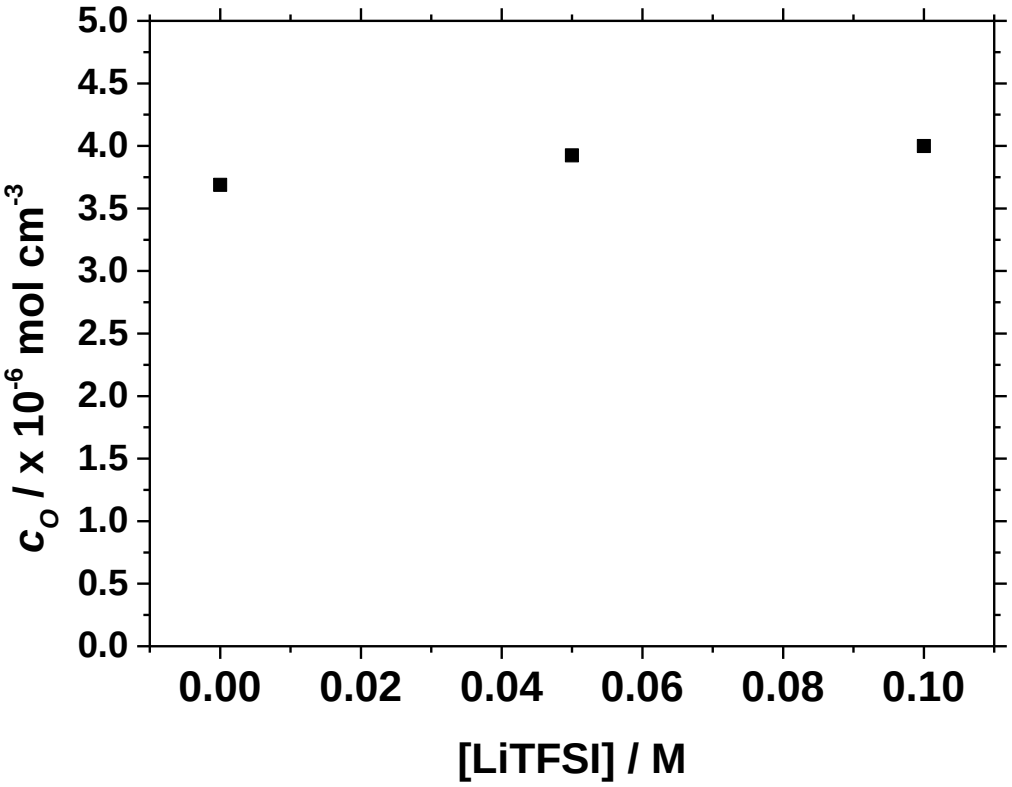

Figure 7.10: final concentration of O_2 in PYR_{14} TFSI *vs*. LiTFSI concentration for five experiments with PYR_{14} TFSI solutions containing no EtV $(OTf)_2$ and various amounts of LiTFSI. These values were determined using the pressure drop in a stagnant solution at room temperature. The O_2 concentrations were calculated using Equation 7.9. The cell was vacuumed for approximately 3-4 hours before the experiment. The O_2 was passed into the cell and the ionic liquid stirred after 30 minutes until the pressure became constant. This was used to calculate these values.

Figure 7.10 shows the final concentration of O_2 dissolved in the ionic liquid when the ionic liquid was fully saturated. These values were determined from the total pressure drop using Equation 7.9. This figure shows that the concentration of LiTFSI has no effect on c_O. There is a slight increase in c_O as the LiTFSI concentration increases,

however this could be due to differences in temperature or the initial pressure between the experiments.

For these experiments it was observed that there was a small time lag between O_2 being passed into the measurement vessel and O_2 starting to diffuse into the ionic liquid. This can most easily be seen in Figure 7.11. This figure shows the amount of O_2 dissolved in the ionic liquid as function of $t^{1/2}$. There is a time lag at the very start of the experiment between O_2 passing into the cell at $t = 0$ and the pressure starting to decrease at approximately 5 seconds. This small delay may be due to the O_2 diffusing over the ionic liquid interface into the ionic liquid. This interfacial diffusion step may have a smaller diffusion coefficient than that of diffusion through the bulk ionic liquid. This small time lag was seen in ionic liquids for all LiTFSI and $EtV^{\bullet+}$ concentrations, indicating that this interfacial step is not affected by the presence of $EtV^{\bullet+}$ or LiTFSI.

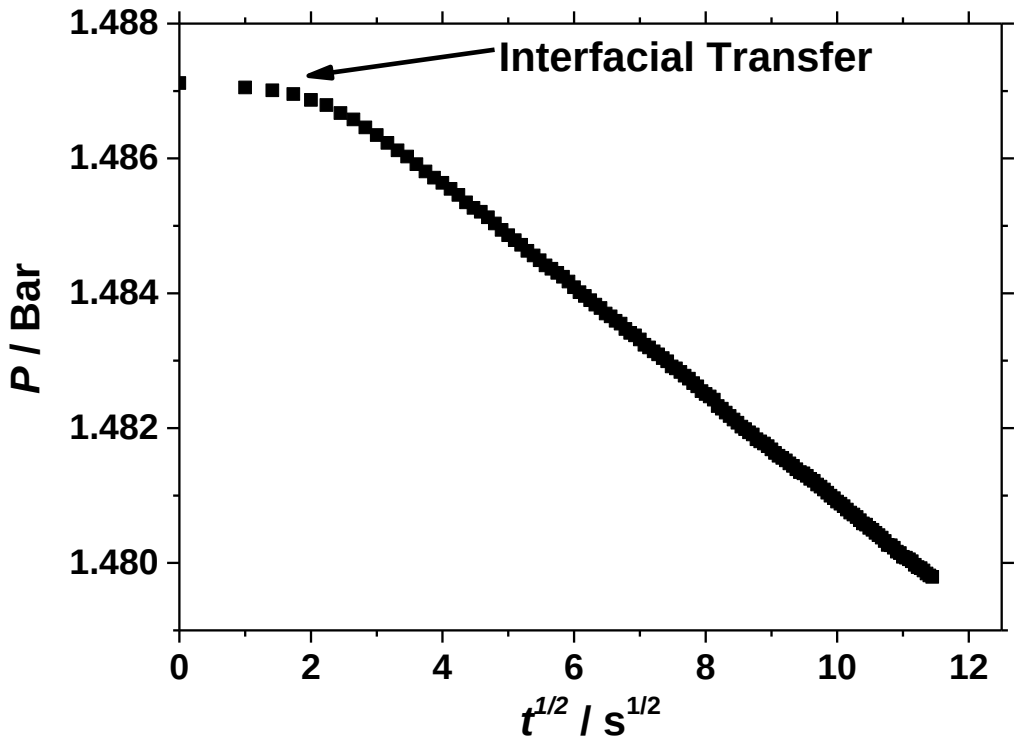

Figure 7.11: graph showing the pressure in the vessel as a function of $t^{1/2}$ for the first 100 seconds of a pressure drop experiment. This experiment used pure PYR_{14} TFSI with no LiTFSI or EtV $(OTf)_2$ The interfacial transfer can be seen between 0 and 2 $s^{1/2}$.

7.3.2 Ionic Liquid Containing Ethyl Viologen Ditriflate

The ionic liquids containing reduced ethyl viologen ditriflate showed a distinct colour change from blue to colourless during the experiment as O_2 diffused into the ionic liquid and oxidised the viologen. One experiment is shown in Figure 7.12. At the start of the experiment at t = 0 the entire solution is blue, at t = 10 mins the interfacial layer of the solution has been decolourised by O_2 diffusing into the ionic liquid. This layer extends further and further down at t = 30 minutes as more O_2 diffuses further into the ionic liquid. At 30 minutes the stirring was started. The increased convection increased the absorption of oxygen and decolourising the remaining solution within 10 minutes, as shown at t = 40 minutes.

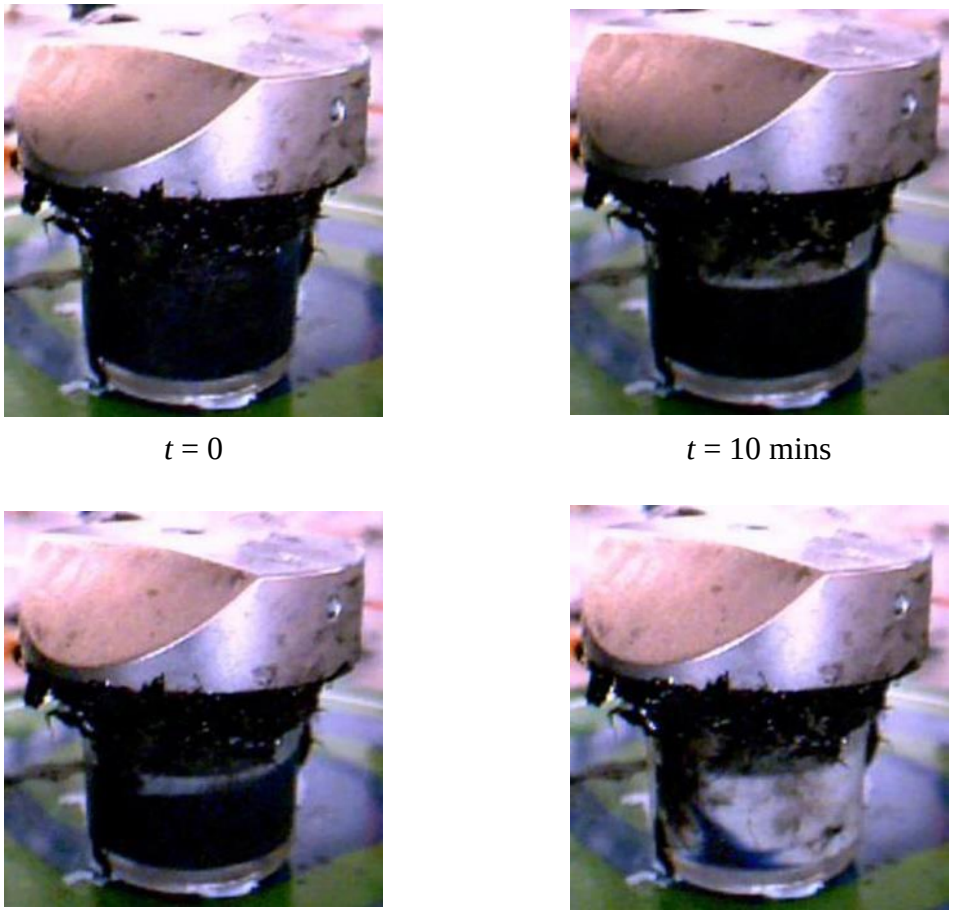

Figure 7.12: pictures at various time intervals in a pressure drop experiment using 0.1 M LiTFSI and 0.1 M $EtV^{\bullet+}$, showing the colour change from blue to white as O_2 diffuses into the solution.

The values of D_O and c_O were calculated in the same manner as previously described. Equation 7.8 assumes that there is only pure diffusion occurring into the ionic liquid from the cell headspace. This equation does not take the heterogeneous reaction between O_2 and $EtV^{\bullet+}$ into account. Because of this the values of D_O for solutions containing $EtV^{\bullet+}$ are actually a pseudo-diffusion coefficients instead of true diffusion coefficients.

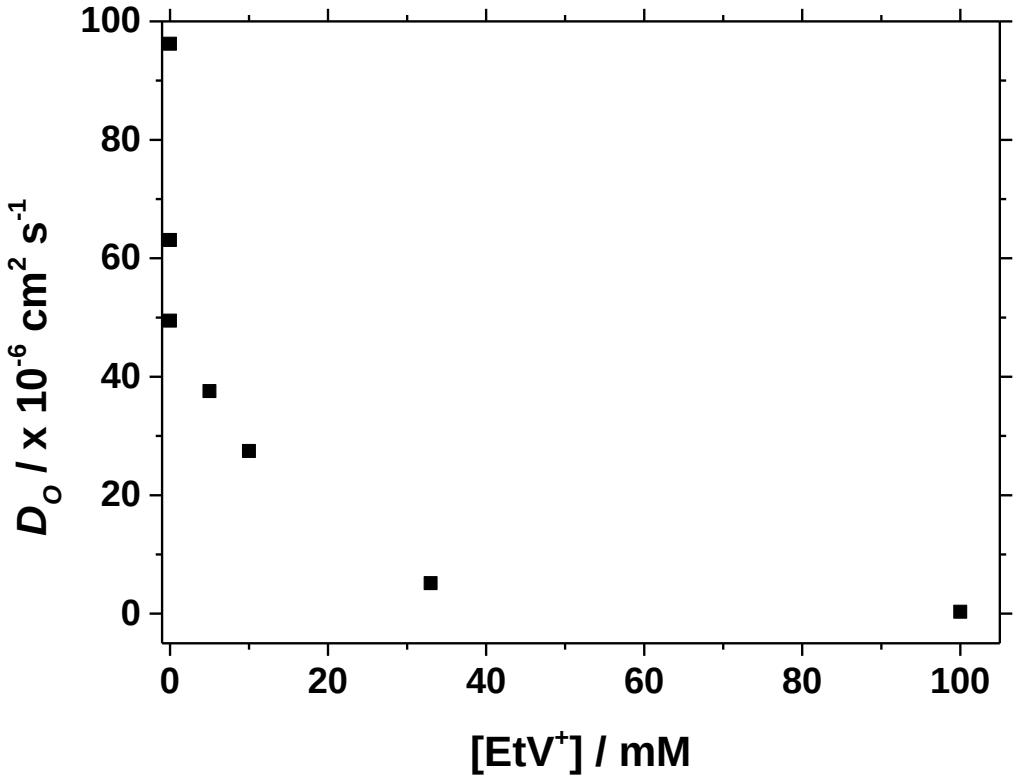

Figure 7.13: diffusion coefficients of O_2 in PYR_{14} TFSI measured *vs*. $EtV^{\bullet+}$ concentration for solutions containing no LiTFSI. The values were calculated using the pressure drop in a stagnant solution at room temperature. The values for diffusion coefficient for solutions containing $EtV^{\bullet+}$ are pseudo-diffusion coefficients. The diffusion coefficients were calculated using Equation 7.8. The cell was vacuumed for approximately 3-4 hours before the experiment. The O_2 was passed into the cell and the ionic liquid held stagnant for 30 minutes to determine these values.

Figure 7.13 shows the values of D_O in ionic liquid containing ethyl viologen ditriflate without LiTFSI. This indicates that D_O rapidly decreases as the concentration of ethyl viologen in the solution increases. It was noted that large amounts of reduced viologen increased the viscosity of the ionic liquid rather substantially. It has been observed that the viscosity of a solution PYR_{14} TFSI containing LiTFSI and EtV^{2+} dramatically

increased upon the addition of lithium titanate. The oxidation of EtV^{2+} by lithiated lithium titanate also liberates additional lithium ions, as shown in Equation 7.2. These lithium ions are present in the ionic liquid and may increase the viscosity of the ionic liquid and decrease D_O. This indicates that the increase in the viscosity may be partly due to an increase in the lithium ions liberated during the viologen reduction as well as the increased concentration of ethyl viologen ditriflate.

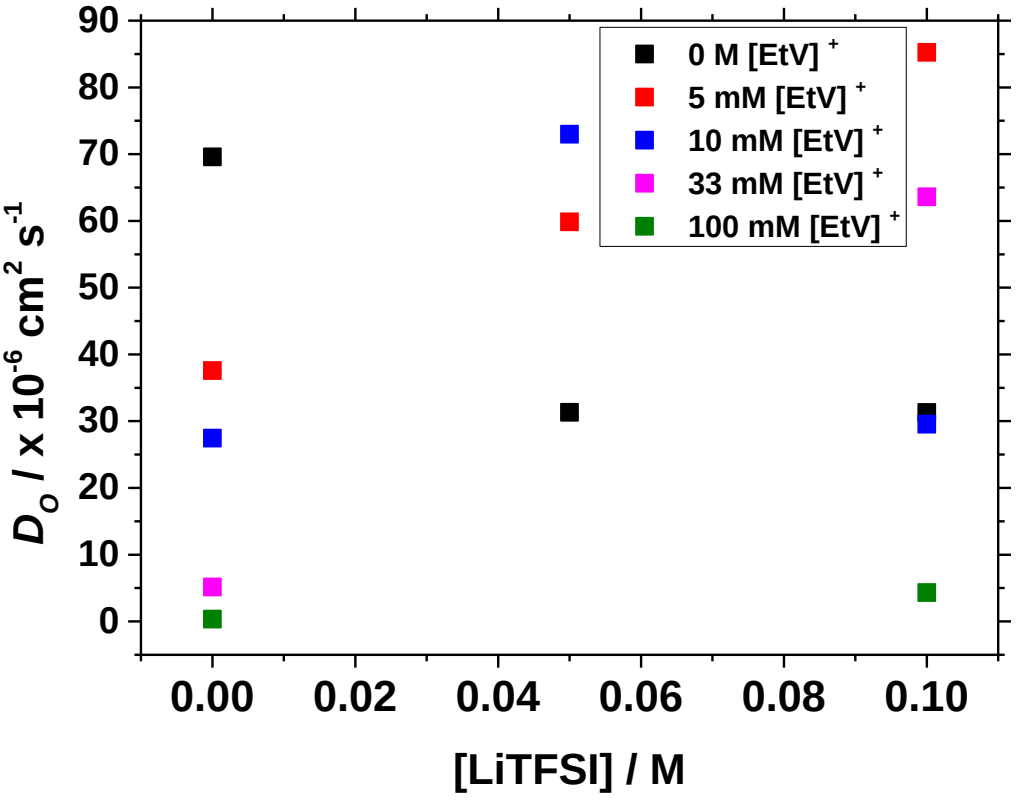

Figure 7.14: average diffusion coefficients of O_2 in PYR_{14} TFSI *vs.* LiTFSI concentration, for data obtained from the pressure drop experiments at room temperature. The values for diffusion coefficient for solutions containing $EtV^{\bullet+}$ are pseudo-diffusion coefficients. The diffusion coefficients were calculated using Equation 7.8. The cell was vacuumed for approximately 3-4 hours before the experiment. The O_2 was passed into the cell and the ionic liquid held stagnant for 30 minutes to determine these values.

Figure 7.14 shows the average values of D_O in the ionic liquid containing varying amounts of LiTFSI and $EtV^{\bullet+}$. This figure shows that for the solutions containing no LiTFSI, as was previously observed D_O decreases as the ethyl viologen concentration increases. For the solutions containing LiTFSI, D_O appears to be greater for solutions containing 5 to 10 mM $EtV^{\bullet+}$. This indicates that the viologen is increasing the rate of removal of O_2 from the atmosphere of the cell through the method shown in Equation

7.1. This also indicates that Li^+ may improve the O_2 reduction of the ethyl viologen. Lithium ions present in the solution are able to react with the superoxide formed in Equation 7.1 to form Li_2O_2. This Li_2O_2 is insoluble in the ionic liquid and precipitates out of the ionic liquid. This chemically removes O_2 from the ionic liquid creating an increasing concentration gradient of O_2. This causes more O_2 to move along the concentration gradient and diffuse faster from the cell headspace into the ionic liquid, increasing the rate of movement of oxygen into the ionic liquid. This indicates that for smaller LiTFSI concentrations, the addition of ethyl viologen does increase the rate of movement of O_2 into PYR_{14} TFSI compared to PYR_{14} TSFI solutions that do not contain ethyl viologen. The addition of $EtV^{\bullet+}$ to PYR_{14} TFSI containing LiTFSI will increase D_O, counteracting the increased viscosity caused by increasing the LiTFSI concentration.

For PYR_{14} TFSI solutions containing greater ethyl viologen concentrations, up to 100 mM of $EtV^{\bullet+}$ the value of D_O decreases dramatically. This may be caused by the much increased viscosity of the ionic liquid due to the high LiTFSI and ethyl viologen concentrations. The increased diffusion caused by the increased amount of $EtV^{\bullet+}$is not enough to counteract the effect of the increased viscosity of the ionic liquid.

These results indicate that the addition of a small amount of ethyl viologen ditriflate, ≈ 5 to 10 mM, at least doubles the rate of diffusion of oxygen into solutions containing a small amount of ionic liquid. However much greater concentrations of ethyl viologen, up to 0.1 M, increase the viscosity of the ionic liquid to such a degree that they decrease the rate of diffusion of O_2 into the solution by up to a factor of 10.

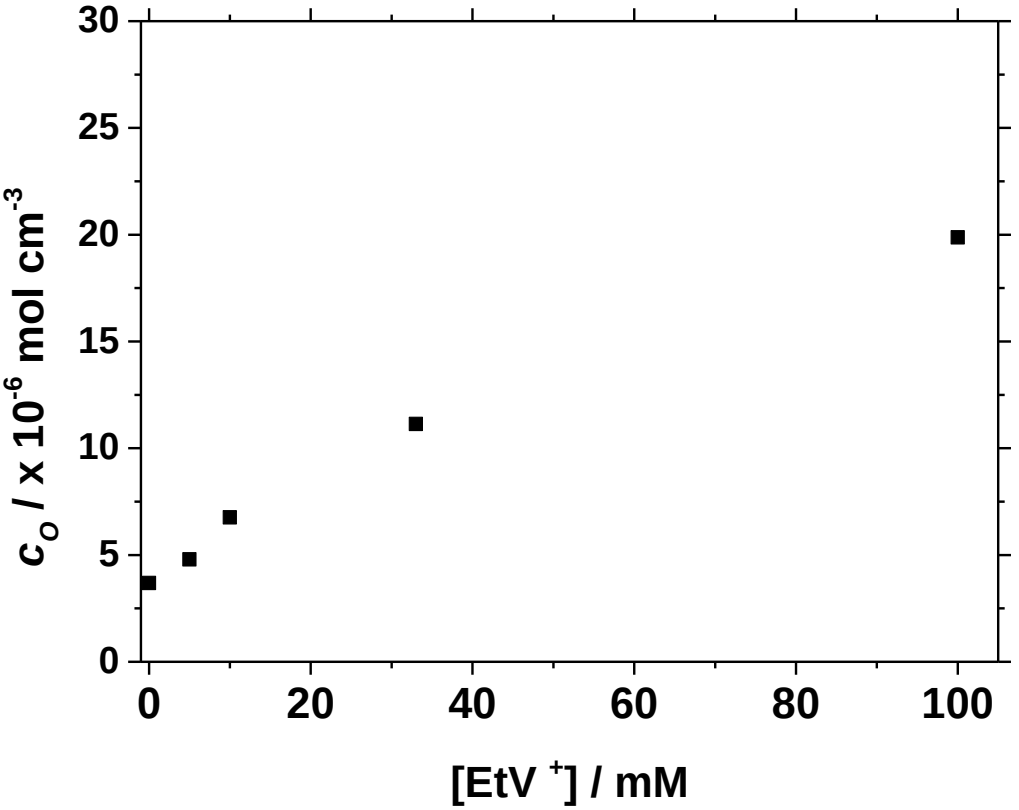

Figure 7.15: final concentration of O_2 dissolved in PYR_{14} TFSI containing no LiTFSI against the $EtV^{\bullet+}$concentration. These values were determined from the pressure drop over the timescale of the experiment at room temperature. The O_2 concentrations were calculated using Equation 7.9. The cell was vacuumed for approximately 3-4 hours before the experiment. The O_2 was passed into the cell and the ionic liquid stirred after 30 minutes until the pressure became constant. This was used to calculate these values.

Figure 7.15 shows the final amount of O_2 dissolved in ionic liquid containing no LiTFSI as a function of the ethyl viologen ditriflate concentration. This shows that the concentration of O_2 in the ionic liquid increases as the concentration of $EtV^{\bullet+}$ increases. This may be caused by the $EtV^{\bullet+}$ increasing the solubility of O_2. The lithium ions present in the solution from the lithium titanate reduction of EtV^{2+} may react with the superoxide formed during the reaction occurring in Equation 7.1 to form Li_2O_2.This would disproportionate out of solution increasing the free volume in the ionic liquid available for the O_2 to dissolve into from the headspace of the cell.

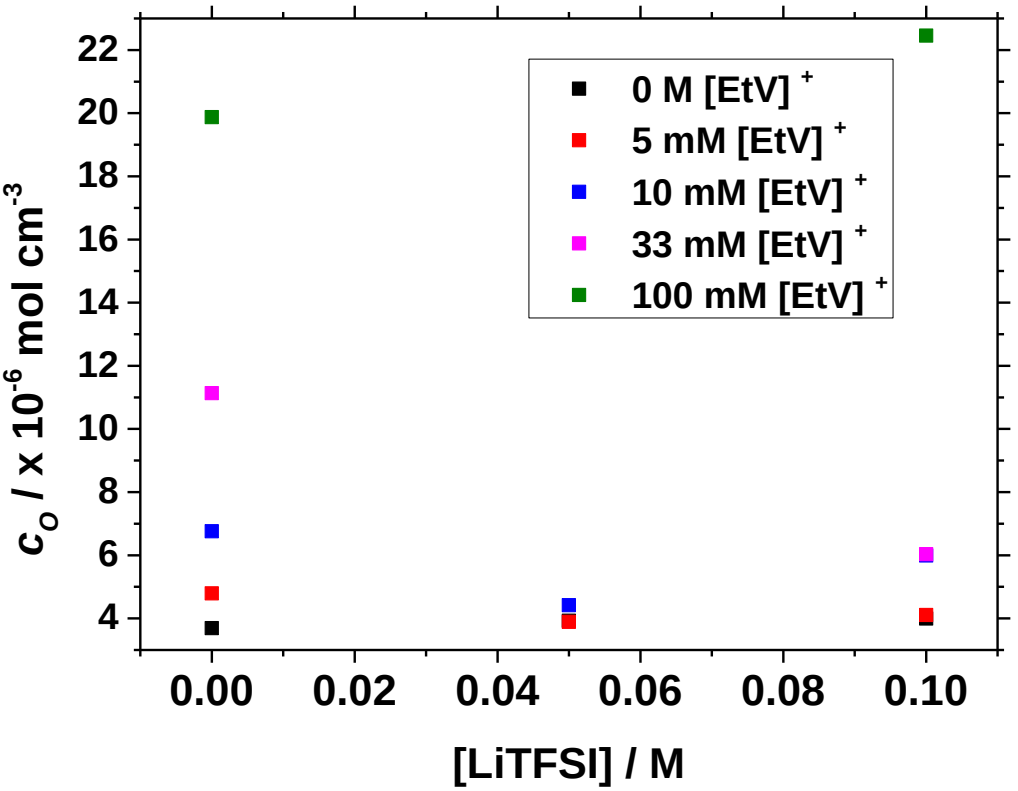

Figure 7.16: the final average concentrations of O_2 in PYR_{14} TFSI, measured against the LiTFSI concentration for solutions containing varying concentrations of $EtV^{\bullet+}$ determined from the pressure drop over the timescale of the experiment at room temperature. The O_2 concentrations were calculated using Equation 7.9. The cell was vacuumed for approximately 3-4 hours before the experiment. The O_2 was passed into the cell and the ionic liquid stirred after 30 minutes until the pressure became constant. This was used to calculate these values.

Figure 7.16 shows the average final concentrations of O_2 dissolved in the ionic liquid as a function of the LiTFSI concentration. This shows that for an ionic liquid which does not contain any LiTFSI, the c_O value increases as the $EtV^{\bullet+}$ concentration increases. This was previously observed in Figure 7.15.

In solutions containing LiTFSI and low ethyl viologen concentrations, 5 to 10 mM of $EtV^{\bullet+}$, c_O is decreased. This may be because the large amount of LiTFSI and ethyl viologen dissolved in the ionic liquid occupies a large amount of free volume in the ionic liquid, leaving less room for the O_2 to dissolve into it.

For solutions containing LiTFSI and high ethyl viologen concentrations, 33 to 100 mM of $EtV^{\bullet+}$, c_O increases greatly compared to that of pure ionic liquid. This may be caused by the superoxide, formed by the reaction of O_2 with the viologen, reacting with the

large amount of lithium present in the solution to form Li_2O_2. The Li_2O_2 precipitates out of the ionic liquid as a white solid on the bottom of the sample chamber. This was observed after all the experiments involving a high $EtV^{\bullet+}$ concentration.

$EtV^{\bullet+}$ reacts with O_2 in a 1:1 ratio. For the solutions containing a low concentration of $EtV^{\bullet+}$, only 5 or 10 mM of O_2 could be removed from the ionic liquid *via* chemical sequestration and reaction with $EtV^{\bullet+}$. This would be a small proportion of the total O_2 removed from the atmosphere of the cell, with a larger proportion removed *via* diffusion into the ionic liquid. The increase in the free volume due to disproportionating lithium peroxide would also be negligible compared to the decrease in the free volume caused by the addition of ethyl viologen ditriflate.

However, for solutions containing a high concentration of $EtV^{\bullet+}$ up to 0.1 M of O_2 could theoretically be removed from the headspace of the cell *via* the reaction with $EtV^{\bullet+}$. This would be greater than the amount removed *via* natural diffusion into the ionic liquid and would increase the amount of oxygen removed from the headspace of the cell. However, the O_2 that reacts with the $EtV^{\bullet+}$ later precipitates out of the ionic liquid as Li_2O_2. Because of this the actual amount of oxygen dissolved in the ionic liquid would be much less than the amount of oxygen removed from the ionic liquid *via* formation and precipitation of lithium peroxide. Therefore these values of c_O in PYR_{14} TFSI are unreliable as they do not indicate how much O_2 was precipitated out of the ionic liquid as Li_2O_2.

7.3.3 Comparison with Electrochemical Measurements

The value of c_O in pure PYR_{14} TFSI determined by the pressure drop experiments is 3.69×10^{-6} mol cm^{-3}. This is very close to the value of 4.34×10^{-6} mol cm^{-3}, determined by potential step chronoamperometry measurements in Chapter 5. This indicates that the values of c_O obtained from the pressure drop experiments are quite reliable.

The D_O measurements shown in Figure 7.9 indicate that D_O decreases as the viscosity increases. This trend was seen in the Chapter 5 as D_O also decreased as the viscosity of the ionic liquids increased. This indicates that the pressure drop experiments are showing the same trends for D_O as the electrochemical experiments do. However the values of D_O in pure PYR_{14} TFSI measured at the pressure drop experiment (69.6×10^{-6}

$cm^2\ s^{-1}$) is 16 times greater than that obtained in Chapter 5 ($4.34 \times 10^{-6}\ cm^2\ s^{-1}$). There may be several explanations for this difference in the values obtained. One reason may be that the pressure drop experiments are giving incorrect values of D_O. This could be due to errors in measuring the internal volume of the cell or the pressure change in the cell. This seems to be unlikely as a small error in measuring the internal volume of the cell has an insignificant effect on the final D_O value and would also affect the measured value of c_O. This difference in D_O is also too large to be caused by differences in temperature between the experiments.

One major difference between the experiments is the pressure at which each experiments were undertaken. The electrochemical experiments were undertaken at normal atmospheric pressure of 1 bar while the pressure drop experiments were undertaken at an initial pressure of 1.3 to 1.4 bar. However there seems to be little correlation between D_O determined by the pressure drop experiments and the initial pressures in the pressure drop cell. The pressure above the interface of an ionic liquid should have no effect on the diffusion coefficient of O_2 moving through the bulk of the ionic liquid.

One of the largest differences between the electrochemical measurements and the pressure measurement experiments was in the preparation of the ionic liquids. In the electrochemical experiments, the PYR_{14} TFSI was heated under a vacuum to remove all Ar, N_2, O_2 and H_2O from the ionic liquid, as even traces of these could affect the D_O value. The ionic liquid was then saturated with O_2 before the potential step chronoamperometry was undertaken. This meant that any single O_2 molecule was diffusing towards the electrode through ionic liquid that was already saturated with other O_2 molecules.

For the pressure measurement experiments, a vacuum was applied to the ionic liquid while it was stirring to remove volatile impurities. O_2 was then added to the cell and the pressure drop was measured over time. The O_2 was diffusing into an ionic liquid that did not contain any other O_2 molecules. This would mean that there was a much greater free volume in this ionic liquid than for the ionic liquid that was saturated with O_2. This free volume allowed O_2 to diffuse through the ionic liquid faster than it would be able to diffuse through an O_2 saturated ionic liquid. This indicates that the value of D_O in PYR_{14} TFSI may be concentration dependent.

This theory was tested in one experiment where pure ionic liquid was saturated with O_2 as was previously done with the other pressure experiments. Once the ionic liquid was fully saturated with O_2, more O_2 was added into the headspace above the cell and the experiment was repeated. When the ionic liquid was once again saturated, more O_2 was added to the headspace and the experiment continued. The pressure trace of this experiment is shown in Figure 7.17.

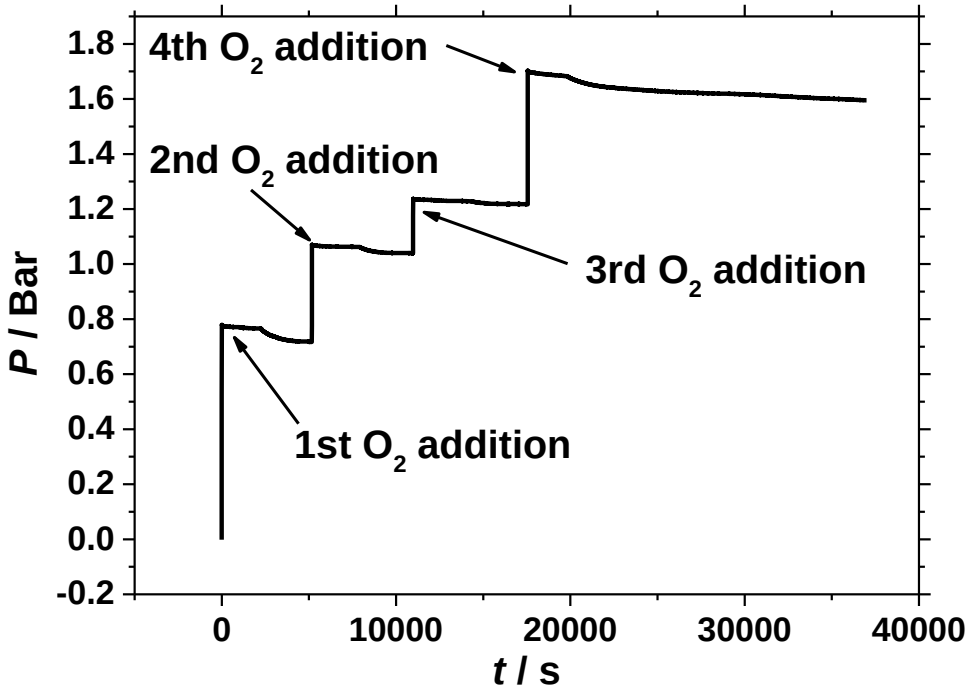

Figure 7.17: graph showing the pressure *vs*. time for the experiment with multiple additions of O_2 to the cell headspace. This experiment used pure PYR_{14} TFSI at room temperature.

For each O_2 addition the values of D_O and c_O were determined using the method described previously. These values are shown in Table 7.1.

Table 7.1: diffusion coefficient and solubilities of O_2 calculated for each addition of O_2.

O_2 Addition	Initial Pressure / Bar	T / K	Diffusion Coefficient of O_2 / $\times 10^{-6}$ cm^2 s^{-1}	O_2 Solubility / x 10^{-6} mol cm^{-3}	k_H / $\times 10^7$ kPa mol^{-1} cm^3
1	0.78	293	19.3	1.8	4.08
2	1.07	294	4.8	2.6	3.99
3	1.24	296	2.3	3.1	3.88
4	1.70	297	5.4	5.4	3.01

Table 7.1 shows that for the first O_2 addition, where there is no O_2 dissolved in the ionic liquid, the value of D_O is 19×10^{-6} cm^2 s^{-1} at 293 K. This is much greater than the electrochemically measured D_O from Chapter 5 of 4.34×10^{-6} cm^2 s^{-1} at 298 K. For the later addition of O_2 to the cell headspace, where O_2 is already dissolved in the ionic liquid, the value of D_O decreases to a similar value to that found during the potential step measurements. This is seen more easily when the value of D_O is plotted against the initial concentration of O_2 dissolved in the ionic liquid as shown in Figure 7.18.

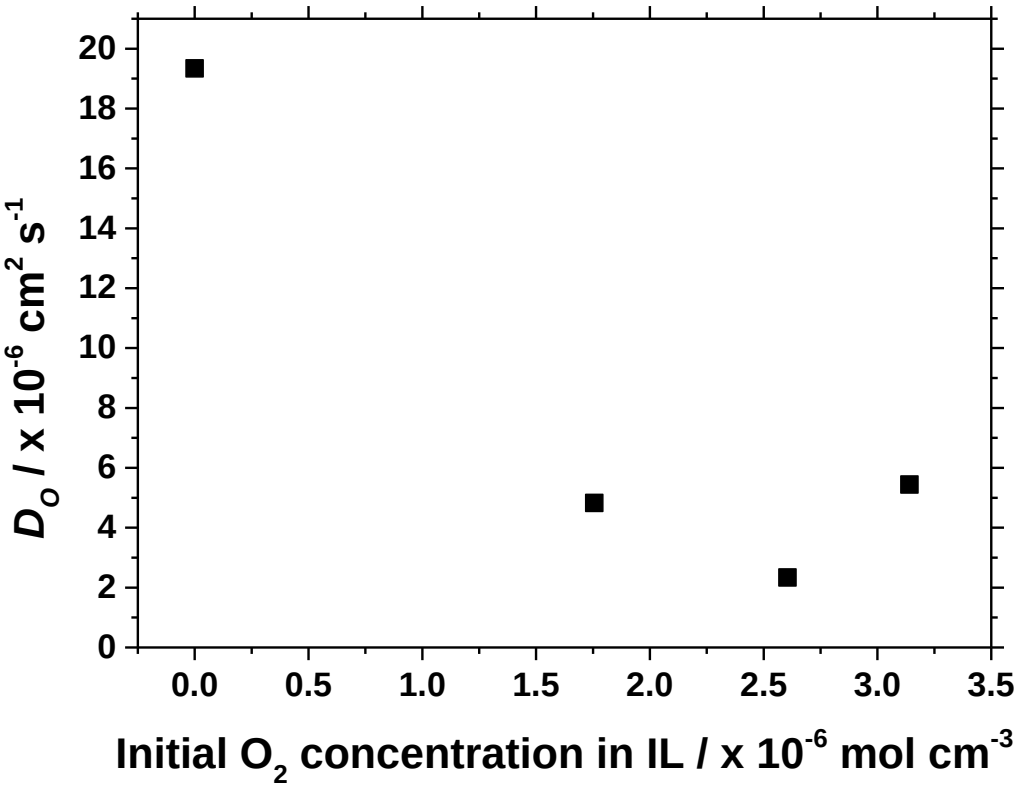

Figure 7.18: graph showing the diffusion coefficient of O_2 against the concentration of O_2 dissolved in the PYR_{14} TFSI before the O_2 was added to the headspace for the experiment shown in Figure 7.17.

This figure indicates that D_O is greatest when there is no O_2 previously dissolved in the ionic liquid. If there is little or no O_2 dissolved in the ionic liquid, there is a greater amount of free volume available for the O_2 to dissolve through, hence the D_O is increased. As the concentration of O_2 in the ionic liquid increases, the free volume in the ionic liquid becomes less, therefore D_O decreases.

This would explain the large differences in D_O measured by different research groups that have different methods of purifying the ionic liquid. Research groups that are using

vacuum to remove impurities would have a greater D_O if the ionic liquid had not been fully saturated with O_2 prior to measurements being undertaken. It has been previously observed that the presence of impurities such as Ar or N_2 in the ionic liquid have decreased the value of D_O.[10] The free volume offers an explanation for this observation.

Further research will have to be done to confirm these results, however the preparation of the ionic liquid and the free volume within it must be taken into account when determining the diffusion coefficients of gases in ionic liquids.

7.4 One-Dimensional Diffusion Experiments Results and Discussion

The experiments using a thin film of PYR_{14} TFSI containing $EtV^{\bullet+}$ were undertaken to determine D_O.

The microscope was used to determine the movement of O_2 through the ionic liquid by observing the movement of a decolourisation front, caused by the oxidation of $EtV^{\bullet+}$ through the ionic liquid. A sample of the movement of the front is shown in the photos in Figure 7.19.

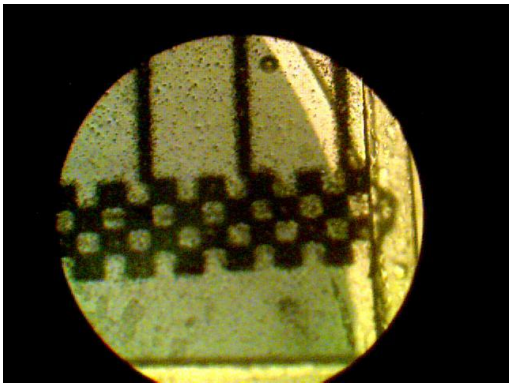

Start t = 0. Front moved 0.35 mm

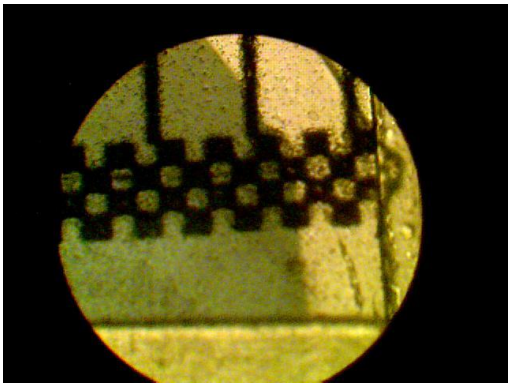

t = 10 min. Front moved 1 mm

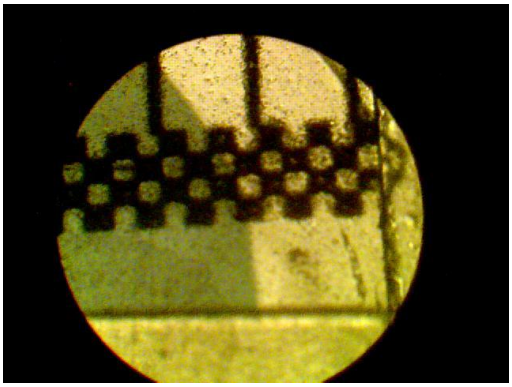

t = 30 mins. Front moved 1.65 mm

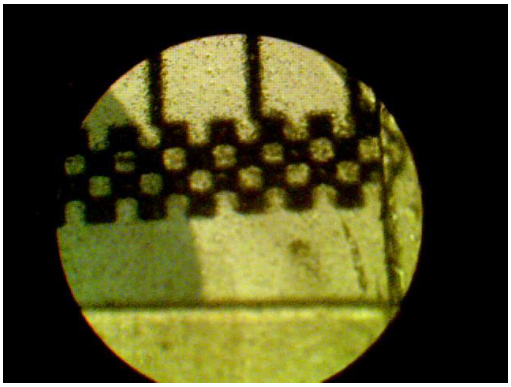

t = 60 mins. Front moved 2.5 mm

Figure 7.19: movement of the decolourisation front through the ionic liquid at various time intervals in a typical slide experiment at room temperature.

The distance the front moved was measured as a function of time. A typical plot is shown in Figure 7.20.

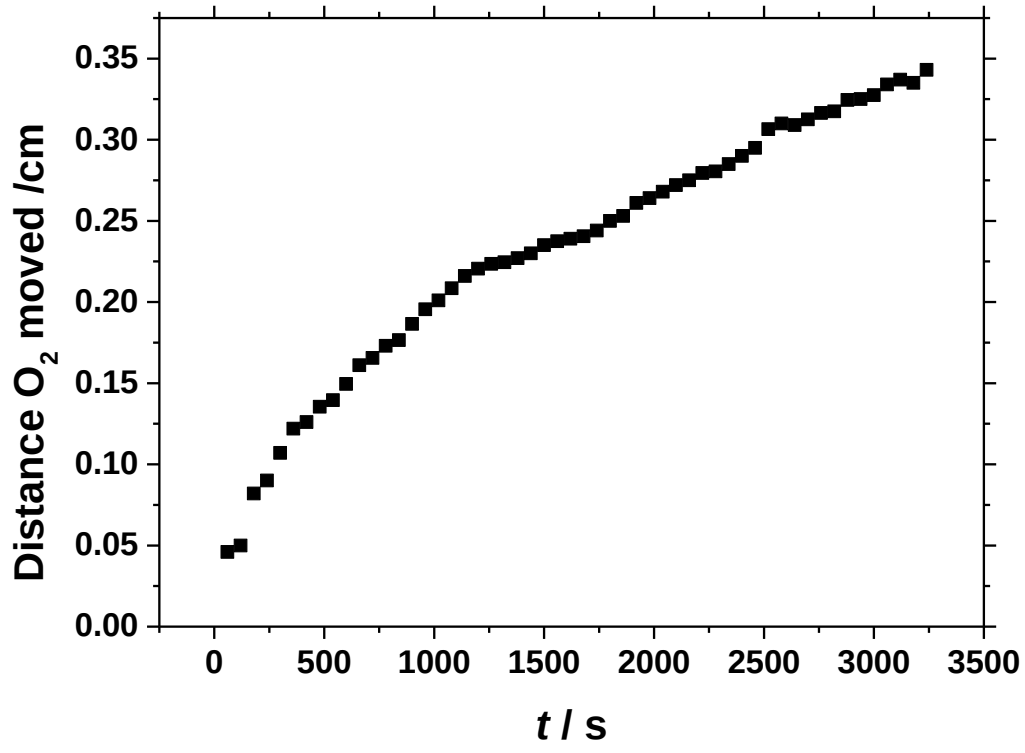

Figure 7.20: distance O_2 moved through the thin film of PYR_{14} TFSI against time for a typical slide experiment using 0.1 M LiTFSI and 5 mM $EtV^{\bullet+}$ at room temperature.

Figure 7.20 shows that the diffusion front moves quickly through the ionic liquid at the beginning of the experiment. As the front moves further away from the interface its speed decreases. This is because the O_2 has an increasingly longer path to diffuse from the oxygen/ionic liquid interface to the edge of the diffusion front where it encounters $EtV^{\bullet+}$. Because of this the concentration of oxygen decreases linearly as the distance from the interface increases. This develops a decreasing concentration gradient away from the interface. This means that increasing the concentration of oxygen at the interface would increase the distance and rate at which oxygen travels from the interface through the thin film.

To further analyse Figure 7.20, the graph was linearized by plotting the distance the reaction front moved against $t^{1/2}$. This is shown in Figure 7.21.

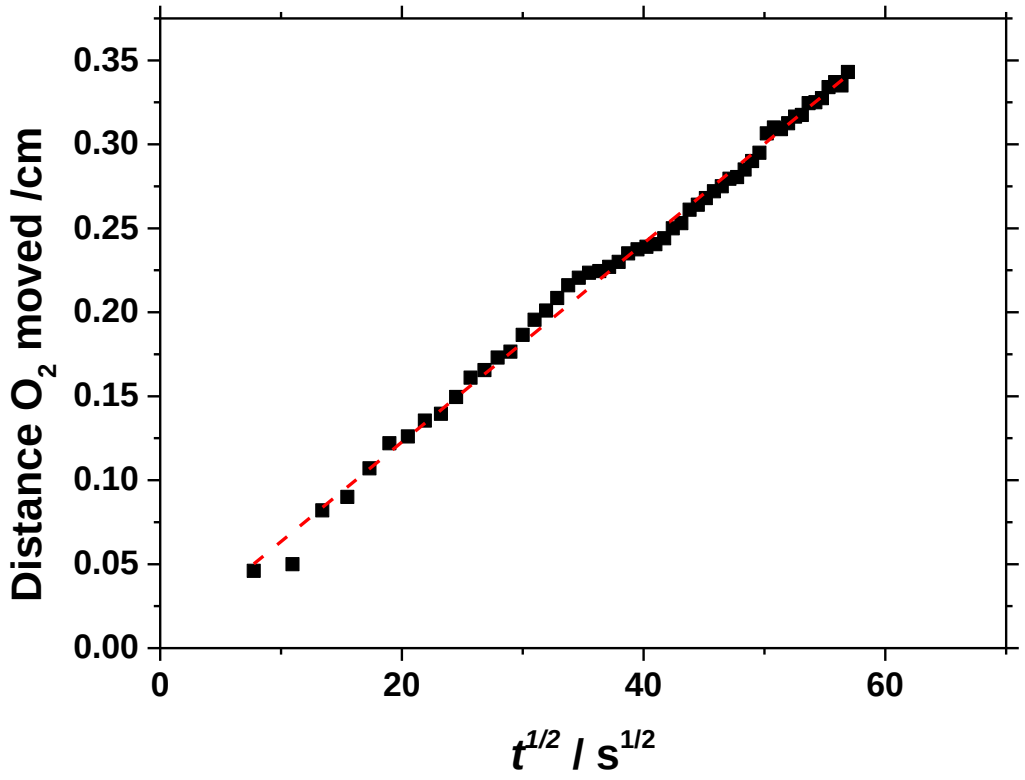

Figure 7.21: distance the front moved against $t^{1/2}$ for the data shown in Figure 7.20. The slope of the plot is equal to $D_O^{1/2}$.

Only the first 20 minutes of each experiment were linearized to reduce the effect of convection which could occur at long timescales.

The fact that the curve shown in Figure 7.20 becomes linearized in Figure 7.21 shows that the distance the front moves is proportional to the square root of the time since the start of the experiment. This can be used to elucidate Equation 7.10 which relates the distance the front moves (x in cm) to the time since the experiment started (t in s) and the diffusion coefficient of O_2 (D_O in $cm^2\ s^{-1}$) in the ionic liquid.

$$x = \sqrt{D_O t} \qquad \textbf{(7.10)}$$

Using Equation 7.10, the slope of the line in Figure 7.21 can be used to find the value of the diffusion coefficient in the ionic liquid. The slopes from the $t^{1/2}$ plot for each slide experiment were used to determine D_O in the ionic liquid.

Figure 7.22 shows D_O plotted against the LiTFSI concentration of the ionic liquid.

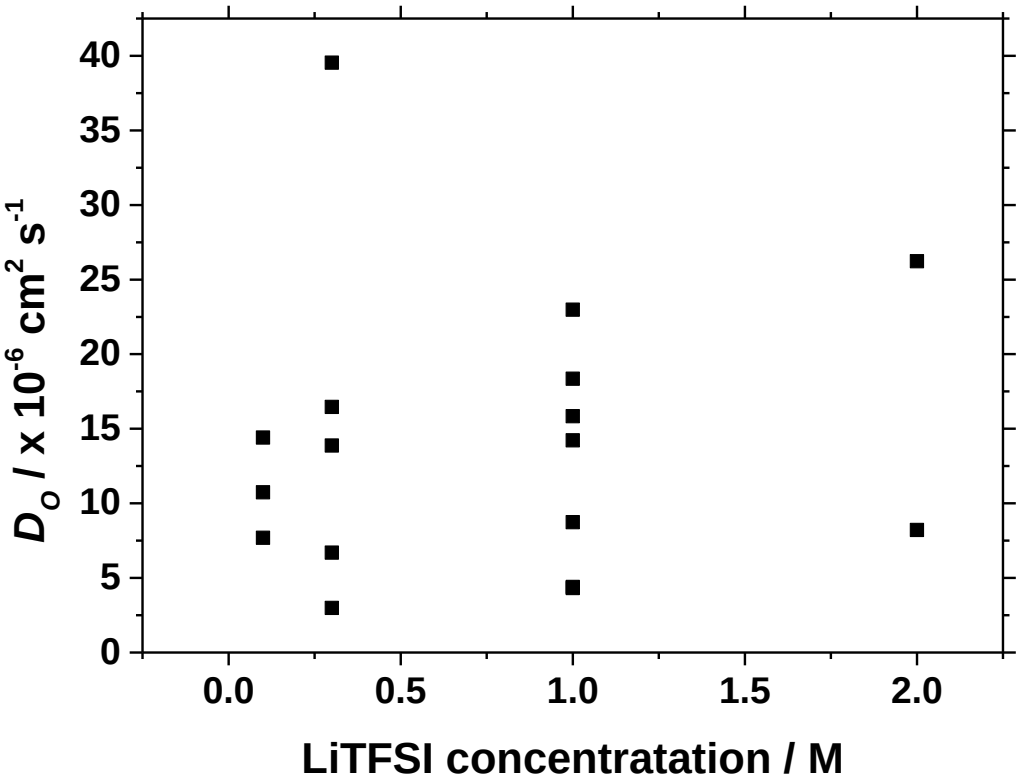

Figure 7.22: diffusion coefficients of O_2 in PYR_{14} TFSI plotted against the LiTFSI concentration, calculated from the one dimensional diffusion slide experiments.

Figure 7.22 shows that there is a large amount of variation between the results obtained from several experiments at the same lithium concentration. This variation may be due to differences in the temperature at which the experiment was undertaken or slight differences in the concentration of $EtV^{\bullet+}$. Another cause could be slight differences in the thickness of the ionic liquid film. There may have been slight variations in the thickness of the parafilm between experiments, which would give a greater volume of ionic liquid for O_2 to diffuse through.

The large variation in the results makes it difficult to discern any clear trends with respect to the effect of LiTFSI concentration on D_O. The average values of D_O for each lithium concentration are given in Figure 7.23.

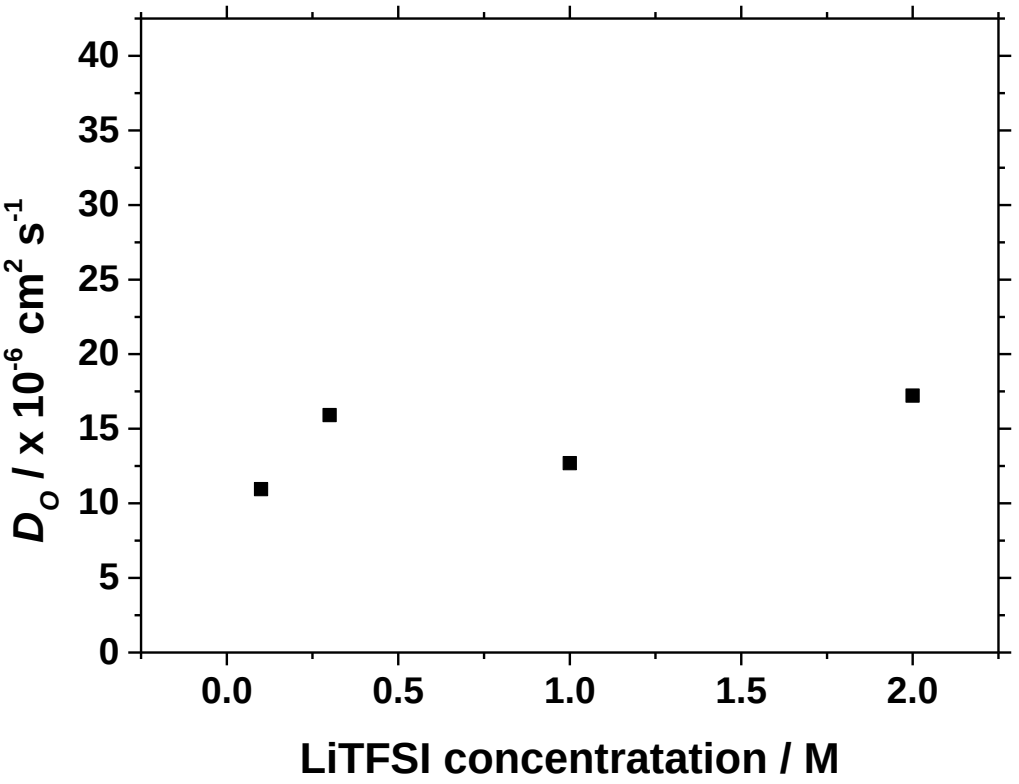

Figure 7.23: average diffusion coefficients of O_2 in PYR_{14} TFSI plotted against the LiTFSI concentration, calculated from the one dimensional diffusion slide experiments.

Figure 7.23 shows a slight increase in D_O as the LiTFSI concentration of PYR_{14} TFSI increases. This may be due to the lithium ions reacting with the superoxide formed by the reaction of O_2 and $EtV^{\bullet+}$. The Li_2O_2 formed may precipitate out of the ionic liquid, leaving more free volume available for O_2 to diffuse through. However due to the large variation between the values of D_O obtained, these results will need to be confirmed with further experiments before any certain conclusions can be reached.

These experiments could be repeated controlling the temperature of the cell. Further improvements could also be made by keeping the thickness of the parafilm constant to ensure a reproducible thickness between the slides.

7.5 Conclusions

Experiments were undertaken to investigate the use of a pressure drop cell to determine D_O and c_O in ionic liquid containing LiTFSI. This showed that the determination of D_O and c_O in PYR_{14} TFSI containing LiTFSI is possible using the pressure drop measurements. The effects of ethyl viologen ditriflate on D_O and c_O were also able to be determined using this method. It was found that a small concentration of $EtV^{\bullet+}$ was able to increase the rate of oxygen diffusion into ionic liquid, however large $EtV^{\bullet+}$ concentrations decrease the rate of O_2 diffusion into the ionic liquid. O_2 solubility is increased in the presence of $EtV^{\bullet+}$ due to the removal of O_2 by reaction with Li^+ to form Li_2O_2. The values of D_O determined through the pressure measurement experiments are greater than those determined through electrochemical measurements. This may be due to the vacuum used in the pressure measurement experiments removing all volatile components such as N_2 or Ar from the ionic liquid, increasing the free volume of the ionic liquid. This would give a greater volume for O_2 to diffuse into the ionic liquid.

Experiments using a thin film of ionic liquid and $EtV^{\bullet+}$ as an indicator were done to determine D_O in the ionic liquid. It was found that the rate of oxygen diffusion is related to the square root of the time since the start of the experiment. These results showed a large amount of variation in the values obtained. More investigation is required before any reliable conclusions can be drawn from the results of the slide experiments.

The aims of these experiments were to determine the diffusion coefficient and solubility of oxygen in PYR_{14} TFSI containing LiTFSI, as well as to determine the effect of ethyl viologen ditriflate on the transport of oxygen into the ionic liquid. The diffusion coefficient and solubility of O_2 in ionic liquids containing LiTFSI has been successfully calculated. Also it has been found that ethyl viologen ditriflate increases the rate of O_2 absorption and amount of O_2 removed from the cell atmosphere. Both of these objectives have been successfully completed.

7.6 References

[1] D. E. Camper, C. Becker, C. Koval, R. D. Noble, *Ind. Eng. Chem. Res.* **2006**, *45*, 445–450.

[2] P. Husson-Borg, V. Majer, M. F. Costa Gomes, *J. Chem. Eng. Data* **2003**, *48*, 480–485.

[3] J. Jacquemin, M. F. Costa Gomes, P. Husson, V. Majer, *J. Chem. Thermodyn.* **2006**, *38*, 490–502.

[4] J. L. Anthony, E. J. Maginn, J. F. Brennecke, *J. Phys. Chem. B* **2002**, *106*, 7315–7320.

[5] J. L. Anthony, E. J. Maginn, J. F. Brennecke, *J. Phys. Chem. B* **2001**, *105*, 10942–10949.

[6] J. L. Anthony, J. L. Anderson, E. J. Maginn, J. F. Brennecke, *J. Phys. Chem. B* **2005**, *109*, 6366–6374.

[7] R. Condemarin, P. Scovazzo, *Chem. Eng. J.* **2009**, *147*, 51–57.

[8] M. J. Lacey, J. T. Frith, J. R. Owen, *Electrochem. Commun.* **2013**, *26*, 74–76.

[9] L. E. Barrosse-Antle, L. Aldous, C. Hardacre, A. M. Bond, R. G. Compton, *J. Phys. Chem. C* **2009**, *113*, 7750–7754.

8. Conclusions and Further Work

8.1 Conclusions

Within this thesis, many different experiments have been undertaken to study the electrochemical reduction of O_2 in ionic liquids. The aim of this thesis was to determine the suitability of several ionic liquids for use in a working lithium-air battery.

Chapter 2 investigated the electrochemical reduction of O_2 in the ionic liquid PYR_{14} TFSI using cyclic voltammetry. Oxygen reduction in pyrrolidinium based ionic liquids occurred by two one-electron reduction reactions. The first reduction occurred from O_2 to superoxide while the second reduction occurred from superoxide to peroxide. These reactions were reversible, indicating that the superoxide is stable in PYR_{14} TFSI. The values of the diffusion coefficient (D_O) and solubility (c_O) of O_2 in the ionic liquids were determined using potential step chronoamperometry at a microdisc electrode. These results showed that as the temperature of the ionic liquids increased the value of D_O increased as well, due to a decrease in the viscosity of the ionic liquid caused by the increasing temperature. The increasing temperature also decreased the value of c_O for the ionic liquid, due to the decreasing solubility of O_2. The values of D_O and c_O were combined to give the diffusion coefficient-solubility product, a measure directly proportional to the steady state current of the battery. This value was found to increase with temperature, due to the increase in D_O as the temperature increases.

Chapter 3 investigated O_2 reduction in several pyrrolidinium and imidazolium based ionic liquids by cyclic voltammetry at a microdisc electrode. These experiments showed that the reduction of oxygen is irreversible in imidazolium ionic liquids. The O_2 is reduced to superoxide which reacts with the labile proton on the imidazolium cation. This removes the superoxide from the solution and makes the reaction irreversible in the ionic liquid. Several pyrrolidinium based ionic liquids were provided by our partner institution. O_2 reduction in pyrrolidinium ionic liquids was found to occur in the same manner as in PYR_{14} TFSI, as seen in Chapter 2. It was determined that superoxide was stable in all of the pyrrolidinium ionic liquids analysed with the exception of the ionic liquid that contained FSI anions, which showed no superoxide oxidation peaks on the reverse scan. Because of the need for a reversible oxygen reduction reaction, ionic liquids that contain either imidazolium cations or FSI anions were determined to be unsuitable for use in the LABOHR battery.

Chapter 4 investigated the use of electrochemical impedance spectroscopy to study the reduction of O_2 in PYR_{14} TFSI and C_2MIM TFSI. The Nyquist plots taken at potentials where O_2 reduction occurs corresponded to a circuit containing two resistor/capacitor parallel combinations and a Warburg element corresponding to a hemispherical diffusion field with a transmissive boundary, due to O_2 diffusion towards the working electrode. Impedance measurements taken at different potentials showed that the onset potential of the O_2 reduction reaction can be observed by a large decrease in the charge transfer resistance and the onset of Warburg diffusion of O_2 towards the electrode.

Chapter 5 investigated the diffusion coefficient and solubility of O_2 in four of the pyrrolidinium based room temperature ionic liquids at various temperatures by using potential step chronoamperometry at gold and platinum microdisc electrodes. These results showed that care must be taken to fully saturate the ionic liquid with O_2 prior to undertaking the experiment. The solutions that were bubbled with O_2 at each temperature gave much more reproducible results than solutions that had allowed O_2 to diffuse naturally into the ionic liquid. The values of D_O, c_O and $D_O c_O$ calculated showed the same trends observed in PYR_{14} TFSI.

It was found that the highly fluorinated ionic liquids, PYR_{14} BETI and PYR_{14} IM_{14}, had the greatest values of c_O as fluorinated compounds have a higher O_2 solubility, however they had much lower values of D_O due to the much smaller viscosity caused by the increased anion size. Overall at the LABOHR cell operating temperature of 333 K the PYR_{14} IM_{14} ionic liquid gave the greatest value of $D_O c_O$. This makes it the most suitable ionic liquid for the LABOHR cell based on O_2 transport properties alone.

Chapter 6 showed the attempts to determine the values of D_O, c_O and $D_O c_O$ in ionic liquids containing large amounts of LiTFSI. The presence of Li^+ ions in the ionic liquids causes the formation of lithium peroxide upon the reduction of O_2. This insoluble, electrically insulating compound can precipitate on the surface of the microdisc electrode. It was shown that this occurs during the initial cyclic voltammogram sweep, making potential step chronoamperometry impossible to undertake. The Lewis acid tris(pentafluorophenyl)borane (TPFPB) was added to the ionic liquid in an attempt to increase the solubility of Li_2O_2 in the ionic liquid. It was found that TPFPB does increase the solubility of Li_2O_2 and can increase the speed at which an electrode passivates. However it was also found that TPFPB dramatically increases the viscosity

of the ionic liquid, making accurate determination of D_O impossible. TPFPB was also found to be rather volatile, with a portion being lost when bubbling the ionic liquid with O_2, reducing its effectiveness. Because of this, no further research was done on this method.

Chapter 7 showed attempts to determine D_O and c_O in ionic liquid containing LiTFSI using a pressure drop measurement. This chapter also investigated the effect of the redox shuttle compound ethyl viologen ditriflate on the values of D_O and c_O. EtV $(OTf)_2$ was also used as an indicator to determine the values of D_O and c_O using a thin film of PYR_{14} TFSI. It was discovered that the values of c_O determined using the pressure drop technique were similar to those obtained using electrochemical techniques. However the value of D_O was much greater than those obtained using electrochemical measurements. This may be due to the free volume of the ionic liquid. The pressure drop experiments were prepared by vacuuming the cell removing all the O_2 from the ionic liquid and increasing the free volume of the ionic liquid. This increased volume allows O_2 to diffuse faster into the ionic liquid than it would in an ionic liquid that is already saturated with O_2. This gives a larger value of D_O.

It was found that small amounts of EtV $(OTf)_2$ could increase the rate of O_2 diffusion into the ionic liquid by removing O_2 from the atmosphere of the cell *via* a chemical reaction. However larger amounts of EtV $(OTf)_2$ decreased the rate of O_2 diffusion by increasing the viscosity of the ionic liquid substantially. EtV$(OTf)_2$ did increase the value of c_O by reducing O_2 which then reacted with LiTFSI to precipitate out of solution as Li_2O_2. These results indicate that a small amount of a redox shuttle compound may be beneficial to increase the diffusion coefficient and solubility of O_2 in the LABOHR battery.

Most of the aims and objectives of this thesis have been successfully achieved. The mechanism of the oxygen reduction reaction in pyrrolidinium based ionic liquids and imidazolium based ionic liquids has been successfully determined. The diffusion coefficients and solubilities of oxygen in several pyrrolidinium based ionic liquids have also been determined using PSCA at a microdisc electrode. The oxygen reduction reaction has been studied in PYR_{14} TFSI and C_2MIM TFSI using electrochemical impedance spectroscopy and the diffusion coefficient of oxygen has been determined in PYR_{14} TFSI containing LiTFSI using a pressure drop method. The only major objective

that was not achieved was the determination of the diffusion coefficient and solubility of oxygen in PYR_{14} TFSI containing LiTFSI by using PSCA at a microdisc electrode. This was due to the passivation of the microelectrode with lithium peroxide. The values were later determined using a pressure drop method in Chapter 7.

This thesis has provided a large amount of data for the LABOHR project. The increased understanding of the oxygen reduction mechanism will help with the development of the battery. The values of the diffusion coefficient and solubility of oxygen in the pyrrolidinium based ionic liquids will help to determine which ionic liquid is most suitable to be used as the electrolyte and oxygen transport medium in the battery. The mechanism of oxygen reduction and values of the diffusion coefficient and solubility of oxygen in PYR_{14} TFSI containing LiTFSI will enable more understanding of how the oxygen reduction will occur in the high lithium environment of the battery.

Overall the experiments shown in this thesis have been successful and have shown many valuable insights into the chemistry occurring in the lithium-air battery and the reduction of oxygen in ionic liquids. The data provided by these experiments will help the development of the LABOHR battery.

8.2 Further Work

There are many improvements and further experiments which could be undertaken to improve and build upon the research done in this thesis.

The cyclic voltammetry and potential step chronoamperometry could be undertaken at a greater number of temperatures and using different ionic liquids to determine if any ionic liquids have greater diffusion coefficients than those investigated in this thesis.

A substantial amount of further investigation could be undertaken into the use of electrochemical impedance spectroscopy to investigate the oxygen reduction reaction. A full analysis of the SPEIS impedance done in PYR_{14} TFSI and C_2MIM TFSI ionic liquid. Further investigation could be undertaken using different electrode, frequencies and bias potentials. The change in the equivalent circuit at the onset potential of the oxygen reduction reaction could be further studied using smaller bias potential steps.

Further investigation could be undertaken into the pressure drop experiments. Controlling the temperature of these experiments would increase the reliability of the experiments. Further experimentation could be done using different ionic liquids and gases as well as investigating the free volume of the ionic liquid by testing various degrees of saturation of the ionic liquid. Other redox shuttle compounds could also be investigated to further enhance D_O and c_O in the ionic liquid.

Alternative methods of determining the values of D_O and c_O in an ionic liquid containing LiTFSI could be investigated. The use of high surface area nanostructured working electrodes could be investigated, as the high surface area would make them less likely to become passivated with Li_2O_2. Alternatively, other Lewis acid compounds could be investigated to increase the solubility of Li_2O_2 in the ionic liquid.